| | |
|---|---|
| **Titre:**<br>Title: | Exploring Ferrite-Loaded SIW Topology and Demonstrating Full-Duplex Transceiver Architecture for 5G Wireless Systems and Beyond |
| **Auteur:**<br>Author: | Amir Afshani Aghajari |
| **Date:** | 2021 |
| **Type:** | Mémoire ou thèse / Dissertation or Thesis |
| **Référence:**<br>Citation: | Afshani Aghajari, A. (2021). Exploring Ferrite-Loaded SIW Topology and Demonstrating Full-Duplex Transceiver Architecture for 5G Wireless Systems and Beyond [Thèse de doctorat, Polytechnique Montréal]. PolyPublie. https://publications.polymtl.ca/6648/ |

| | |
|---|---|
| **URL de PolyPublie:**<br>PolyPublie URL: | https://publications.polymtl.ca/6648/ |
| **Directeurs de recherche:**<br>Advisors: | Ke Wu |
| **Programme:**<br>Program: | Génie électrique |

**POLYTECHNIQUE MONTRÉAL**

affiliée à l'Université de Montréal

# Exploring ferrite-loaded SIW topology and demonstrating full-duplex transceiver architecture for 5G wireless systems and beyond

**AMIR AFSHANI AGHAJARI**

Département de génie électrique

Thèse présentée en vue de l'obtention du diplôme de *Philosophiæ Doctor*

Génie électrique

June 2021

# POLYTECHNIQUE MONTRÉAL

affiliée à l'Université de Montréal

Cette thèse intitulée:

# Exploring ferrite-loaded SIW topology and demonstrating full-duplex transceiver architecture for 5G wireless systems and beyond

présentée par **Amir AFSHANI AGHAJARI**
en vue de l'obtention du diplôme de *Philosophiæ Doctor*
a été dûment acceptée par le jury d'examen constitué de:

**Jean-Jacques LAURIN**, président
**Ke WU**, membre et directeur de recherche
**Gunes KARABULUT-KURT**, membre
**George V. ELEFTHERIADES**, membre externe

# DEDICATION

*To my beloved wife Pegah who I love her,*

*and supported me in this journey.*

*and*

*To my dear family who I miss them.*

# ACKNOWLEDGEMENTS

I would like to express my sincere gratitude to my supervisor Prof. Ke Wu for his continuous support and motivation. I am very grateful for his excellent guidance, encouragement, and patience during this long Ph.D. journey. I would also like to express my heartfelt gratitude to him for his constant availability for the financial and scientific support I received. He taught me how to turn into a researcher aspiring high goals and enjoying everyday research life.

My sincere thanks and gratitude also go to the jury members, namely Prof. Jean-Jacques Laurin, Prof. Gunes Karabulut-Kurt, Prof. George V. Eleftheriades, and Jolanta-Ewa Sapieha for agreeing to be members of the examination board of my Ph.D. thesis.

In addition, I want to show my appreciation to my friends, colleagues, and the staff in Poly-Grames for their valuable instrumental support and advice in the development and publication of my research.

I also would like to acknowledge the financial support from the Fonds de recherche du Québec Nature et technologies (FRQNT) in the form of a Doctoral Fellowship.

I would like to express my deepest gratitude and love to my parents, who have provided me with emotional support in my life and even in my Ph.D. duration from a long distance.

Last but not least, I would like to thank my dear wife, Pegah, for her ongoing and endless support, love, and kindness that accompanied me through this long journey. This would not be possible without her.

# RÉSUMÉ

Le transpondeur duplexe intégral (ou FD, pour « *full-duplex transceiver* ») est un candidat prometteur pour la 5G et les systèmes sans-fil futurs, car les avantages inhérents aux systèmes FD seraient en mesure d'adresser les demandes complexes des systèmes 5G. Il est connu que les systèmes FD peuvent doubler la largeur de bande, diminuer les latences du système et diminuer les congestions du réseau, ce qui contribue à améliorer la fiabilité et les performances. Le principe d'une communication FD dépend de la transmission et réception simultanée d'un signal, contrairement à une transmission semi-duplexe, basée sur un duplexeur dans le domaine fréquentiel (FDD pour « *frequency division duplexing* ») ou dans le domaine temporel (TDD pour « *time domain division duplexing* »). Cependant, le développement d'un transpondeur FD pose un problème fondamental, c'est-à-dire une interférence du transmetteur avec lui-même (SI pour « *self-interference* »), ce qui peut dégrader ou saturer l'opération du receveur. En conséquence, nous devons annuler le signal SI du receveur pour obtenir un design FD efficace.

Dans cette thèse, nous développons et démontrons un component passif en technologie guide d'onde intégré (SIW pour « *substrate integrated waveguide* ») capable de fournir une isolation de plus de 70 dB entre les canaux du transmetteur et du receveur (T/R pour « *transmitter and receiver channels* »), sur une plage de 80 MHz, dans une bande de fréquence sous les 6 GHz, en utilisant une antenne à double polarisation. À notre connaissance, l'isolation obtenue ici est la meilleure rapportée en configuration passive dans le domaine analogue. Le composant proposé utilise deux modes orthogonaux et deux polarisations pour obtenir une isolation importante. La solution développée ici excède les performances des méthodologies proposées dans la littérature, et ce de plusieurs façons. Premièrement, le composant proposé, un circulateur à modes duals (DM pour « *dual mode* ») et une antenne à polarisation duale (DP, pour « *dual polarized* ») est passif, linéaire et faible bruit. Ceci est en contraste avec les solutions FD existantes, qui nécessitent des circuits actifs. De plus, la technologie utilisée est SIW, qui peut soutenir de plus grandes puissances en comparaison avec les circuits actifs ou les circuits RF intégrés. Deuxièmement, les solutions actuelles de FD impliquent le design additionnel de components RF, RF intégrés, circuits ou chaines de transmission, ce qui résulte en une plus grande complexité et une consommation plus importante de puissance. Cependant, la solution proposée ici possède la même complexité que les transpondeurs typiques, à ceci près que le circulateur monomode et l'antenne monomode sont remplacés par un circulateur à mode dual et une antenne à polarisation duale. La solution proposée ici est simple, faible coût et efficace en comparaison avec les autres solutions. Troisièmement, le composant proposé possède un mécanisme d'auto-ajustement qui peut être utilisé pour ajuster la fréquence d'opération du dispositif et la bande de fréquence, ce qui résulte en une isolation importante. Finalement, notre méthodologie permet une opération FD sans sacrifier la figure de mérite du transpondeur, au contraire des autres architectures FD. En d'autres termes, le transpondeur FD réalisé ici surclasse les autres transpondeurs rapportés dans la littérature.

Cependant, en plus des avantages rapportés ci-haut pour notre système, nous avons apporté plusieurs nouvelles contributions, notamment de nouvelles théories et de nouveaux composants. Nous avons proposé une théorie pour deux nouveaux composants non-réciproques basés sur les ferrites. En effet, deux composants basés sur différentes topologies peuvent convertir les modes TE10/TE20 en modes TE20/TE10 seulement dans une direction, alors que la propagation des modes dans la direction opposée est conservée. Des circulateurs basés sur cette conversion non-réciproque de modes ont été conçus, prototypés et démontrés pour la première fois.

De plus, nous avons investigué et développé une théorie pouvant être utilisée pour le design de composants non-réciproques multi-modes. En utilisant cette théorie, nous avons démontré, pour la première fois, un prototype de circulateur en mode dual ainsi qu'un gyrateur triple-mode. Aussi, basé sur les techniques SIW multi-modes, nous avons proposé, étudié et démontré une nouvelle antenne à double polarisation pouvant être excitée par une structure SIW à mode dual. La nouvelle antenne et le nouveau circulateur ont été intégrés et dûment modifiés pour créer un composant permettant d'obtenir une isolation importante dans le domaine analogique, nécessaire pour la fabrication de systèmes FD.

Nous anticipons que notre solution aura un impact significatif sur l'architecture des systèmes FD déployés pour la 5G. Puisque notre solution rend pratique les systèmes FD, nous entrevoyons un déploiement grande échelle de systèmes FD pour les systèmes de communication dans un avenir rapproché. Nous croyons que la structure proposée ici sera exploitée dans les systèmes hybrides FDD et transpondeurs FD, à cause de la simplicité, le faible coût, la nature passive du dispositif et sa compatibilité avec l'architecture des transpondeurs conventionnels. De plus, notre recherche ouvrira de nouvelles directions de recherche. Une direction de recherche importante serait de réaliser un système conjoint de radio FD et radar. En effet, puisque le principe de fonctionnement d'un radio FD est le même qu'un système radar, l'intégration de ces deux systèmes serait relativement simple et efficace. De recherches futures pourraient s'intéresser à la modification et l'amélioration de la partie antenne, ou du développement d'un réseau d'antennes pour une application spécifique. Finalement, on pourrait potentiellement apporter de nouvelles fonctionnalités d'ajustement de notre système en incorporant des éléments électriques et magnétiques d'ajustement.

# ABSTRACT

Full-duplex (FD) transceiver is a promising candidate for 5G, and future wireless systems since the inherent advantages associated with FD systems would be able to exceptionally address the demanding requirements in 5G horizons and beyond. It has been well known that FD systems can double communication bandwidth and throughput, hugely lower system latency, and significantly minimize network congestion, which all contribute to enhanced system reliability and performance. The principle of an FD communication transceiver system relies on its simultaneous in-band transmission and reception of a signal compared to conventional half-duplex transceiver techniques based on either frequency division duplexing (FDD) or time division duplexing (TDD). However, the development of an FD transceiver poses a well-known significant fundamental challenge, in which a strong self-interference (SI) from the transmitter signal would disrupt and saturate the receiver operation of the same radio node. Therefore, to accomplish a successful FD system design, the strong SI signal must be canceled in the receiver channel.

In this thesis, we propose, develop, and demonstrate a fully integrated passive substrate integrated waveguide (SIW) front-end component that is capable of providing more than 70 dB isolation between transmitter and receiver (T/R) channels over 80 MHz bandwidth in the sub-6 GHz frequency range, with the aid of a dual-polarized antenna. To our knowledge, this is the current world record isolation of T/R channels reported in the analog domain achieved in passive configuration. The proposed component exploits two orthogonal modes and polarizations to achieve high isolation. The proposed solution exceedingly outperforms other methodologies reported in the literature in several aspects. First, the proposed component that is essentially an integrated dual-mode (DM) circulator and dual-polarized (DP) antenna, is passive and delivers super linear and low noise performance. This is a massive contrast with reference to existing FD enabling solutions, which nearly all rely on active-circuit approaches. In addition, the proposed structure exploits a SIW topology, which can handle higher power signals in comparison to other active or RFICs-based solutions. Second, the current state-of-art solutions that achieve the FD operation usually involve the design of extra RF and RFIC components, circuits, and/or transmission chains, which all result in considerable added complexity and significant power consumption in the transceiver. However, our proposed solution has the same complexity as typical transceivers where single-mode circulator and single-mode polarized antenna are transformed into dual-mode and dual-polarized counterparts, respectively. Therefore, its relatively simple, low-loss, efficient, and low-cost structure is significantly advantageous to other solutions. Third, the proposed component has a self-consistent tuning mechanism that can be used to tune the operating frequency of the device and the frequency range that results in the highest possible isolation. Finally, unlike other FD enabling architectures, our proposed methodology enables the FD operation without much sacrifice in the transceiver's figure of merit. In other words, the realized FD transceiver, based on our proposed solution, can compete and outperform conventional transceivers.

However, apart from the above-mentioned advantages observed in our system demonstration of the final component, we have accomplished several achievements in this thesis, which can be reflected by introducing and developing novel theories and components as an essential expansion of the general knowledge in the field. In this thesis research, we have proposed and developed a fundamental theory to develop two novel ferrite-based nonreciprocal components for the first time. Two components based on different topologies can effectively deploy all ferrite materials to devise a unique device that can convert the TE10/TE20 to TE20/TE10 waveguide modes only in one direction, while the mode of propagating wave is preserved in the reverse direction. To show the applicability of such components, novel circulators based on this nonreciprocal mode conversion have been designed, prototyped, and demonstrated for the first time.

Moreover, we have investigated and developed a theoretical foundation, which can be exploited and used to design nonreciprocal components in a multi-mode configuration. Using the proposed theory, we have demonstrated and prototyped a dual-mode circulator and a triple-mode gyrator for the first time. In addition, on the basis of the proposed multi-mode SIW techniques, we have proposed, studied, and demonstrated a novel dual-polarized antenna that can be excited with a single concurrent dual-mode SIW structure. The latter and former antenna and circulator with a proper modification have been integrated to create the final component, achieving unprecedented high isolation in the analog domain, meeting FD systems' requirements.

We envision that our proposed game-changing solution would hugely impact FD systems' architecture in 5G wireless systems and beyond for its unprecedented advantages. As the proposed solution turns FD systems into a reality, we should expect the ubiquitous deployment of FD systems in large-scale communication systems in the near future. Interestingly, for its simple, low-cost, passive, efficient, and, more importantly, compatibility with transceivers' conventional architecture, we believe this structure will be exploited as a common front-end node in hybrid FDD FD transceivers. We anticipate our research would open up new research directions to expand and enhance the current topology. One significant research direction would be to realize an efficient joint FD radio and radar system. Since the underlying principle of operation of an FD radio is the same as that of a radar system, integrating these two systems would be significantly more straightforward and efficient. Future researchers can also focus on enchantment and modification of the antenna part or its expansion into array antennas depending on specific applications. Moreover, incorporating more tuning functionalities and capabilities by integrating electric and magnetic two-dimensional tuning elements can elevate the proposed solution's tunability.

# TABLE OF CONTENTS

# LIST OF TABLES

# LIST OF FIGURES

List of symbols and abbreviations

| | |
|---|---|
| 4G | The fourth generation of broadband cellular network technology |
| 5G | The fifth generation cellular network technology |
| ADC | Analog-to-digital converter |
| ADS | Keysight advanced design system |
| BPSK | Binary phase shift keying |
| CMOS | Complementary metal-oxide-semiconductor |
| DM | Dual mode |
| DP | Dual polarization |
| EVM | Error vector magnitude |
| FDD | Frequency division Duplex |
| IC | Integrated circuit |
| LO | Local oscillator |
| MIMO | Multiple-input and multiple-output |
| NDW | Nonreciprocally dual-channelized waveguide |
| NRMCW | Nonreciprocal mode-converting waveguide |
| OFDM | Orthogonal frequency division multiplex |
| PCB | Printed circuit board |
| QAM | Quadrature amplitude modulation |
| RF | Radio frequency |
| SIW | Substrate integrated waveguide |
| SNR | Signal to noise ratio |
| TDD | Time division duplex |

# LIST OF APPENDICES

# CHAPTER 1 INTRODUCTION

## 1.1 Motivation:

The advent of cell phones, tablets, and other wireless devices in recent years and their exponential expansion on one hand, and the elevation of data quality such as videos and images over the internet, on the other hand, all indicate that bandwidth requirement is increasing day by day. This trend lights up the path for next-generation wireless network requirements. Also, this is reflected in recent wireless research, as we perceive that new research directions have led to fundamental changes in the design and development of the fifth-generation (5G) of cellular networks and beyond, such as 6G and multifunction wireless systems.

In past years, many debates have been organized in the research community about how the 5G should be defined and the best technology that can cope with the ever-growing need for high-rate data communication. One fascinating candidate with promising potentials for 5G and future wireless systems is the full-duplex (in-band) transmission [1-12], which has emerged out of the keen mind of researchers who question the possibility of anything. This has been said because the essence of full-duplex is in-band simultaneous transmission and reception of the signal, which contrasts with the long-hold notion in communication society that “It is generally not possible for radios to receive and transmit on the same frequency band because of the interference that results” [13].

Currently deployed wireless communication systems use either time-division or frequency-division approaches for bidirectional communication. Nevertheless, in full-duplex (FD) systems, the signals are transmitted and received over the same frequency band simultaneously. The big problem with such a system is that the transceiver will hear its own signal on the receiver, and since it is usually a very strong signal, the receiver may not be able to sense desirable signals from other devices anymore.

FD systems have the potential to double the throughput, as only one channel is adopted for simultaneous transmission and reception. The 100% increase in bandwidth gets even more interesting as we perceive that FD has the flexibility to integrate with current throughput enhancement techniques such as MIMO [14-16], to increase the signal data rate further. Moreover, bandwidth issue is not the only important issue regarding the 5G communication. Low latency is another key feature that must be met in future wireless systems to make instantaneous real-time communications possible, for example, considering an autonomous driving scenario where wireless communication is adopted for long-distance vehicle control. In such a scenario, the end-to-end latency needs to be less than milliseconds for fast and safe long-distance control. Interestingly, FD can result in low latency communication, where a node can receive a signal from one node and simultaneously transmit it to another node. Further, FD can mitigate the hidden terminal problem and the loss of throughput in congested nodes.

Learning the fascinating benefits of full-duplex systems, we get back to the inherent problem associated with these systems that prevent them from their realization in practice. The main problem of FD is a large self-interference (SI) from one node's own transmissions compared to the signal of interest from a distant transmitting antenna. A radio has to entirely cancel the significant self-interference resulting from its own transmission to the received signal to achieve the full-duplex. If such a self-interference is not completely canceled, any residual self-interference acts as noise to the received signal and reduces SNR and consequently throughput [17].

In this work, we mainly focus on the research and development of the analog part of self-interference cancelation (SIC) structures, which is the main challenge for realizing a practical FD system. In the following section, we will present and discuss the core problem that will be dealt with in this thesis, and then we will formulate objectives that will be explored in this work.

## 1.2 Statement of problem

### 1.2.1 Why is SIC challenging?

The first question that may conjure up for SIC is why the self-interference is hard to subtract? Since the transceiver knows the signal being transmitted, subtracting it from the receiver should be relatively simple to realize. Well, this is partially true; actually, the radio knows the clean transmitted digital baseband signal. However, once the signal is converted to an analog format and upconverted to the carrier frequency, the transmitted signal looks quite different from its baseband form. Analog components in the radio Tx chain distort the signal in both linear and nonlinear ways (e.g., transistors create cubic and higher-order components of the signal), active elements add up device noise (e.g., power amplifiers contribute to transmitter noise), device impairments modify the desired signal (e.g., an oscillator is tuned slightly off-center frequency) or delay it by different amounts at different frequencies, and so on. In general, we can say that the transmitted signal is a complicated nonlinear function of the ideal transmitted signal, along with unknown noise [18].

### 1.2.2 Importance of analog cancelation

The final goal of any SIC technique is to model and predict the distortions caused by the Tx chain such that it can cancel them over the receiver side [17]. Two essential effects should be considered for SIC, namely receiver saturation at the analog to digital converter (ADC) side and nonlinear self-interference. The receiver gets saturated if the input signal is beyond a specific level dictated by ADC's resolution. Therefore, a substantial portion of interference signals needs to be canceled in the analog domain; otherwise, ADC will be saturated, and the transceiver will fail to work. In practice, due to the resolution of current ADCs, about 60 dB signal suppression is required in the analog domain.

On the other hand, even if the receiver had infinite resolution and did not have the saturation problem, the leaked self-interference would be a distorted version of the transmitted signal, consisting of several nonlinear harmonic components significantly higher than the noise floor. Therefore, any cancellation must model these distortions in the digital domain and adjust to variations over time. To cancel the remaining interference digitally, cancellation algorithms operating on the digital baseband IQ samples between the transceiver and the baseband modem must model all the nonlinear distortions. Since the modeling of whole distortions is difficult or impossible, a significant portion of these nonlinear distortions must be canceled in the analog domain, and any residual nonlinear leakage is canceled in the digital domain. State of the art for digital cancellation algorithms are much easier to integrate as they are similar to digital pre-distortion (DPD), an increasingly common feature in most wireless systems, in terms of resource requirements and integration [8].

Therefore, a SIC solution is primarily distinguished by technique, size, and complexity of the RF analog cancellation circuit. In this work, we focus on developing a new RF cancelation technique that can outperform current SIC techniques; however, for digital cancelation, we will rely on current successful methodologies; hence it is not a scope of this dissertation.

## 1.3 Research objectives

The main goal of this Ph.D. research project is to propose and develop a methodology to demonstrate a fully integrated and practical front-end for the development of full-duplex systems, which can not only meet expectations from a full-duplex system but also compete with half-duplex techniques in terms of cost, power handling, loss, efficiency, low-latency, tunability as well as being monostatic and integrated.

For this purpose, we explore the non-reciprocity of ferrite-loaded substrate integrated waveguide (SIW) configurations to assess their potential for deployment as nonreciprocal front-end components in FD systems. In particular, our goal is to propose and develop a novel nonreciprocal component or a novel circulator that can break the barrier in achieving higher isolation beyond conventional values around 30 dB associated with current state-of-the-art nonreciprocal components. We have chosen ferrite materials to achieve non-reciprocity since they are passive and can offer high-power handling, high-linearity, and low noise operation, critical for 5G systems. Moreover, ferrite materials exhibit tunability in connection with an external magnetic bias, which presents advantages since control and tuning circuits, can be implemented in a low-cost and straightforward manner. On the other hand, SIW structures are chosen since they are low-loss, low-cost, and have self-consistent electromagnetic shieling favored for FD systems to curb the RF leakage radiation and undesired couplings. Further, SIW configurations support specific modes within themselves, and wave distortion mechanisms are much clearer to investigate than unshielded and conventional structures like microstrip lines that are easily prone to external couplings.

However, this task is challenging even though ferrite materials are known for a long time, and solid theoretical and experimental backgrounds have been established in this field. Therefore, any new and significant developments in this field must be fundamental, employ novel perspectives into their behavior, and apply original and unconventional methodologies to seek unprecedented nonreciprocal phenomena that can be exploited suitably for full-duplex systems. Our primary methodology to achieve high isolation is based on developing and demonstrating a novel orthogonally dual-mode circulator, which can provide high isolation between Rx and Tx channels through two stages of cancelation. First, each mode of the dual-mode circulator is assigned separately to Tx and Rx channels, which can deliver high isolation between them due to the modes' orthogonality. Second, the inherent isolation between a circulator's uncoupled ports would contribute to the isolation.

Our primary goal in this Ph.D. project was to develop and demonstrate a full-duplex transceiver following 5G and future wireless systems requirements. Therefore, several objectives and milestones were defined to accomplish this challenging task, which coherently led us to the final module. Therefore, the specific objectives of this dissertation are stated as follows:

- Our first objective was to investigate and explore ferrite-loaded SIW and other planar transmission lines to appraise their potential in achieving novel nonreciprocal behaviors. More specifically, inspired by the active SIC scheme that cancels any residual leakage signal by shaping the phase and amplitude of a sampled signal from Tx and subtracting it from the Rx signal, we have proposed and demonstrated a ferrite-loaded SIW configuration that can convert TE10 mode into TE20 mode nonreciprocally within a SIW structure. Thus, TE10 and TE20 modes are separately assigned to Tx and Rx signals; this mode conversion allows to achieve a passive SIC by manipulating the converted signal to cancel the residual leakage. We have examined and prototyped two separate novel components to demonstrate the nonreciprocal mode conversion, whose results have been published in the two following articles.

  **Article 1: A. Afshani** and K. Wu, "Non-reciprocal Mode Converting Waveguide and Circulator," in IEEE Transactions on Microwave Theory and Techniques, vol. 67, no. 8, pp. 3350-3360, Aug. 2019, doi: 10.1109/TMTT.2019.2919591.

  **Article 2: A. Afshani** and K. Wu, "Modal Nonreciprocity and Circulator Based on Nonreciprocal Mode Conversion," in IEEE Transactions on Microwave Theory and Techniques, vol. 67, no. 12, pp. 4922-4934, Dec. 2019, doi: 10.1109/TMTT.2019.2951566.

- The second objective consistent with our central methodology to attain high isolation with passive non-reciprocal components is developing a dual-mode (DM) circulator. However, we have advanced further by proposing and developing a generalized theory to design multi-mode nonreciprocal ferrite-based SIW components in fulfilling this goal. In other words, we have presented a theoretical foundation that can be used to design any nonreciprocal components in a multi-mode operation, including a dual-mode circulator. The results of this work have been reported in Article 3.

- **Article 3: A. Afshani** and K. Wu, "Generalized Theory of Concurrent Multi-Mode Reciprocal and/or Nonreciprocal SIW Ferrite Devices," IEEE Transactions on Microwave Theory and Techniques, (submitted April 2021).

- The third objective follows previous objectives, where a dual-polarized antenna is required to be employed in conjunction with a dual-mode circulator, so the antenna does not degrade the isolation of the dual-mode circulator. Further, the antenna's topology must be consistent with the dual-mode circulator in supporting concurrently first two modes of the SIW. Therefore, we have proposed and demonstrated a novel dual-polarized antenna excited by a dual-mode SIW. The results of this work have been reported in Article 4.

  **Article 4: A. Afshani** and K. Wu, "Dual-Polarized Patch Antenna Excited Concurrently by a Dual-Mode SIW," IEEE Transactions on Antennas and Propagation, (submitted March 2021).

- Further, we have integrated the dual-mode circulator and dual-polarized antenna into a single final compact front-end module to minimize the antenna's loading effect and boost the isolation. Our last objective is to demonstrate a full-duplex transceiver exploiting the proposed methodology and components. In this connection, we have prepared and established an RF setup to emulate the transmitting and receiving chains within an FD transceiver connected to the proposed module for testing. This objective is pursued in Chapter 7.

Our proposed solution to enable a full-duplex front-end module is illustrated in Figure 1.1. Figure 1.1(a) depicts a conventional single-mode circulator loaded with a single-polarized antenna. In a full-duplex scenario, since transmission and reception signals are simultaneous and at the same frequency, there are two strong components of Tx-to-Rx interference due to antenna reflection and internal leakage of the circulator. In our solution as shown in Figure 1.1(b), we propose an integrated dual-mode circulator and dual-polarized antenna, where $TE_{10}$ and $TE_{20}$ waveguide modes are assigned to Tx and Rx channels, respectively. Since transmission and reception modes are orthogonal, Tx-to-Rx interference due to antenna reflection and circulator leakage is substantially suppressed. Furthermore, as will be illustrated a tunable nonreciprocal mode-conversion mechanism can be applied to further cancel the residual leakage.

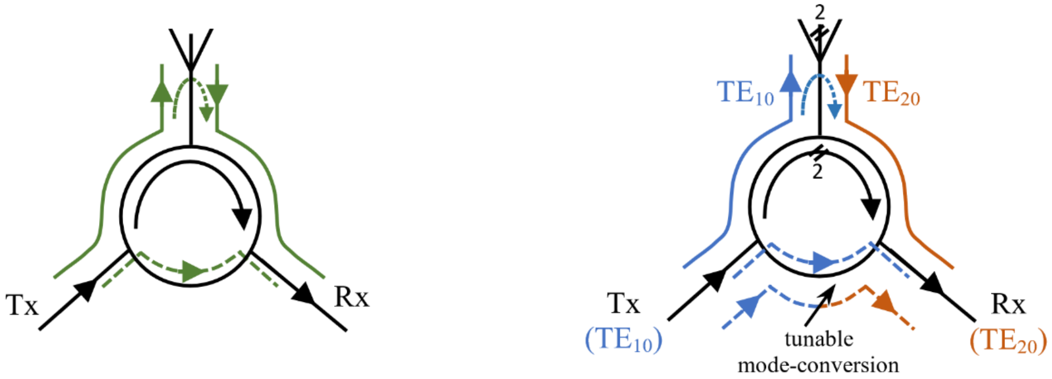

(a) (b)

Figure 1.1 Conceptual schematic of: (a) conventional single-mode circulator and single-polarized antenna configuration, (b) the proposed dual-mode circulator and dual-polarized antenna

## 1.4 Organization of the thesis

This thesis consists of 8 chapters. Chapter 1 serves as an introduction starting from stating the motivations of this work. Further, particular questions and problems sought in this thesis are identified and stated. Finally, the specific objectives of this work are presented.

Chapter 2 presents a critical literature review discussing the current state-of-art of full-duplex systems. In particular, it categorizes the SIC techniques into different categories and discusses each one separately with reviewing the most significant works carried out in recent years.

Chapters 3, 4, 5, and 6 include our four scientific articles that have been published or submitted. In Chapter 3 (Article 1), for the first time, we propose and demonstrate a nonreciprocal mode-converting waveguide that converts TE10 mode into TE20 mode only in one direction while the mode is preserved in the reverse direction. This component is based on ferrite-loaded SIW, where ferrite slabs are attached to sidewalls of the SIW, and ferrite material has a large saturation magnetization. Chapter 4 (Article 2) demonstrates a different nonreciprocal mode-converting component with a different configuration suitable for low-saturation ferrite materials. Further, in this article, we present a theoretical foundation that can be exploited to create a dual-channelized waveguide with the ferrite-loaded SIW configuration. In particular, this methodology indicates that it is possible to manipulate electromagnetic fields within the device to create two different paths for forward and reverse directed waves. In Chapter 5 (Article 5), inspired by the previous articles' theoretical revelations, a generalized theory is developed and demonstrated to synthesize any nonreciprocal component into a multi-mode function from the multi-channelized waveguide topology. This chapter introduces and demonstrates a dual-mode and a triple-mode gyrator for the first time. Chapter 6 (Article 4) presents a novel dual-polarized (DP) antenna excited by a single dual-mode SIW structure. This antenna is purposely designed in this configuration to be integrated with a dual-mode circulator. The antenna's theoretical aspects and measurement results are discussed in this chapter.

In Chapter 7, we have proposed a technique to exploit the dual-mode circulator concept introduced in Chapter 5 into a dual-mode circulator with ultra-high isolation purposed for FD operation. To accomplish this task, we have designed a special excitation technique of the DM circulator that allows in-phase and out-phase excitation of the Tx and Rx channels, respectively. Further, we have implemented a technique to integrate the DM circulator and the DP antenna to accomplish a compact and efficient module and to minimize the isolation-degradation due to intermediate transitions.

Finally, this thesis concludes in Chapter 8 by summarizing our contributions and achievements. Moreover, it is followed by suggestions to be considered for further enhancement of this work and recommendations for any future works.

## 1.5 Coherence of the articles in relation to the research goals:

This thesis follows the article-based format for Chapters 3 to 6, including four peer-reviewed journal articles written as part of this Ph.D. project. Chapters 3 and 4 present published works, while Chapters 5 and 6 presents recently submitted works. The articles are thoroughly consistent with the research goals in terms of complementarity and sequential progress of the whole thesis. However, it should be mentioned that in this Ph.D. research journey, whenever we faced a new observation or phenomenon, we took a holistic approach to investigate and study the particular behavior to develop and present a comprehensive theory and a related practical device regarding that phenomenon.

Therefore, in Articles 1 and 2, we have demonstrated a nonreciprocal mode-converting waveguide. Initially, this component was developed to implement a means of producing a passive SIC, where a mode conversion was exploited to couple and manipulate a desired portion of the Tx channel into the Rx channel to cancel residual leakage. However, after witnessing this behavior in our earlier works, we investigated the structure thoroughly to establish a fundamental theoretical basis to understand and harvest this behavior and turn it into a novel component.

Similarly, in Article 3 we aimed to develop a dual-mode circulator pertaining to our primary goal in realizing high isolation through a passive nonreciprocal device, in which we were successful, and the developed theory was flourished in Chapter 7 to achieve more than 70 dB isolation over 80 MHz bandwidth at 5GHz center frequency with tunability property. However, in Article 3, and thanks to our holistic approach, we have extended the theory into not only other nonreciprocal components but also for higher-order modes, realizing a generalized theory to develop multi-mode nonreciprocal devices.

In Article 4, we have demonstrated a dual-polarized antenna consistent with the dual-mode circulator's topology in exploiting the concurrent propagation of the first two dominant modes within a SIW. This Article, as a stand-alone work, demonstrates a novel technique to achieve a high isolation DP antenna; however, as shown in Chapter 7 and congruous to our primary goal, it can be integrated with a modified DM circulator to realize a final solution capable of providing high isolation at the front-end of the transceiver.

## 1.6 Review of ferrite materials and permeability tensor

Throughout this thesis, we model ferrite materials using permeability tensor. Therefore, here we present a briefly related mathematical relations governing the ferrites at microwave frequencies.

Ferrites exhibit magnetic anisotropy in presence of a magnetic bias. From a microscopic point of view, each spinning electron within an atom creates a magnetic field resulting in a magnetic dipole moment. In isotropic materials, electron spins are in pairs with opposite signs, so the net magnetic moment of the material is zero. However, in magnetic anisotropic materials like ferrites, a significant portion of the electron spins are unpaired. Without an external magnetic field, these magnetic dipoles are distributed at random directions producing a zero net magnetic moment. But, in the presence of a DC magnetic bias field, the magnetic dipoles become organized and produce a net moment that precesses with a frequency in proportion to the external magnetic bias. Since the precession has a preferred sense of direction due to the inherent spin of the electron, the microwave waves with different sense of circular polarization propagate differently within magnetic anisotropic materials.

For microwave applications, a macroscopic mathematical model in form of a permeability tensor for the ferrite materials can be deduced from the microscopic view of the atom. Detailed mathematical procedure to derive the permeability tensor from microscopic interactions within the atom, can be found in [81]. Generally, for a ferrite medium that is biased in $\hat{z}$ direction, the permeability tensor can be defined as [81]:

$$\mu = \begin{bmatrix} \mu & j\kappa & 0 \\ -j\kappa & \mu & 0 \\ 0 & 0 & \mu_0 \end{bmatrix} \qquad (1.1)$$

The fact that the permeability tensor is not symmetric indicates the nonreciprocal nature of the ferrite materials concerning the direction of the wave propagation. In this equation, $\mu_0$ is the free space permeability. Elements of the permeability tensor are:

$$\mu = \mu_0 (1 + \frac{\omega_0 \omega_m}{{\omega_0}^2 - \omega^2}) \qquad (1.2)$$

$$\kappa = \mu_0 \frac{\omega \omega_m}{{\omega_0}^2 - \omega^2} \qquad (1.3)$$

Where $\omega$ is the frequency of operation, $\omega_0$ and $\omega_m$ are:

$$\omega_0 = \mu_0 \gamma H_0 \qquad (1.4)$$

$$\omega_m = \mu_0 \gamma M_s \qquad (1.5)$$

In these equations $H_0$ (A/m) is the applied DC magnetic bias, $Ms$ (A/m) is the saturation magnetization of the ferrite material, and $\gamma$ is the gyromagnetic ratio equal to $2.21 \text{x} 10^5$ rad/s per A/m.

By modeling the ferrite with the permeability tensor, wave propagation within the ferrite can be solved using Maxwell equations. Depending on whether wave propagation is in parallel or transverse to the magnetic biasing, different field behaviors are discerned. In all the works in this thesis, wave propagation is transverse to the magnetic biasing field. Therefore, here we briefly discuss the wave propagation within an infinite ferrite medium in presence of a transverse DC bias, to find useful relations and insights.

Consider an unbounded ferrite region biased in $\hat{y}$ direction. We will investigate the propagation of a plane wave in $\hat{z}$ direction. Solving the Maxwell equation in correlation with permeability tensor of the ferrite, and with some mathematical simplification we will have [81]:

$$\beta^2 E_x = \mu_0 \omega^2 \varepsilon E_x \tag{1.6}$$

$$\mu(\beta^2 - \omega^2 \mu\varepsilon) E_y = -\omega^2 \varepsilon \kappa^2 E_y \tag{1.7}$$

This system of equations has two sets of answers. The first answer corresponds to the case where $E_y$=0, and $\beta_0 = \omega\sqrt{\mu_0\varepsilon}$. This is called the ordinary wave since wave propagation is not affected by the ferrite anisotropy. This case happens when the magnetic fields are not transverse to the magnetic bias field. For a TE wave this corresponds to the case where DC magnetic bias is not in parallel with the electric field.

The second answer corresponds to the case where $E_x$=0, and we have:

$$\beta_e = \omega\sqrt{\mu_e \varepsilon} \tag{1.8}$$

$$\mu_e = \frac{\mu^2 - \kappa^2}{\mu} \tag{1.9}$$

In this case, the wave is significantly affected by ferrite anisotropy and has an effective permeability defined as above. This case occurs when propagating magnetic fields are transverse to DC magnetic bias field. For a TE wave, the DC magnetic bias will be aligned to the electric field. This answer is the interested solution in this work as it corresponds to all the ferrite structures discussed in this thesis.

Finally, we should make a note about the units used in this thesis. Traditionally, for convenience in dealing with magnetics, CGS units are used rather than SI units. In this regard, magnetic field strength ($H_0$) is in Oersteds (Oe) and we have $4\pi \times 10^{-3}$ Oe = 1 A/m, magnetization is measured in Gauss (G) and 1 G = $10^{-4}$ Weber/m$^2$. Thus, we have $\mu_0$ = 1 G/Oe in CGS units. Also, saturation magnetization ($Ms$) is expressed as $4\pi Ms$ Gauss and the gyromagnetic ratio is $\gamma/2\pi$ = 2.8 MHz/Oe [81].

# CHAPTER 2 LITERATURE REVIEW

For a successful communication link, signal interference (SI) must be canceled down to the receiver chain's signal noise level to maintain the transceiver's whole input dynamic range. The SI signal or leakage signal from the transmitter chain into the receiver chain has many components, including the main transmitted signal, harmonics and non-linear components of the transmitted signal, and noise associated with the transmitted signal. Therefore, a successful self-interference canceling (SIC) method must be able to cancel all components down to the noise floor. For example, for a typical Wi-Fi transceiver with 20 dBm output power and a nominal -90 dBm noise floor, SIC must be better than 110 dB over whole frequency ranges. Such a large SIC can be achieved in various domains, exploiting a cascade of different techniques. For example, part of the SI can be eliminated in the analog domain, and the rest can be eliminated in the digital domain. Generally, SIC in the digital domain is easier since we know what ‘signal’ is being transmitted, so it is convenient to subtract it from the baseband receiver using digital signal processing resources. However, the main challenge resides in the analog domain and mainly in the RF domain. In the analog domain, many non-ideal components of the signal are created and added to the desired Tx signal, like harmonics and noise. These non-idealities are difficult or impossible to be eliminated with digital SIC since they are unknown. On the other hand, even if non-idealities could be somehow modeled and canceled in the digital domain, still a large portion of the required SIC must be implemented in the analog domain. Since ADCs have limited resolution, they become saturated with a leakage signal and insensitive to the desired Rx signal. Therefore, at least 60 dB (depending on Tx power) of SI must be canceled in the analog domain, so receivers of the ADC can operate in their full dynamic range. Figure 2.1 shows an example of the SIC budget for a Wi-Fi modem if supposed to operate in Full-Duplex (FD) mode [17].

Further, SIC in the analog domain can be further decomposed into two levels: air interface or passive SIC or primary isolation and active SIC. Therefore, SIC methodologies and techniques can be divide into three main groups, as depicted in Figure 2.2 [19]. Research activities in the literature are focused on one method or a combination of two or three methods. Digital cancellation exploits the fact that we know the clean baseband interference signal, and it operates to cancel interference after the received signal is converted to a digital signal and quantized by the ADC [20, 21]. For this, the receiver first extracts the SI and then subtracts it from the received signal. Therefore, the main problem is extracting the SI signal. One method to do so is based on coherent detection, where it is used to detect the self-interfering signal. The detector correlates the incoming signal with the clean transmitted signal, which is available at the transmitter's output. The main challenge in subtracting the known signal is estimating the delay and phase shift between the transmitted and the received signals [22]. Techniques such as the correlation peak-based algorithm can be exploited for channel estimation. The transmitted signal is correlated with the received signal, and a peak detection algorithm is used to distinguish the delay and phase shift. Having the delay and phase shift estimated, the SI is reconstructed, and by subtraction from the received signal, interference cancelation is fulfilled.

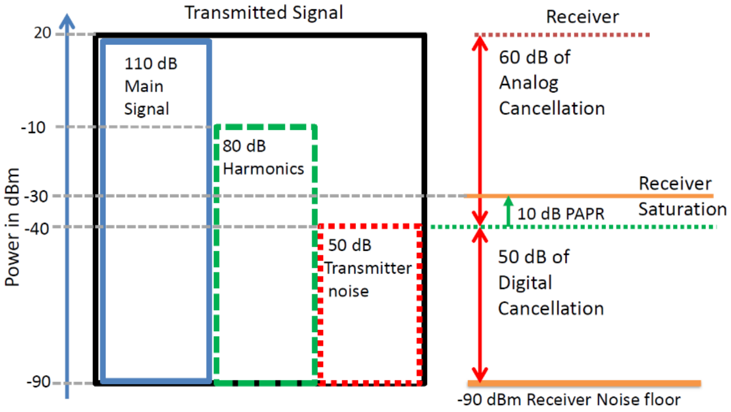

Figure 2.1 Different components of the transmitting signal and their effect on SIC requirements at the receiver [17]

Although there are other methods to perform digital cancelation, the advantage of this technique is that, unlike other methods, it does not require any special pre-amble or post-amble, and it is modulation-independent [21]. Digital SIC is always the last step to cancel the interference signal, has well developed in recent years, and the current state-of-art in digital cancelation can provide more than 40 dB SIC [17], [23-25]. Therefore, this chapter's focus is to review significant research carried out in the analog domain to enhance SIC in terms of both depth and bandwidth.

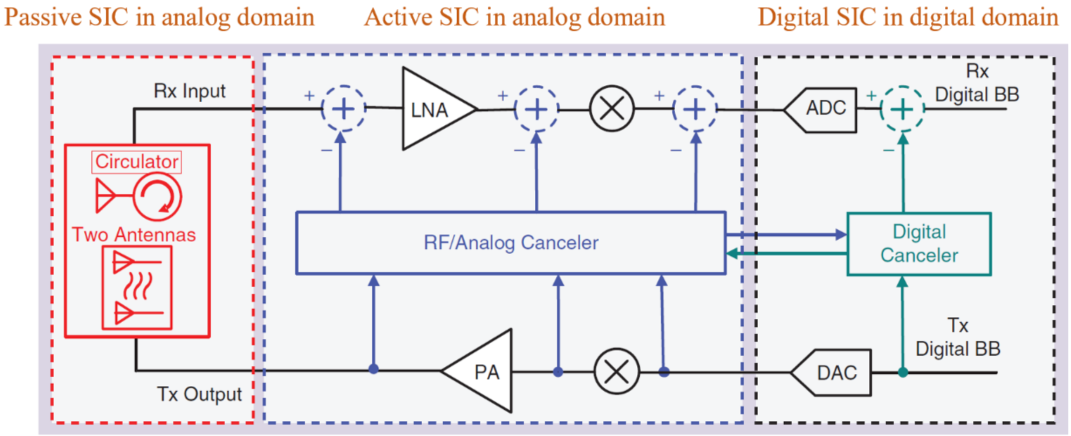

Figure 2.2 SIC can be realized in three domains [19]

## 2.1 Passive SIC or Primary Isolation

Passive SI suppression is defined as any passive methodology that can provide certain isolation levels between Tx and Rx chains at the first stage; hence, called primary isolation as well. The main advantage of passive suppression is that since it is in the analog domain and there are no active elements, suppression is applied to all signal interference components, including harmonics, noise, delays, and device impairments. Therefore, it is desirable to cancel the interference signal by passive suppression as much as possible to reduce the complexity and cost of other sections. Further, unlike active cancelation (which needs digital control) and digital cancelation, passive suppression does not introduce latency into the network. This is an essential feature in 5G transceivers and highlights the importance of the existence of an effective passive suppression to decrease digitally computational time.

Classic circulators are used to provide around 20-30 dB passive SIC, which is simply far from the required standards in FD systems. Therefore, circulators still are being used in conjunction with other active analog SIC methods to provide higher isolations. Another primary and earlier solution for passive SIC is exploiting two separate antennas for Tx and Rx chains. Antenna separation can typically provide more than 30 dB isolation; however, it has significant disadvantages. Such configuration is biostatic, limiting many practical applications in communications, and suffers from an increased layout size of the device to provide physical distance between two antennas. However, like circulators and in some applications, separate antennas may be used along with other active analog SIC methods to provide high isolation.

Apart from conventional circulators and two-antenna configurations with limited isolations, some novel passive structures have been investigated in recent years to provide high isolation in a monostatic configuration. Two of the most popular methodologies are introduced here.

### 2.1.1 Electrical Balance Duplexer (EBD)

Another technique for achieving the primary isolation is using an Electrical Balance Duplexer (EBD) [26-29]. EBD is a 4-port network assigned for antenna, Rx, Tx ports and an additional port for a balanced impedance network. The EBD schematic is depicted in Figure 2.3, illustrating transmission and reception modes. A balanced impedance network is, in principle, a tunable load that must mimic the impedance of the antenna. In this structure, the PA signal splits in phase between the antenna and the balanced network since they have the same impedance. Since the hybrid transformer on the LNA side is differential, the Rx path is isolated from the Tx path. This solution is a narrow band in nature, and the depth of isolation depends on how the balanced network can mimic the antenna's impedance. Using this method, authors in [26] claim to have measured about 50 dB interference cancelation over 6 MHz bandwidth.

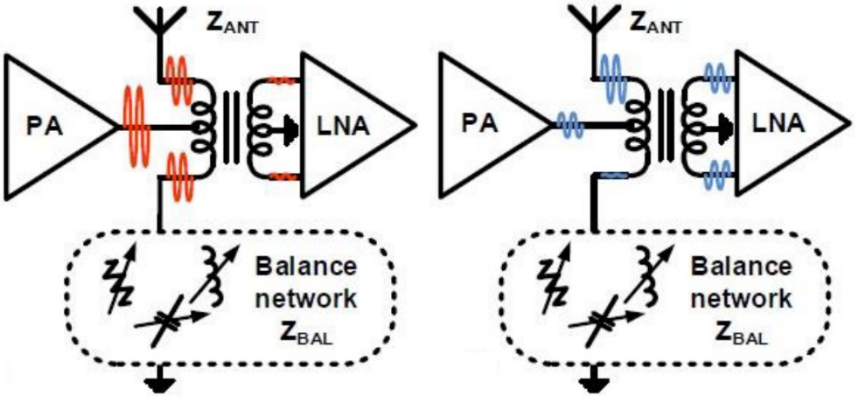

Figure 2.3 Principle of EBD operation: Left: Tx mode, Right: Rx mode [26]

This technique has drawn some attention to its compact structure that can be implemented with RFIC techniques. However, it suffers from a significant disadvantage. In this technique, 3dB of power in each Tx and Rx chain is wasted and delivered to the balanced impedance network. Further, digitally assisted control signals and algorithms are required to tune the balanced network's impedance. We believe these crucial disadvantages rule out this technique for being employed in future full-duplex systems.

### 2.1.2 Dual-Polarized (DP) Antenna

Dual-polarized antennas are an attractive solution for providing immense primary isolation over broader bandwidth compared to other solutions. In the last decade, dual-polarized antennas have become a popular choice in many radar and communication applications. In FD systems, DP antennas are exploited while Tx and Rx chains are assigned separately to one of the polarizations. Typically, this technique can provide more than 30 dB wideband isolation between Tx and Rx chains, depending on the structure and technique of implementing the dual-polarization.

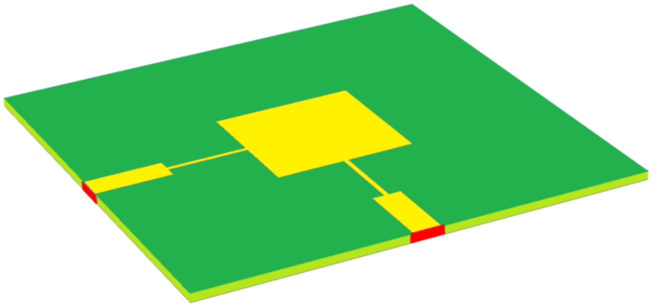

Figure 2.4 Schematic of a typical dual-polarized patch antenna with orthogonal patch excitation

The DP antennas exploit the propagation channel's polarization channel to separate the Tx and Rx channels in space. DP configuration holds a high potential for yielding high inter-port isolation in an FD transceiver within a monostatic topology without compromising antenna performance. Dual polarization can be implemented in several configurations where a radiating element is shared between two excitation feeds with orthogonal modes. As a popular antenna in communication systems for its compact, low cost, simple structure, and omnidirectional pattern, a patch antenna can be easily enhanced into a DP antenna by adopting an additional orthogonal port, as depicted in Figure 2.4. However, this topology has limited isolation concerning FD requirements for several reasons, including its asymmetrical topology, high cross-polarization, unshielded and adjacent ports that expose the potential of port coupling. Besides, this structure has limited bandwidth. Therefore, in the last few years, researchers have focused on proposing novel DP configurations that can enhance both bandwidth and depth of isolation in DP antennas. Some good works in this field have achieved noticeably higher isolations [30-37] in the sub-6 GHz region with relatively broader bandwidth with reference to previous passive SIC methods. However, broadband solutions typically have resulted in either large-profile integrated antennas or other non-integrated configurations. Hence, since integrated solutions are favored or required for many practical systems, still an integrable solution with high isolation and broad bandwidth is a hot field of research. Next, we will review some of the interesting DP antenna topologies in the literature that have resulted in high isolation over a relatively broad bandwidth. This review focuses on single-element antennas since the isolation of array antennas depends on their antenna-building element.

In [31], the authors have designed a wideband magnetically coupled DP patch antenna, as shown in Figure 2.5(a-b). In this technique, two vertical substrates have been employed to implement the feeding microstrip lines required for magnetic coupling. The structure provides better than 39 dB isolation in the frequency range of 2.25-3.0 GHz (Figure 2.5(c)), thanks to a symmetrical structure and semi-differential excitation. Besides, feeding transmission lines are implemented on separate substrates minimizing electromagnetic coupling between two feeds. This structure's main drawback is its large profile and non-integrated structure, limiting its usage in many applications.

In [32], a differentially-fed, dual-band DP antenna based on a hybrid patch and slot geometry has been implemented, as shown in Figure 2.6. This structure's chief advantage is its dual-band feature that facilities using this structure in multi-function and multi-band systems. Authors claim that the structure has better than 37 dB isolation in 3.28-3.72 GHz and 4.80-5.18 GHz frequency ranges. High inter-port isolation is mainly due to the differential excitation of the antenna. However, S-parameters are measured in a single-end configuration and are converted to differential S-parameter results. Therefore, in practice, isolation would be less than the reported values, as the required balun for differential excitation of the antenna would reduce the isolation. Besides, this antenna has an extensive profile and is non-integrated, making it less appealing for compact and integrated systems.

In [34], a differentially fed DP magnetic dipole antenna is proposed to yield better than 45.2 dB isolation in the frequency range of 5.1–5.8 GHz. The structure has a built-in balun circuit at the opposite side of the bottom ground, with high inter-port isolation for the antenna's differential feeding. The schematic, the picture of the fabricated prototype, and the proposed antenna's isolation measurement results are depicted in Figure 2.7. Differential feeding topology, electromagnetic shielding between feedings and balun, and designing a balun with high inter-port isolation are the main reasons for high isolation. However, large profile, complex and non-integrated structure are disadvantages of this solution.

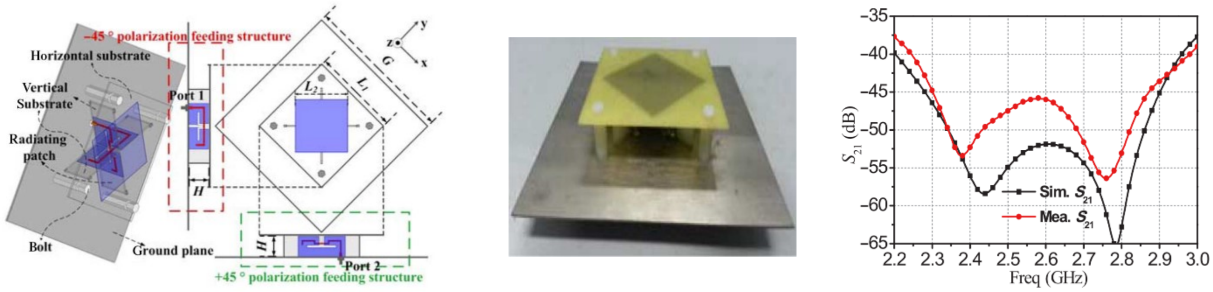

(a) (b) (c)

Figure 2.5 Magnetically coupled DP patch antenna [31]: (a) Schematic, (b) fabricated prototype, and (c) results regarding the proposed antenna's isolation

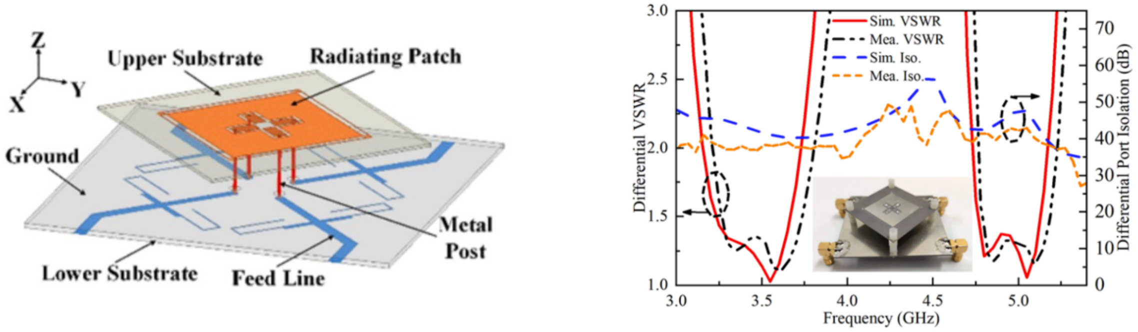

(a) (b)

Figure 2.6 (a) Schematic and (b) measurement results of the dual-band differentially fed antenna in [32]

Among the presented methods as solutions for primary isolation, none excels thoroughly over other methods in providing superior performance in terms of isolation, bandwidth, compactness, and integrability. However, we believe the DP antenna topology is the most practical and effective technique for achieving primary isolation. Unlike the EBD technique that wastes 3 dB power in both transmission and reception channels, the DP antenna does not introduce any significant loss. Furthermore, unlike two-separate antenna topologies, DP antennas provide a monostatic solution where the same radiating element is shared for receptions and transmission while substantial isolation is attained. Moreover, compared to conventional circulators with narrowband and limited isolation, the DP antennas can provide higher isolation in a relatively broader bandwidth. Finally, they can eliminate antenna reflection problems associated with other monostatic solutions.

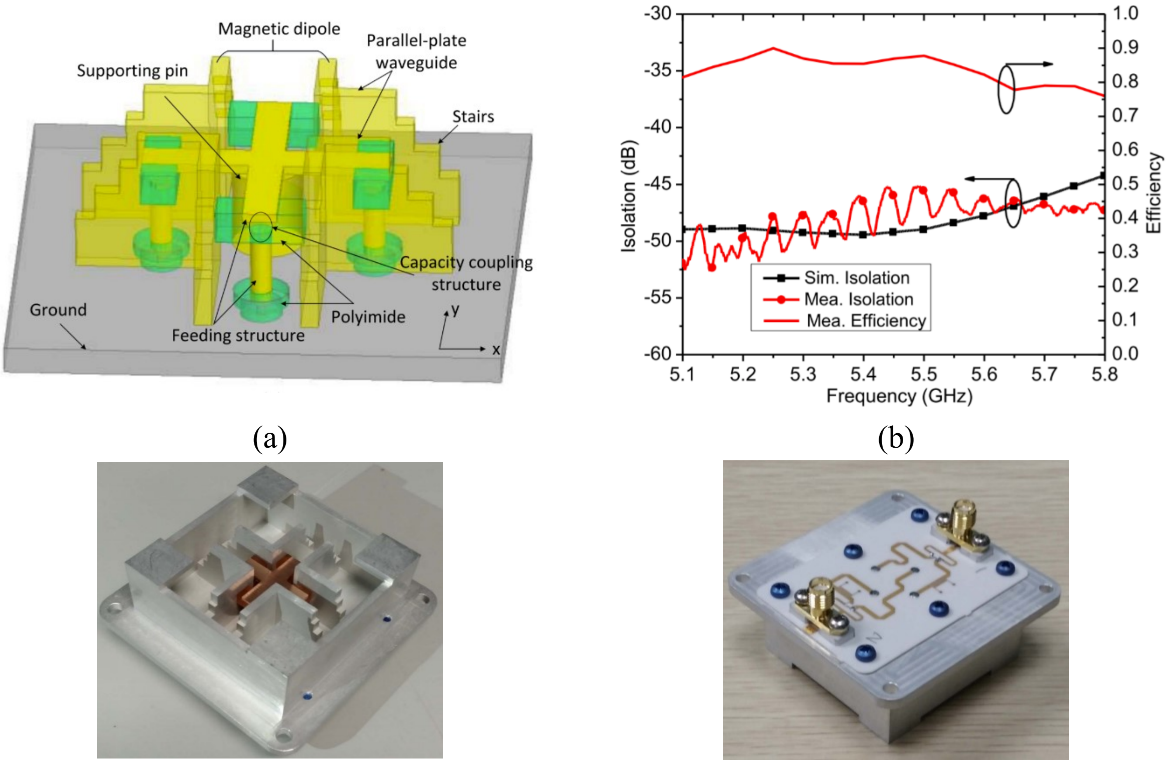

(a) (b)

(c) (d)

Figure 2.7 Differentially fed DP magnetic dipole antenna: (a) Schematic, (b) measured isolation, fabricated prototype (c) top and (d) bottom views of the antenna in [34]

## 2.2 Active SIC

Active SIC in the RF analog domain has become a dominant methodology and the most promising solution in the current state-of-art of FD systems, which enables obtaining high isolations required for FD operation. This technique relies on a simple solution in which the leakage signal from passive SIC can be further canceled by subtracting it with a reconstructed replica of the Tx leakage. Therefore, the primary problem is set to reproduce a precise replica of the leakage signal in the analog RF domain. An accurate replica of the leakage signal must have the same amplitude and phase as the original leakage signal over the desired frequency range. However, this becomes challenging as we have learned that the leakage signal is a complex waveform that contains the desired modulated RF Tx signal together with nonlinearity, harmonics, distortions, and noise contributed from all active circuits in the Tx chain. Therefore, numerous researchers in recent years have focused on advancing various techniques to generate a more accurate replica of the leakage signal. These techniques can be classified into four main categories, as illustrated in Figure 2.8 [38], and are described further in the following sub-sections.

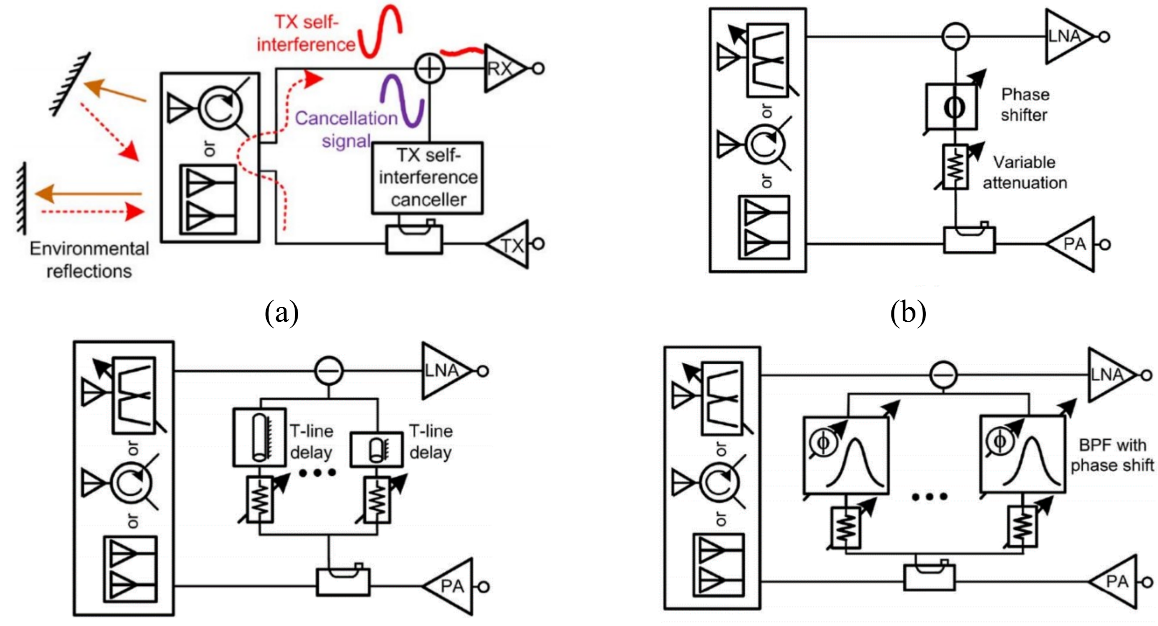

(a)

(b)

(c)

(d)

Figure 2.8 (a) General topology of active SIC technique, Different methods for implementing active SIC: (b) single tap topology, (c) multi-tap, time domain, (d) multi-tap frequency domain [38]

## 2.2.1 The basic form of active SIC with a single tap

RF active SIC in its simplest form is depicted in Figure 2.8(b). In this method, a Tx signal sample is tapped before the antenna using a directional coupler, which contains all desired and undesired components (harmonics, distortions, and noise) of the Tx signal. This signal is then fed into a circuit consisting of a tunable attenuator and a tunable phase shifter, which allows for adjusting the phase and amplitude of the signal. Finally, the altered signal is added to the Rx chain using another coupler. The major drawback of this this methodology is that it is incredibly narrowband since the signal can be modified only for one single frequency. Many papers have used this methodology in conjunction with other passive SIC techniques like DP antennas or circulators to obtain high isolation, but over a minimal bandwidth [39-44]. Therefore, the foremost challenge to overcome concerning this technique is to provide wideband solutions, for which other methodologies depicted in Figure 2.8 arise.

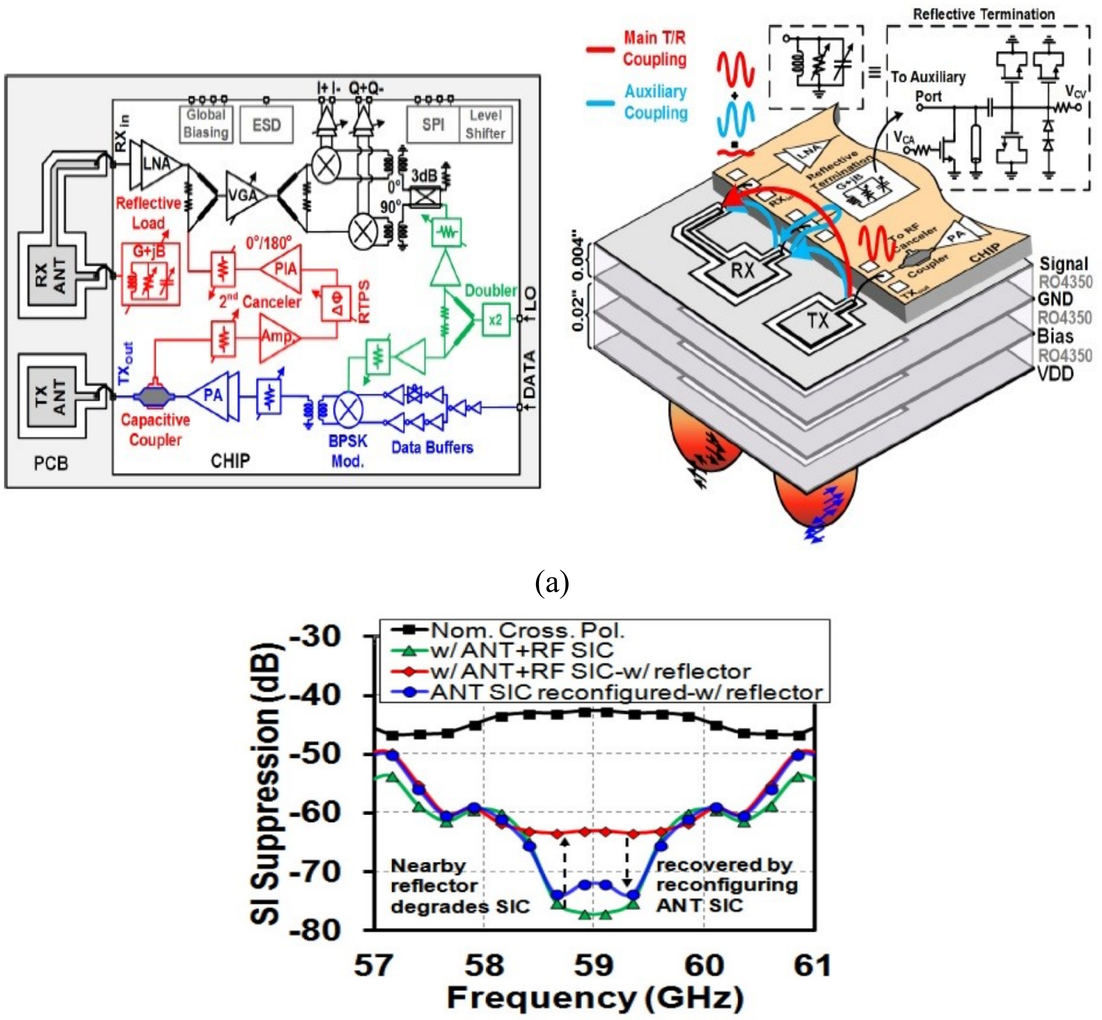

(a)

(b)

Figure 2.9 Full-Duplex transceiver on a chip at 60 GHz: (a) schematic of the proposed structure, which consists of passive and active SIC, (b) measurement results demonstrating 70 dB isolation over 1 GHz bandwidth (1.6 % bandwidth) [41]

In [41], the authors have implemented a 60-GHz FD transceiver on a chip in 40-nm CMOS technology, as portrayed in Figure 2.9. In this work, various techniques, including antenna separation, dual-polarization, tunable reflective load, and active cancelation, have been consolidated to realize 70 dB SIC over 1 GHz bandwidth (1 % bandwidth). The receiver antenna has two ports with orthogonal polarizations, where one port is terminated to a reconfigurable reflective load. By controlling the reflective load through digital adaptive circuits, it is possible to enhance interference cancelation. This topology results in limited SIC if there are objects near the antenna, causing strong reflections back to the antenna. To subdue the reflection problem, a secondary active cancelation circuit, as explained in this section, is used to assure the transceiver's robust performance. Two-separate orthogonal polarized antennas provide about 40 dB isolation. The reconfigurable reflective load and active SIC circuit contribute an additional 30 dB isolation.

## 2.2.2 Wideband active SIC based on a multi-tap configuration

The general solution for affording wideband active SIC is to use several taps instead of one single tap to leverage the freedom of design in reproducing the replica of leakage signal over more frequency points. However, to avoid frequency interference of taps, each tap should adjust the sampled Tx signal only over a specific frequency range of the total bandwidth. In other words, in each tap, the Tx signal sample must be channelized before phase and amplitude adjusting; hence, a filter must be adopted to accomplish this task. The implementation of the filter is fulfilled in either the time domain (Figure 2.8(b)) or the frequency domain (Figure 2.8(c)), which are explained further in the following sub-sections, respectively.

### 2.2.2.1 Wideband active SIC based on analog FIR filter: time domain implementation of the filter

The filter's time domain implementation is equivalent to implementing an FIR filter. The idea is to reconstruct the leakage signal using sampling theory that is widely known in the digital signal processing, where delay lines and tunable attenuators account for sampling times and sampling magnitude, respectively [17].

In [45], the authors have demonstrated an adaptive FIR filter with four taps employing discrete RF components that gain a SIC better than 60 dB over 120 MHz at 2.45 GHz center frequency. However, 50 dB of total isolation was contributed from a two separate antenna setup at the front-end for Tx and Rx channels, which is not a surprise. In [46], the authors have implemented an eight-tap FIR filter with discrete RF components and microstrip delay lines to reach 83 dB isolation over a 20 MHz bandwidth, where 45 dB of isolation was attained using a two-antenna configuration.

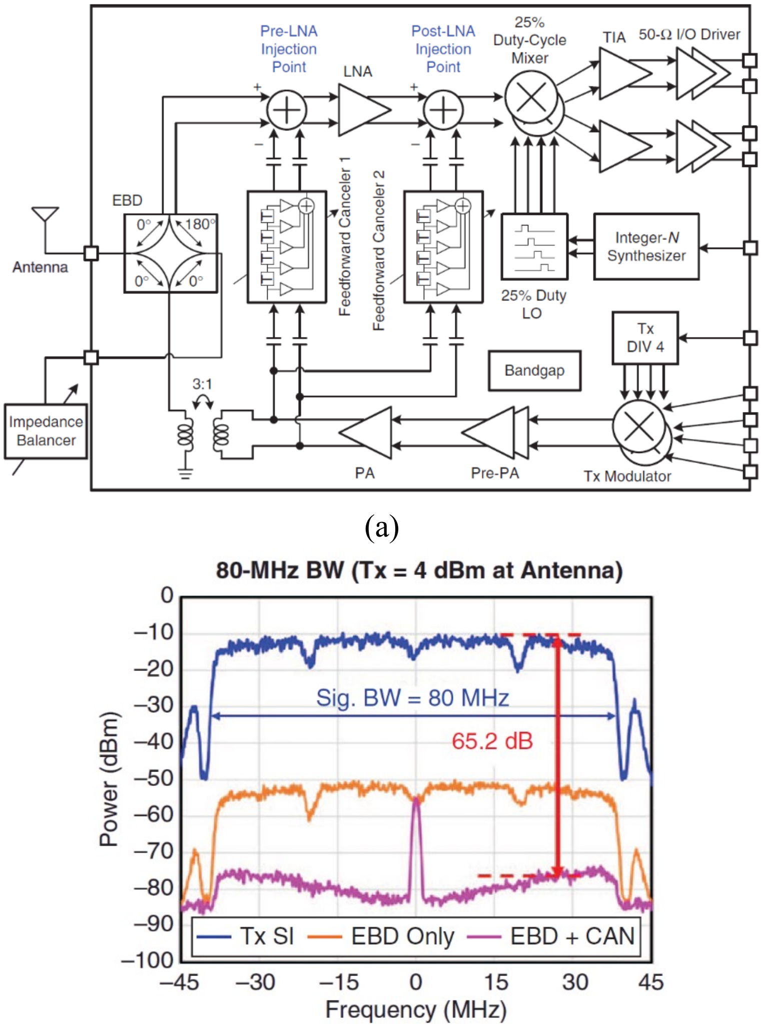

(a)

(b)

Figure 2.9 (a) Proposed FD transceiver in [19] employing EBD as primary isolation and dual-injection FIR filters for active SIC, (b) Measurement results demonstrating 65.2 dB isolation over 80 MHz bandwidth

These works unveil that FIR filters' capability to improve isolation in wide bandwidth is restricted for two reasons. On one hand, the limited resolution of delay lines due to the technology barrier curbs the filter's precision. The required resolution of the delay lines at microwave frequencies is in nanoscale, challenging to achieve, at least in PCB technology. On the other hand, even if the resolution issue could be solved by phenomenal technology advancement, the filter's operating bandwidth is related linearly with the number of taps, settling in inappropriately large circuits for typical bandwidth requirements in 5G wireless systems. In [47], the authors have demonstrated an

FD transceiver on a chip in 40-nm CMOS technology. To improve the FIR filter's performance, they have employed a dual-injection technique that exploits 5-tap FIR filters in two paths. One path cancels the leakage signal in the RF domain and before the LNA, while the other path cancels the leakage signal after the mixer in the IF domain. Delay lines have been substituted with RC circuits for an RF IC solution, making a trade-off between this solution's performance and integrability. With this technique, the authors have demonstrated an FD transceiver with 50 dB isolation over 50 MHz bandwidth, where 30 dB isolation is gained through a circulator. The same authors in a similar work in [19] have implemented the architecture with an EBD at the front-end, attaining 62 dB isolation over 80 MHz bandwidth, where 38 dB isolation was gained from primary isolation of the EBD.

In [48], a dual-injection FIR filter topology, like previous work, has been implemented in a two-element MIMO FD transceiver on a chip in a 65 nm CMOS technology. In a MIMO transceiver, the leakage signal is intensified since cross-talk must be canceled in addition to the original SIC. In this work, 45 dB SIC in the same transmitter-receiver channel and 55 dB SIC in cross-talk have been demonstrated over a 20 MHz bandwidth at 2.2 GHz center frequency, benefiting circulators after each antenna with 15 dB isolation.

As mentioned before, this methodology's bottleneck is the delay lines, which must be in nanoscale. As explained, to meet this demanding requirement, some works have demonstrated this method in sub 65 nm CMOS technology, benefiting from nanoscale CMOS filters at the expense of complex RFIC circuitry and costly technology, though with limited improvements. Further, the need for a digital tuning algorithm and the followed latency are other drawbacks of this technique, which make this solution less appealing to be employed in future wireless systems.

#### 2.2.2.2 Wideband active SIC based on bandpass filters (BPF): frequency domain implementation of the filter

Frequency domain implementation of the filter demands significantly narrowband BPFs to channelize the signal. This methodology has become a reality thanks to recent advances in CMOS technology to realize reconfigurable high-Q nanoscale filters, referred to as N-path filters [49, 50]. In N-path filters, tunable high-Q and phase-controlled responses are achieved based on linear periodically time-variant (LPTV) circuits. An input signal to the filter is divided into N branches; in each branch, an RC circuit is in series with a switch. The switches are turned on and off periodically, with LO clocking at non-overlapping periods and 360/N phase differences. The center frequency is defined by the switching frequency, while the bandwidth is determined by the RC time and duty cycle of the clocking. One of the main downsides of this approach is that N RF clocks with different phases must derive the switches, which raises the complexity and power consumption of the circuit.

In [38], the authors have implemented a hybrid FD and FDD transceiver based on two 4-Path filter banks, earning a total of 60 dB isolation (primary isolation + active SIC isolation) over a 20 MHz bandwidth at 1.37 GHz center frequency. Primary isolation of about 35 dB is gained using the two-separate antenna arrangement. In [51], the authors have demonstrated a tunable FD two-element MIMO transceiver with 48 dB isolation (24 dB primary isolation) over 20 MHz bandwidth, represented in Figure 2.12. The transceiver's significant achievement is the wideband tunability applied in 0.5-2.5 GHz frequency ranges, which has been made possible by exploiting a 4-Path filter in 65-nm CMOS technology, though isolation degrades at other frequencies.

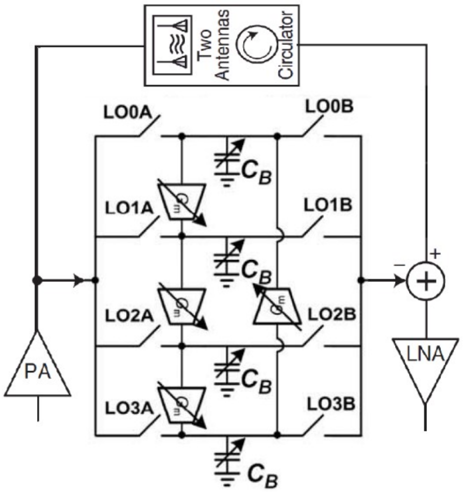

Figure 2.10 Schematic of N-path filtering as active SIC [38]

Generally, N-path filters feature noticeable performance in reproducing a replica of leakage signal over a wide bandwidth regarding FIR filter-based techniques. Moreover, they provide a robust tunability solution to tune the whole transceiver over very wideband frequency ranges. However, their main shortcomings are that they suffer from large power consumption due to driving N LO clocking signals, and they require complex design and advanced CMOS technology for implementation. Besides, similar to time-domain approaches, the SIC bandwidth depends on the number of taps that linearly increases the circuit's complexity and size.

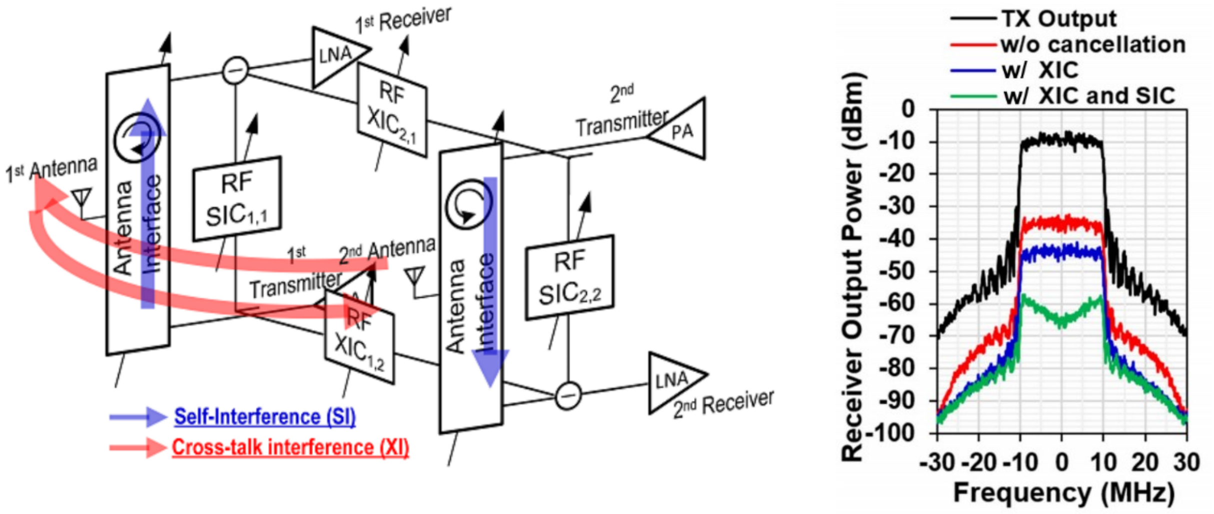

(a) (b)

Figure 2.11 (a) Schematic of the proposed two-element MIMO FD transceiver with N-path filters, (b) measurement results demonstrating 48 dB isolation over 20 MHz bandwidth in [51]

### 2.2.3 Digitally assisted active SIC

Digitally assisted analog active SIC relies on powerful digital signal processing and digital filtering resources. This method reproduces a replica of the leakage signal in the baseband and upconverts it to the RF. This method's notable advantage is that baseband signal processing techniques can be employed to adjust the leakage signal over a wide bandwidth with high resolution. However, this technique's main drawback is that Tx sampling is implemented in baseband where non-idealities of Tx signal such as distortions, phase noise, nonlinearity, and harmonics created in the RF domain, are excluded. Hence, these non-idealities cannot be canceled with this methodology. To tackle this problem, some architectures employ an auxiliary Tx chain to emulate the RF domain's non-idealities into the replica signal. However, this technique imposes a more complex and larger architecture as an additional Tx chain must be implemented, inflicting even more power consumption and tremendously inefficient architecture.

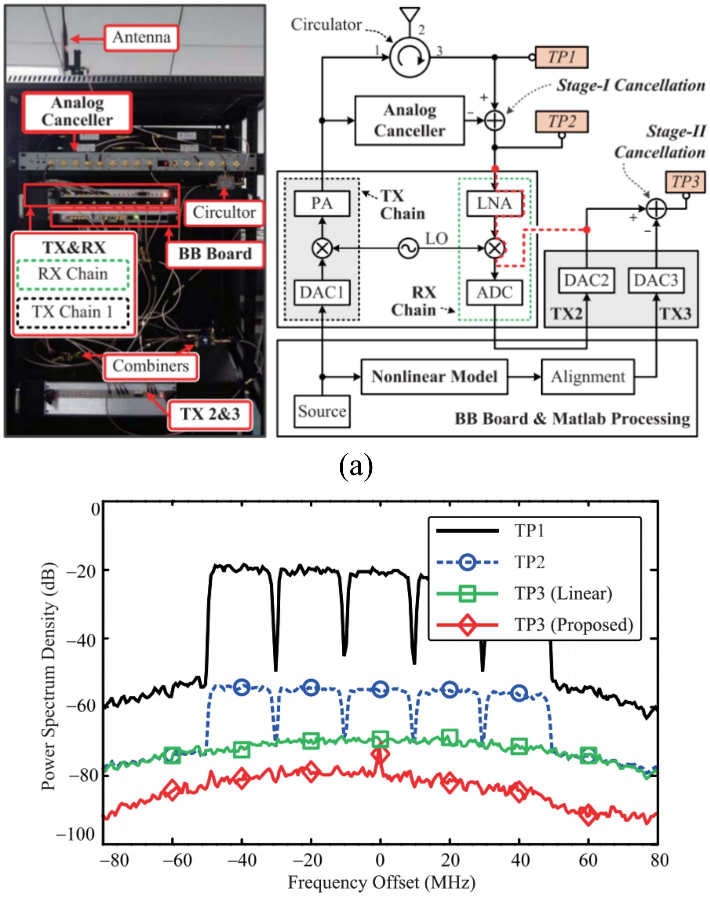

(a)

(b)

Figure 2.12 Proposed hybrid FIR filter and digitally assisted SIC in [52]: (a) Schematic and prototype of the implemented front-end system, (b) Measurement result for an OFDM signal with 100 MHz bandwidth at the center frequency of 2.45 GHz

In [53], the authors have demonstrated 63 dB SIC over 80 MHz bandwidth using an auxiliary Tx chain at the center frequency of 1.95 GHz. In this method, 23 dB of isolation is provided by the circulator, and the rest of the 40 dB isolation is contributed from digitally assisted active SIC. In a similar work [54], 14 dB isolation improvement has been realized with digitally assisted SIC over 20 MHz bandwidth at the center frequency of 2.14 GHz, in conjunction with 40 dB isolation from a commercial circulator. In [52], the authors have implemented a hybrid solution with two active SIC stages. The first stage of cancelation is an FIR filter-based active cancelation in the RF domain. The second stage of cancelation uses a digitally assisted auxiliary Tx chain to remove the remaining leakage signal in the IF domain. Moreover, the second stage exploits an algorithm to predict a nonlinear model for the RF Tx chain to improve cancelation. In this work, the authors have reached 63 dB active SIC over 100 MHz bandwidth at the center frequency of 2.45 GHz.

Generally, digital-assisted active SIC methods can provide broader isolations due to exploiting high-resolution digital filtering. However, they must be used in conjunction with other active SIC methods to be able to eliminate non-idealities of Tx signals produced in the RF domain. More importantly, this method significantly increases the complexity, power consumption, and cost of the transceiver since an extra Tx chain must be affixed to the circuit.

## 2.3 Conclusion on analog domain SIC

Reviewing state-of-art technologies and methodologies for SIC in the analog domain exposes that existing approaches for demonstrating FD systems are not mature yet, and each has significant shortcomings. Reviewed works are summarized in Table 2.1 and Table 2.2 for comparison. Proposed solutions are mostly very narrowband, while wideband solutions rely on active SIC methods, which are all very costly, complex, power consuming, resulting in significantly larger circuits than other conventional transceivers. Besides, in active SIC methods, the number of required filters, the structure's complexity, and the power consumption increase linearly with bandwidth increase, limiting their feasibility in many applications. Currently, active SIC methods are the only technique in the literature that can enable FD systems by providing additional isolation over primary isolation to reach the 60-70 dB isolation benchmark required in 5G systems; however, at tremendous costs. Besides the mentioned problems concerning power consumption and complexity, since these solutions are based on active circuits at the front-end, they limit the structure's power handling, which is a critical issue in future wireless systems. They also raise the system's noise figure and impose latency into the network due to digital adaptive filtering. These limitations are significant regarding their benefits that prevent these methods from being employed in practice, as they cannot compete with existing solutions for communication systems such as 5G FDD/TDD and MIMO transceivers. Therefore, fresh concepts and innovative approaches are required to enable efficient and high-performance FD systems in practice.

Reviewing these works reveals that realizing very high isolation in the passive analog domain is limited by several key bottlenecks. The first constrain is fabrication tolerance that may impose infinitesimal mode or port coupling. Although these mode couplings can be neglected in conventional systems and circuits, they become crucial for FD applications and limit isolation. In PCB technology, limitation in fabrication precision, restraint in precise alignment of different layers, gap or non-uniform epoxy between layers are main fabrication tolerances that restrict the isolation that can be realized in practice. From our observation in the literature and our own experience in the fabrication of several passive circuits, it is concluded that the maximum achievable primary isolation is around 40-50 dB for integrated and PCB designs. Other non-PCB technologies or topologies like metallic waveguide structures may go further; however, they are bulky, costly, and non-integrated structures employed only in specific applications. The second major constraint is the antenna's cross-polarization and multiple reflections from near objects around the antenna. The third constraint is the antenna input reflection (limited impedance matching) in monostatic single-polarized antenna structures. Even if a hypothetical circulator with infinite isolation is connected to a single-polarized antenna, the isolation would still be limited by the antenna reflection coefficient. Because once a transmitted signal is reflected by the antenna input port, it would be similar to a received signal and propagate in the Rx channel. Therefore, to mitigate this inherent problem, we believe that employing dual-polarized antennas instead of single-polarized antennas is the only way to achieve monostatic FD systems. Forth constraint is the presence of surface waves, higher-order modes, and undesired inter-port coupling through air or substrate within the structure resulting in undesired coupling between Tx and Rx channels. The latter constraint can be minimized through a careful design procedure; however, the first two constraints cannot be eliminated in passive structures, and they must be canceled by subtracting them from a replica signal. In other words, multi-stage cancelation approaches must be adopted to overcome these restrictions. This is why so far, only active SIC solutions have been capable of realizing isolations beyond 50 dB in monostatic-integrated configurations.

Therefore, any anticipated approach for FD systems must be able to cope with the mentioned challenges to break the isolation barrier. Following radio requirements in 5G and future wireless systems, an FD transceiver must provide better than 70 dB isolation over at least 80 MHz bandwidth at sub-6 GHz frequency ranges while having a relatively simple, low cost, low noise figure, and be capable of high-power operation with efficient performance regarding other transceiver technologies. A passive structure for the front end is favored for low-noise and high-power operations. Another vital issue for 5G FD transceivers is tunability. In agreement with new radio (NR) requirements that demand multi-function and multi-band operation, any proposed approach for FD systems should incorporate tunability into the structure.

Table 2.1 Summery and comparison of existing state-of-art techniques and methodologies for full-duplex systems

| Ref. | Freq. (GHz) | Pri. Iso. (dB) | Active SIC Iso. (dB) | Total Iso. (dB) | BW (MHz)/ BW (%) | Methodology/ Technology | Integ. | Tunab. | Major Cons/ Remarks |
|---|---|---|---|---|---|---|---|---|---|
| [29] | 120 | 30 | - | 30 | 14000 (11 %) | - EBD<br>- 40-nm CMOS | ✓ | | 3 dB Loss in Tx & Rx |
| [30] | 3.5 | 43 | - | 43 | 750 (21%) | DP antenna | | | Large profile |
| [34] | 5.45 | 45.2 | - | 45.2 | 700 (12%) | - DP antenna<br>- waveguide structure | | | Large profile |
| [35] | 4.85 | 40 | - | 40 | 250 (5%) | DP antenna | ✓ | | |
| [39] | 1.01 | 25 | 30 | 55 | 4 (0.4%) | -Integrated non-magnetic circulator and single-tap active canceler based on N-path filters<br>- Digital cancelation<br>- 40-nm CMOS | ✓ | | - Significantly low BW<br>- Complex structure<br>- High power consumption<br>- Low power operation |
| [41] | 60 | 40 | 30 | 70 | 1000 (1.6%) | - Two separate orthogonal polarized antennas<br>- Single-tap active SIC<br>- Reconfigurable load in the Rx antenna<br>- 40-nm CMOS | ✓ | ✓ | - 3 dB loss in Rx<br>- Complex structure<br>-High power consumption<br>- Low-power operation |
| [45] | 2.45 | 50 | 10 | 60 | 120 (5%) | - Two separate antenna<br>- Four-tap FIR filter | ✓ | | - Low isolation regarding two-antenna configuration.<br>- Very large PCB. |
| [46] | 2.45 | 45 | 38 | 83 | 20 (0.8%) | - Two separate antenna<br>- Eight-tap FIR filter | ✓ | | - Low bandwidth<br>- Very large PCB. |
| [46] | 2.45 | 45 | 38 | 83 | 20 (0.8%) | - Two separate antenna<br>- Eight-tap FIR filter | ✓ | | - Low bandwidth<br>- Very large PCB. |

Table 2.2 Summery and comparison of existing state-of-art techniques and methodologies for full-duplex systems (cont'd)

| Ref. | Freq. (GHz) | Pri. Iso. (dB) | Active SIC Iso. (dB) | Total Iso. (dB) | BW (MHz)/ BW (%) | Methodology/ Technology | Integ. | Tunab. | Major Cons/ Remarks |
|---|---|---|---|---|---|---|---|---|---|
| [19] | 2.45 | 38 | 24 | 62 | 80 (3%) | - EBD<br>- Dual-injection five-tap FIR filter<br>- 40-nm CMOS | ✓ | ✓ | - 3 dB loss in Rx & Tx<br>- Very Complex Structure<br>- Low-power applications |
| [48] | 2.2 | 15 | 30 | 45 | 20 (0.9%) | - Circulator<br>- Dual-injection FIR filter<br>- MIMO (2x2) structure<br>- 65-nm CMOS | ✓ | ✓ | - Low isolation<br>- Low bandwidth<br>- Complex structure<br>- Low-power operation |
| [38] | 1.37 | 35 | 25 | 60 | 20 (1.45%) | - Two-separate antenna<br>- Two 4-path filters<br>- 40-nm CMOS | ✓ |  | - Low isolation regarding two-antenna configuration.<br>- Low bandwidth<br>- Very Complex Structure<br>- High Power consumption<br>- Low-power operation |
| [51] | 0.5-2.5 | 24 | 24 | 48 | 20 (1%) | - Circulator<br>- 4-path filter<br>- MIMO (2x2)<br>- 40-nm CMOS | ✓ | ✓ | - Low bandwidth<br>- Very Complex Structure<br>- High Power consumption<br>- Low-power operation |
| [52] | 1.95 | 23 | 40 | 63 | 80 (4%) | - Circulator<br>- Digital assisted SIC | ✓ |  | - Very complex structure<br>- Significant power consumption |
| [54] | 2.45 | 20 | 40 | 63 | 100 (4%) | - Circulator<br>- Hybrid active SIC<br>- Two-tap FIR filter<br>- Digitally assisted SIC | ✓ |  | - Same as above |

Pri.: Primary; Iso.: Isolation; Integ.: Integrated; Tunab.: Tunability.

# CHAPTER 3 ARTICLE 1: NON-RECIPROCAL MODE CONVERTING WAVEGUIDE AND CIRCULATOR

Amir Afshani, Graduate Student Member, IEEE, and Ke Wu, Fellow, IEEE

This article pursues our first objective of the thesis in realizing a novel non-reciprocal component for the first time that is capable of the performing non-reciprocal mode-conversion. The configuration introduced here is suitable for ferrite materials with high saturation magnetization. This article was published in IEEE Transactions on Microwave Theory and Techniques (August 2019).

## 3.1 Abstract

In this work, a class of anti-symmetrically biased ferrite-loaded substrate integrated waveguides (SIW) is studied in detail along with the definition of three main regions of operation. With focus on one of those newly defined regions, a non-reciprocal mode waveguide (NRMW) is introduced for the first time and its related design procedure is explained and illustrated. Further, a fundamental approach is proposed and devised for developing a fully integrated structure called non-reciprocal mode-converting waveguide (NRMCW). This ferrite-based device is capable of effectively converting $TE_{10}$ mode into $TE_{20}$ mode only in one direction, thereby suggesting that the original mode be preserved in the reverse direction. In other words, the mode conversion in this case is unidirectional, which has never been reported so far. To substantiate the usefulness of the proposed structure and physical mechanism, a class of circulators is designed, fabricated and demonstrated on the basis of the introduced NRMCW, thus validating the formulated theory of NRMCW in this work and providing an application example of such devices. Both theoretical and experimental results are presented in support of the claims made in this work regarding the proposed circuit concept and its related foundation work.

*Index Terms*—circulator, ferrite, mode conversion, non-reciprocal, non-reciprocal mode converting waveguide (NRMCW), substrate integrated waveguide (SIW), $TE_{20}$ mode.

## 3.2 Introduction

Throughout the years, dominant microwave and millimeter-wave (mmW) engineering and its related building technologies have smoothly gone from bulky rectangular waveguides to planar transmission lines and then to substrate integrated waveguides (SIW). Concurrently, theory and practices of ferrite devices have evolved over decades with a rich history of research to adapt themselves to emerging technologies. As ferrite theory has evolved and matured, and as technologies have advanced, more features of ferrites have been brought to light [55-57]. The ongoing development suggests that ferrites are generally irreplaceable materials in microwave engineering.

As the unique planar integrated version of rectangular waveguides, SIWs are attractive guided-wave structures to embed ferrite materials since they are compact, low loss, low cost, compatible with standard planar processing techniques such as PCB and LTCC, capable of high power handling, and self-shielding [58-64]. More importantly, inside rectangular waveguide and SIW, there are distinguished regions where either dominantly RH (right-handed) or LH (left-handed) circularly polarized waves exist. Since ferrites exhibit the fundamental property of non-reciprocity in the RH and LH circularly polarized regions, SIW structures and techniques would be much more functional and flexible for developing ferrite-loaded devices than a microstrip line and any other planar counterparts.

Different design schemes have been applied, each offering a unique approach to exploiting the inherent non-reciprocity of ferrites. Junction circulators, for example, utilize two modes of the RH and LH circularly polarized magnetic fields to rotate the standing wave pattern inside the junction toward one of the ports to yield non-reciprocity [65-67]. Non-reciprocal phase shifters are devised to benefit from different phase shifts in forward and reverse directions [68-70]. Various types of isolators such as resonance, field displacement, and edge guided mode make use of ferrites in different ways to attenuate the wave only in one desired direction [63], [71-72] and so forth [73-77].

In this paper, we propose and present a fundamental method to exploit the non-reciprocity of ferrites by devising a non-reciprocal mode waveguide (NRMW), which offers different mode-profile and phase-shift in forward and reverse direction to maximize the non-reciprocity. Further, NRMW is used to develop and demonstrate, for the first time, a unique device so-called “nonreciprocal mode converting waveguide (NRMCW)" which was very briefly presented and discussed in [78]. In this paper, a generalized theory of antisymmetrically biased ferrite-loaded SIW is presented to map and categorize different behavior of the device in regard to the variation of propagation constants, leading to the emerging of NRMW as a specific category. Further, a detailed theory and methodology of NRMCW and a new type of circulator are described and developed. The NRMCW exclusively converts $TE_{10}$ mode into $TE_{20}$ mode (and vice versa) in one direction, while preserving the mode in the other direction. A mode converter device, specifically $TE_{10}$ to $TE_{20}$ converter, has been already realized in [78] where a reciprocal bended waveguide was designed to reciprocally convert the modes. However, this is completely different compared to the scenario of NRMCW that will be introduced in this work. It is believed that NRMCW can serve as a fundamental technique to design a new class of non-reciprocal ferrite devices ranging from isolators, phase shifter and gyrators to multi-port circulators.

This paper is organized as follows. In Section II, we will investigate and characterize a twin-slab antisymmetrically biased ferrite-loaded SIW structure to distinguish and spot different regions of operation, each of which provide different features and are specifically useful for certain applications. In Section III, we will focus on a particular region with exclusive features and the concept of non-reciprocal mode waveguide (NRMW) will be formulated and studied. In Section IV, we will exploit NRMW as a cornerstone to propose and demonstrate the theory of non-reciprocal mode converting waveguide (NRMCW) related to the above-mentioned region of interest. In Section V, NRMCW will be exploited to develop a class of circulators as a primary showcase of NRMCW for various applications. This circulator will be analyzed in details for design and realization. Simulation and measurement results will be presented to validate the development of circulator as well as the formulated NRMCW theory. Finally, this paper will be concluded in the last Section.

## 3.3 Non-reciprocal Twin-Slab Ferrite Loaded SIW and Non-reciprocal Mode Waveguide (NRMW)

In this section, we will develop a well-rounded study of a twin-slab ferrite loaded SIW which is anti-symmetrically biased and whose ferrite slabs are loaded along the sidewalls of SIW. We will examine different configurations of such a structure, which result in completely different behaviors and functionalities of the device. In this analysis, three completely different regions of operation for non-reciprocal ferrite loaded SIW are identified and discussed. It will be shown that one specific region accommodates and establishes non-reciprocal modes within the SIW. This will lead the development of the concept of non-reciprocal mode waveguide (NRMW) which is the primary subject of interest in this work. It should be noted that the focus of this work is on the implementation of SIW ferrite devices. In almost all cases, 'SIW' and 'waveguide' are however interchangeable notions.

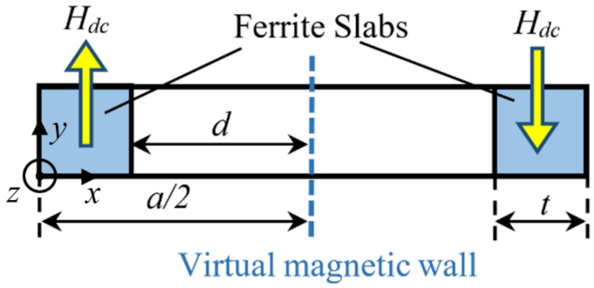

Figure 3.1 Cross section of antisymmetrically ferrite loaded SIW

In Figure 3.1, the cross section of a ferrite loaded SIW is illustrated. It can be seen that two identical ferrite slabs are loaded symmetrically inside the SIW, where they are magnetically biased with the same strength but different sign or polarization. In [80], it is indicated that if ferrites at either side are biased in opposite direction, a non-reciprocal and uni-directional device is created. In this paper, all possible scenarios of this topology under different parameter variations are first of all extensively examined and then categorized into different regions. Subsequently, it is demonstrated that with a careful design of the structure, a bi-directional device possessing a non-reciprocal mode profile in different directions can be realized.

To analyze the structure, the Maxwell equations must be solved for the ferrite loaded SIW, in which the permeability tensor is used to describe the ferrite behavior under the condition of a transvers bias [81]. Due to the magnetic symmetry at the center of SIW, a magnetic wall can be considered at the center of the device, resulting in a simplified analysis. Two sets of equations can be derived for electric and magnetic fields inside the structure, thereby leading to a single characteristic equation by imposing boundary conditions. The characteristic equation is used to calculate the propagation constant in both forward and reverse directions, which is the key to distinguish and analyze different regions of operation. The characteristic equation of structure in Figure 3.1is derived as [81]:

$$\frac{\mu_e}{\mu_0} k_a \tan(k_a \text{ d}) - k_f \cot(k_f \text{ t}) - \frac{\kappa\beta}{\mu} = 0 \qquad (4.1)$$

$$k_a^2 = k^2 - \beta^2, \qquad k_f^2 = \omega^2 \mu_e \varepsilon - \beta^2 \qquad (4.2)$$

where $k_a$ and $k_f$ are cut-off wave-numbers for substrate and ferrite regions, respectively. Also $t$ is width of ferrite, $d$ is half width of the waveguide ($d=a/2$), $\mu_e$ is effective permeability of ferrite, $\kappa$ and $\mu$ are elements of the permeability tensor for the ferrite biased in $y$ direction. Further, $\beta$ and $k$ are propagation constant and wave number of the waveguide, respectively.

The elements of permeability depend on the choice of a ferrite type and the strength of magnetic bias. The width of SIW and the permittivity of substrate are selected on the basis of frequency of operation and applications, herein inferring that $k$ and $a$ are usually predefined. Therefore, design parameters are the width of ferrite $t$, strength of internal magnetic bias $H_{dc}$, and ferrite saturation magnetization $Ms$ concerning a specific type of ferrite of interest. Among these three parameters, the ferrite type is typically predetermined due to applications in mind, leaving us with two degrees of freedom to change and control the behavior of device.

The characteristic equation can be solved numerically to find $\beta$. However, a better way of analysis is to divide the equation into two parts and solve the equation graphically. Although this method provides less accurate results (though sufficient enough for the design step), it becomes more insightful in the analysis of device and helps us understand the nature of the device, specifically, while varying different parameters. This will be illustrated in next sections. To do so, we divide (3.2) into two functions $F1$ and $F2$ as follows:

$$F1(\beta) = \frac{\mu_e}{\mu_0} k_a \tan(k_a \text{ d}) - k_f \cot(k_f \text{ t}) \qquad (4.3)$$

$$F2(\beta) = \frac{-\kappa\beta}{\mu} \qquad (4.4)$$

Since the $\beta$ parameter in $F2$ changes sign with propagation direction, the cross-point of $F1$ and $+F2$ yields $\beta_f$ (propagation in forward direction) and cross-point of $F1$ and $-F2$ results in $\beta_b$ (propagation in reverse direction).

An important and critical observation is that different locations of $\beta_f$ and $\beta_b$ in regard to $k$ (waveguide wave-number) result in different mode profiles in wave propagation. If propagation constant $\beta$ is smaller than wavenumber $k$, then $k_a$ is real which imposes a sinusoidal variation of fields over the cross-section of waveguide in the substrate region. On the contrary, if $\beta$ is larger than $k$, $k_a$ becomes imaginary which implies a hyperbolic variation of fields across the waveguide. Therefore, the root locus of propagation constant defines the operation region of device which can completely change the behavior of device and related applications. Hence, three regions of operation can be defined as follows:

### 3.3.1 Region 1: Non-reciprocal Phase

If, in a graphical solution of the characteristic equation, $F1$ crosses both $+F2$ and $-F2$, and both the cross points ($\beta$) are smaller than $k$, then electromagnetic fields in both directions take a sinusoidal form and thus have the same mode. Nevertheless, propagation constants ($\beta$) in different direction can be different, meaning that phase is non-reciprocal. Such a device has applications in non-reciprocal phase shifters or in the realization of gyrators. Figure 3.2(a) illustrates an example in which the roots of (3.3) and (3.4) fall into this region. The ferrite type and design parameters for this example and examples of the following regions are summarized in Table 1. In these examples presented in this section, the dielectric constant of the substrate and the ferrite is 10.2 and 13.2 respectively at operation frequency of 6 GHz.

Another possible scenario with a similar outcome is that both crossing points are bigger than k, resulting in a hyperbolic type of field patterns. Also in this case, the wave propagation in both directions has the same mode but different phase.

### 3.3.2 Region 2: Non-reciprocal and Unidirectional

In this scenario, $F1$ crosses either $+F2$ or $-F2$, but not both of them. This means that propagation constant $\beta$ is real only for one direction and it is imaginary and cut-off in the opposite direction. In Figure 3.2(b), an example of such a behavior is illustrated with design parameters shown in Table 1. An important distinction between this isolator and conventional isolators is that, in this type of isolator, the isolation is achieved through wave attenuation due to the cut-off. Conversely, in the conventional resonance and field displacement types of isolator, the isolation is achieved by attenuation of wave in the resonance region and by using a resistive material, respectively [63, 72].

### 3.3.3 Region 3: Non-reciprocal Mode

In this case, as shown in Figure 3.2(c), the characteristic equation has two roots ($\beta$). One root is smaller than $k$ and the other root is bigger than $k$. If $\beta$ is smaller than $k$, then $k_a$ is real, thus imposing sinusoidal fields over the cross-section of waveguide in the substrate region. On the contrary, if $\beta$ is bigger than $k$, then $k_a$ is imaginary, which results in a hyperbolic variation of fields across the waveguide. This implies that fields along one direction are concentrated in the middle of the waveguide ($\beta$ smaller than $k$). However, in the other direction, fields are more concentrated at the ferrite interface ($\beta$ bigger than $k$). This non-reciprocal mode would be much more pronounced if the roots are placed as far as possible from each other. It must be emphasized that a device operating in this region exhibits both the non-reciprocal mode and non-reciprocal phase, which can in turn maximize the non-reciprocity phenomena.

It is noted that in the above analysis, there is a possibility of higher-order or unwanted modes propagation. In other words, there may be more than one root in (3.3)-(3.4) for either direction, which is undesirable and must be avoided in design procedure.

Further, it should be considered that in the presented examples, the SIW width, substrate and ferrite type are fixed, and only by altering the ferrite width and magnetic bias, it is possible to switch the state of operation from one region to another. Therefore, considering all the design parameters including magnetic bias, ferrite width, SIW width, and ferrite type, it is implied that there are enough degrees of freedom to design a ferrite-loaded SIW in any desired region.

Table 3.1 Design Parameters of Three Regions in Figure 3.2

| | $a$ (mm) | $t$ (mm) | $H_{dc}$ (Oe) | $M_S$ (G) |
|---|---|---|---|---|
| Region I | 16 | 1 | 2000 | 5000 |
| Region II | 16 | 7.5 | 10 | 5000 |
| Region III | 16 | 3 | 700 | 5000 |

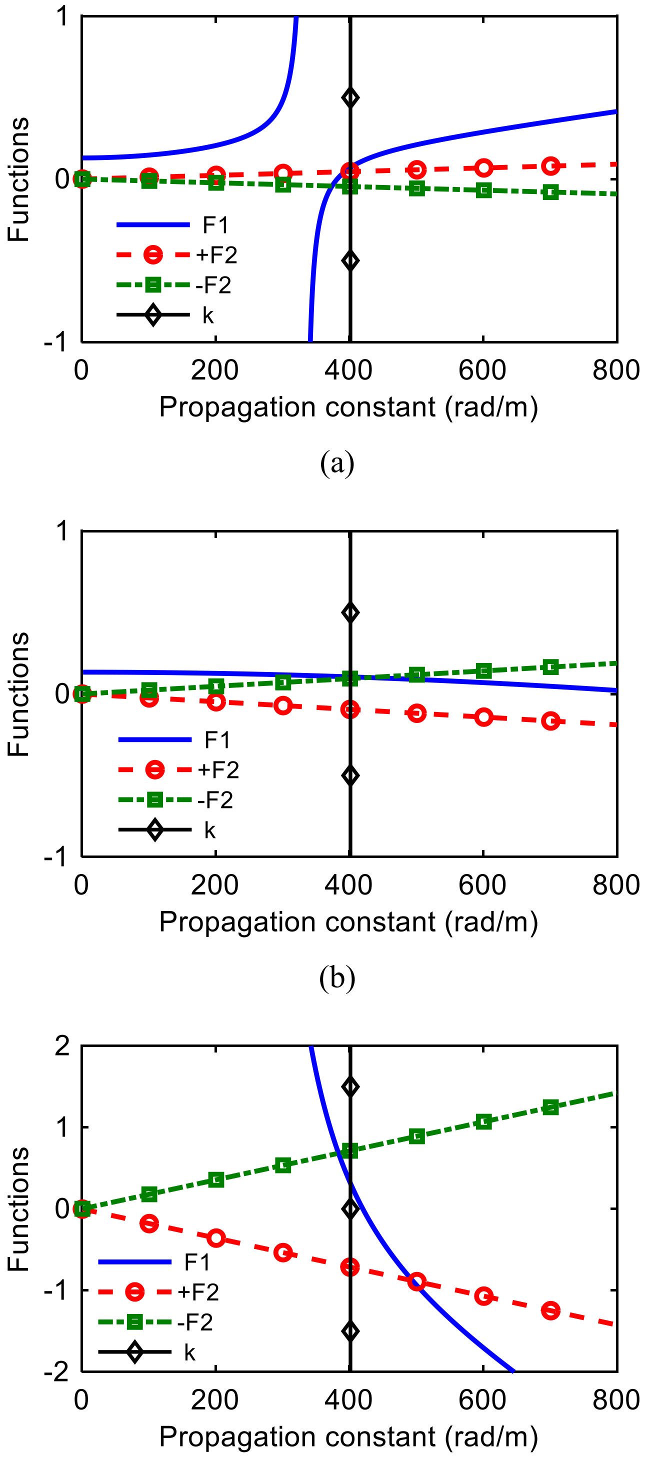

(a)

(b)

(c)

Figure 3.2 Root locus of characteristic equation displaying different regions of operation: (a) region 1: non-reciprocal phase, (b) region 2: non-reciprocal and unidirectional (isolator), (c) Region 3: non-reciprocal mode

## 3.4 Realization of Non-reciprocal Mode Waveguide (NRMW)

All the three above-mentioned regions can be exploited for different RF/microwave applications. Nevertheless, the third region is the subject of interest and discussion in this paper due to its importance. In this region, a distinct non-reciprocal mode propagates in either direction, which holds exclusive and unparalleled features. As can be understood from the above discussion, a non-reciprocal mode is achieved under certain conditions in region 3, which we will present in the rest of this section a design strategy to meet these conditions over desired frequency bands.

To realize a non-reciprocal mode waveguide in region 3, an appropriate width of SIW and ferrite type should be chosen at first depending on application and frequency range. Here, a Nickel ferrite with a high magnetic saturation of 5000 Gauss is selected for operation at the center frequency of 6 GHz. The Nickel ferrite has been selected as it benefits a large bandwidth due to its high saturation magnetization which is favorable in this design. Also, high saturation magnetization ferrite devices provide a high degree of phase shift for small lengths, thus resulting in more compact devices with a high tuning range.

To yield a better matching between SIW and ferrite pieces, a high dielectric constant substrate is favored in this showcase study and hence the dielectric constant is chosen to be 10.2 corresponding to Rogers 6010 substrates. Further, the SIW structure must support both $TE_{10}$ and $TE_{20}$ modes as the non-reciprocal mode waveguide to be exploited in the subsequent sections would unidirectionally convert $TE_{10}$ mode into $TE_{20}$ mode. Accordingly, the width of SIW ($a$) must be wide enough to allow the propagation of both $TE_{10}$ and $TE_{20}$ modes and to become the cut-off for $TE_{30}$ mode. Thus, the width of waveguide is approximated by (3.5) [81]:

$$a_{SIW} = \frac{c_0}{2\frac{f_c(TE_{30})}{3}\sqrt{\varepsilon_r}} \qquad (4.5)$$

In the above formulation, $c_0$ is the velocity of light, $f_c\,(TE_{30})$ is the cut-off frequency of the 3rd mode at the maximum frequency of operation, $\varepsilon r$ is the substrate dielectric constant. In this work, $a$ is selected to be 21 mm corresponding to the 3rd mode cut-off frequency at 6.7 GHz. Frequency of 6.7 GHz is chosen to stay far enough from 6.0 GHz, thus ensuring that the device bandwidth is not limited by the onset of the 3rd mode. It should be noted that in our design and fabrication process, tightly spaced plated slots are deployed for mimicking the SIW walls instead of conventional periodically plated vias, which can be effectively modeled by solid walls at low frequency; thus, the accuracy of (3.5) is sufficient in this design. However, experimental models as reported in [81] may be inspired for designs with plated vias for a better accuracy.

By setting *Ms* (ferrite type) and *a* (waveguide width), we are left with two parameters in the design of the device. Those two parameters, namely magnetic bias $H_{dc}$ and ferrite width *t*, play a fundamental role in deciding the region of operation. For the following two reasons, $H_{dc}$ must be selected so that the effective permeability of ferrite $\mu_e$ is negative. The first reason is that the ferrite should be cut-off so the wave could not propagate inside the ferrite while designing a mode-converting waveguide as illustrated in the next section. Another merit of the cut-off is that the resulting field distribution would be hyperbolic inside the ferrite, so the field is maximum in one direction at the ferrite interface. In the other direction, it can be minimum and almost null, which is a propitious feature for mode conversion. The second reason is related to the observation in Figure 3.2. Figures show that for operation in region 3, the angle between *+F2* and *–F2* lines must be augmented so that respective roots ($\beta$) fall in a larger distance from each other, permitting a chance to realize the operation in region 3. Therefore, the slope of *F2* must be enlarged in (3.4); in other words, we must have $\kappa > \mu$ which corresponds to $\mu_e < 0$. The larger the amplitude of $\mu_e$ gets (larger negative value), the larger *F2* will be achieved, resulting in a substantial difference in $\beta$ in each direction and, consequently, a profound difference in the non-reciprocal mode profile of wave in either direction. On the other hand, as $\mu_e$ becomes more positive, the angle between *+F2* and -*F2* diminishes, engendering roots with a small difference that diminishes the chance to operate in the 3rd region.

As discussed above, we must bias the ferrite into a negative region. Considering the equation of effective permeability in [81], this equation can be expressed in terms of zeroes and poles as:

$$\mu_e = \mu_0 \frac{(H_{dc} - H_{z1})(H_{dc} - H_{z2})}{(H_{dc} - H_{p1})(H_{dc} - H_{p2})} \tag{4.6}$$

where zeroes and poles respectively are:

$$H_{z1,2} = -Ms \pm \frac{f}{\gamma}, \quad H_{p1,2} = -\frac{1}{2}\left( Ms \pm \sqrt{Ms^2 + 4\left(\frac{f}{\gamma}\right)^2} \right) \quad (4.7)$$

In the above equation, $H_p$ and $H_z$ are poles and zeroes of the function. Further, $Ms$ is the saturation magnetization of the ferrite sample, $f$ is the operation frequency and $\gamma$ is the gyromagnetic ratio and equals to 2.8 MHz/Oe. From (3.7), it is obvious that the first pole and the first zero have a negative value; therefore, in practice where applied $H_{dc}$ is a positive value, they can be neglected. The second zero may be positive or negative depending on the frequency of operation and ferrite type, but the second pole is always a positive number and bigger than both zeroes. A close inspection of (3.6) reveals that $\mu_e$ will be negative for bias values between the zero and the pole of the function. Hence, an accurate range, in which the exact value of magnetic bias must be sought, is determined analytically. Accordingly, $\mu_e$ is plotted in Figure 3.3 against magnetic bias $H_{dc}$ for three different frequencies to examine the shape of $\mu_e$ over a magnetic bias sweep and at adjacent frequencies.

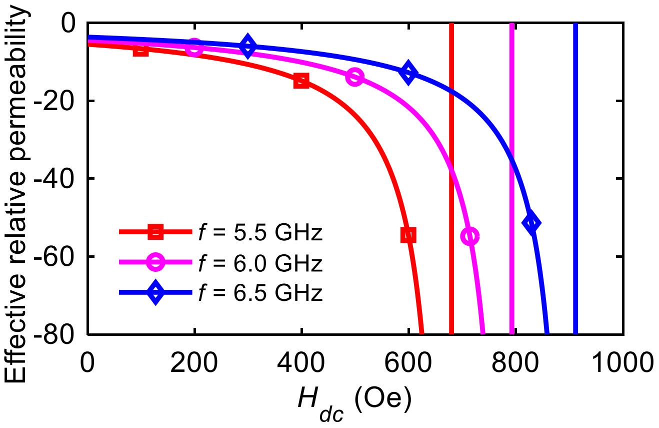

Figure 3.3 Effective permeability of ferrite with $Ms$=5000 $G$ versus magnetic bias field, with negative permeability

Evaluating (3.6) for the selected ferrite and frequency, it can be seen that both zeros are negative and only one positive pole exists at 679, 793 and 912 Oe corresponding to the frequency points of 5.5, 6.0, and 6.5 GHz respectively, which are clearly indicated in Figure 3.3 by vertical lines (asymptotes). Assuming a 1 GHz bandwidth for the device, it is decided that the magnetic bias must be smaller than 679 Oe to yield a negative $\mu_e$ over the whole bandwidth.

Determining a proper range of $H_{dc}$, we must narrow down and specify the exact value of $H_{dc}$ and $t$. As the ferrite plays the critical role in non-reciprocity, the width of ferrite must be sufficiently large. On one hand, if the ferrite is too narrow, the non-reciprocal mode would not be fully realized as unwanted modes (waveguide modes) may propagate in the device; on the other hand, as the fields inside the ferrite are hyperbolic and decay exponentially in magnitude, a very wide ferrite may be unnecessary. Further, wider ferrite slabs result in a smaller space in the substrate region for a fixed SIW width, and hence, the mode separation between the forward and reverse waves deteriorates. Therefore, the minimum ferrite width that avoids the propagation of unwanted modes is favored. In Figure 3.4, (3.3)-(3.4) have been solved for three different values for the ferrite slab width. It is implied from the figure that for narrow ferrite slabs, the unwanted mode (SIW mode) propagates inside the structure. However, as the ferrite width increases, the *F1* function shifts downward until there is no crossing between *F1* and *F2* in a low region at $t=4$ mm. Interestingly, it is discerned that the main roots are almost unaffected by change in ferrite width, which is due to the exponential decay of fields inside the ferrite as stated previously.

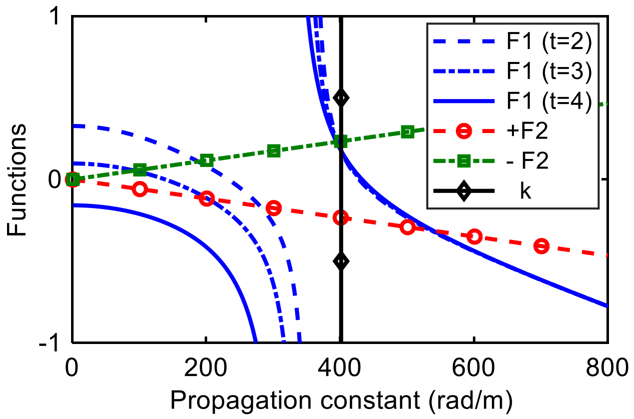

Figure 3.4 Solving equation (3.5) for various widths of ferrite

To determine the precise value for $H_{dc}$, the field distribution across the device cross-section is plotted for various values. In Figure 3.5, E-field, $H_z$-field and $H_x$-field distributions are plotted for three values corresponding to 400, 500, and 600 Oe, where the ferrite slabs are distinguished with green areas. In each figure, curves are all normalized to the maximum of the corresponding field in the forward direction. From those figures, it can be observed that a non-reciprocal mode profile is

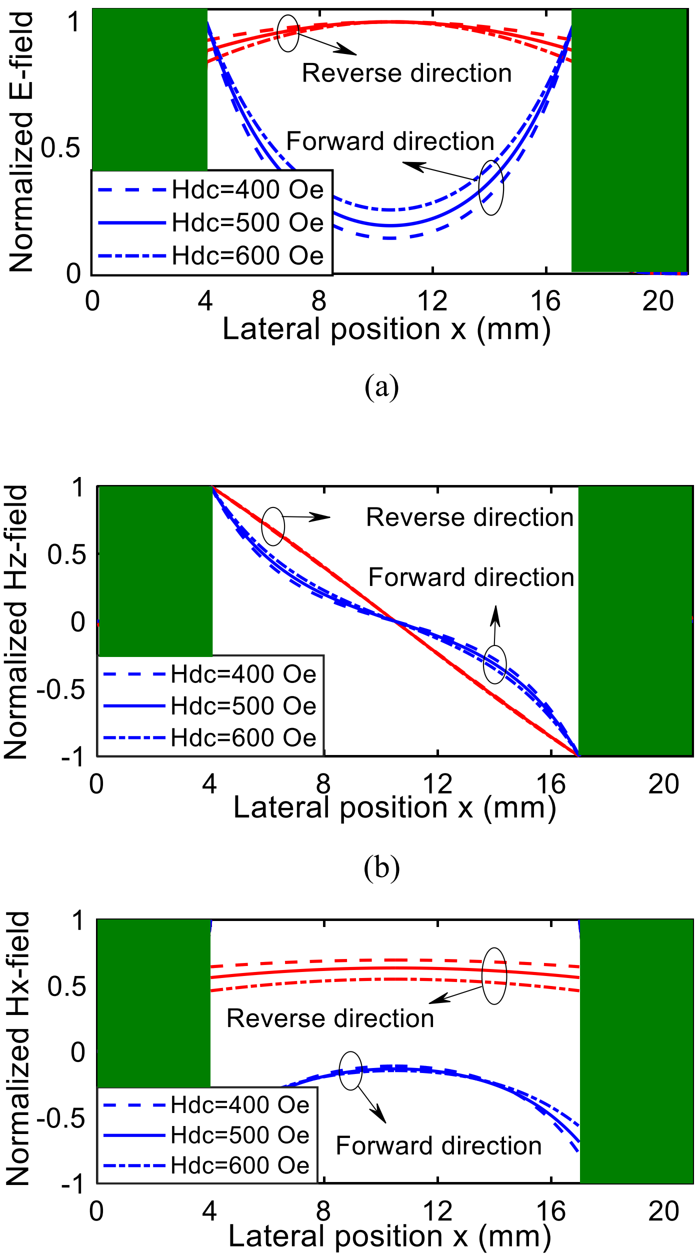

(a)

(b)

(c)

Figure 3.5 EM field patterns for forward and reverse direction propagation at the cross section of NRMW: (a) Ey (b) Hz (c) Hx

achieved for all the bias values inside the substrate region as the wave concentration is dominant in the middle of waveguide for the curves in the reverse direction, while for the curves in the forward direction wave is concentrated at the ferrite interface. Also, the ferrite region is clearly cut-off and field components are small for most of the cross section. Comparing the E-field distributions for different values of magnetic bias in Figure 3.5, it is inferred that for small bias values up to 400 Oe, the field distribution in the reverse direction is close and similar to a plane wave, which is not preferable here. On the other hand, as the magnetic bias increases up to 600 Oe, the E-field in the middle of SIW gets stronger in the forward direction which is not desired as well. Therefore, there is a trade-off in choosing the optimum magnetic bias and an average value must be chosen to compromise the effects in the forward and reverse directions and also the bandwidth. Hence $H_{dc}$ = 500 Oe is determined here as the optimum value for this device demonstration.

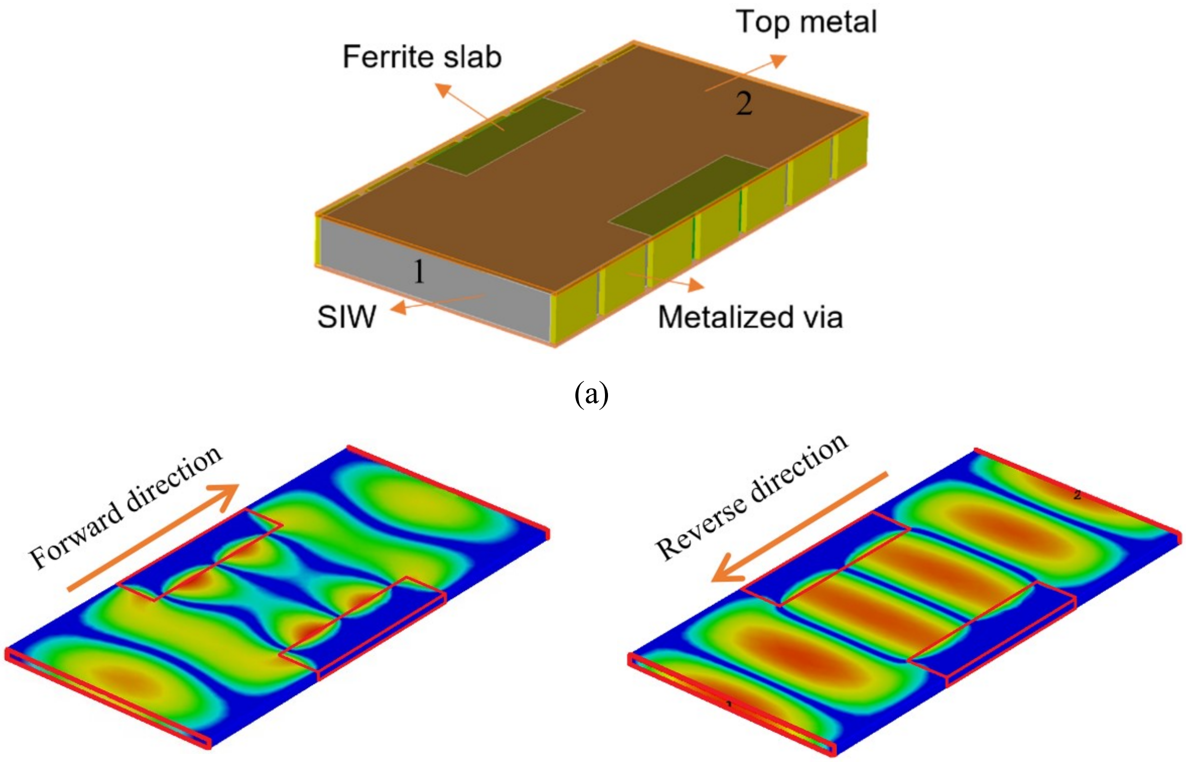

(a)

(b)

(c)

Figure 3.6 (a) Schematic of proposed NRMW, (b) $TE_{10}$ e-field pattern of NRMW in forward direction, (c) $TE_{10}$ e-field pattern of NRMW in reverse direction

To verify the mathematical modelling of NRMW in region 3, the device is designed and simulated using CST Microwave Studio. The electric field patterns inside NRMSIW are illustrated in Figure 3.6 which are in a complete agreement with the $TE_{10}$ field pattern plotted analytically in Figure 3.5.

The picture displays simulated electric fields inside the structure. Comparing two pictures, it is revealed that in Figure 3.6(b) the wavelength is smaller than that of Figure 3.6(c), showing a larger propagation constant for the forward direction than the reverse direction. Further, the wave propagating in the reverse direction is rather concentrated in the middle of SIW like ordinary $TE_{10}$ mode (normal mode). However, wave propagating in the forward direction is concentrated on the edge of the ferrite slabs forming semi-decoupled waves at either side of the waveguide (edge mode).

Presenting the theory of NRMW and demonstrating the theoretical foundation through simulations, we conclude this section. In the next section, we will develop the basis of designing a unique non-reciprocal mode-converting waveguide using NRMW as discussed and demonstrated in this section.

## 3.5 Non-reciprocal Mode Converting Waveguide (NRMCW)

While in the previous section, we have developed the concept of NRMW and demonstrated the device based on theoretical foundation. In this section, we intend to exploit NRMW to investigate and demonstrate through design a device having some unique and interesting features. This new device is called “non-reciprocal mode-converting waveguide (NRMCW)” which converts the SIW modes in one direction while preserving the modes in the reverse direction. In other words, $TE_{10}$ mode is converted into $TE_{20}$ mode in one direction or vice versa, while in the other direction the $TE_{10}$ or $TE_{20}$ mode is guided normally and unaffectedly.

As in the edge mode of NRMW, the wave is concentrated along the sides of waveguide and is semi-decoupled; the wave in this mode is prone to a drastic change if bends are introduced in the ferrite-loaded section of SIW. This means that inserting a bend along NRMW provides two different paths for the semi-decoupled waves at each side of SIW. The scenario is similar to a road with sidewalks at either side: if there is a turn over the road, two pedestrians on each sidewalk would walk through different path lengths. Similarly, the portion of the wave here at the inner side of the bend travels less distance than the portion at the outer side of the bend. Therefore, with a careful design of the bend, where the ferrite slabs at the inner and outer sides of the bend differ in length about a half wavelength, a mode conversion can be achieved. Accordingly, through a similar procedure, one wavelength (or equivalently any integers of wavelength) difference in length of the inner and outer slabs of the ferrite results in the preservation of the mode. This mode conversion/preservation is solely dependent on the difference in length of the ferrite slabs at either side of the bend; in other words, it depends only on the angle of the bend and is independent of the radius of the bend. Therefore, in mathematical terms and considering Figure 3.7(a), the difference in length of arcs at either side is expressed as:

$$Arc_{out} - Arc_{in} = \theta(R + a - t/2) - \theta(R + t/2) \qquad (4.8)$$

Hence we have:

$$\begin{cases} \theta = \dfrac{Arc_{out} - Arc_{in}}{a-t} = \dfrac{n\lambda}{a-t} & \text{mode preservation} \\ \theta = \dfrac{(n-0.5)\lambda}{a-t} & \text{mode conversion} \end{cases} \qquad (4.9)$$

In the above formula, *a* is the width of SIW and *t* is the width of each ferrite slab, theta (*θ*) is the angle of the bend in radian, $Arc_{out}$ and $Arc_{in}$ are the lengths of ferrite slabs in the outer and inner sides of the bend respectively, and the difference must be an integer multiple of λ to preserve the mode or odd integer multiple of λ/2 to convert the mode. As expressed in (3.9), we perceive that the mode conversion or preservation at edge mode is completely independent of the radius of the bend.

However, interestingly in the normal mode (reverse propagation), the scenario is different. As the wave is sinusoidal and concentrated in the middle of SIW it behaves similarly to a normal $TE_{10}$ mode. In this mode, both radius and angle of the bend can affect the mode and be designed to preserve the mode or convert it from $TE_{10}$ to $TE_{20}$ mode [78]. As such, here by fixing the angle of the bend, we can preserve the mode in the edge mode (forward propagation), and by fixing the radius (while the angle is already known), we can convert the mode in the normal mode (reverse direction) or vice-versa.

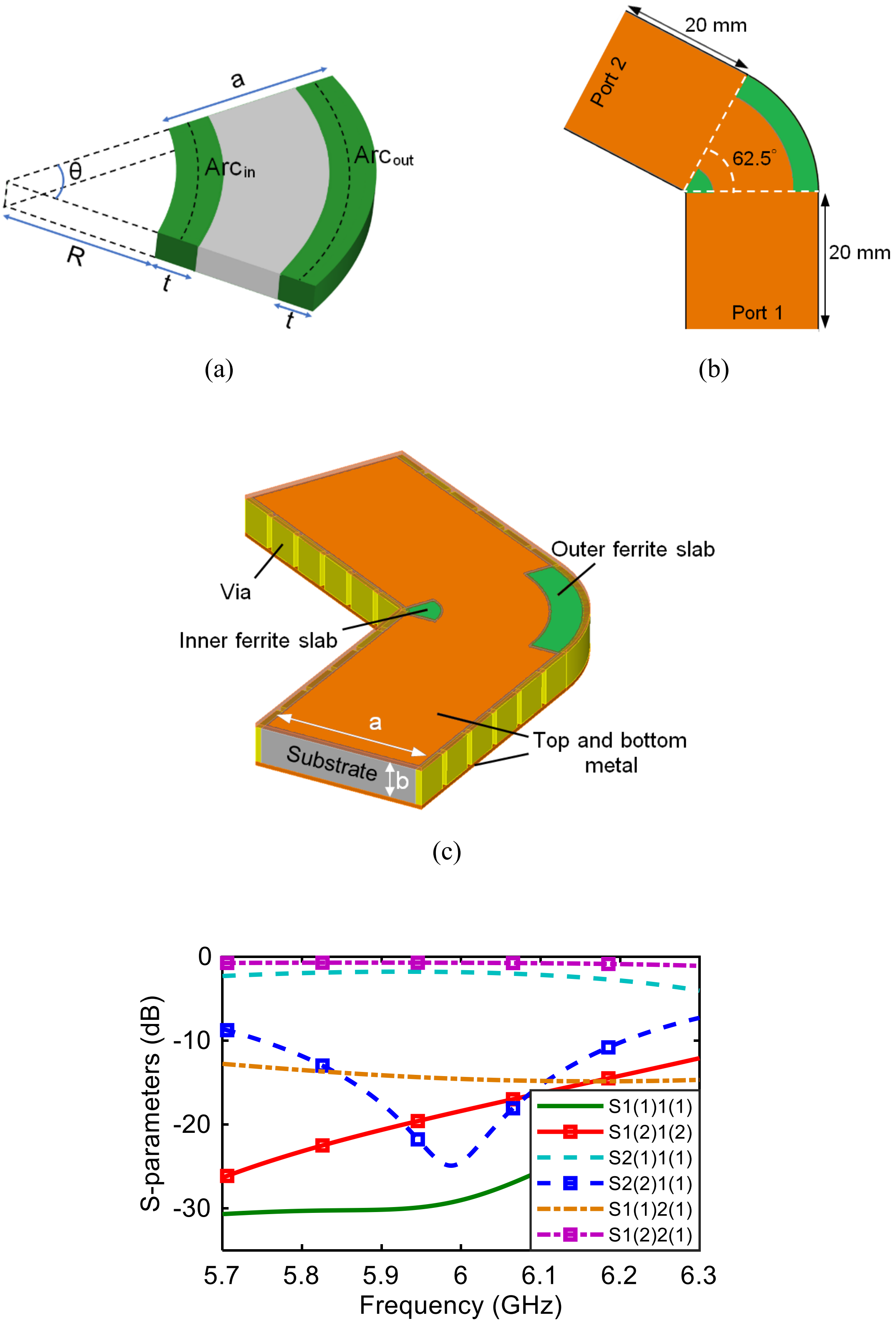
a
θ
Arc$_{in}$
Arc$_{out}$
R
t
t
20 mm
Port 2
62.5°
20 mm
Port 1
Via
Outer ferrite slab
Inner ferrite slab
a
Substrate
b
Top and bottom metal
0
-10
-20
-30
S-parameters (dB)
5.7
5.8
5.9
6
6.1
6.2
6.3
Frequency (GHz)
S1(1)1(1)
S1(2)1(2)
S2(1)1(1)
S2(2)1(1)
S1(1)2(1)
S1(2)2(1)

(a) (b)

(c)

(d)

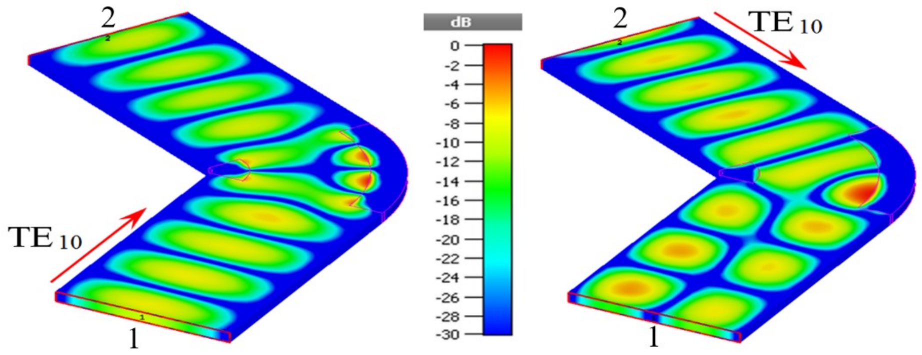

(e) (f)

Figure 3.7 Schematic of (a) bended NRMW, (b) top view, (c) 3-D view, (d) s-parameters of NRMCW simulated in CST, (e) e-field pattern of NRMCW in forward direction and (f) reverse direction

We have designed and demonstrated an NRMCW using the NRMW structure realized in Section III with the Nickel ferrite at 6 GHz. The proposed NRMCW is simulated in CST software. Since both $TE_{10}$ and $TE_{20}$ mode exist along the structure, we use waveguide ports for the two modes in the simulation, which allow us to excite each mode independently. In fact, by introducing the dual mode ports, the simulation is performed by four independent ports which are able to ease the simulation process as there is no need to introduce extra ports to excite $TE_{20}$ modes.

To better illustrate the non-reciprocal mode conversion mechanism while the device is excited at both directions with $TE_{10}$ mode, E-field patterns inside the SIW in Figure 3.7 are depicted and the device's *S*-parameters are plotted in Figure 3.7(d). In Figure 3.7(e), the device is excited with $TE_{10}$ mode at the bottom port (port 1, mode 1) and the same mode is delivered to the top port (port 2, mode 1) as the mode is preserved in the bend. Clearly from the picture, it is observed that at the bend, due to the edge-mode effect, the wavelength is much smaller than elsewhere in the unloaded SIW. Further, the semi-decoupled wave portions travel over a different length. At the outer side, the wave goes through two periods, whereas at the inner side it is guided through only one period. However, since the difference is one full period at the end of the bend, the phase of two portions are the same, and as a result the mode remains unchanged. On the contrary, as shown in Figure 3.7(f), even though the device is excited with $TE_{10}$ mode at the top port (port 2, mode 1), $TE_{20}$ mode is delivered to the bottom port (port 1, mode 2). At first glance at the figure, it is interpreted that at the bend, due to being a normal-mode, the wavelength is almost the same as the unloaded

SIW. Secondly, due to a sharp turn in the structure, the mode is changed as it may change in an unloaded bended waveguide [78].

The simulated device suggests that the NRMCW structure is successfully demonstrated, and the next step is to fabricate the device. However, exciting two modes simultaneously only works in simulation, and in practice the physical ports must be implemented inside the device to excite the $TE_{20}$ mode. Interestingly, introducing an additional $TE_{20}$ mode port into the device readily results in a circulator if proper excitation ports are implemented. Therefore, in the next section, we present a circulator based on the NRMCW scheme which serves as both the validation of the NRMCW concept and the presentation of one interesting NRMCW application.

## 3.6 Applications: Advent of New Type of Circulator

The non-reciprocal mode conversion opens up a concept to develop a new class of non-reciprocal devices as it provides a non-reciprocal routing of signals with different modes. Hence, we introduce the development of an NRMCW-based circulator structure that should be considered as a new class of circulators whose design is quite straight forward, easy, high-power, compact, and unsymmetrical; the latter one could be considered as an advantage or disadvantage pertaining to the application of interest. For example, for a transceiver front-end where each of three ports has different input and output requirements, the symmetry is not required and takes up one degree of freedom in design (like conventional Y junction circulator). In terms of mathematical description, more design specifications would urge more design variables. Then, if design variables are not enough in number to satisfy all the requirements, specifications are partially satisfied; for instance, resulting in a lower bandwidth. Accordingly, in the design of symmetrical circulators all the ports must be tuned together (more design specifications). Therefore, some design variables are dedicated to these requirements, limiting degree of freedom in the design. But, in asymmetrical design, since each port can be tuned separately, an extra degree of freedom could be exploited to enhance the performance of device such as isolation or return loss of one of the ports which is more critical (like isolation between Tx and Rx ports).

Before explaining the design process for the circulator based on NRMCW, it is instructive to glimpse at the *S*-parameter matrix of an ideal NRMCW in (3.10), where at each side of the device, two ports for the $TE_{10}$ and $TE_{20}$ modes are considered, forming a total of four ports.

$$S=\begin{bmatrix} S_{1^{TE_{10}},1^{TE_{10}}} & S_{1^{TE_{10}},2^{TE_{10}}} & S_{1^{TE_{10}},1^{TE_{20}}} & S_{1^{TE_{10}},2^{TE_{20}}} \\ S_{2^{TE_{10}},1^{TE_{10}}} & S_{2^{TE_{10}},2^{TE_{10}}} & S_{2^{TE_{10}},1^{TE_{20}}} & S_{2^{TE_{10}},2^{TE_{20}}} \\ S_{1^{TE_{20}},1^{TE_{10}}} & S_{1^{TE_{20}},2^{TE_{10}}} & S_{1^{TE_{20}},1^{TE_{20}}} & S_{1^{TE_{20}},2^{TE_{20}}} \\ S_{2^{TE_{20}},1^{TE_{10}}} & S_{2^{TE_{20}},2^{TE_{10}}} & S_{2^{TE_{20}},1^{TE_{20}}} & S_{2^{TE_{20}},2^{TE_{20}}} \end{bmatrix}=\begin{bmatrix} 0 & 0 & 0 & 1 \\ 1 & 0 & 0 & 0 \\ 0 & 1 & 0 & 0 \\ 0 & 0 & 1 & 0 \end{bmatrix} \qquad (4.10)$$

The *S*-parameter matrix of an ideal NRMCW is exactly the same as that of the four-port circulator. Therefore, to design a four-port circulator based on NRMCW, we only need to design the proper physical excitation ports according to each mode. Further, if one of the exciting modes is short-circuited, a three-port circulator is realized.

### 3.6.1 Theory and Simulation

To design a three-port circulator based on NRMCW, one physical port must be implemented to realize the $TE_{20}$ mode excitation. To do so, a longitudinal slot is etched on the top broad side of SIW between the first port and the ferrite section. The longitudinal slot couples the $TE_{20}$ mode from/to another SIW placed on top of the NRMCW. Figure 3.8 illustrates the proposed three-port circulator structure, where dimensions are: $t_{via}$ = 18 mils, $L_{via}$ = 90 mils, $d_{via}$ = 10 mils, $X_{slot}$ = 14.5 mm, $Y_{slot}$ = 6.75 mm, $L_{slot}$ = 8.5 mm, $W_{slot}$ = 60 mils, $a$ = 21mm, $a_2$ = 15 mm, $t$=4 mm, $R$ = 0.5mm, $\Theta$ = 62.5°, $L_{cpw1}$ = 6.8mm, $\alpha_1$ = 59.3°, $\alpha_2$ = 35.2°. In the figure, the ferrite slabs at the bend are clearly visible, and the top substrate is clearly distinguished which couples EM energy to the main SIW through the etched aperture between the layers. Further, SIW to CPW transitions are used to realize the planar TEM ports (CPW) which are suitable for the purpose of measurements. To summarize the design procedure and explain how this type of circulator operates, a signal routing of the device is explained below as well as illustrated graphically in Figure 3.9.

The excitation of port 1 results in a TE10-mode wave propagating to port 2. As there is no mode conversion in this direction, the wave is terminated into port 2, and port 3 is isolated. When port 2 is excited, the TE10 mode travels toward ports 1 and 3, passing through the bend. As the mode converts in this direction, the resulted TE20 mode is reflected back from port 1 and establishes a standing wave in front of port 1 and beneath the longitudinal slot with a $TE_{20}$ pattern. Therefore, the signal from port 2 excites the SIW on top of NRMCW and terminates in port 3. It is noticed that once the $TE_{20}$ mode signal is coupled into the top SIW, it will excite a $TE_{10}$ mode in the top layer; therefore, port 3 excites a $TE_{10}$ mode wave. Finally, the input signal from port 3 excites a $TE_{20}$ mode beneath the slot resulting in two traveling signals toward other ports. The signal is reflected back from port 1 due to the orthogonality of modes (short-circuited) and travels back toward port 2. The length between the center of slot and port 1 is one quarter wavelength. Therefore, additive in-phase $TE_{20}$ mode waves pass through the bend with no mode conversion and again get reflected from port 2 (short-circuited). They pass the bend once again, but this time the mode converts into $TE_{10}$ mode which now terminates into port 1. For a longer path that wave has to travel through in this direction, the insertion loss from port 3 to port 1 is higher than other directions.

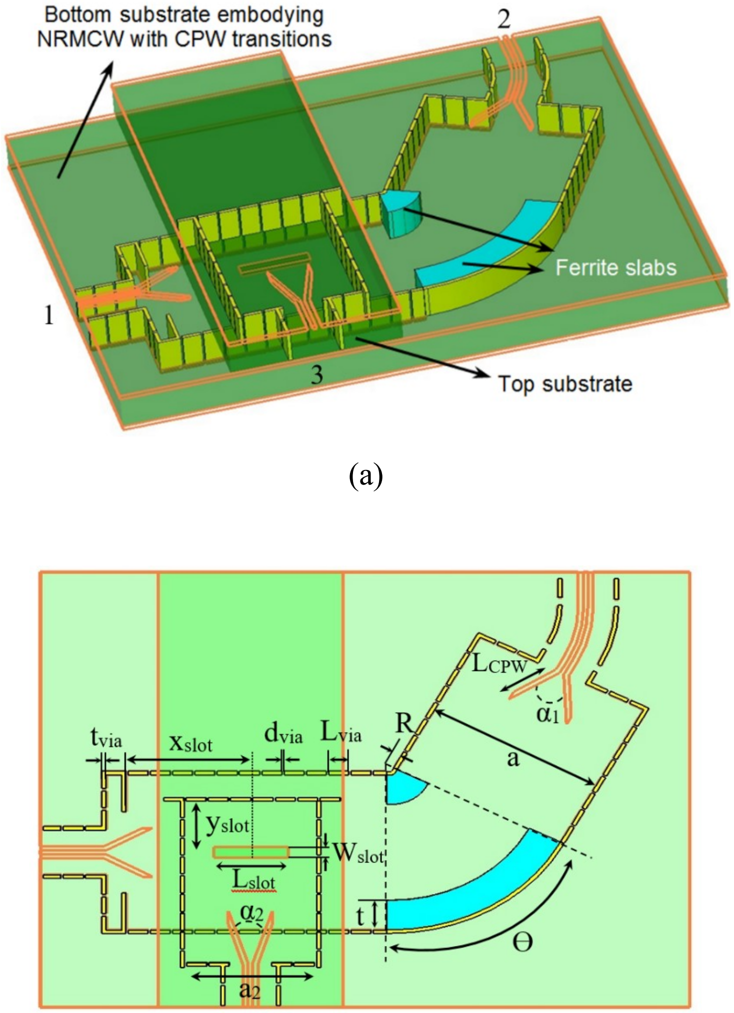

(a)

(b)

Figure 3.8 (a) 3-D view and (b) top view and dimensions of proposed 3-port circulator based on NRMCW

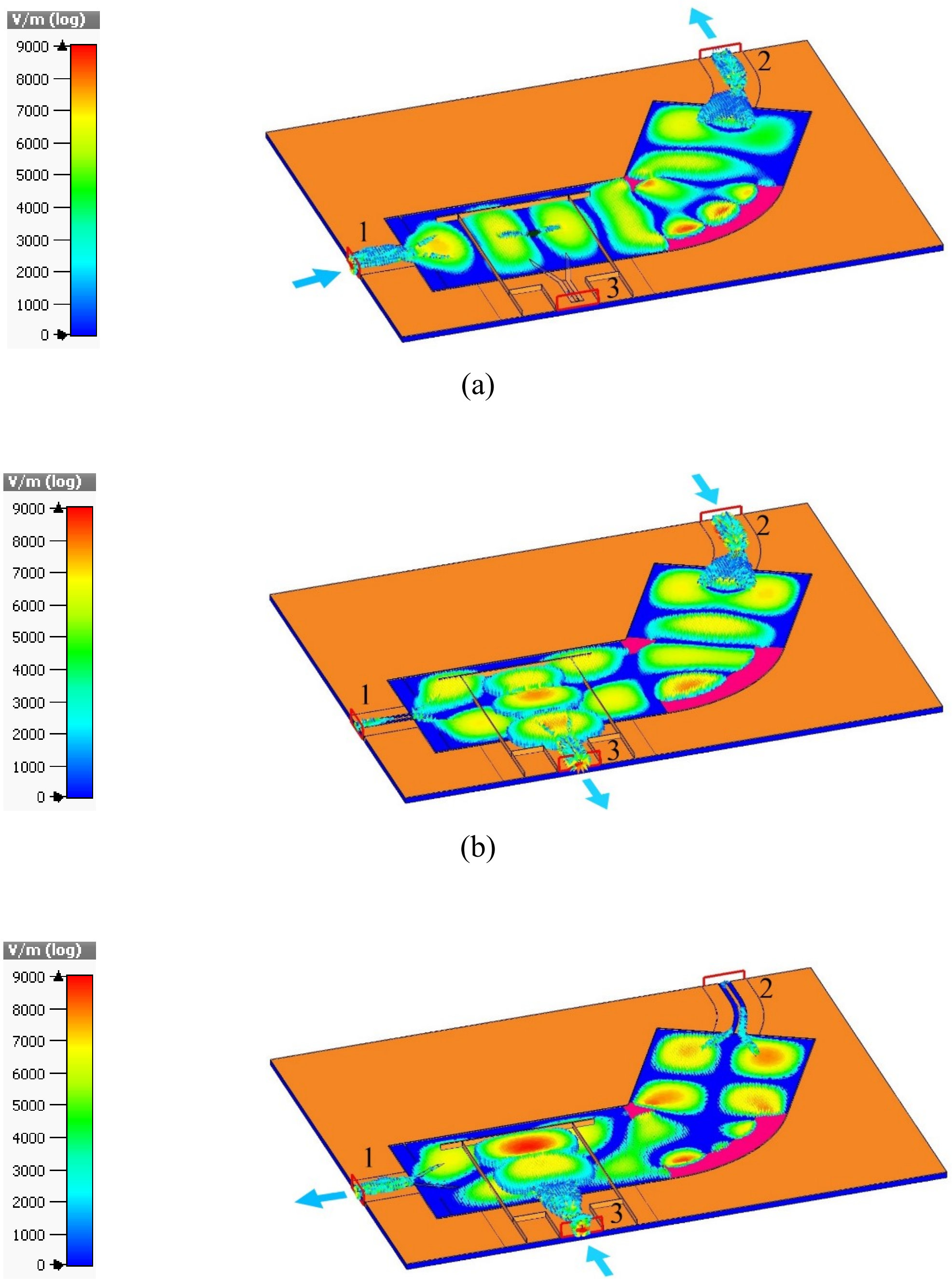

(a)

(b)

(c)

Figure 3.9 E-field pattern for each port excitation of circulator: (a) port 1 excitation, (b) port 2 excitation (c) port 3 excitation

Interestingly, if another longitudinal slot is introduced after the bend but before port 2, a four-port circulator is readily realized, and also the issue of a higher insertion loss from port 3 to port 1 would be partially relaxed for having a shorter path. This is one of the advantages of the NRMCW scheme which provides itself as an easy and straightforward cornerstone platform to realize different types of circulator and non-reciprocal devices on the same design platform with similar procedures.

### 3.6.2 Measurement and Results

To fabricate the NRMCW circulator, we have used Rogers RT/Duroid 6010 substrates with the dielectric constant value of 10.2, loss tangent of 0.0023 and thickness of 30 mils. The Nickel ferrite is a NF-5000 type provided from TCI ceramics Inc, which has a saturation magnetization value of 5000 Gauss and a line width of 90 Oe. The thickness of ferrite is the same as the substrate for compatibility purposes. The fabricated prototype of the proposed circulator is depicted in Figure 3.10. Two piece of ferrite slabs are embedded inside SIW and taped by copper tapes. For a further quality electrical contacts between the copper tapes and SIW body, the tapes are soldered to the SIW.

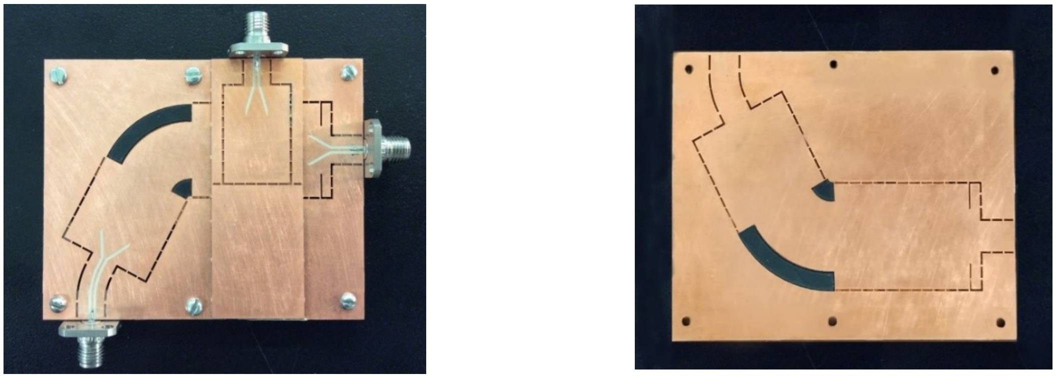
(a) (b)

Figure 3.10 Fabricated prototype of 3-port circulator: (a) top view and (b) bottom view

For measurements, SIW to planar transmission line transitions are required. Hence, we have designed a set of SIW-to-CPW tapered transitions for all the three ports for simultaneous matching of impedance and fields, where the transitions match the SIW ports into the 50 Ω CPW transmission lines.

The biasing setup is shown in Figure 3.11 depicting a tunable magnet that provides the magnetic biasing. The magnet can support a uniform magnetic biasing up to 6000 Oe in one direction if DUT is placed between the rods. However, in our case, an antisymmetrically biasing is required: two upward soft-iron bars are bolted to each rod where the device fixture is placed on it. Finally, to enclose the magnetic field loop, a soft iron plate is placed on top of the device. Preliminary tests indicated that the altered magnetic bias setup can provide up to 0.4 T which is quite sufficient for this test.

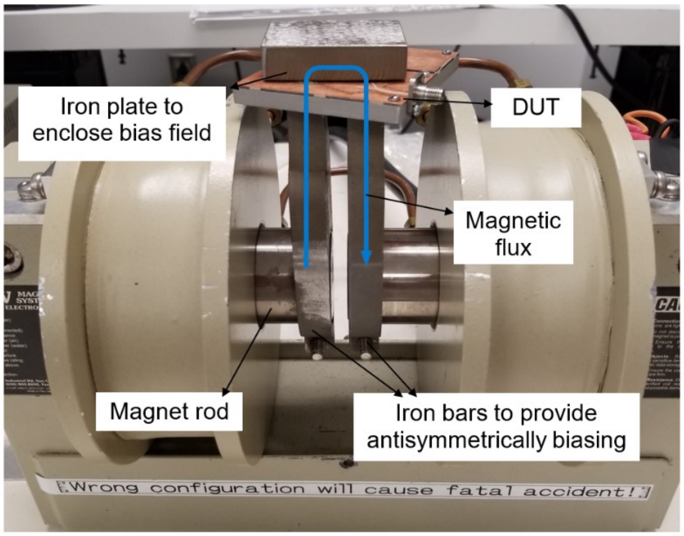

Figure 3.11 DC magnetic biasing setup configuration

The measurement results are depicted in Figure 3.12 and compared with the simulation results obtained in CST. For a better illustration of the results, all reflection coefficients are shown in Figure 3.12(a) where the solid lines show simulation results and the dashed lines present measurement results. From the figures, we can see that the device is well matched at all the ports. Also, the insertion loss and isolation coefficients are presented in Figure 3.12(b) and Figure 3.12(c) respectively, indicating a bandwidth of 400 MHz in connection with a return loss better than 10 dB. However, considering the transmission curves, it is perceived more bandwidth may be realized if device is tuned for a better matching. Further, device performance at the center frequency is summarized at Table II.

The insertion loss is higher than the simulated counterpart for various reasons. First and foremost, the operation frequency for the Nickel ferrite is low, and the low field loss degrades the performance of the device. To eliminate this problem, either the frequency of operation must be increased or another type of ferrite with lower saturation magnetization must be used. Secondly, since the size of ferrite slabs are different due to the bend, the demagnetization factors of the slabs

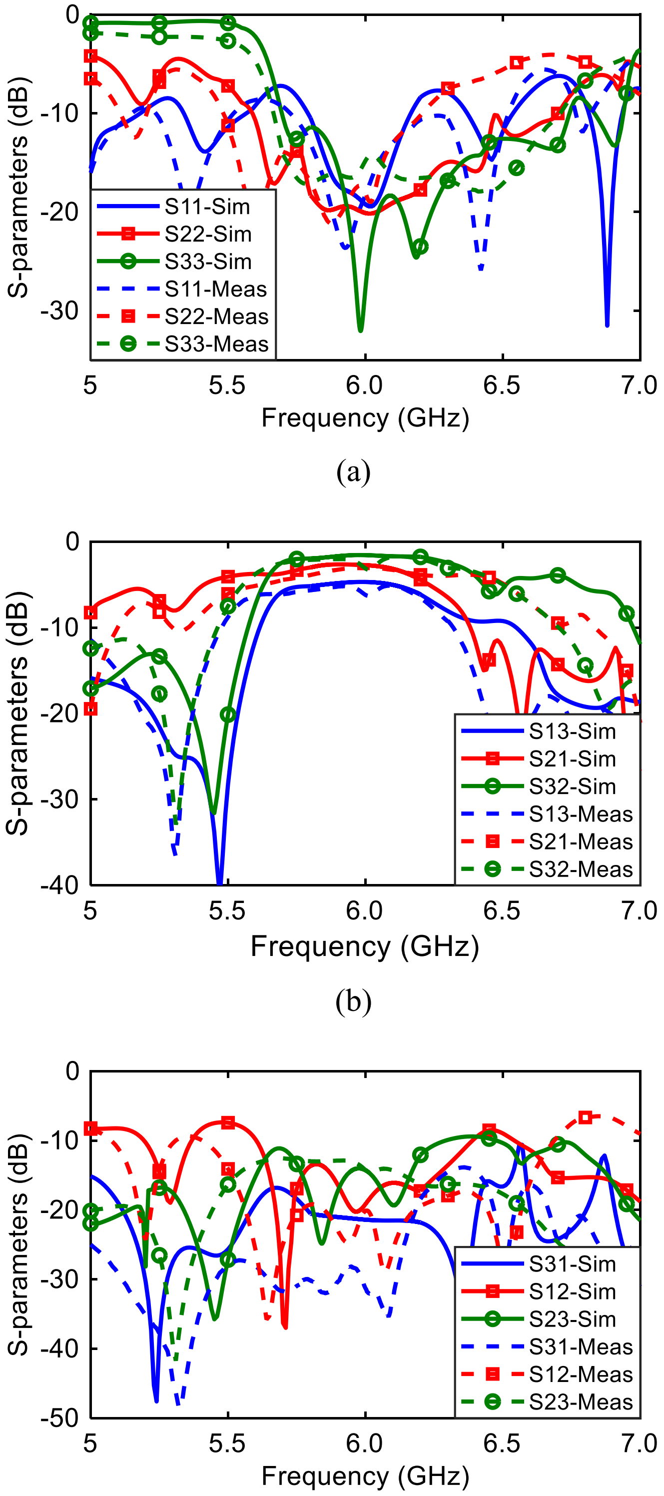

(a)

(b)

(c)

Figure 3.12 Measurement vs. simulation results of 3-port circulator: (a) reflection coefficients, (b) insertion loss and (c) isolation coefficients

Table 3.2 Circulator performance at 6 GHz for each port excitation

| *Excitation at:* | *Return loss (dB)* | *Isolation (dB)* | *Insertion loss (dB)* |
|---|---|---|---|
| Port 1 | 18.2 | 31.3 | 3.1 |
| Port 2 | 18.1 | 20.2 | 3.1 |
| Port 3 | 14.9 | 14.3 | 5.5 |

are not identical. Therefore, the internal biasing of ferrite pieces may be slightly different, thus resulting in a degraded performance and more loss. Finally, in the measurement results, connectors contribute to the loss in regard to simulations. Considering these effects, we can claim that an excellent agreement between the simulation and measurement results validates the design and demonstration of the presented circulator as well as the NRMCW concept.

Further from the figures, we can observe that the $S$-parameters are not symmetrical between ports as expected. For example, the isolation between port 3 and port 1 ($S_{31}$) is higher than the other ports, which can be used to provide a better isolation between transmitter and receiver chains in a transceiver. Similarly, it can be seen that the insertion loss from port 3 to 1 is higher than others as explained in the previous section, but it is not an issue in many practical applications. Considering the same example of a transceiver, while the asymmetrical design would provide a better isolation from the transmitter port into the receiver port, having a high insertion loss in the reverse direction would not be problem, since there is no desired signal flow in this direction.

## 3.7 Conclusion

In this work, we have comprehensively proposed, studied and demonstrated a fully integrated anti-symmetrically ferrite loaded SIW topology to identify and characterize different regions of operation, each benefiting from specific features. On the basis of this study, we have developed a non-reciprocal mode waveguide (NRMW) technique through well-rounded mathematical modelling and theoretical foundation. This special waveguide is then exploited to develop and demonstrate a novel device called NRMCW, which may find many known and unknown applications. The NRMCW structure is found to have an exceptional feature as the mode can be converted from the $TE_{10}$ mode into the $TE_{20}$ mode (and vice versa) only in one direction, whereas in the backward direction both $TE_{10}$ and $TE_{20}$ modes are not converted. The theoretically predicted unidirectional mode conversion is illustrated and discussed through simulations and analyses. Finally, on the basis of the proposed NRMCW scheme, we have introduced the possibility of developing a new class of circulators by prototyping a three-port circulator. The measurement results are compared to the simulation counterparts, thereby showing an excellent agreement which has effectively validated the proposed concept of NRMCW. Also, as an example, it proves important merits of the presented theories and the demonstrated novel device.

## 3.8 Acknowledgment

The authors would like to thank T. Antonescu, and J. Gauthier of Poly-Grames Research Center, École Polytechnique de Montréal, Montréal, QC, Canada, for their support in the realization of the prototypes.

# CHAPTER 4 ARTICLE 2: MODAL NONRECIPROCITY AND CIRCULATOR BASED ON NONRECIPROCAL MODE CONVERSION

Amir Afshani, Graduate Student Member, IEEE, and Ke Wu, Fellow, IEEE

This article also pursues our first objective of the thesis with a different configuration and suitable for ferrite materials with low saturation magnetization. The topology introduced in this article was employed as the core of the nonreciprocal multi-mode components in next chapters. This article was published in IEEE Transactions on Microwave Theory and Techniques (December 2019).

## 4.1 Abstract

In this work, we first discover and investigate the pattern diversity of electromagnetic fields within an anti-symmetrically biased twin-ferrite loaded substrate integrated waveguide (SIW) structure. A special scenario is identified in which two separate guided-wave channels can be created exclusively for each direction of wave propagation within the same ferrite-loaded SIW body. A detailed theoretical foundation is formulated and presented to develop the so-called 'nonreciprocally dual-channelized waveguide (NDW)' in this work. Next, this NDW structure is used to devise and demonstrate a fully integrated fundamental nonreciprocal building element called 'nonreciprocal mode converting waveguide (NRMCW)', which manifests modal nonreciprocity. In other words, this ferrite waveguide interchangeably converts $TE_{10}$ and $TE_{20}$ modes within the SIW, only in one direction. A fundamental approach to design such a unidirectional mode-converting device is proposed through unsymmetrical perturbation loading inside an NDW. Furthermore, a class of 4-port circulator is devised and demonstrated for the first time, in which operation mechanism is based on the one-way mode-conversion. Measurement results of the proposed circulator are in agreement with those of simulation and mathematical models, thereby validating the theoretical foundation and the concept of 'NRMCW'.

*Index Terms*— anti-symmetry, circulator, ferrite, mode conversion, nonreciprocity, nonreciprocally dual-channelized waveguide (NDW), nonreciprocal mode converting waveguide (NRMCW), substrate integrated waveguide (SIW), $TE_{20}$ mode, unsymmetrical perturbation.

## 4.2 INTRODUCTION

Nonreciprocity is a vital, unique and fundamental signal transmission characteristic widely required in a large number of RF, microwave and millimeter-wave circuit, and module applications which include communication systems, radar, and measurement equipment. With an ever-growing demand for quality performance in terms of bandwidth, loss, compactness, and integration, significant research interests have been directed in exploring unconventional and unique approaches for realizing nonreciprocity by means of different methods, structures and technologies. Without any doubts, nonreciprocal properties are indispensable for the development of emerging circuits and systems such as the highly anticipated in-band full-duplex transceiver systems. Fundamental approaches to creating nonreciprocal devices can be divided into different categories, depending on the nature of enabling technologies or materials, each having their pros and cons. Ferrite devices make use of their inherent magneto gyrotropic effect [83-86], whereas nonreciprocal active devices benefit from the unidirectionality of active devices such as transistor [87-89]. More recent techniques that generate nonreciprocity through other physical means include time-varying transmission lines [90, 91] and switching transmission lines [92-94].

In spite of the inherent advantages of other approaches, ferrite materials still stand out as the best approach to achieve nonreciprocity thanks to its universally-recognized and unparalleled advantage of being passive. Passiveness is of paramount importance since ferrite devices, such as circulators and phase shifters, are typically used in RF front-ends where highly linear and low-noise devices and circuits are essential for realizing superior system performances. Furthermore, ferrite devices are well adapted to high power applications unlike many active-circuit solutions which are doomed to low-power applications. With this superiority, ferrite devices are prevalently deployed in a wide range of microwave applications, though emerging ferrite-based methods are being explored and proposed to improve the performance and overcome disadvantages of such existing devices. For instance, traditional ferrite devices were bulky, but recent advances in technology have offered solutions of integration such as ferrite-loaded SIW [58-59], [64] and [71] and LTCC based techniques [67-69] and [71] which result in planar and compact ferrite devices in microwave and millimeter wave regions. Also, it is worthy to mention that recent researches in magnonic devices has resulted in techniques to exploit spin waves in ferrites, to realize micro-and nanostructured magnetic devices [97, 98].

Typically, the study of ferrite-loaded transmission lines is mainly focused on determining and observing phase constants, rather than studying changes in the field pattern, which can manifest device performances in more and subtle details. Specifically, this procedure is emphasized in ferrite-loaded waveguide configurations, where a majority of reported research interests are concerned with the study of the phase constant and the design of phase shifters [59], [70,71], [68], [99] and [101,102]. This may be attributed to the fact that the propagation constant, as the eigenvalue of the boundary condition problem, can sufficiently describe the behavior of a device in one single term. Furthermore, in the past, the lack of powerful computational and modeling resources naturally hindered a detailed study of field configurations, and therefore, the study of phase constant that present a measurable quantity in the design and development process was naturally practiced and encouraged.

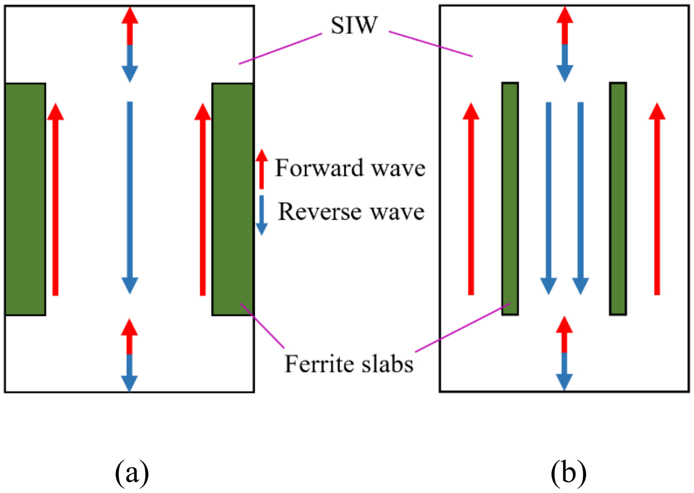

Figure 4.1 Top view of ferrite loaded SIWs and nonreciprocal signal routing diagram in: (a) reference [104], (b) in this work

Even though limited investigations in the literature have shown the field configurations inside ferrite-loaded transmission lines as the target of study [55], [102-104] we present a systematic approach in this work to investigate and showcase a ferrite-loaded SIW based on an electromagnetic-field pattern synthetization. A specific (nonreciprocal) electromagnetic-field configuration is the target or parameter of study rather than the typical phase constant. Based on this approach, a special ferrite-loaded SIW device is demonstrated to create two physically separate channels respectively for the forward and reverse directed waves within the same SIW structure, which is referred to as 'nonreciprocally dual-channelized waveguide (NDW)' in this paper. A slightly similar work was carried out in our previous work [78, 106] where the forward and reverse directed waves have rather different mode profiles than separate channels. In other words, waves propagate in the same channel in both directions in [105], but power concentrations in both directions are semi-orthogonal; whereas, in this work, ferrite slabs physically separate the forward and reverse channels. The operating schematic of a nonreciprocal signal routing in both devices is illustrated and compared in Figure 4.1.

Furthermore, we devise and demonstrate, thanks to the concept of NDW, an interesting nonreciprocal SIW element which manifests nonreciprocity through mode or modal nonreciprocity. More specifically, if port 1 is excited with $TE_{10}$/$TE_{20}$ modes, the modes would be converted, and thus $TE_{20}$/$TE_{10}$ mode would emerge at port 2. However, along the reverse direction, if port 2 is excited with either $TE_{10}$ or $TE_{20}$ mode, the mode would be preserved, and the same mode will be delivered to port 1. Such a device is comparable to basic nonreciprocal elements like a gyrator or an isolator which exhibit similar nonreciprocity through phase and amplitude, respectively. The concept of this device was first proposed and demonstrated by the authors in [78, 105], which was called 'nonreciprocal mode-converting waveguide (NRMCW)'. In this paper, we propose a different methodology to realize the NRMCW. More specifically, a bend in the structure imposes uneven ferrite lengths over bilateral side paths in [105], consequently resulting in mode conversion in the forward direction. Nevertheless, in this work, unequal propagation constants at either side of the device (only in forward direction) are created to convert the mode. Different propagation constants are imposed to the device by means of introducing an unsymmetrical perturbation which will be explained in details. The methodology devised in this work outperforms the previous scheme in a number of reasons. First, a ferrite with smaller saturation magnetization ($Ms$) is deployed which requires a lower magnetic bias field and results in a lower magnetic loss. Second and more importantly, the structure is bend-free, resolving a main drawback of the previously developed scheme. In the previous scheme, since ferrite slabs have different sizes, the demagnetization factors of ferrite slabs are slightly different. This would create different internal magnetic bias inside each ferrite slab; hence degrading the performance of the device. Furthermore, while a bend-free structure relaxes this problem, the use of a ferrite with low saturation magnetization ($Ms$) reduces the effect of the demagnetization factor to a minimum.

The outline of this work was briefly presented in [106]; while, in this paper, a detailed design methodology involving field engineering of the proposed device is discussed. Furthermore, the concept of NDW and NRMCW is fully portrayed and mathematically modeled to illustrate the principle of the work and to establish the foundations for future works, where these fundamental nonreciprocal devices are exploited to develop novel devices or applications.

This paper is organized as follows. In section II, the field pattern diversity within an anti-symmetrically biased twin-slab ferrite loaded SIW is investigated, while certain device parameters as design variables are varied. With the understanding of the effect of each design variable, to the extent that each parameter influences field variations, a special type of nonreciprocal field pattern is targeted; leading to realization of the NDW. Section III formulates a detailed and general methodology to realize the NDW, supported by a design example. Further, the NDW is exploited to propose and demonstrate a nonreciprocal mode-converting waveguide in section IV. This nonreciprocal building waveguide element is used to develop a 4-port circulator for the first time for which the design procedure and measurement results are all presented in section V, prior to the conclusion of this work.

## 4.3 Nonreciprocally Dual-Channelized Waveguide in an Anti-Symmetrically Biased Twin-Slab Ferrite Loaded SIW

In this section, we will first analyze the structure of an anti-symmetrically biased ferrite loaded SIW based on mathematical models. In this ferrite waveguide, the ferrite slabs are positioned at arbitrary distances (symmetrically) from the waveguide sidewalls. Then, we will investigate and examine different configurations of such a topology, and more specifically, we will look into the power distribution for different topologies in order to distinguish different features.

### 4.3.1 Mathematical Model

The schematic of an anti-symmetrically biased ferrite loaded SIW is shown in Figure 4.2. Considering a magnetic wall at the center of SIW, the electric fields inside the structure can be expressed as [81]:

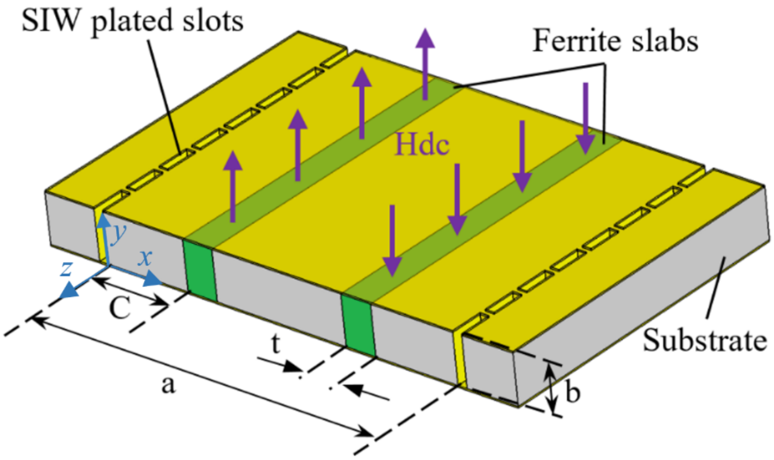

Figure 4.2 Perspective view of a section of an anti-symmetrically twin-slab ferrite loaded SIW

$$E_y = \begin{cases} A\sin\left(k_a x\right)e^{-j\beta z} & 0 < x < C \\ \left(Ce^{jk_f x} + De^{-jk_f x}\right)e^{-j\beta z} & C < x < C+t \\ B\cos\left(k_a\left(L/2 - x\right)\right)e^{-j\beta z} & C+t < x < a/2 \end{cases} \tag{5.1}$$

In such equations, $A$, $B$, $C$, and $D$ are arbitrary coefficients of the fields in each region. Also, $k_a$ and $k_f$ are cutoff wavenumbers for substrate and ferrite regions, respectively. Parameter $t$ is the width of ferrite; and $C$ is the distance of the ferrite slabs from the sidewalls of waveguide. The corresponding magnetic fields can be determined through the following equations:

$$H_x = \frac{1}{\omega\mu\mu_e}(-\mu\beta E_y - \kappa\frac{\partial E_y}{\partial x}) \tag{5.2}$$

$$H_y = \frac{j}{\omega\mu\mu_e}(\kappa\beta E_y + \mu\frac{\partial E_y}{\partial x}) \tag{5.3}$$

where $\mu_e$ is the effective permeability of ferrite, and $\kappa$ and $\mu$ are elements of permeability tensor for a ferrite material. Imposing the tangential boundary conditions over surfaces of the ferrite results in four equations which can be solved to yield a characteristic equation. The characteristic equation is used to determine propagation constant in the forward and backward directions, and more importantly to find unknown coefficients in (4.1) afterwards; enabling us to understand and analyze the behavior of the proposed device in details. The characteristic equation of the structure in Figure 4.2 can be derived as [81]:

$$k_f^2 + \left(\frac{\kappa\beta}{\mu}\right)^2 - \left(\frac{k_f}{\mu_0}\cot k_f t + \frac{\kappa\beta}{\mu_0\mu}\right)\mu_e k_a \cot k_a c + \left(\frac{\mu_e k_a}{\mu_0}\right)^2 \cot k_a c . \tan k_a d$$
$$+\left(\frac{k_f}{\mu_0}\cot k_f t - \frac{\kappa\beta}{\mu_0\mu}\right)\mu_e k_a \tan k_a d = 0 \qquad (5.4)$$

$$k_a^2 = k^2 - \beta^2, \qquad k_f^2 = \omega^2 \mu_e \varepsilon - \beta^2 \qquad (5.5)$$

where $\beta$ and $k$ are propagation constant and wavenumber of waveguide, respectively.

As mentioned earlier, unlike the typical approach which focuses on behavior of the phase constant, we adopt a more detailed and comprehensive approach by turning our attention to electromagnetic-field configurations and finding ways to adapt fields in our favor. Scrutinizing (4.1)-(4.5) suggests that electromagnetic fields inside the structure can be manipulated to various extents, in a number of ways. First, considering the first sentence in (4.1), if the cutoff wavenumber for the substrate region ($k_a$) becomes imaginary, then E-fields within the substrate region will take a hyperbolic form which will alter the field configuration significantly. To further assess this argument, we should evaluate (4.5) to find conditions leading to an imaginary or real value of $k_a$. In (4.5), one can see that if $\beta$ (propagation constant) gets bigger than $k$ (wavenumber of waveguide), then $k_a$ will become imaginary; otherwise it will be real. Real-value $k_a$ ensues modes very similar to waveguide modes; however, imaginary-value $k_a$ leads to a hyperbolic form of fields in which, unlike normal waveguide modes, wave concentration takes place at the interface of ferrite and substrate regions rather than at the middle.

Second, considering the third sentence in (4.1), a real or imaginary value of $k_f$ (cutoff wavenumber in ferrite) can cause a huge change in nature of the wave propagation inside the ferrite slabs. In the case of a real $k_f$, electromagnetic fields inside the ferrite will be sinusoidal, and hence the wave will propagate inside the ferrite slabs. This causes a substantial difference since the ferrite dielectric constant is high; a significant portion of the wave will be absorbed into the ferrite and will propagate within the ferrite slabs. On the contrary, if $k_f$ is imaginary, then fields inside the ferrite slabs will be exponential; the wave will concentrate only at one side of the ferrite; and they will be localized at the interface of ferrite. In (4.5), it is inferred that if $\mu_e$ is negative, $k_f$ will be imaginary for all values of $\beta$, thus indicating that this condition only depends on ferrite material and bias value. Furthermore, a negative $\mu_e$ makes the ferrite slab cutoff, and accordingly no real power can propagate inside the ferrite.

Finally, the distance between the ferrite slabs and the waveguide side walls ($C$) can determine the position where field distortion due to the presence of ferrite is at a maximum. Moreover, a variation of $C$ in (4.4) can drastically shift the propagation constant of the device, thus causing significant changes in the EM field distribution.

Considering all the facts and observations, it is inferred that ferrites are fully capable of changing and distorting the field configuration beyond the waveguide modes, where some of these distortions may result in interesting and unprecedented nonreciprocal behaviors. Therefore, in the next part, power flow distribution over the cross section of a twin-ferrite loaded SIW will be discussed for different configurations with regard to the aforementioned effects.

### 4.3.2 Diversity of Electromagnetic Field Configurations

In this section, we will focus on electromagnetic fields and explore their configurations under different conditions which will result in significant changes in or pronounced impact on the device's behavior. Then, we will explain and predict the influence of each parameter to discover effective ways to manipulate the fields and achieve the signal routing depicted in Figure 4.1(b).

To illustrate the subject of study, an example of twin-ferrite loaded SIW is given in this work. Its design variables are carefully chosen and varied within different scenarios so that a broad diversity of electromagnetic field configurations in such a structure is depicted. In all the numerical studies presented in this section, waveguide width ($a$) is 30 mm so that only the dominant mode of waveguide can propagate at 5 GHz. Furthermore, the dielectric constant of substrate is 2.94; the dielectric constant of ferrite slabs is 13.9; and the ferrite saturation magnetization is 800 G. It should be noted that the showcase study presented in this section is not limited to a specific frequency or ferrite material, and that it can be extended to other frequencies with different types of ferrite material as the deductions are general. Ferrite width ($t$), ferrite distance from sidewalls ($C$) and magnetic DC bias ($H_{dc}$) are three design parameters of interest which will be used to alter electromagnetic field configurations of the device in this work.

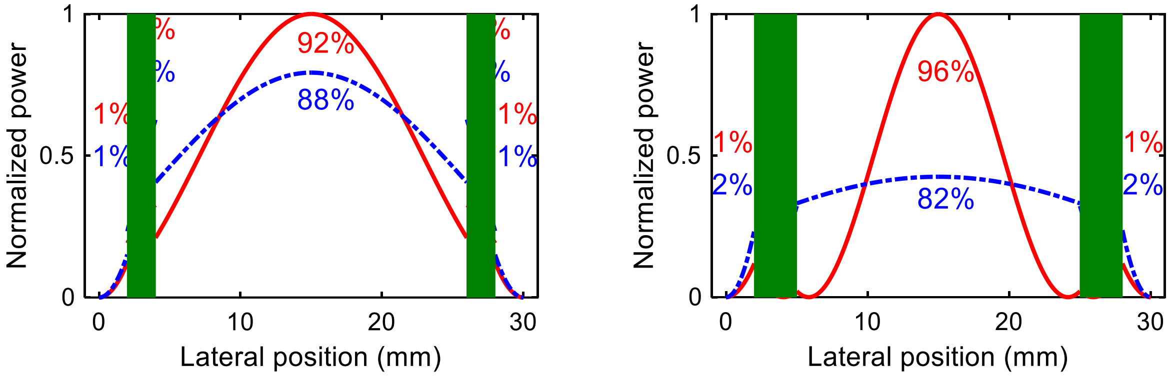

(a) *t* = 2 mm, *C* = 2 mm, *Hdc* = 400 Oe (d) *t* = 3 mm, *C* = 2 mm, *Hdc* = 1200 Oe.

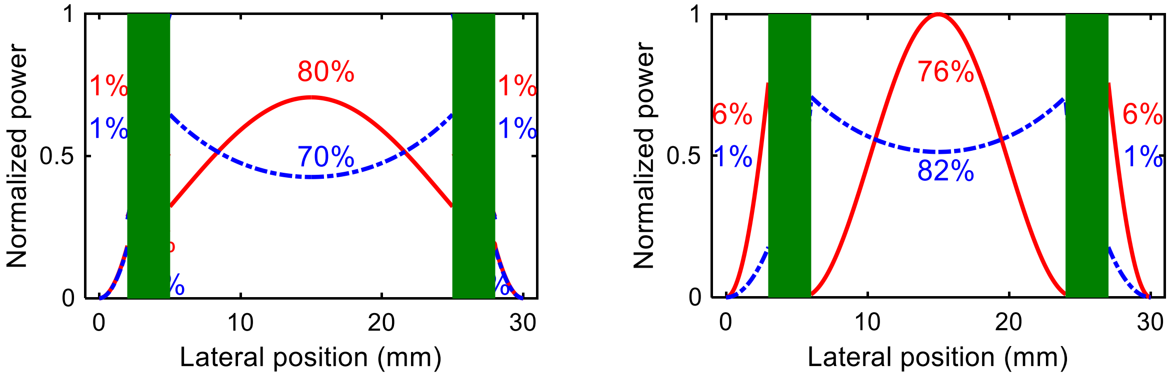

(b) *t* = 3 mm, *C* = 2 mm, *Hdc* = 400 Oe (e) *t* = 3 mm, *C* = 3 mm, *Hdc* = 1200 Oe.

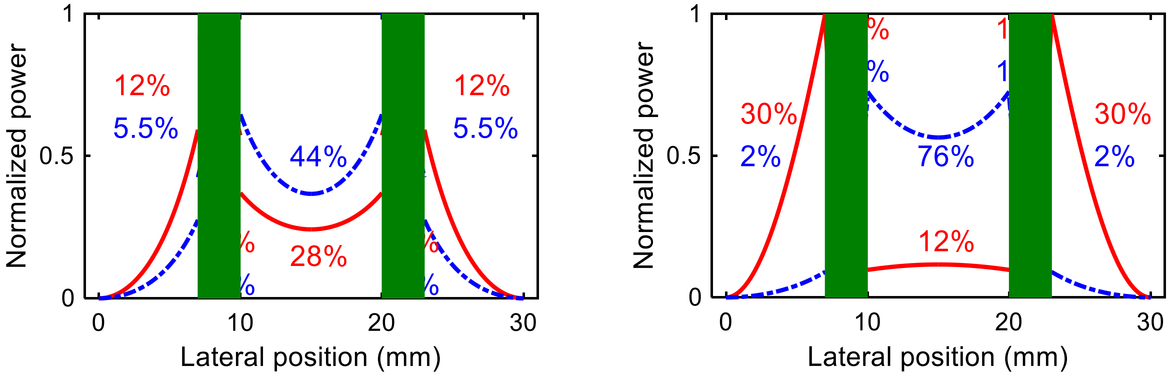

(c) *t* = 3 mm, *C* = 7 mm, *Hdc* = 400 Oe. (f) *t* = 3 mm, *C* = 7 mm, *Hdc* = 1200 Oe.

Figure 4.3 Nonreciprocal power distribution and diversity of electromagnetic fields within a twin-slab ferrite loaded SIW

In Figure 4.3, nonreciprocal power flow distributions in the cross section of a ferrite loaded SIW are plotted for various configurations. Solid red lines depict power distribution in the forward direction of propagation, and dashed blue lines depict power distribution in the reverse direction of propagation. They cover all possible scenarios of this device and are arranged in a specific order so that the influences of each parameter are visualized. Power flow is defined as the cross product of E-field and H-field (transverse to the propagation direction) components of the waves, and its plotted curves are normalized to the unit input power. The reason for depicting the power flow distributions is that the power flow in the direction of wave propagation can effectively show a variation of both electric and magnetic field components. It also illustrates how much power is allocated in each region of the structure to distinguish the effective channels responsible for different patterns of wave propagation. In this connection, the powers allocated in each region for both directions are shown in all the figures.

In Figure 4.3(a)-(c), the ferrite is biased so that $\mu_e$ is positive, and so $k_f$ is real. Contrastingly, a different bias value is applied in Figure 4.3(d)–(f), so $\mu_e$ is negative and $k_f$ is imaginary. In comparing the power distribution in the ferrite region in these two groups of figures, as expected in the second group, it is verified that power distribution is exponential and mainly concentrated at one interface of each ferrite slab. Though, for the first set, a larger portion of the power is within the ferrite slabs (comparing Figure 4.3(b), (d) and Figure 4.3(c) and (f)).

In examining all the figures in order, we see first that in Figure 4.3(a) modes in both directions are very similar to the $TE_{10}$ mode of SIW and are slightly disturbed. This is logical since a very thin ferrite slab is only capable of causing small distortions to electromagnetic fields, specifically if placed at low power regions of the waveguide. However, in Figure 4.3(b), it is perceived that a small increase in ferrite thickness noticeably changes the power distribution in the reverse direction, where fields in the substrate region take the hyperbolic form. This change is a direct consequence of shift in $k_a$ from a real value to an imaginary one, which (according to (4.5)) occurs when the propagation constant in the reverse direction ($\beta_r$) exceeds $k$. In Figure 4.3(c), by sliding the ferrite slabs considerably away from the sidewalls, the effect of ferrite distance from the sidewalls can be visualized. We can see that both waves in the forward and reverse direction take a strongly hyperbolic form; signaling that the propagation constant in both directions exceeds $k$.

These effects imply that an increase in both $t$ and $C$ can cause a huge rise in $\beta$, resulting in a hyperbolic profile. This can be intuitively understood that displacing the ferrite slab towards the center of the waveguide, where the field density is stronger, boosts the propagation constant. Because the dielectric constant of the ferrite is much larger than the substrate; hence, placing it in regions where its interaction with the fields is augmented, would increase the effective permittivity and thus the propagation constant. While wave profile is in a strong hyperbolic form, more power is concentrated toward the ferrite slabs. Furthermore, since the ferrite in this figure is not cutoff, the power is absorbed into the ferrite slabs, and a significant portion of the wave is trapped and propagates inside the ferrite slabs.

In Figure 4.3(d), for the first time, the ferrite bias is changed so that the effective permeability becomes negative. In fact, it has the same parameters as the device simulated in Figure 4.3(b), except for $\mu_e$ is negative. Comparing Figure 4.3(b) and Figure 4.3(e), an important implication that comes out to our attention is that in the first case, fields are inclined toward inner interfaces of the ferrite slabs for both direction of propagation. But, in the latter case, fields inside the ferrite region are inclined toward opposite interfaces of slabs regarding the direction of propagation. More specifically, in the forward direction, fields are inclined toward the outer side of ferrite slabs (facing the waveguide sidewalls), while in the reverse direction they are inclined toward the inner side. However, since the gap between the ferrite slab and the waveguide sidewalls is very narrow, waves cannot propagate properly and their amplitude is very weak. In Figure 4.3(e), the position of ferrite slabs is incremented slightly toward the middle of the waveguide. As a result, the power of the forward wave at the ferrite interface rises sharply. Following the track of changes, the ferrite slabs are moved further toward the center of the waveguide in Figure 4.3(f). From the plot, we can see that the power distribution in the forward and reverse directions are significantly different in their respective regions. In the reverse direction, a significant percentage of power is trapped in the space between two ferrite slabs, whereas in the forward direction, an enormous percentage of power is distributed in the bilateral gaps between ferrite slabs and sidewalls as if waves are travelling in distinctly different paths, leading to separated channels.

In this section, we have shown that it is possible to realize a nonreciprocally dual-channelized waveguide (NDW) with a twin-ferrite loaded waveguide, and that the effects and contributions of each parameter can be understood in the manipulation of electromagnetic fields. In the following, a detailed methodology to create an NDW over a designated frequency band suitable for mode conversion applications will be presented.

## 4.4 Design Methodology of NDW

In this section, we will present a thorough methodology to realize an NDW at a specific frequency band, adequate for unidirectional mode conversion applications. One important modification from the showcase design presented in the previous section is in the waveguide width selection so that both $TE_{10}$ and $TE_{20}$ modes can propagate inside SIW [82] at 5 GHz. In this case, $a$ is 47.5 mm. Other predefined parameters are the substrate dielectric ($\mathcal{E}_r = 2.94$), and the saturation magnetization of ferrite ($Ms = 800$ G). Consequently, $t$ (ferrite thickness), $H_{dc}$ (magnetic bias) and $C$ (slab position) are three degrees of freedom which are left for the design process. Generally, three main conditions must be met to realize an NDW, and three parameters of design are subsequently determined according to these conditions.

The first condition is that the effective permeability of the ferrite must be negative to yield imaginary $k_f$, which determines $H_{dc}$. The effective permeability can be expressed mathematically in terms of poles and zeroes to give an analytical relation for the authentic range of $H_{dc}$ which has a negative $\mu_e$ [105]. Alternatively, a graphical representation provides better insight into the design process by presenting more detail, such as the slope of curves at each point. In Figure 4.4, $\mu_e$ is depicted over frequency for a few magnetic bias values. It is perceived that $\mu_e$ is negative between its pole and zero; further, it is visualized that $\mu_e$ is sharp near the location of poles and smooth near zeros. Accordingly, the ferrite is biased closer to the location of the zero to gain a wider bandwidth performance. Therefore, a magnetic bias of 1100 Oe is opted as the optimum bias in this case.

The second condition states that to achieve the wanted dual-channelized property, it is essential to have a strong exponential field distribution within the ferrite to localize the wave at only one of the ferrite interfaces. In other words, since the ferrite is responsible for the nonreciprocally dual-channelized effect, the fields must be bound to one side of the ferrite slabs as much as possible. In this regard, position of slab $C$, and more importantly thickness of ferrite slab $t$ are crucial parameters.

To assess this feature, the power density at both interfaces of the left ferrite slab is investigated in both directions for a wide variation of $C$ and a few selected thicknesses ($t$) in Figure 4.5. Obviously,

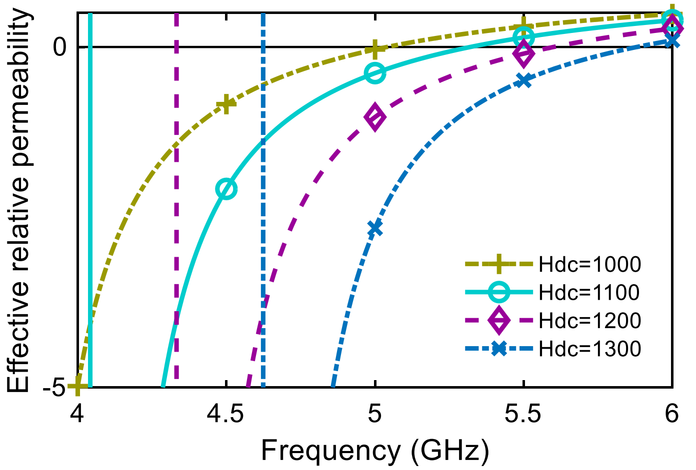

Figure 4.4 Dispersion diagram of effective relative permeability ($\mu_e$)

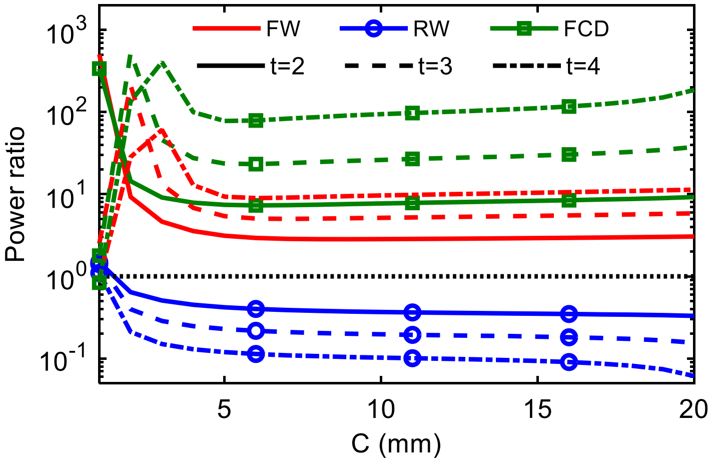

Figure 4.5 Field power ratio of left interface to right interface for forward and reverse directions

the power density for the ferrite slab at the right side of the waveguide will be the same but reversed at interfaces. In Figure 4.5, unmarked (red in the color edition) curves show the ratio of power density at the left interface to the power density at the right interface in the forward direction, whereas circle-marked (blue in the color edition) curves depict the same ratio in the reverse direction. In fact, this curve shows how strongly the wave is inclined toward any side of the ferrite slab. A ratio bigger than the unit implies that the tendency is toward the left interface; while a ratio smaller than unit shows that the field concentration is on the right interface. The ratio of power density is depicted in a logarithmic scale to better describe the deviation from unit, where a larger deviation from unit in each direction indicates a stronger concentration at one specific side.

Curves show that, at intermediate values of $C$, power density is almost constant for each value of $t$, implying that the boundary conditions of SIW have less influence on the performance of the device as if the wave is only guided along the ferrite, similar to a dielectric slab waveguide. As $t$ increases, intensity of fields at either ferrite interface increases for both direction, meaning that the wave becomes more bounded to the ferrite slab. Moreover, as the slabs get closer to the structure's boundaries, the electric wall ($E = 0$, for $C = 0$) or the magnetic wall ($H = 0$, for $C = a/2$), the power density starts to vary, implying that the wave is not freely bounded to the ferrite anymore. Therefore, at intermediate points, the contribution of $C$ to the ratio of power density is negligible, and $t$ mainly determines the value of the ratio. To better illustrate the effect of $t$ on the nonreciprocal field concentration, 'field concentration directivity' is defined as the ratio of power density in the forward direction divided by the same ratio in the reverse direction at the left interface as shown in Figure 4.5. In fact, the field concentration directivity is defined to measure the degree of field concentration at one side (or equivalently degree of exponentiality of the field), as well as the degree of nonreciprocity in one single term and relating both directions. It is observed that as $t$ increases, the field concentration directivity rises progressively, which is favorable. The only drawback is that the wider the ferrite slab is, the worse is the matching of the structure to a corresponding unloaded waveguide. Accordingly, a tradeoff must be made between strength of nonreciprocity and channel separation and the return loss. Here, $t = 3$ mm is selected as an intermediate solution.

The third condition dictates the single-mode operation, demanding that the characteristic equation must have only one root in each direction so that higher order modes are avoided. Furthermore, the forward and reverse channels must be wide enough so that waves can propagate without being cutoff. From another viewpoint, the third condition assures that evanescent (in regard to transverse direction) dielectric modes bounded to ferrite slabs are not perturbed by strict boundary conditions. The third condition is assessed by solving the characteristic equation to determine the remaining design parameter $C$.

To solve the characteristic equation (4.4), the equation is transformed into a quadratic equation in the form of a cosine function which yields the solution for the unknown position of ferrite slab $C$ as a function of propagation constant in either direction [102]. Using this equation, the propagation constant as a function of the slab position is plotted in Figure 4.6 for a few sample frequency points to reveal the dispersion of propagation constant. In the figure, the elliptical curves with lower phase constants are the unwanted modes and must be avoided. From the third condition, it is best to choose $C$ at the vicinity of one quarter of the waveguide width (so each channel is wide enough) where unwanted modes are cutoff. In this case, $C = 11$ mm is thus selected as an optimum solution.

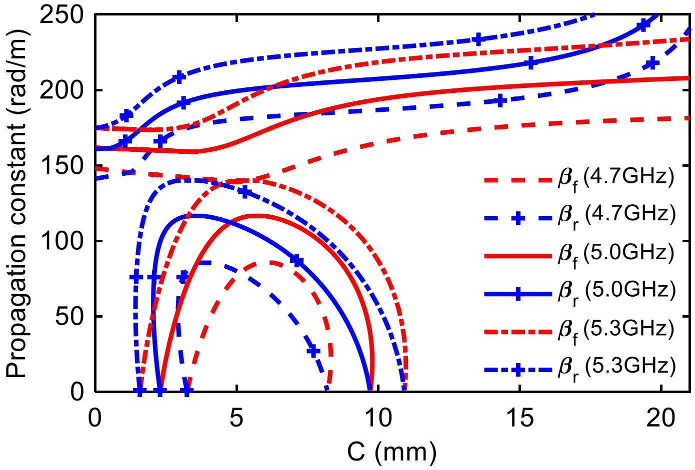

Figure 4.6 Propagation constants vs slab position for three sample frequency points

By selecting $C$ as the final parameter, the design process is completed. Once a solution is realized, design parameters can be tuned to slightly alter the performance of the device. For instance, $t$ can hold larger values to stress nonreciprocity further, which results in a larger isolation in the introduced circulator in section V, though at the cost of lower matching. The structure has been simulated in CST and HFSS simulation software where the obtained results were identical; assuring that modeling is valid. Here in this paper, to avoid report of identical plots we have included the simulations only from CST Microwave Studio. The E-field pattern of the designed NDW is illustrated in Figure 4.7, in which the forward and reverse channels are clearly distinguished.

The three aforementioned conditions can be summarized in short: the NDW is realized only if the field configuration inside the structure is significantly transformed by the ferrite slabs so that the rectangular waveguide mode is completely transformed into dielectric waveguide mode, where each ferrite slab plays the role of a dielectric waveguide due to having a negative $\mu_e$.

## 4.5 Theory of Nonreciprocal Mode-Converting Waveguide (NRMCW) Based on NDW

In this section, the nonreciprocally dual-channelized waveguide will be exploited to design a nonreciprocal basic building element which converts the mode only in one direction while preserving the mode in the reverse direction. Inspecting and studying the field patterns of NDW in both directions in Figure 4.7 reveal that, in the reverse direction, the fields are trapped between two ferrite slabs, much like in optical fibers where light is guided due to perfect internal reflection. Therefore, most of the energy is guided between the ferrite slabs. A negligible wave is leaked out into the region between the ferrite slabs and the waveguide sidewalls due to exponentially decaying fields inside the ferrite. This means that, in the reverse direction, the effective boundary condition is mainly constituted by the ferrite interfaces, leaving a negligible contribution from the conductive sidewalls. This feature suggests an important trait: moving the sidewalls (changing the waveguide width) will have a negligible effect on the reverse-directed wave, if distance between ferrite slabs is maintained. In this case, we refer to this behavior as insensitiveness of reverse wave to cross channel perturbation.

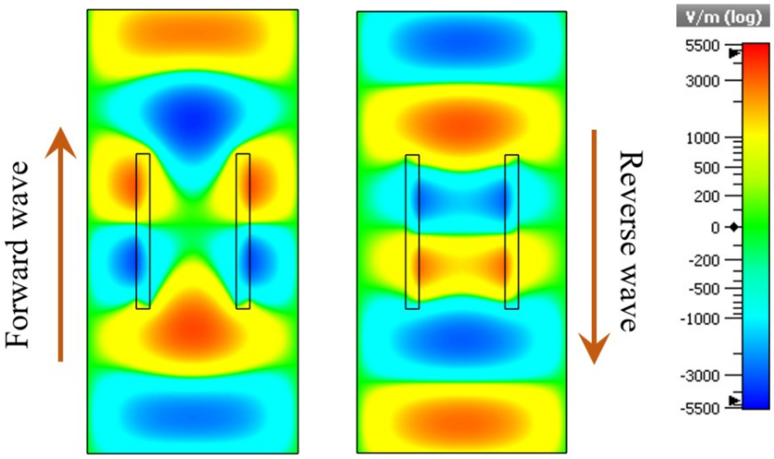

Figure 4.7 E-field pattern in forward (left) and reverse (right) directions

On the other hand, in the forward direction, the wave is divided into two semi-decoupled segments, where each segment propagates at one side of the waveguide independently. Since the segments are decoupled, any perturbation at one side of the waveguide will have a negligible effect on the opposite side. Hence, if an unsymmetrical perturbation is specifically designed to shift the propagation constant, it will cause a change in the forward propagation constant only for one segment of the wave. In other words, under this condition, two segments of forward-directed wave can propagate with different propagation constants. Consequently, if the effect of perturbation is increased so that the phase difference between two segments becomes 180 degrees, the mode unidirectionally will be converted from $TE_{10}$ into $TE_{20}$.

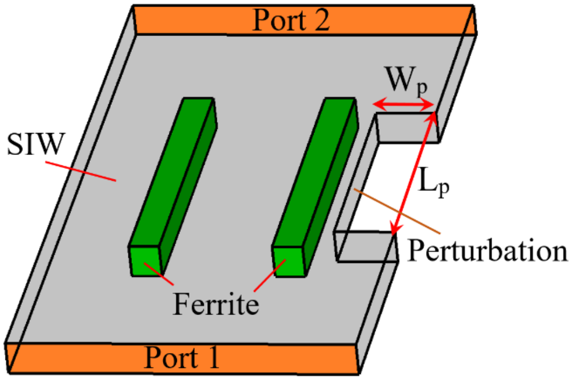

Figure 4.8 Structure of proposed NMCW

In Figure 4.8, the main approaches which imply to cause a great shift in propagation constant are mainly due to modifications in the waveguide width ($a$) or the slab position ($C$). Each of the mentioned modifications can greatly shift $\beta$; though, an approach including both modifications will hugely shift $\beta$. Considering this point, our proposed approach is to move one of the sidewalls inward for a width of $W_p$ and length of $L_p$ as illustrated in Figure 4.8. Here, based on this approach, both parameters of $a$ and $C$ are reduced in the perturbed area, since obviously waveguide width is reduced and the ferrite slab is now closer to the right sidewall. In fact, from the viewpoint of the segmented forward wave in the perturbation area, the whole propagation medium is a different waveguide with a width of '$a' = a - 2W_p$' and slab position of '$C' = C - W_p$'. So $\beta'$ (propagation constant of segmented wave at perturbed side) can be determined with the revised parameters from the modified equation of (4.4), as used to plot Figure 4.6. In Figure 4.9, the difference between two propagation constants ($\Delta\beta = \beta - \beta'$) is plotted as a function of $W_p$ for both directions since this difference causes a mode conversion.

At the first glance, Figure 4.9 indicates that the shift rate in propagation constant is not the same for two directions when perturbation gets wider, and it is much faster in the forward direction for low values of $W_p$. Confirming that, in the reverse direction, the wave is insensitive to the perturbation in the cross channel, if perturbation is relatively far from the ferrite slabs. At large values of $W_p$ and at around 9 mm, propagation shift in the reverse direction starts to boost suddenly, alarming that the sidewalls are very close to the ferrite slabs, and thus violates the dielectric mode assumption for the reverse direction. Therefore, choosing any $W_p$ smaller than this threshold assures a unidirectional mode conversion, though the degree of insensitiveness for the reverse direction varies.

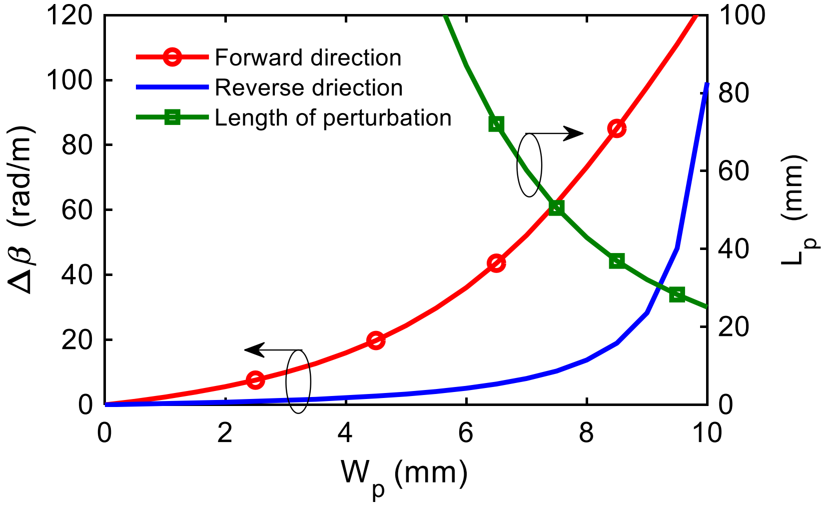

Figure 4.9 Propagation constants vs slab position for three sample frequency points

To realize a mode conversion in the forward direction, the phase shift between two segments in the forward direction must be 180 degrees. Therefore, the length of perturbation for a fixed $W_p$, can be determined as follows:

$$L_p = \frac{\pm(2k-1)\pi}{\Delta\beta_f}, \quad \text{k=1,2,3,...} \tag{5.6}$$

this relation is visualized for $k = 1$ in Figure 4.9 in the green squared curve yielding the dimensions of perturbation which produces the desired mode conversion. For instance, in this curve, a perturbation with 8 mm width ($W_p$ = 8 mm) yields the perturbation length of $L_p$ = 42.9 mm. This can be regarded as a good option since the perturbation is compact while $\Delta\beta_f$ is large and $\Delta\beta_r$ is small.

In Figure 4.10, the forward and reverse propagation constants of the perturbed waveguide with '$a'$ = $a$ - 2$W_p$ = 31.5 mm' and '$C'$ = $C$ - $W_p$ = 3 mm' are plotted and compared to the original one to check if the structure operates with a single mode in both directions. Vertical green lines and arrows indicate ferrite slab position for original (dashed), and perturbed structure (solid). The figure confirms the single mode operation of the perturbed waveguide. Moreover, this figure shows that in the reverse direction, the propagation constant is almost unchanged; but, more importantly, in the forward direction it is dropped almost to its minimum value and is much lower than $k$ (substrate cutoff wavenumber). Whereas before perturbation, it is higher than $k$ which implies that in the forward direction the field profile is greatly transformed due to the perturbation. This must be noted since initially we assumed that in this direction the wave was semi-decoupled and the assumption seems to be violated. Simulating the structure in CST Microwave Studio shows that $Lp$ = 42.9 mm causes 280 degrees of phase shift at the perturbed side of NRMCW instead of 180 degrees, signaling that the length of perturbation is more than enough. This confirms that our initial assumption is violated, and in fact, the accuracy of (4.6) is limited to small $W_p$ and it degrades as $W_p$ gets wider. Nevertheless, this violation turns out to be useful and in favor of mode conversion; this will be explained shortly.

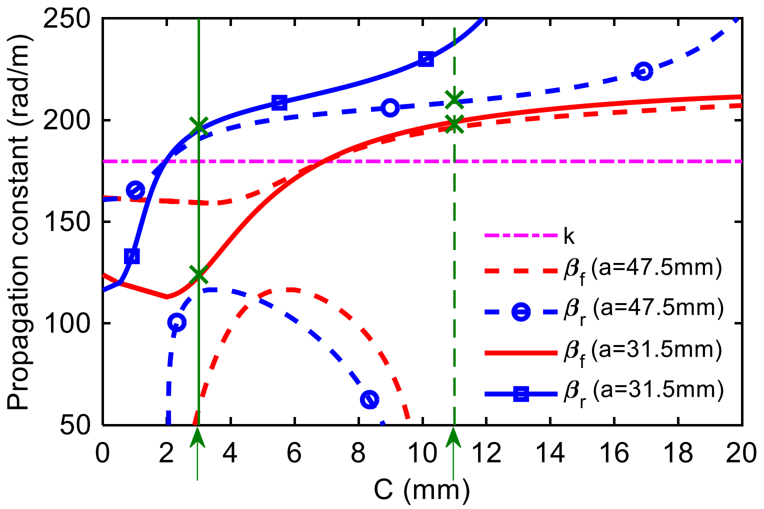

Figure 4.10 Propagation constants vs slab position for original and perturbed SIW

To increase the accuracy of mathematical modeling, we can consider the forward-directed wave as the superposition of coupled and decoupled segments, which here we refer them as coupled and decoupled modes. These modes are clearly distinguished for the forward-directed wave in Figure 4.2(e) as both modes exist simultaneously in this configuration. Two wave segments, which are bound to the outer interface of the ferrite slabs and travel independently in the bilateral space at sides of waveguide, constitute the decoupled modes. While the wave segment, which is at the center of the waveguide, is considered as the coupled mode. Because each half is not independent from the other half and cannot be tuned separately. In the structure, as $C$ decreases, the share of the coupled mode increases and the decoupled mode starts to vanish as shown in Figure 4.2(d), where $C$ is very small. On the contrary, as shown in Figure 4.2(f), as $C$ increases the decoupled mode dominates and the coupled mode decreases. In another point of view, the decoupled mode refers to a dielectric waveguide mode and the coupled mode refers to a waveguide mode. Hence, inside the device the ratio of the decoupled mode to the coupled mode quantifies the ferrite capability in changing the field configuration from waveguide mode to dielectric waveguide mode. For the decoupled mode, the analysis illustrated in Figure 4.9 and in equation (4.6) are authentic, but the story is different for the coupled mode.

The coupled mode is like an ordinary waveguide $TE_{10}$ mode, where the field concentration is in the middle. In an unloaded waveguide supporting first two dominant modes and excited with $TE_{10}$ mode, any asymmetry in the width of waveguide excites $TE_{20}$ mode, causing partial (reciprocal) mode conversion. Thus, it is concluded that mode conversion happens in the coupled mode as well due to asymmetry. Interestingly, such a mode conversion is in phase with the one resulting from the decoupled mode and contributes to the mode conversion; thus, the total phase change at the perturbed side is more than those formulated by (4.6).

To determine the exact length of perturbation, the share of coupled and decoupled modes in mode conversion must be calculated. Calculating the exact share of each mode is possible using a mode matching technique. However, it is unnecessary here as an adequately accurate initial value is provided by (4.6). Therefore, CST and HFSS simulation software can be utilized to optimize the length of non-symmetry section at the final step.

Generally, the wider the perturbation width is, the larger the share of the coupled mode is, hence the contribution of the coupled mode in the mode conversion. Therefore, for a wider perturbation a much shorter perturbation is required than what is predicted in (4.6). On the other hand, the thinner the perturbation is, the higher the share of decoupled mode is, and consequently, the length of perturbation is closer to (4.6). Furthermore, while a wider perturbation benefits a shorter length, it suffers from slightly larger mode conversion in the reverse direction. Therefore, opting for a proper dimension is a trade-off between compactness, lower loss and desired device performance.

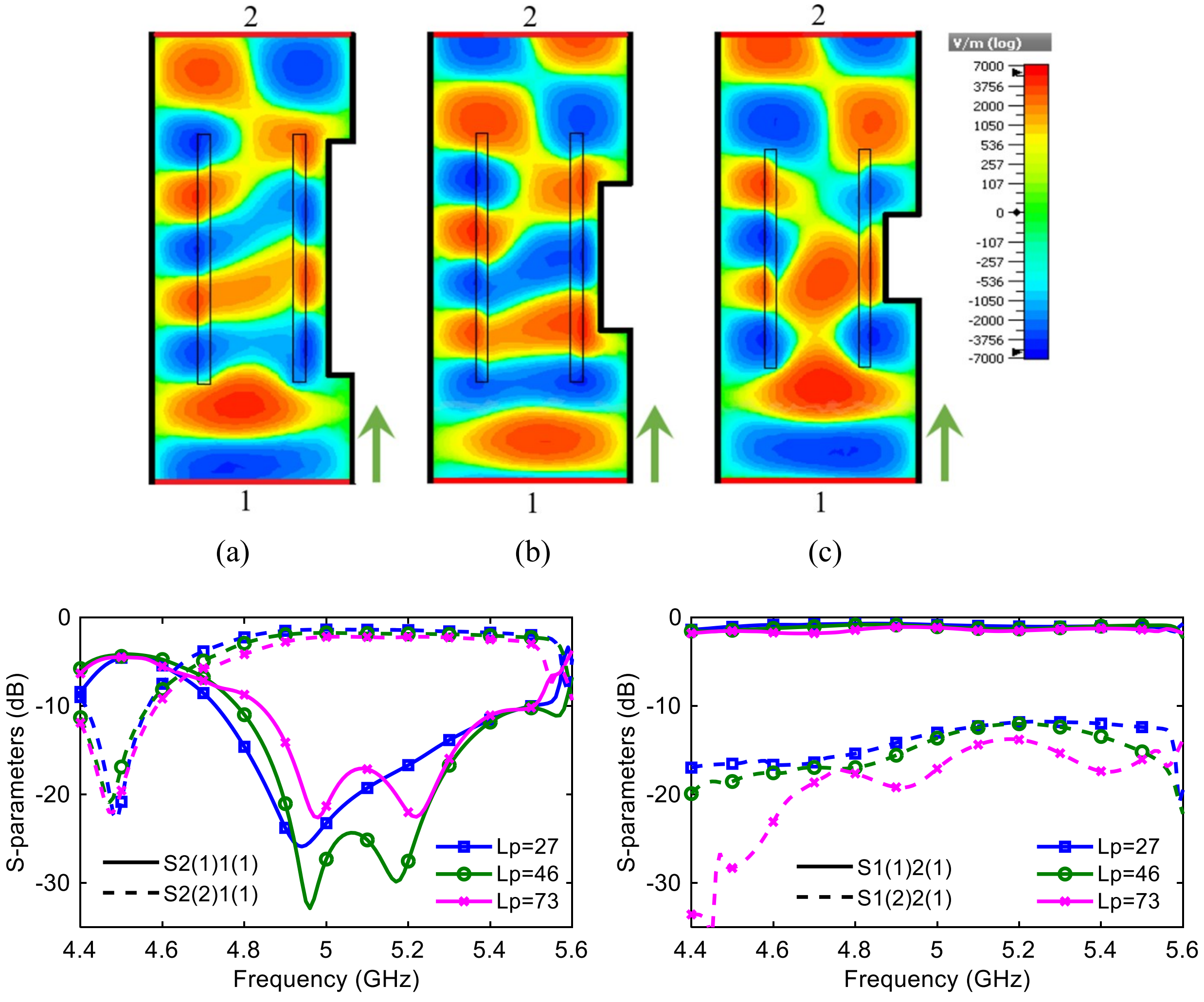

(a) (b) (c)

(d) (e)

Figure 4.11 E-field pattern for mode conversion in forward direction for three different *Wp*: (a) 6 mm, (b) 7 mm, (c) 8 mm, and s-parameter simulation for (d) port 1 and (e) port 2 excitations

To illustrate the differences, a mode conversion in the forward direction is depicted for three solutions in Figure 4.11. An initial dimension of perturbation is derived from Figure 4.9 and is tuned in CST software to yield final dimensions. Figure 4.11 obviously exhibits a complete mode conversion for all the solutions, where the NRMCW is excited with $TE_{10}$ mode at the bottom port, and $TE_{20}$ mode is delivered to the top port. Contemplating the E-field patterns reveals many interesting notes which are in complete agreement with the analysis given before. First of all, at the left side of NRMCW in all the three designs, we see that the semi-decoupled segment of wave is travelling along the ferrite slab almost independently as predicted. Second, at the right side and at the small gap between ferrite slab and perturbation, the wave propagates with longer wavelength (lower $\beta$), since propagation constant is shifted to a lower value at this side. Finally, some portion of the wave is leaked into the middle of the device, contributing to a coupled mode wave. The share of the coupled mode is increased from Figure 4.11 (a) to Figure 4.11 (c) as the perturbation gets widened. In other words, at the thinnest perturbation, the wave mostly consists of the decoupled mode, and the smoothly differential phase between two segments becomes 180 degrees, producing the $TE_{20}$ mode. While at the widest perturbation, a larger portion of wave is guided in the middle area (coupled mode), resulting in a faster mode conversion. Furthermore, the ratio of the tuned length to the length suggested by (4.6) is calculated in each case, showing that as width of perturbation is increased, the ratio is decreased, referring to an increased role of coupled mode in the mode conversion. These explanations can be quantitatively discerned at S-parameter curves of three configurations. Hence, in Figure 4.11(d) and (e) transmission S-parameters are plotted for $TE_{10}$ mode excitation at port 1 and 2 respectively. Therefore, the concept of the superposed coupled and decoupled waves is validated through the simulations. Among the three designs presented, the last one with perturbation dimensions of $W_p = 8$ mm and $L_p = 27$ mm is chosen as the final design case here for compact layout. The field distribution and S-parameters for $TE_{10}$ and $TE_{20}$ modes, in both forward and reverse directions, are illustrated in Figure 4.12 where a nonreciprocal mode conversion is clearly illustrated.

## 4.6 Circulator Based on NRMCW

### 4.6.1 Theory and Simulation

Nonreciprocal mode conversion has a great potential to find many known and unknown applications in designing nonreciprocal devices and systems. In this connection, one interesting application of NRMCW is to design multiport circulators. In [106], it is shown that the S-matrix of an ideal NRMCW is basically the same as the S-matrix of a circulator, and a 3-port circulator was demonstrated accordingly. In this paper, in a similar strategy, a 4-port circulator is demonstrated on the basis of the nonreciprocal and unidirectional mode conversion.

For measurement purposes, planar ports must be deployed; thus, a set of SIW to microstrip transitions are considered and designed for all the four ports. Two orthogonal transitions, each matching one of the microstrip ports to the corresponding $TE_{10}$ and $TE_{20}$ mode ports of SIW, are designed at each side of NRMCW. Different topologies may be adopted to design the transitions. However, a design that minimizes the mutual coupling between two different modes at each side is favored.

The schematic of the proposed circulator is depicted in Figure 4.13, where dimension are: $L_{tr}$ = 8.5 mm, $W_{tr}$ = 6.9 mm, $L_{wall}$ = 12.75 mm, $Z_{via}$ = 7.75 mm, $X_{via}$ = 4.85 mm, $W_{slot}$ = 0.2 mm, $W_{SIW}$ = 47.5 mm, $L_m$ = 7.5 mm, $L_s$ = 15.5 mm.

The transitions are deployed in a two-layer structure and cascaded to the opposite ends of the NRMCW. At each input of the NRMCW, one port is connected to an in-plane microstrip at the bottom substrate, whereas another port feeds a microstrip at the top substrate. $TE_{10}$ mode is excited in the NRMCW with the typical microstrip to SIW transitions [107-109]. However, the second transition is implemented via an additional layer at top of the first substrate to minimize the mutual coupling between two transitions [110]. $TE_{20}$ mode is excited by means of an intermediate grounded slotline etched on the top wall of the SIW shorted at both ends, which couples the energy from the microstrip fed by port 2 and couples it forward into the SIW. Since a simultaneous tuning of both transitions at the same frequency with low mutual coupling is difficult, additional tuning elements are required. In this regard, two symmetrical vias at two sides of the slotline are inserted, which can compensate the capacitive effect of the slotline in connection with the $TE_{20}$ mode of SIW. Also, placing a partial-width via-wall at the intersection of the microstrip and SIW can help as tuning elements. This via-wall firstly constitutes an effective wall for reflection of the $TE_{20}$ mode, providing a resonance beneath slotline. Secondly, it matches the in-plane microstrip fed by port 1 to the SIW $TE_{10}$ mode.

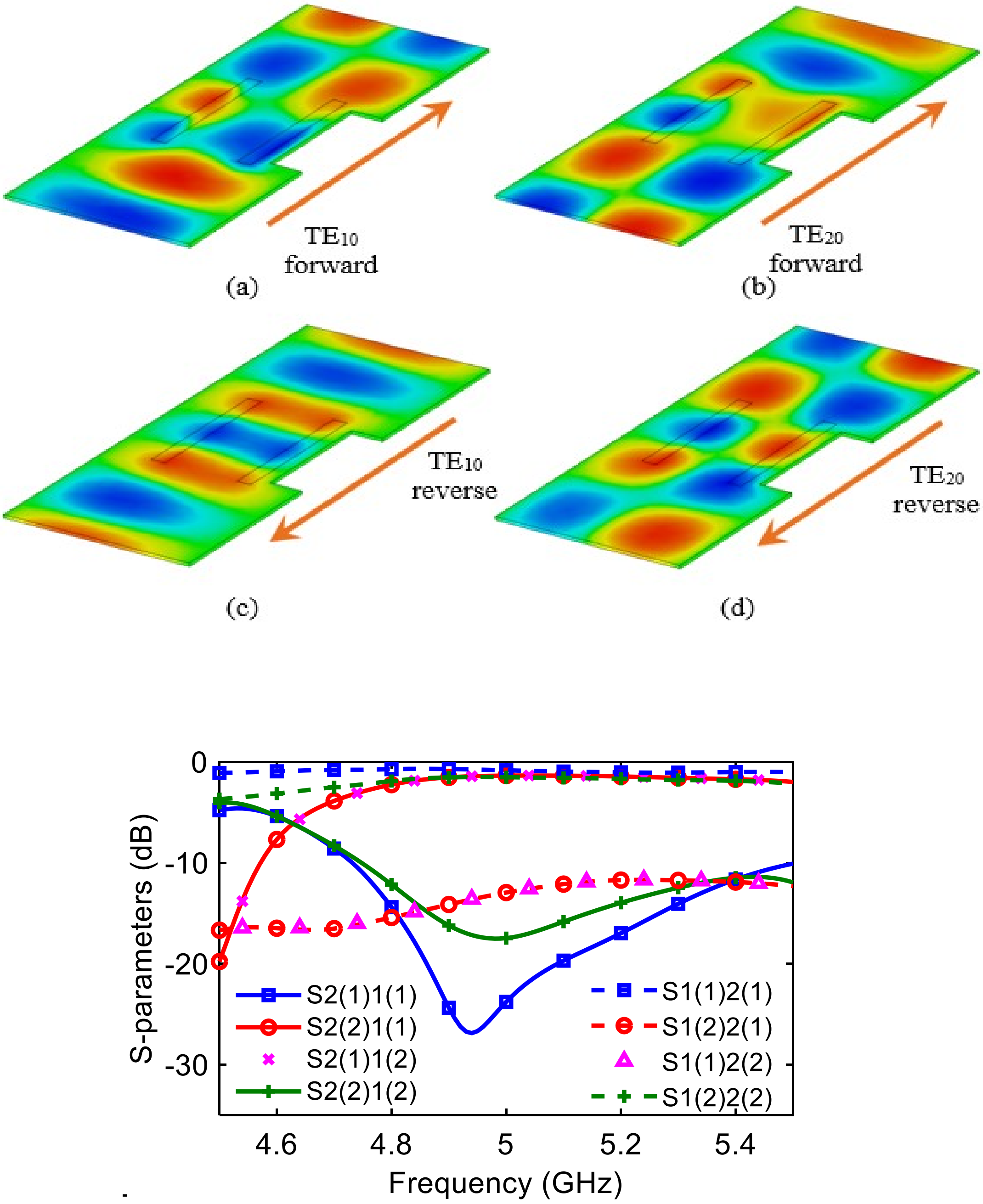

(a) (b) (c) (d) (e)

Figure 4.12 E-field pattern for proposed NMW: (a) $TE_{10}$ excitation at port 1, (b) $TE_{20}$ excitation at port 1, (c) $TE_{10}$ excitation at port 2, (d) $TE_{20}$ excitation at port 2, and (e) s-parameter results

Tuning elements are optimized by commercial CST Microwave Studio to yield the best possible performance while mode coupling is at a minimum. In Figure 4.13(b), the details and dimensions of transitions are shown.

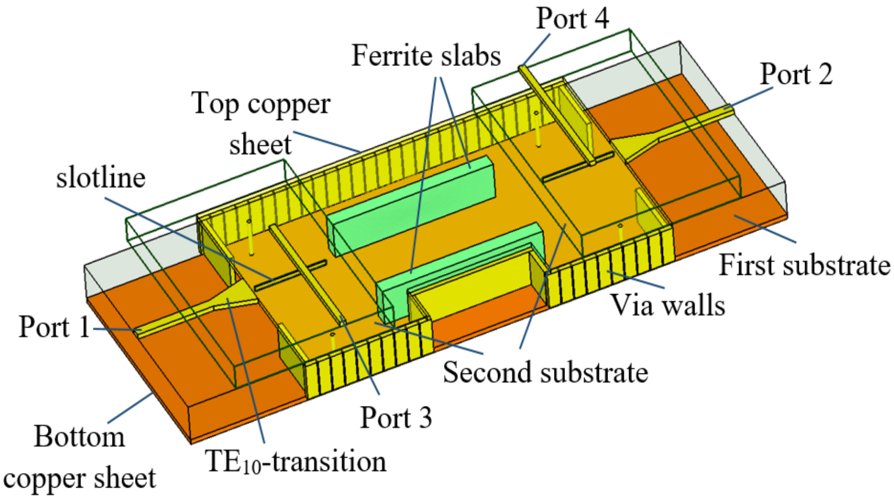

(a)

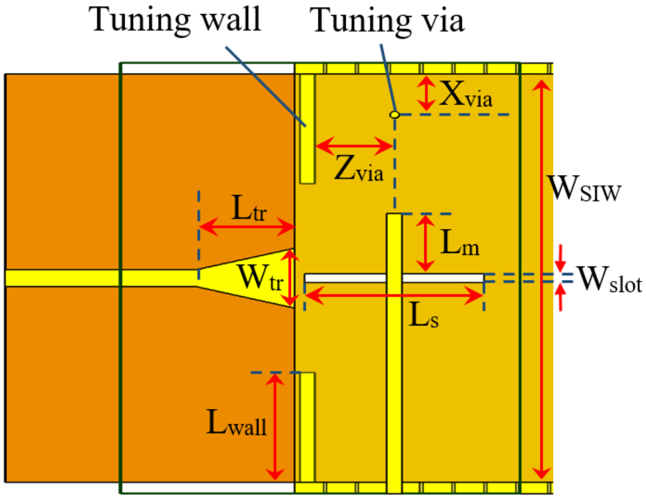

(b)

Figure 4.13 Schematic of proposed (a) 4-port circulator (3D view) and (b) top view of the microstrip transitions to SIW

### 4.6.2 Measurement Results

For fabrication, Rogers 6002 substrates with a dielectric constant of 2.94 and loss tangent of 0.0012 are utilized for the bottom and top substrates with 30 mils and 20 mils thickness, respectively. Photographs of our fabricated prototype are shown in Figure 4.14. Microstrip lines of port 1 and port 2 are printed on top of the first substrate. Furthermore, tuning elements and via-walls are implemented within the first substrate using laser cutting. Microstrip lines of port 3 and port 4 are printed on the second substrate. Then, the two layers are glued together with an epoxy paste. To embed the ferrite slabs into the SIW, two slots sized to fit the ferrite slabs are drilled into the SIW with a laser cutter in our fabrication process. Once the fabrication is done, the ferrite slabs are placed at drilled holes and covered with copper tape at the bottom and top of SIW and soldered to SIW for quality contact. Though, to access the ferrite drilled holes and to be able to tape them, the middle part of the top substrate is removed in the fabrication process before gluing the two substrates to each other. The ferrite material used in this work is an AL-0800 garnet provided by TCI Ceramics with saturation magnetization of 800 Gauss and linewidth of 30 Oersted. The magnetic bias setup is similar to the setup used in [105], where a tunable electromagnet has been utilized to provide the desired magnetic bias. Due to the demagnetization effects, amount of the required external biasing field is larger than the internal (simulated) biasing field [81]. In this work, it is assumed internal biasing field within the ferrite is uniform. Nevertheless, the actual magnetic biasing field is not ideally uniform and may distort the desired performance of the device. However, the obtained measurement results have revealed that in this work, the effect of the non-uniform biasing field can be neglected.

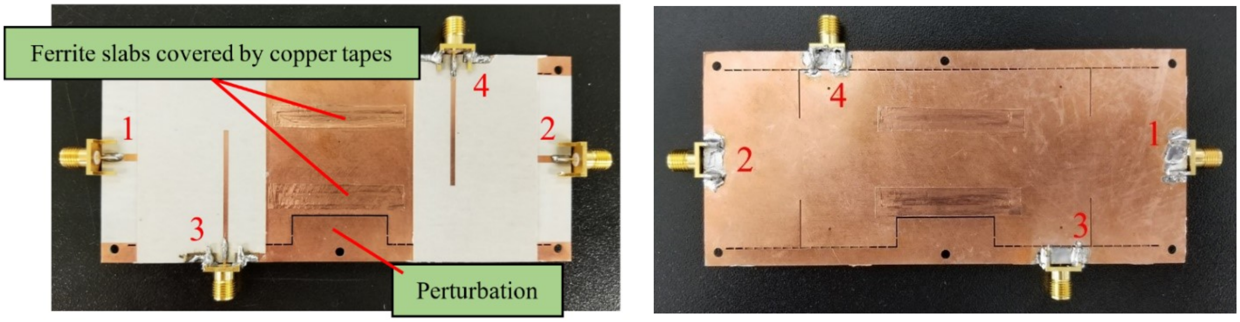

(a) (b)

Figure 4.14 Fabricated 4-port NRMCW circulator: (a) top view, (b) bottom view

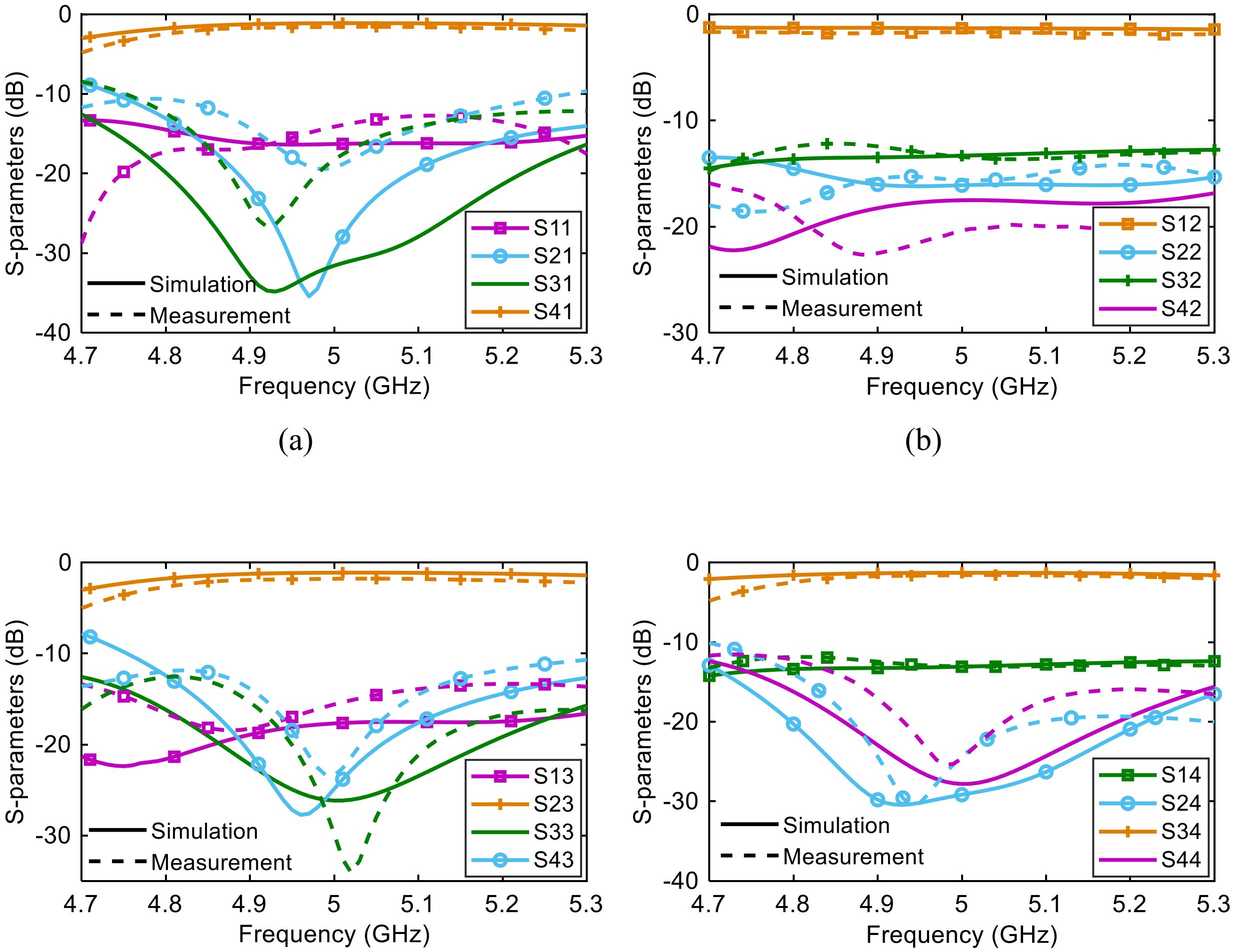

(a) (b)

(c) (d)

Figure 4.15 Measurement vs. simulation results: (a) Port 1 excitation ($TE_{10}$ mode at the forward direction in SIW), (b) port 2 excitation ($TE_{10}$ mode at the reverse direction in SIW), (c) port 3 excitation ($TE_{20}$ mode at the forward direction in SIW), (d) port 4 excitation ($TE_{20}$ mode at the reverse direction in SIW)

To accomplish the calibration, the short-open-line-thru (SOLT) method was used to provide reference planes at the input coaxial connectors of the device. S-parameters are acquired with a Keysight 4 port vector network analyzer (VNA) and are plotted in Figure 4.15 separately for each port excitation. Also, the measurement results are compared to simulation results generated in CST Microwave Studio. Measured insertion loss is better than 1.8 dB at 5GHz at worst case (for S23), which are slightly larger than simulated counterparts mainly due to connector loss. At one glance, S12 response confirms that the mode conversion happens at the frequency of interest, as there is a strong null at 5GHz.

Considering the presence of ferrite materials, simulation and measurement results are in excellent agreement. A discrepancy between simulation and measurement results can be attributed to few factors such as non-uniform magnetic biasing field, unbalanced biasing field applied to the ferrite slabs, non-perfect contact between ferrite slabs and SIW due to fabrication error, non-perfect copper contact on top and bottom of the ferrite slabs, connector loss, etc.

## 4.7 Conclusion

In this work, a fully integrated nonreciprocally dual-channelized waveguide (NDW) has been devised and demonstrated for the first time on the basis of an anti-symmetrically biased twin-ferrite loaded SIW. A detailed methodology to derive such a nonreciprocal device has been formulated and developed by the consideration of an electromagnetic field synthetization. In the NDW, the forward-directed wave, while being bifurcated into semi-decoupled segments, propagates in physically separate channels at the bilateral sides of SIW than the reverse-directed wave, which propagates at the middle channel, all within the same SIW structure. Any perturbation in an NDW created in either forward or reverse channel has a negligible effect on the other channel. By exploiting this main feature, a nonreciprocal mode-converting waveguide (NRMCW) has been proposed by inserting an unsymmetrical perturbation to the NDW. It has been found that the unsymmetrical perturbation leads to different propagation constants for each semi-decoupled forward-directed wave segments, resulting in a unidirectional mode conversion. The proposed NRMCW is considered a basic nonreciprocal element which manifests the unusual nonreciprocity by mode or modal nonreciprocity. In other words, in the forward direction, mode is converted in this device, while in the reverse direction, mode is not changed. In this connection, this device complements the concept of nonreciprocity against its known counterparts, gyrator and isolator, which manifest nonreciprocity through phase and amplitude, respectively. Finally, through the exhibition of one example application of NRMCW, a class of 4-port circulator has been demonstrated for the first time on the basis of this discovered unidirectional mode conversion. An excellent agreement between measurement and simulation results has successfully validated the whole theoretical foundation of this work and the concept of NDW and NRMCW as the primary contributions of this work.

## 4.8 Acknowledgment

The authors would like to thank T. Antonescu, D. Dousset, and J. Gauthier of Poly-Grames Research Center, Polytechnique Montréal (University of Montreal), Montréal, QC, Canada, for their support in the realization of the prototypes.

# CHAPTER 5 ARTICLE 3: GENERALIZED THEORY OF CONCURRENT MULTI-MODE RECIPROCAL AND/OR NONRECIPROCAL SIW FERRITE DEVICES

Amir Afshani, Graduate Student Member, IEEE, and Ke Wu, Fellow, IEEE

This article fulfills our second objective in presenting a general and comprehensive theory to develop multi-mode nonreciprocal ferrite-based components. This article is submitted to IEEE Transactions on Microwave Theory and Techniques (April 2021).

## 5.1 Abstract

In this work, we propose, develop, and demonstrate a fundamental and comprehensive theoretical foundation for the first time to formulate and devise known and unknown reciprocal and/or nonreciprocal ferrite components with arbitrarily concurrent multimode features based on the substrate integrated waveguide (SIW) technology. To achieve such a universal design, a nonreciprocal unit cell (NRUC) is first defined and characterized. Then, an approach is proposed and investigated to deploy a sufficient number of NRUCs next to each other as a kernel multimode SIW topology. The kernel configuration transforms the incident guided-wave into several separate segments, propagating in parallels independently and along each NRUC, which can be manipulated separately. This methodology grants a general solution to forge ferrite components in a multimode configuration, discussed in detail to corroborate the proposed generalized theory. Finally, two multimode components are studied and demonstrated for the first time as application examples for the proposed theory. Namely, a dual-mode circulator and a triple-mode gyrator are prototyped, fabricated, and measured, exhibiting an excellent agreement with simulation results that effectively validate the presented theoretical foundation in this work.

*Index Terms*—Dual-mode, circulator, ferrite, gyrator, multimode, nonreciprocal, nonreciprocal unit cell (NRUC), substrate integrated waveguide (SIW), $TE_{20}$ mode, $TE_{30}$ mode, triple-mode.

## 5.2 Introduction

Ferrite devices have played an instrumental role in developing and evolving radar, communication, satellite, and other telecommunication systems, thanks to their tunability or non-reciprocity features. SIW technology has widely been known to present low-loss and high-powered handling capacity, integrability, self-consistent electromagnetic shielding or packaging, and low fabrication costs. Thus, this technology is appealing for deploying and integrating ferrite materials to realize various ferrite-loaded SIW components, such as isolators [60, 63], phase shifters [62, 69], circulators [67, 111], and so forth. On the other hand, with emerging 5G and beyond-5G technologies, wireless communication and radar systems' proliferation suggests a grand trend of architectural and functional unification. This consolidation demands the exploitation of various multi-function components, ranging from multimode and multi-band filters, antennas, and other passive components, to active circuits like multimode and multi-band PAs, LNAs, mixers, and so on. Although multimode devices prevalently dominate the microwave world, multimode functionality has never been considered and practiced in the realm of ferrite devices. Instead, there have been some research activities on dual-band [112, 113], or dual-polarized [114, 115] ferrite devices. The latter involves some published works, mainly from decades ago, regarding the demonstration of Faraday rotation phase shifters. Such phase shifters are set to deploy two horizontal and vertical polarizations in the waveguide to create RHCP and LFCP waves. These waves propagate at different velocities within a longitudinally biased ferrite medium to attain two different phase shifts, which suffer from generally complicated and bulky waveguide structures. Also, most importantly, they are limited only to phase shifter applications. Nevertheless, despite the mentioned dual-polarized phase shifters, arbitrarily multimode ferrite devices, to our knowledge, have not been the subject of any research in the past.

In this work, we propose and establish a comprehensive theoretical foundation to explore and realize fully integrated multimode SIW reciprocal and/or nonreciprocal ferrite devices for the first time. Three phases will be discussed to accomplish this goal. In the first phase, we will define and investigate a nonreciprocal unit cell (NRUC), which serves as a cornerstone in our theoretical and experimental development. The defined NRUC applies to any frequency range with different substrates and ferrite materials as long as the required magnetic bias can be provided in practice. In the second phase, a unique approach to synthesize a multimode reciprocal and nonreciprocal

SIW kernel topology will be proposed and developed. This kernel component consists of several NRUCs that are tactfully placed next to each other within a SIW and creates distinct channels that can effectively carry the segments of a wave. Essentially, the kernel component is able to break down the incident $TE_{n0}$ wave into several segments at one end, to provide a basis to modify or reroute each segment separately along the channel, and finally to reconstruct the altered segments into a $TE_{m0}$ waveguide mode at the other end. The third phase involves sculpting the desired specific multimode ferrite component from a corresponding kernel topology. For two-port devices, it is always possible to introduce perturbations within each channel of the kernel topology, thus leading to phase and/or amplitude manipulations that can contribute to each mode separately. For multi-port devices, it is possible to reroute waves propagating within a channel into an additional port with aperture coupling or other techniques introduced in this paper. Interestingly, these approaches for creating specific components can be the subject of future research for each component separately, where various innovative techniques that may lead to superior performances are explored. In general, we envision that this theory will establish the groundwork for the straightforward implementation of known and unknown compact multimode ferrite devices in future microwave systems.

The idea of this work was briefly outlined in [116] with a concise description of the NRUC and presented measurement results for the dual-mode circulator. However, in this paper, a thorough theoretical foundation and mathematical modeling of both NRUC and kernel configurations are explored and presented while investigating three different kernel topologies. In addition, a triple-mode gyrator is demonstrated in this paper.

This paper is organized onwards as follows. In Section II, we investigate the theoretical aspects of exciting a particular mode within an unloaded multimode SIW using an array of equally spaced current sources. This study will lead to an understanding of how to exploit NRUCs within a SIW to derive multimode functionality. In Section III, an NRUC compatible with SIW technology and its related theoretical foundation will be proposed and explained in detail. A methodology to exploit NRUCs to realize multimode kernel configurations will be presented in Section IV. Three specific examples of dual-mode and triple-mode ferrite-loaded SIWs will be discussed to shed further light on the proposed methodology. Two application examples will be covered and discussed in Sections V and VI, where, for the first time, a dual-mode circulator and a triple-mode gyrator will be demonstrated, respectively.

## 5.3 Exclusive Mode Excitation Within Multimode SIW: A Theoretical Investigation

This section will investigate and develop a generalized theoretical foundation to excite an arbitrary mode exclusively within a multimode SIW. Only TE$_{n0}$ modes exist within the SIW, and for a z-directed wave, transverse fields of different modes can be written as:

$$\overline{E}_y^n = A_n \bar{e}_n \; e^{-j\beta_n z} = yA_n \sin(\frac{n\pi x}{a})e^{-j\beta_n z} \qquad (6.1)$$

$$\overline{H}_x^n = A_n \bar{h}_n \; e^{-j\beta_n z} = -x\frac{A_n}{Z_n}\sin(\frac{n\pi x}{a})e^{-j\beta_n z} \qquad (6.2)$$

where $n$ is the mode number; $A_n$ is the amplitude of each mode; $\beta_n$ and $Z_n$ are the propagation constant; the mode impedance at $n$th mode and $a$ is the waveguide width. For a multimode SIW, the waveguide's width must be wide enough to propagate all the desired modes within the frequency band of interest. Assuming $f_{end}$ as the maximum operational frequency band and letting $N$ propagating modes in the SIW, f$_{\text{end}}$ must be less than the cut-off frequency $(N+1)$th mode. Hence, the width of a SIW supporting $N$ propagating modes can be calculated in the following relation:

$$a_{N\_\text{mode}} < \frac{(N+1)c}{2f_{end}\sqrt{\varepsilon_r}} \qquad (6.3)$$

where $c$ is the speed of light in the vacuum, and $\varepsilon_r$ is the dielectric constant of the SIW. For matching considerations, it is typically better to choose the width of the SIW to be equal to the value in (5.3).

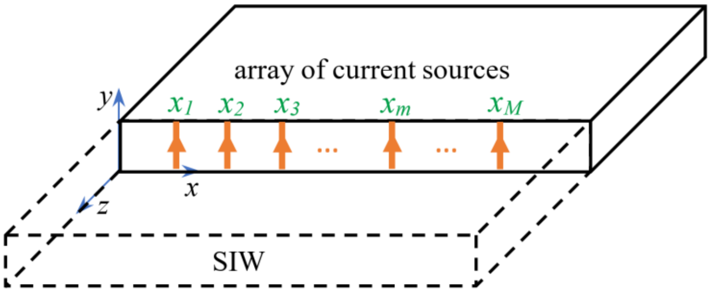

Figure 5.1 Multi-mode excitation of SIW by an array of $M$ current sources within the SIW

To model the waves' excitation, we can consider either or both magnetic and electric current sources. In this attempt, we consider an array of y-directed current sources with infinitesimal diameters at different $x$ locations over the cross-section of the SIW, as illustrated in Figure 5.1. In the rest of this section, we will investigate this configuration to derive a formulation to excite each mode exclusively and solely within the SIW by determining each current element's amplitude and position.

Consider an array of current elements with amplitude $I_m$ located at $x_m$ away from the origin. Such a current can be mathematically modeled as:

$$\overline{J_m} = yI_m\delta(x - x_m)\delta(z) \qquad (6.4)$$

By the superposition of all sources and by referencing to [81], the amplitude of each excited mode due to the current array will be:

$$A_n = \frac{Z_n}{a}\sum_{m=1}^{M} \mathrm{I}_m^n \sin(\frac{n\pi x_m}{a}) \qquad (6.5)$$

In this equation, $n$ represents the mode number, and $m$ represents the current source's position within the current array with $M$ sources. From (5.5), it is deduced that sources may have constructive or destructive interferences, thereby respectively leading to the excitation or cancelation of a mode within the SIW, and thus hinting at a mechanism to impose or avoid the propagation of specific modes.

Our goal is to find a complete set of solutions where each solution exclusively excites one specified mode within the SIW. The solution for this problem is not unique, as the number of sources can arbitrarily be increased to leverage the freedom of design. Here, however, we enforce using the minimum number of sources within the array. For a SIW with $N$ propagating modes, there must be at least $N$ sources within the array to guarantee that all the modes can be excited solely ($M$=$N$). Therefore, position $x_m$ and amplitude $I_m^n$ of each source within the array will be the problem variables.

This problem is analogous to a Fourier series. Thus, in our proposed solution, the elements of current sources are first distributed at equal distances from each other. Second, we must determine each current element's amplitude and for each mode separately. For exclusive mode excitation, $A_n$ must be non-zero only for the current array values in the desired mode and zero for values of the current array in all other modes. Therefore, we can make an educated guess (inspired by the Fourier series) that currents' distribution must be orthogonal from one mode to another. Hence, we can consider that a sinusoidal distribution of the amplitude of current sources takes the form of:

$$\mathrm{I}_m^{(n)} = \mathrm{I}_0 \sin(\frac{n\pi}{2N}(2m-1)) \qquad (6.6)$$

Therefore, our problem has narrowed down to finding the value of $I_0$, which can be found by substituting (5.6) in (5.5) and using the orthogonality identity. After some mathematical manipulations, it will result in:

$$\mathrm{I}_m^{(n)} = \frac{A_n a}{NZ_n}\begin{cases} 2\sin(\frac{n\pi}{2N}(2m-1)) & \mathrm{n} \neq \mathrm{N} \\ \sin(\frac{n\pi}{2N}(2m-1)) & \mathrm{n} = \mathrm{N} \end{cases} \qquad (6.7)$$

which yields the value of each current source in the array, which will exclusively excite one mode within the SIW. Hence, our problem is solved. To illustrate this problem, the amplitude distribution of the current array is calculated in Table 5.1, where up to four modes are shown in this case. In calculating this table, for simplicity without losing generality, the $A_n a/Z_n$ coefficient has been factorized from (5.7). Also, each column represents the amplitude of the current element in the corresponding position. From the table, it can be noted that the dot product of each two rows is zero, validating that current arrays are orthogonal and that they exclusively excite the corresponding mode. The main feature of this table is how the current distribution for even and odd modes is symmetrical and anti-symmetrical, respectively, and how the polarization of each current source has a meaningful impact on each mode. In addition, it is implied that the amplitude and phase of each current source in each mode represent the relative power and polarization of the field in the corresponding segment of the waveguide.

This section has developed a mathematical approach to separately excite each propagating mode within a SIW by using an array of line-wise current sources. We have shown that an array of equally

Table 5.1 Amplitude distribution of current sources for arbitrary single mode excitation in a multi-mode SIW

| Mode to be excited ($TE_{n0}$) | Amplitude of current-source elements: $I_m^{(n)}$ | | | | | | | | |
|---|---|---|---|---|---|---|---|---|---|
| | Dual-mode SIW | | Triple-mode SIW | | | Quad-mode SIW | | | |
| | ***m1*** | ***m2*** | ***m1*** | ***m2*** | ***m3*** | ***m1*** | ***m2*** | ***m3*** | ***m4*** |
| |  | |  | | |  | | | |
|  | $+\frac{\sqrt{2}}{2}$ | $+\frac{\sqrt{2}}{2}$ | $+\frac{1}{3}$ | $+\frac{2}{3}$ | $+\frac{1}{3}$ | $+\frac{\sqrt{2-\sqrt{2}}}{4}$ | $+\frac{\sqrt{2+\sqrt{2}}}{4}$ | $+\frac{\sqrt{2+\sqrt{2}}}{4}$ | $+\frac{\sqrt{2-\sqrt{2}}}{4}$ |
| 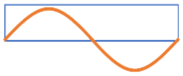 | $+\frac{1}{2}$ | $-\frac{1}{2}$ | $+\frac{\sqrt{3}}{3}$ | 0 | $-\frac{\sqrt{3}}{3}$ | $+\frac{\sqrt{2}}{4}$ | $+\frac{\sqrt{2}}{4}$ | $-\frac{\sqrt{2}}{4}$ | $-\frac{\sqrt{2}}{4}$ |
| 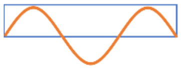 | × | | $+\frac{1}{3}$ | $-\frac{1}{3}$ | $+\frac{1}{3}$ | $+\frac{\sqrt{2+\sqrt{2}}}{4}$ | $-\frac{\sqrt{2-\sqrt{2}}}{4}$ | $-\frac{\sqrt{2-\sqrt{2}}}{4}$ | $+\frac{\sqrt{2+\sqrt{2}}}{4}$ |
| 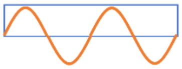 | × | | × | | | $+\frac{1}{4}$ | $-\frac{1}{4}$ | $+\frac{1}{4}$ | $-\frac{1}{4}$ |

spaced $N$-element current sources is sufficient to excite an arbitrary mode within an $N$-mode SIW. This approach can be inspired to design proper transitions to excite each mode in a multimode SIW.

However, from another viewpoint regarding this mathematical model, a fascinating deduction can be made, which is not only the preferred observation of this work but for the rest of this paper. The developed mathematical model suggests that a complete set of $TE_{n0}$ modes can manifest themselves in $N$ discrete points as if to consider $N$ discrete localized waves at these points. Moreover, suppose we replace line-wise current sources with hypothetical line-wise phase and/or amplitude perturbations. In that case, it is possible to fully manipulate these modes within the SIW (like shifting phase, attenuating, blocking, matching, converting mode, etc.) by adjusting each mode merely through these focal perturbations. The last statement is the inspiration of this work and leads to the design of multimode nonreciprocal SIWs, whose theory will be developed in the following sections.

## 5.4 Nonreciprocal Unit Cell (NRUC)

In this section, we will first propose a nonreciprocal ferrite unit cell. Then, we will investigate its properties and identify how its fields can be manipulated by varying some key cell parameters. This study will lead to the creation of a nonreciprocal unit cell that serves as the cornerstone in developing the generalized theory of nonreciprocal multimode SIW structures.

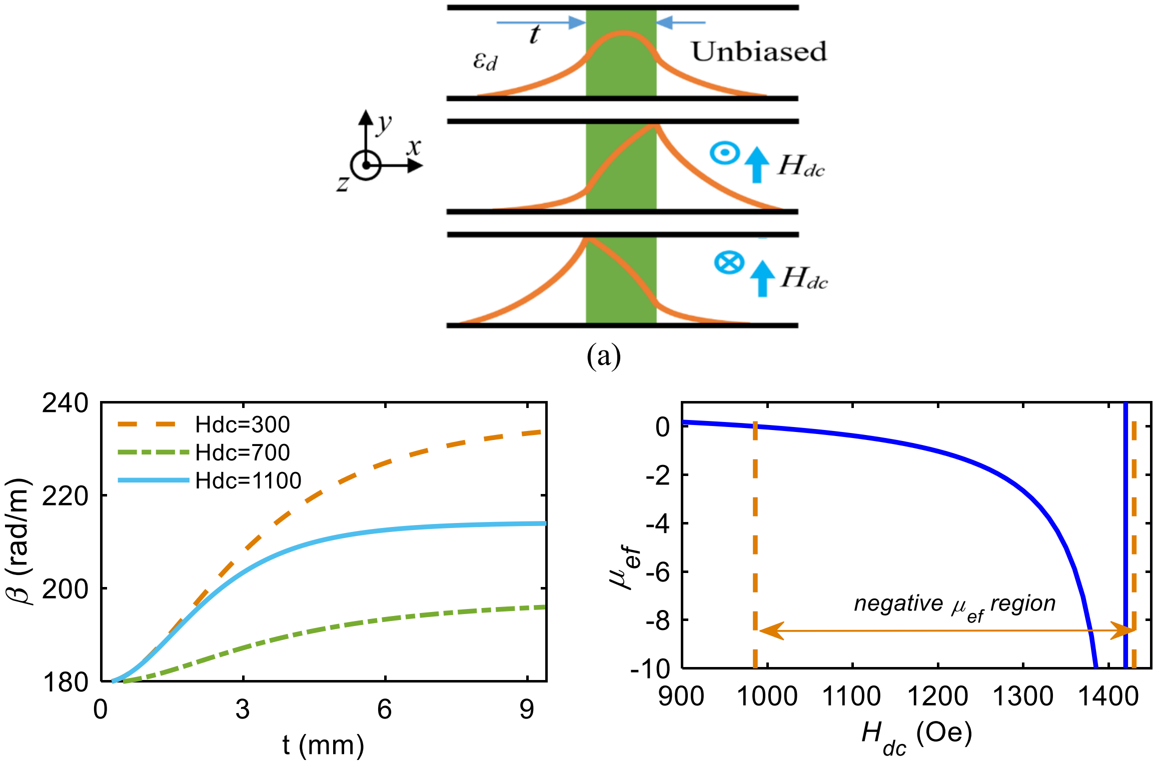

(a)

(b)

(c)

Figure 5.2 (a) Behavioural illustration of nonreciprocal propagation in a transversely biased ferrite slab for a TE mode wave, (b) negative region of effective relative permeability plot versus internal magnetic bias, (c) propagation constant of unit cell versus ferrite width for different biases

Consider a ferrite slab embedded within a substrate integrated parallel waveguide, where the surrounding dielectric has a relatively low dielectric constant and stretches out to infinity at both sides. Since the ferrite's permittivity is high, the ferrite slab will become a dielectric waveguide. Such a waveguide supports the $TE_{n0}$ waves confined within the ferrite slab. Fields outside the ferrite will be evanescent and decaying outward, implying that the impedance looking outward from the ferrite/dielectric interface is imaginary [104]. If a transverse magnetic bias is applied to the ferrite, it will exhibit nonreciprocal behavior by displacing electromagnetic fields toward different sides in the forward and reverse direction of propagations (equivalently when the direction of magnetic bias is reversed), as illustrated in Figure 5.2(a).

We can study the nonreciprocal unit cell and formulate it analytically by writing the governing expressions for magnetic and electric fields in both mediums [80]. Enforcing the boundary conditions yields a characteristic equation, leading to the finding of the propagation constant and further coefficients of the fields for a complete analysis. Nevertheless, here, without getting lost in the mathematical modeling of the unit cell, the principal behavior of the unit cell can be deduced simply from expressions of the cut-off wavenumber of the ferrite and substrate, which can, respectively, be written as:

$$k_f = \sqrt{(\omega / c)^2 \mu_{eff} \varepsilon_f - \beta^2} \qquad (6.8)$$

$$k_d = j\sqrt{\beta^2 - (\omega / c)^2 \varepsilon_d} \qquad (6.9)$$

where $c$ is the speed of light in vacuum; $\varepsilon_d$ and $\varepsilon_f$ are the relative dielectric constants of substrate and ferrite, respectively; $\beta$ is the propagation constant, and $\mu_{eff}$ is the effective permeability of the ferrite. For a ferrite transversely biased to the direction of the propagation (the current case), the effective permeability can take negative values for a certain range of magnetic bias [78], [105, 106], and [117] giving exceptional properties to the unit cell. From (5.8), it can be discerned that if $\mu_{eff}$ becomes negative, then $k_f$ will become imaginary like $k_d$. Imaginary $k_f$ imposes an exponential field profile inside the ferrite instead of a sinusoidal profile, causing a stronger accumulation of fields toward one interface. In other words, a negative $\mu_{eff}$ will localize more of the electromagnetic wave at one interface of the ferrite. The effective permeability can be expressed through a set of poles and zeros as [105]:

$$\mu_{eff} = \mu_0 \frac{(H_{dc} - H_{z1})(H_{dc} - H_{z2})}{(H_{dc} - H_{p1})(H_{dc} - H_{p2})} \qquad (6.10)$$

where $H_{dc}$ is the applied internal magnetic bias, and $H_z$ and $H_p$ are the zeros and poles of the function. However, only $H_{z2}$ and $H_{p2}$ are positive and can be realized using the following relations:

$$H_{z2} = -Ms + f / \gamma \qquad (6.11)$$

$$H_{p2} = 0.5(-Ms + \sqrt{Ms^2 + 4(f / \gamma)^2}) \qquad (6.12)$$

where *f* is the operation center frequency in MHz; *Ms* is the ferrite saturation magnetization in Gauss; $\gamma$ is the gyromagnetic ratio and equals 2.8 MHz in CGS units. The parameter $\mu_{eff}$ in (5.10) undergoes a negative value from the positive zero up to the positive pole. In this work, for *f*=5 GHz and *Ms*=800 *Gauss,* the negative range of $\mu_{eff}$ corresponds to the values of $H_{dc}$ between 985.7 Oe and 1430 Oe, as illustrated in Figure 5.2(b). As shown in the figure, relative permeability in the negative region is strongly nonlinear. Therefore, for a broader bandwidth performance of the unit cell, it is best to choose the center frequency at the lower side of the negative region, where the curve is semi-linear. In this work, we have $H_{dc}$=1100 Oe for the initial design.

To understand the effect of the magnetic bias in the strong localization of power, next, we turn our attention to the width of the ferrite as the second key parameter. If the ferrite is too narrow, it will have a loose interaction with the magnetic fields, thus failing to alter the unit cell fields effectively. As such, waves will propagate in the waveguide with the slightest perturbation due to the ferrite. However, by increasing the ferrite thickness, the ferrite's interaction will be more potent and more effective, leading to the total confinement of the fields within the ferrite. On the other hand, since fields are exponential within the ferrite, field intensity would diminish fast from one interface to another, making much wide ferrites unnecessary. To assess the ferrite width role, the propagation constant as a function of the ferrite thickness is plotted in Figure 5.2(c) for the positive and negative values of the effective permeability. This figure confirms our reasoning as the propagation constant reaches its saturation much faster for the curve with a negative permeability ($H_{dc}$=1100 Oe).

To devise a criterion to determine the ferrite's width, we define a ratio to evaluate the field displacement within the ferrite. The ratio of the field power at the two interfaces of the ferrite can be a good reference point to compare different configurations of the unit cell, as follows:

$$\textit{Field displacement ratio} = \left| \frac{E(x=-t/2)}{E(x=t/2)} \right|^2 \tag{6.13}$$

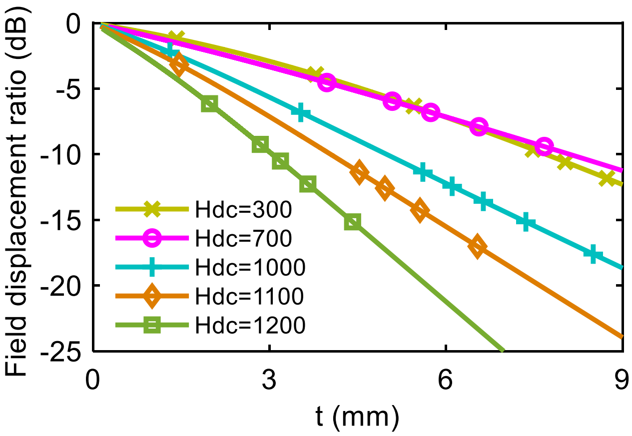

Figure 5.3 Field displacement ratio (in dB) versus ferrite thickness in a unit cell, for various magnetic bias points

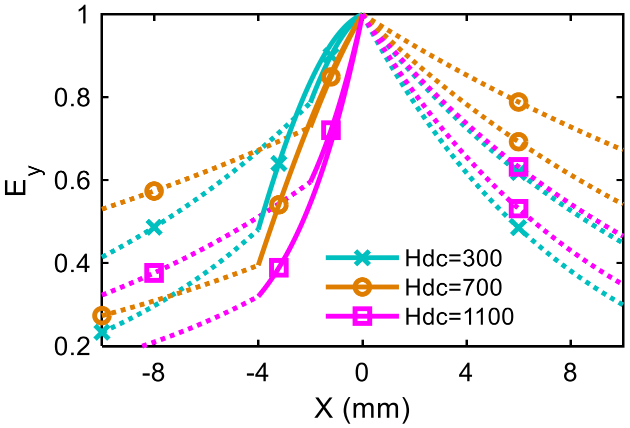

Figure 5.4 Electric field distribution in the unit cell for different magnetic bias points ($H_{dc}$=300, 700, 1100 Oe), and two ferrite widths ($t$=2 and 4 mm)

In this relation, the interface with the lower field intensity is the numerator of the ratio, which yields numbers between zero and one. By knowing all the fields across the unit cell from solving the Maxwell equations, the field displacement ratio is calculated in dB as a function of the ferrite width ($t$) for various magnetic bias points and is displayed in Figure 5.3. The figure reveals the impact of the ferrite's effective permeability and width on the field displacement. For the positive values of the effective permeability ($H_{dc}$=300, 700 Oe), the field displacement is smaller due to the sinusoidal field profile. Furthermore, as the effective permeability becomes increasingly negative ($H_{dc}$=1000, 1100, 1200 Oe), the field displacement gets much more pronounced. Considering a -10 dB threshold for the non-reciprocity of the unit cell, a ferrite width of a minimum of 3.5 mm would be a good choice at the operating magnetic bias.

Finally, to observe and compare the nonreciprocal field distribution in the unit cell over different configurations, the unit cell's electric field intensity in the forward direction is plotted in Figure 5.4. The ferrite region fields are plotted with solid lines to illustrate this more clearly, while fields outside the ferrite region are plotted with dotted lines. Besides, for comparison purposes, the plot's origin is fixed at the ferrite's right interface in both cases. The curves demonstrate two important features that we have discussed so far. First, the spillover wave will be significant for narrow ferrites and will not effectively be trapped within the ferrite. Nevertheless, with an increase in ferrite width, the wave is confined within the ferrite, and only a tiny portion of the wave leaks into the substrate region. Again, due to the exponential effect, a further increase in the ferrite width results in a slight change in the field profile. Moreover, the curves show that for non-negative $\mu_{eff}$ the fields within the ferrite are non-exponential and consequently hold more power within the entire ferrite. Therefore, the field displacement is weaker than the curves with a negative $\mu_{eff}$. Second, Figure 5.4 clearly shows that the fields are strongly localized at the ferrite's right interface for the proper parameters of $\mu_{eff}$ and $t$. Notably, if either the propagation direction or the magnetic bias direction reverses, the field concentration will swap to the left interface; however, the amplitude and phase will remain the same. Therefore, the non-reciprocity in this unit cell only manifests itself when the field is displaced toward different sides relative to the direction of the traveling wave. It should be noted that although choosing wider ferrite slabs slightly enhances the non-reciprocity of the unit cell; it might result in a narrowband matching with an unloaded SIW. Although this trade-off can be adjusted according to Figure 5.2-4 for different applications, in the rest of this paper, we adopt an NRUC with the parameters $t$=3.5 mm and $H_{dc}$=1100 Oe.

It should be said that the developed theory of this section and the rest of this paper applies to other frequency ranges and different ferrite materials (with different *Ms*) without any loss of generality.

This section demonstrates that a ferrite unit cell can have two crucial properties, as proposed in this work. First, it exhibits non-reciprocity by displacing fields toward the opposite sides in oppositely directed waves. Second, this unit cell is capable of effectively localizing the power into a small area, indicating a point-wise wave propagation.

## 5.5 A General Solution for Designing Multi-Mode Reciprocal/Nonreciprocal SIW Devices

In Section II, we demonstrate that the $TE_{n0}$ modes of a SIW can be completely manipulated through a finite number of discrete points. The key idea to devise and develop multimode nonreciprocal devices is to embed NRUCs within the SIW at such points and expect to yield similar multimode outcomes, as seen in Section II. Two reasons explain this. First, the NRUC localizes power into point-wise areas, like the point current sources in Section II. Second, NRUCs yield a nonreciprocal property to the device through a nonreciprocal field displacement, while the amplitude and phase of the wave remain the same in the forward and reverse directions of propagation. This property is the critical characteristic of the NRUC, which makes this idea feasible; the *S*-parameters of the unit cell are reciprocal, and consequently, the analysis of Section II remains valid. Before presenting a mathematical model for the structure and analyzing the problem in detail through Maxwell equations, we present a short description to offer qualitative insight into the multimode nonreciprocal waveguide operation and the physical meaning of exploiting this structure to achieve any other type of known ferrite devices.

### 5.5.1 Nonreciprocal Wave Propagation Through N Parallel NRUC: a Qualitative Insight

Let us consider wave propagation within *N* laterally parallel NRUCs, which are hypothetically placed next to each other, as illustrated in Figure 5.5(a). In this hypothetical situation, it is assumed that the surrounding dielectric of each NRUC stretches out to an infinite value so that NRUCs do not interfere with each other and are not disturbed by any other boundary condition. According to the illustration in Figure 5.5(a), it is discerned that distinct and unique channels are created along with each ferrite slab that separates forward and reverse directed waves. In the forward direction, fields are concentrated only at each ferrite slab's left interface, whereas for the reverse direction, the field concentration swaps to the right interface. Our proposed methodology in some sense is similar to the quasi-optical technique in the spatial power combining of active circuits, where several fin-line TLs are used to sample waveguide modes and reconstruct them after amplification [118, 119]. In this case, the parallel NRUCs are capable of sampling waves at one end and reconstructing them at the other end, while it is possible to nonreciprocally modify or reroute the samples along the ferrites as desired.

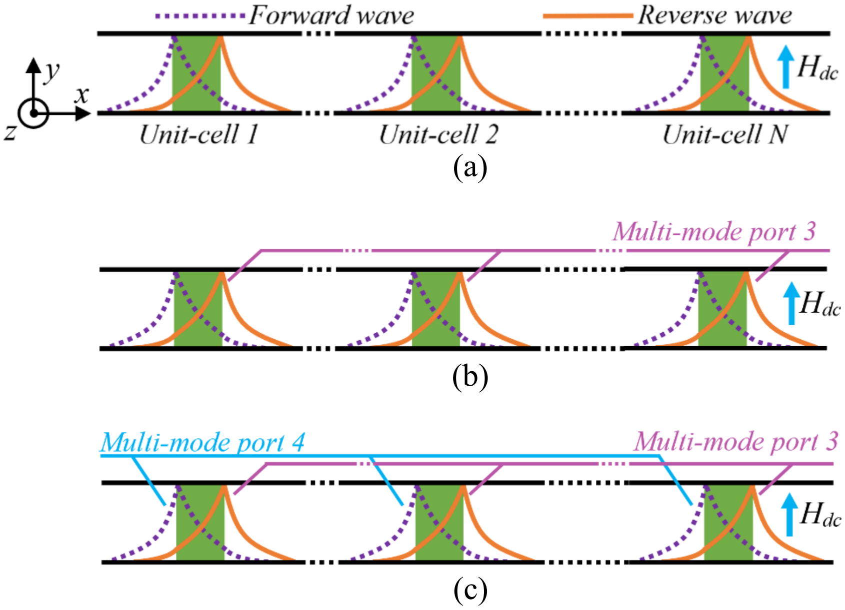

Figure 5.5 Cross-section view of parallel NRUCs as a basis to synthesize multi-mode nonreciprocal: (a) two-port, (b) three-port and (c) four-port devices

This unique nonreciprocal field distribution allows for perturbing the configuration in creative ways to benefit nonreciprocal behaviors. For example, it is possible to introduce proper phase and/or amplitude perturbations only at one side of the ferrite slabs to yield a multimode nonreciprocal phase shifter or isolator. Furthermore, it would be possible to design a 3-port circulator by adding a multimode port that interferes only at one side of each ferrite slab to nonreciprocally circulate the wave in the desired direction, as shown in Figure 5.5(b). Similarly, adding an extra multimode port at the opposite side of unit cells would yield a 4-port circulator, as described in Figure 5.5(c). In practice, it is possible to create additional ports through aperture coupling on the top or bottom of the conductors adjacent to the ferrite slabs.

It must be mentioned that the direction of bias in each NRUC can be arbitrarily reversed to swap the field pattern from one side of the NRUC to the other. This feature can be used to realize various applications, as discussed in the following sub-sections.

So far, we have introduced how the configuration of parallel NRUCs can result in a multimode nonreciprocal operation. However, two critical issues must be addressed in an actual physical problem. First and foremost, precise geometry and solution must be defined to arrange NRUCs next to each other as a monolithic unit that can support $TE_{n0}$ modes. Second, a procedure to uniquely excite each mode within the proposed configuration must be anticipated. Our solution for both challenges is to embed NRUCs within a SIW for several reasons. First, the configuration of parallel NRUCs is entirely compatible with the technology and topology of ferrite-loaded SIWs. Second, only $TE_{n0}$ modes can propagate within a SIW that are desired modes in this structure. Moreover, the techniques that excite different modes within a SIW are known and practical, while the theoretical aspects are covered earlier in this paper. Finally, the SIW can provide superior EM compatibility that is important for emerging wireless systems.

Although embedding the NRUCs into a SIW suggests a possible solution for our problem, in turn, it raises a counterargument against the initial assumption that the surrounding of an NRUC should stretch out to infinity at each side. In other words, embedding NRUCs within a SIW imposes new boundary conditions on each unit cell due to the closeness to other unit cells or SIW walls, which may question the intuitive explanation given so far. To scrutinize this argument, a mathematical model for the NRUCs-loaded SIW must be derived and analyzed to practice our proposed theory accurately.

### 5.5.2 Mathematical Model for Multi-ferrite Loaded SIW

In the following, we will assess the methodology to solve the problem for a general case, where $N$ NRUCs are placed within the SIW at an arbitrary distance $C$ from each other and the SIW walls. In this paper, this configuration is referred to as a kernel. Full-wave Maxwell equations can be adopted to solve the problem either numerically or analytically. We will show that in a multimode ferrite-loaded SIW, having a width abiding by (5.3), for the value $C$ that reaches one-quarter of SIW width, the structure's propagation constant approaches the vicinity of the propagation constant of a single NRUC. This reveals that waves are partitioned into semi-decoupled segments, each of

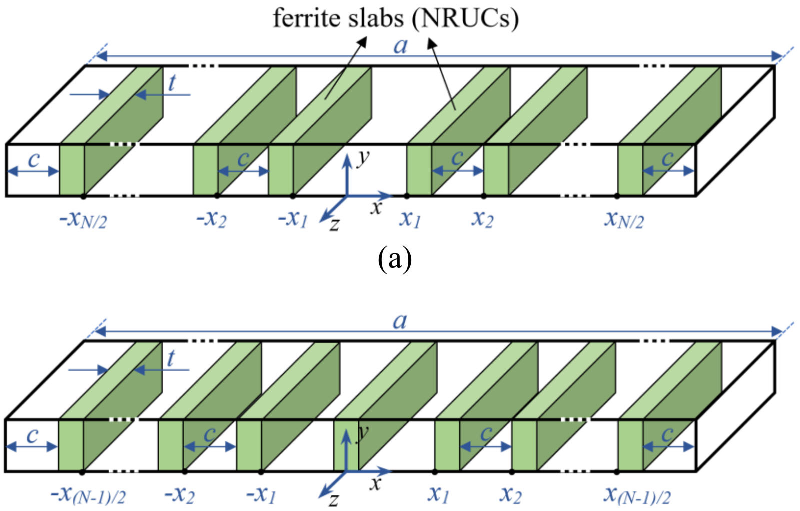

(a)

(b)

Figure 5.6 General topology of multi-ferrite slab loaded SIW for: (a) even and (b) odd number of ferrite slabs

which propagates effectively along with ferrite interfaces, which validates the theory presented in this section.

Consider the general configuration in Figure 5.6(a) and (b), which illustrate the cross-section of a SIW loaded with NRUCs for an even and an odd number of ferrites, respectively. For the even number of ferrite slabs supporting $N$ modes within the SIW, by fixing the origin of the coordinate system at the center of SIW and by factoring the $e^{-j\beta_n z}$ expression, the electric fields can be expressed as:

$$E_y^n = \begin{cases} A_N^n \sin(k_d^n(a/2 - x)) & x_{N/2} + t < x < a/2 \\ A_{N-1}^n \sin(k_f^n(x_{N/2} + t - x)) + B_{N-1}^n \sin(k_f^n(x - x_{N/2})) & x_{N/2} < x < x_{N/2} + t \\ A_{N-2}^n \sin(k_d^n(x_{N/2} - x)) + B_{N-2}^n \sin(k_d^n(x - x_{N/2-1} - t)) & x_{N/2-1} + t < x < x_{N/2} \\ \vdots & \\ A_0^n \sin(k_d^n(x_1 - x)) + B_0^n \sin(k_d^n(x + x_1)) & -x_1 < x < x_1 \\ \vdots & \\ A_{-N+2}^n \sin(k_d^n(x_{N/2-1} + t + x)) + B_{-N+2}^n \sin(k_d^n(x + x_{N/2})) & -x_{N/2} < x < -x_{N/2-1} - t \\ A_{-N+1}^n \sin(k_f^n(x_{N/2} + x)) + B_{-N+1}^n \sin(k_f^n(x + x_{N/2} + t)) & -x_{N/2} - t < x < -x_{N/2} \\ A_{-N}^n \sin(k_d^n(a/2 + x)) & -a/2 < x < -x_{N/2} - t \end{cases} \tag{6.14}$$

where superscript *n* refers to the mode number, and subscripts refer to the corresponding position number of NRUCs within the SIW. Also, $A_m^n$ and $B_m^n$ ($m$=-$N$: $N$) are coefficients of fields in each area. Furthermore, $k_d{}^n$ and $k_f{}^n$ are cut-off wavenumbers of the *n*th mode for both dielectric and ferrite mediums, respectively. These are determined from (5.8) and (5.9) with a slight modification whereby $\beta$ in those relations is replaced by $\beta^n$. The fields in (5.14) are written so that the enforcement of the boundary condition yields easier equations. To reduce the number of unknown parameters, the position of each ferrite slab can be written as a function of two variables of *a* and *C*, where *a* is the SIW width and *C* is the distance of each NRUCs and the SIW walls, as shown in Figure 5.6:

$$\begin{aligned} &x_{m-1} = x_m - C - t, \quad 1 < m < N/2 \\ &x_{N/2} = a/2 - C - t \end{aligned} \tag{6.15}$$

The corresponding magnetic fields in the ferrite region can be found from the following equations:

$$H_x = \frac{1}{\omega\mu\mu_e}(-\mu\beta E_y - \kappa\frac{\partial E_y}{\partial x}) \tag{6.16}$$

$$H_z = \frac{j}{\omega\mu\mu_e}(\kappa\beta E_y + \mu\frac{\partial E_y}{\partial x}) \tag{6.17}$$

in which $\kappa$ and $\mu$ are elements of the permeability tensor for a ferrite biased in the *y*-direction. For the dielectric region, magnetic fields can also be derived from (5.16) and (5.17) by setting $\kappa$=0 and $\mu_e$=1. If the direction of the magnetic bias for any ferrite slab is swapped, the effect can be modeled by changing the sign of $\kappa$ in (5.16) and (5.17) for the corresponding ferrite.

Enforcing the boundary conditions for equations (5.14) and (5.17) will yield a matrix equation whose determinant must vanish. A characteristic equation is derived whose roots generate the propagation constants by fixing the determinant to zero. Similarly, with a slight modification, for the odd number of ferrite slabs, equations can be expressed as:

$$E_y^n=\begin{cases} A_N^n \sin(k_d^n(a/2\text{-}x)) & x_{(N-1)/2}+t<x<a/2 \\ A_{N-1}^n \sin(k_f^n(x_{N/2}+t\text{-}x))+B_{N-1}^n \sin(k_f^n(x-x_{N/2})) & x_{(N-1)/2}<x<x_{(N-1)/2}+t \\ A_{N-2}^n \sin(k_d^n(x_{N/2}\text{-}x))+B_{N-2}^n \sin(k_d^n(x-x_{N/2-1}-t)) & x_{(N-1)/2-1}+t<x<x_{(N-1)/2} \\ \vdots & \\ A_0^n \sin(k_f^n(x-t/2))+B_0^n \sin(k_f^n(x+t/2)) & \text{-}t/2<x<t/2 \\ \vdots & \\ A_{-N+2}^n \sin(k_d^n(x_{N/2-1}+t+x))+B_{-N+2}^n \sin(k_d^n(x+x_{N/2})) & \text{-}x_{(N-1)/2}<x<\text{-}x_{(N-1)/2-1}\text{-}t \\ A_{-N+1}^n \sin(k_f^n(x_{N/2}+x))+B_{-N+1}^n \sin(k_f^n(x+x_{N/2}+t)) & \text{-}x_{(N-1)/2}\text{-}t<x<\text{-}x_{(N-1)/2} \\ A_{-N}^n \sin(k_d^n(a/2+x)) & \text{-}a/2<x<\text{-}x_{(N-1)/2}\text{-}t \end{cases} \tag{6.18}$$

the main difference in (5.18) is that at the center of the SIW there exists a ferrite region rather than dielectric region. However, the rest of the procedure to solve the problem remains identical to the case with the even number of ferrite slabs. In the following sub-sections, we will solve and analyze the problem for three different cases to validate the presented theory.

### 5.5.3 Dual-mode Twin-ferrite-loaded SIW Kernel with Ferrites Magnetically Biased in the Same Direction

The S-parameters of a twin-ferrite loaded SIW with ferrites biased in the same direction are reciprocal, even though each ferrite unit cell propagates the wave nonreciprocally. Here, we will solve the boundary condition problem for this structure to find the propagation constants and analyze the device's behavior.

From (5.3), let us consider a SIW with the width a=47.5 mm and a dielectric constant of 2.94. Applying the boundary conditions to (5.14) and (5.17) for *N=2*, the structure is solved for different *C* values. The E-field pattern over the device's cross-section is plotted at three different ferrite locations for two dominant modes in Figure 5.7. Scrutinizing this figure reveals some exciting features. First, the fields in both modes are not symmetrical, which is due to the structure itself not being symmetrical, as all ferrite slabs are biased in the same direction. Second, both modes have their maxima at each ferrite slab's left interface, which are in-phase and out-of-phase for the first and second modes, respectively. Third, it is discerned that for small or large *C* values, the first and second modes propagate dominantly along different ferrite slabs. This occurs as equation (5.9) results in very different $k_d$ for each mode, which is decisive in shaping the field profile. However, for the intermediate values around $C=a/4$, both modes propagate on both ferrite slabs; the amplitudes of the maxima approach each other, and the order of asymmetry decreases. This indicates that $k_d$ (or $\beta$) of the modes converge toward each other. An important consideration is that both modes exist simultaneously within the structure and, depending on excitation type, a linear combination of these two modes will propagate. If the structure is excited with SIW modes, since the $TE_{10}$ and $TE_{20}$ waveguide modes are symmetrically in-phase and out-of-phase, the resulting combination of excited modes within the structure will be semi-common and semi-differential modes, especially for intermediate values of $C$. However, this structure would produce some order of mode conversion due to its asymmetrical nature.

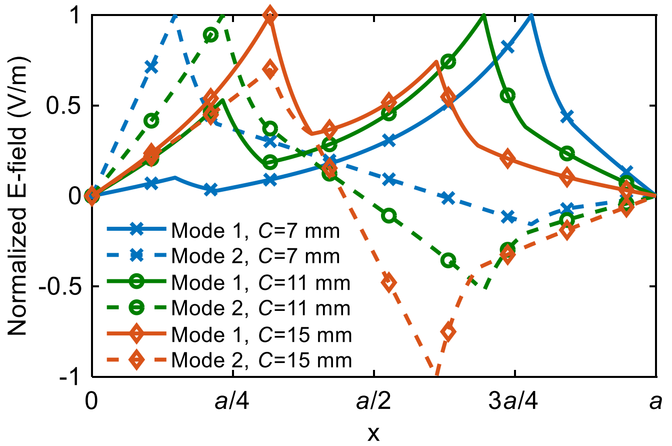

Figure 5.7 Electric field plot for first two dominant modes at the cross section of a twin-ferrite loaded SIW with ferrites biased in the same direction

To further analyze the structure, the first two dominant propagation constants are provided versus the position of ferrite slab $C$, as shown by solid lines in Figure 5.8(a), where design parameters are $t$=3.5 mm, $H_{dc}$=1100 Oe, $f_0$= 5 GHz, $a$=47.5 mm and $a$=63.34 mm for dual-mode and triple-mode configurations, respectively. In this figure and similar figures in the following sections, higher-order modes are excluded to avoid confusion, as these modes exist for small values $C$ and disappear for intermediate values. This figure suggests that both modes converge toward the propagation constant of a single NRUC, shown in Figure 5.2(c) for $t$=3.5 mm, though at different paces. According to Figure 5.7, for small $C$ values, the first mode dominantly propagates along the ferrite's left interface at the right side and, therefore, is loosely disturbed by the SIW wall boundary condition. Hence, the ferrite quickly adopts the behavior of an NRUC as it moves slightly away from the SIW wall. On the other hand, since the second mode dominantly propagates along the ferrite at the left side, it is significantly disturbed by the SIW wall boundary condition. Hence, it slowly adopts the behavior of an NRUC.

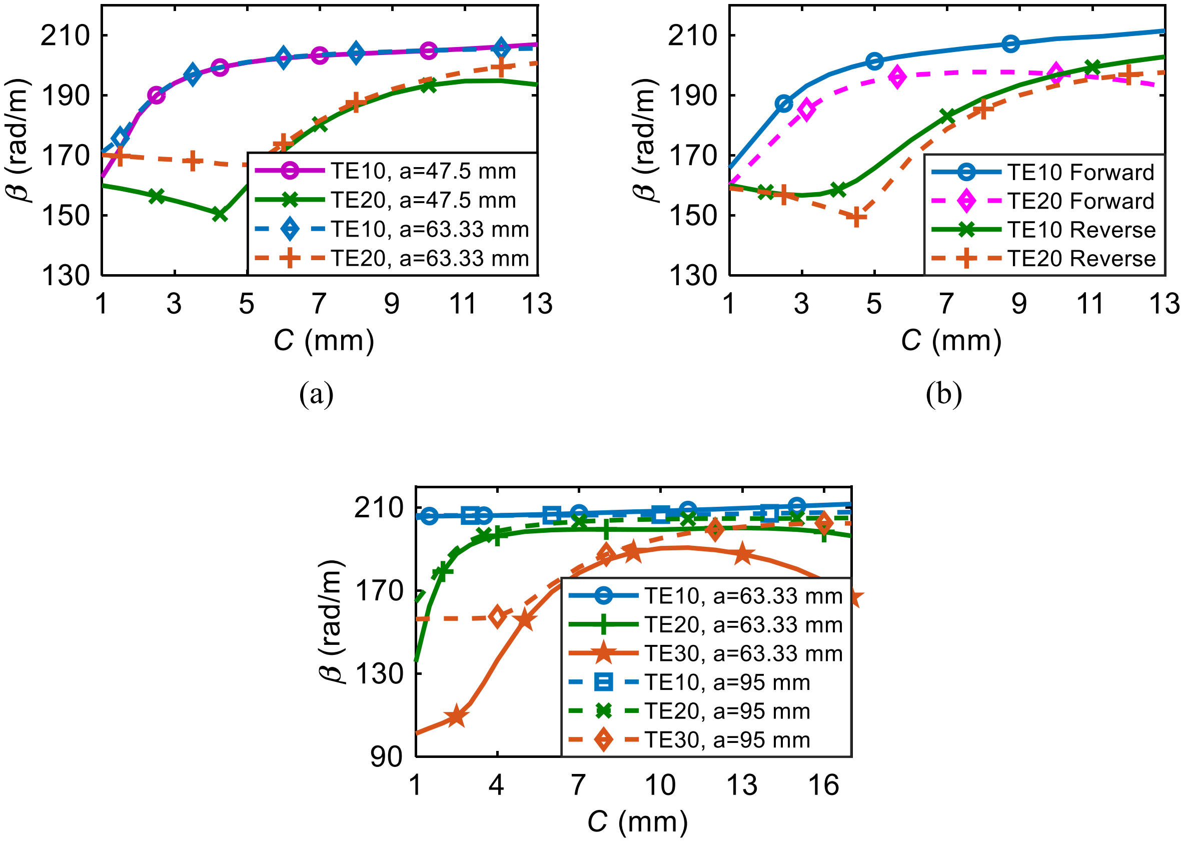

(a) (b)

(c)

Figure 5.8 Propagation constants ($\beta^n$) within a multi-mode ferrite loaded SIW, as a function of slab position *C* for: (a) dual-mode twin-ferrite loaded SIW with the same direction biasing, (b) dual-mode twin-ferrite loaded SIW with anti-symmetrical biasing and (c) triple-mode triple-ferrite loaded SIW with the same direction biasing

Moreover, it is discerned that the second mode starts to decrease again after reaching a peak for large *C* values. This happens since the ferrite starts approaching the other ferrite slab as *C* increases beyond one-quarter of the waveguide width. Thus, the second mode reaches its peak, where ferrites are at a maximum distance from other boundaries on both sides. To attest to the latter remarks, the

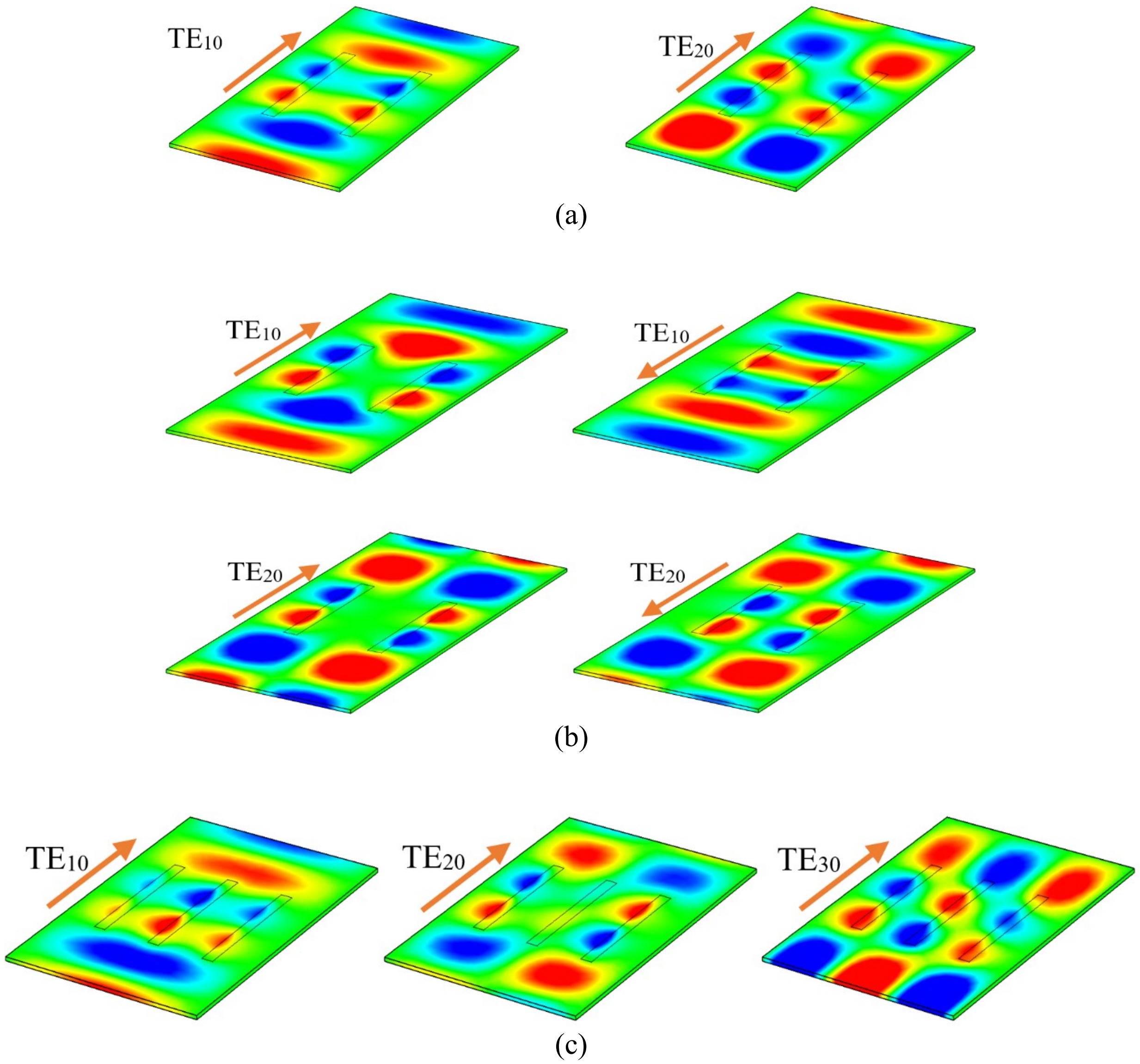

Figure 5.9 Simulated E-field pattern in CST for a multi-ferrite loaded SIW: (a) dual-mode twin-ferrite loaded SIW with the same direction biasing, (b) dual-mode twin-ferrite loaded SIW with anti-symmetrical biasing and (c) triple-mode triple-ferrite loaded SIW with the same direction biasing

first two dominant propagation constants for an oversized SIW loaded with two ferrite slabs are plotted using dashed lines in Figure 5.8(a) to provide a larger margin for each ferrite slab. Such an oversized SIW supports undesired higher-order modes and is not useful; however, its behavior reveals valuable insight into our proposed theory. It is perceived that the two dominant modes of the oversized SIW follow the same behavior of the original SIW, though the second mode continues to approach the propagation constant of the NRUC without dropping until all converge toward one single value.

Finally, the structure excited by two SIW modes is simulated in CST and illustrated in Figure 5.9(a) for *C*=11 mm. Since the structure is reciprocal, only fields in the forward direction are shown, where fields in the reverse direction will swap to the opposite interface of ferrites. These figures clearly show that the fields are concentrated along NRUCS, while the field polarization in each ferrite slab depends on the excitation type.

### 5.5.4 Dual-mode Anti-symmetrically Biased Twin-ferrite Loaded SIW Kernel

This section investigates a similar problem to the previous section but, contrastingly, with the ferrite on the right side being biased in the negative y-direction. An anti-symmetrically biased twin-ferrite-loaded SIW is nonreciprocal and can find applications in designing gyrators, isolators, and circulators. In contrast to the previous structure, this structure is symmetrical. Like in the previous section, (5.14) and (5.17) are adopted to solve the boundary condition problem, except that in (5.17), $\kappa$ takes a negative sign to represent the ferrite with the opposite biasing. This structure was modeled and discussed in detail with field pattern illustrations in [117] for the first mode. Accordingly, this structure creates two distinct channels for the forward and reverse directed waves. The forward-directed wave is divided into two segments that propagate at the sides of the SIW in between the ferrite slabs and SIW walls. Contrarily, the reverse directed wave propagates in the central channel and between two ferrite slabs. Such behavior is also predictable from the theory of parallel NRUCs for this structure.

Here, the problem is solved for two modes and the propagation constants in both forward and reverse directions, plotted in Figure 5.8(b). Both modes in the reverse direction approach their saturation fast, while in the forward direction, both modes take a slow trend to reach the peak due to similar reasoning provided in the previous section. The critical observation here is that the propagation constants of all four waves approach the propagation constant of a single NRUC, thus endorsing the proposed theory of multimode parallel NRUCs. Furthermore, the E-field patterns for both modes and directions are depicted in Figure 5.9(b), which explicitly indicates that both distinct modes propagate along the NRUCs. Also, due to the device's symmetry, it is noticed that field distribution between ferrite slabs is utterly symmetrical for both modes and is unlike the previous structure, which held some degree of asymmetry.

### 5.5.5 Triple-mode Triple-ferrite Loaded SIW Kernel Magnetically Biased in the Same Direction

Let us consider a triple-mode SIW loaded with three ferrite slabs, all biased in the positive y-direction, where one ferrite slab is placed in the middle of the SIW, and the other two are positioned symmetrically at arbitrary positions of *C* from the SIW walls. The width of the SIW is determined using (5.3) as *a*=63.33 mm for the dielectric constant of 2.94 to support the first three SIW dominant modes. In this problem, (5.17) and (5.18) are adopted to derive the field equations. By solving the boundary condition, the E-field pattern for two different *C* values is graphed in Figure 5.10. This scenario is similar to the twin-ferrite loaded topology, where ferrites are biased in the same direction and where, for small values of *C*, each mode prevalently propagates along one of the ferrites. However, as *C* increases and the ferrite slabs move further away from the SIW walls, the field's amplitude and phase distributions along the three ferrite slabs become similar to the first three waveguide modes. Nevertheless, these modes are slightly different from the waveguide modes and are not symmetrical since their structures are asymmetrical. Consequently, a linear combination of these three modes will propagate within the structure if excited by known waveguide modes. The device is simulated in CST Microwave Studio, and the E-field patterns for the waveguide excitation are depicted in Figure 5.9(c) for an optimum value of *C*=12mm.

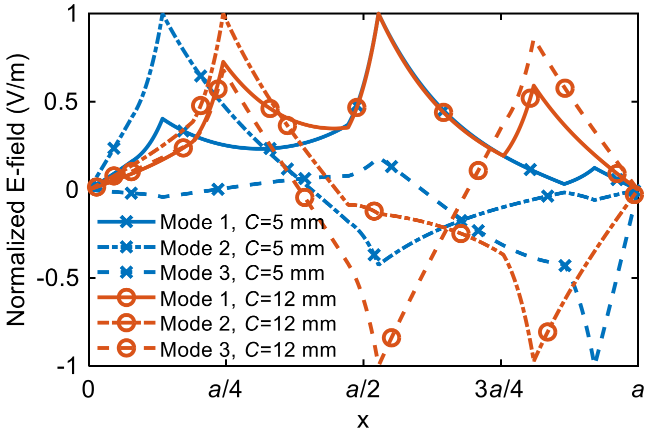

Figure 5.10 Electric field plot for first three dominant modes at cross section of a triple-ferrite loaded SIW with the same direction biasing

The propagation constants of three propagating modes in the triple-ferrite loaded SIW are represented by solid lines in Figure 5.8(c). Similar to the argument raised for the symmetrically biased twin-ferrite loaded SIW, it is discerned that the first two modes rapidly saturate while the third mode slowly reaches its peak. Similarly, the third mode's propagation constant begins to drop after reaching its peak since the side ferrite slabs are closer to the middle ferrite. Moreover, the modes for an oversized SIW are calculated and plotted in dashed lines, which clearly indicates that the propagation constants for all modes approach and converge to the propagation constant of a single NRUC. Hence, the behavior of a multi-ferrite loaded SIW closely follows and mimics the NRUC when the ferrite slabs are positioned sufficiently far from each other.

All the observations from Figure 5.8 and Figure 5.9 validate the proposed theory, which says that if the ferrite slabs are placed far from each other and the SIW walls, the ferrite loaded SIW structure is transformed into a system of parallel NRUCs, and its behavior can be analyzed based on the unit cell with fair accuracy. Therefore, the theory of parallel NRUCs can be adopted to anticipate and develop a kernel multimode ferrite-loaded SIW that can be exploited to design specific ferrite components.

## 5.6 Concurrent Dual-Mode Circulator

This section will exploit the proposed dual-mode kernels to design a dual-mode nonreciprocal SIW by adding an additional port to construct a dual-mode circulator. Although either symmetrically or anti-symmetrically biased twin-ferrite loaded SIW kernel configurations can be used to design the circulator, we adopt the latter due to its symmetrical property. Not only does it facilitate the design, but it also allows for maximum isolation between two modes. Furthermore, in this work, we wish to design the dual-mode circulator in a single layer that is only possible with the second configuration.

### 5.6.1 Circulator Design

In the proposed configuration of a dual-mode ferrite-loaded SIW, the ferrite position is initially determined using Figure 5.8(b) to yield the maximum propagation constant for all modes, where the device performs like parallel NRUCs. According to Figure 5.9(b), this will result in a "nonreciprocally dual-channelized waveguide (NDW)" [117]. The creation of two distinct and separate channels for the forward and reverse propagating waves within an NDW, and the addition of a third dual-mode port on its sides, provide a solution for devising a circulator. The addition of the side ports creates a nonreciprocal junction at each side of the SIW, where the theory of junction circulators may be adopted to design the junction. Here, however, as the SIW is already designed and the nonreciprocal wave concentration on the sides of the ferrite favors the creation of the circulator, the design process is relatively more straightforward. The key point is to create a resonance and standing wave mechanism in the junction to yield a nonreciprocal circulation of waves among the three ports. The nonreciprocal resonator can be manipulated to create a magnetic field null situated in front of one of the ports depending on the excitation port. For example, if port one is excited, the magnetic null resulted from the resonance must be placed in front of port 2 to transmit the whole wave into port 3. The schematic of the proposed dual-mode three-port circulator is shown in Figure 5.11(a), where dimensions are (in mm): *Length* = 100, *Lf* = 15, *W* = 20, $W_g1$=7.25, $W_{g2}$=14.58, $W_{s1}$=2, $W_{s2}$=0.64, $L_g$=14.65, $W_m$=1.95, $D_{ring}$=12.73.

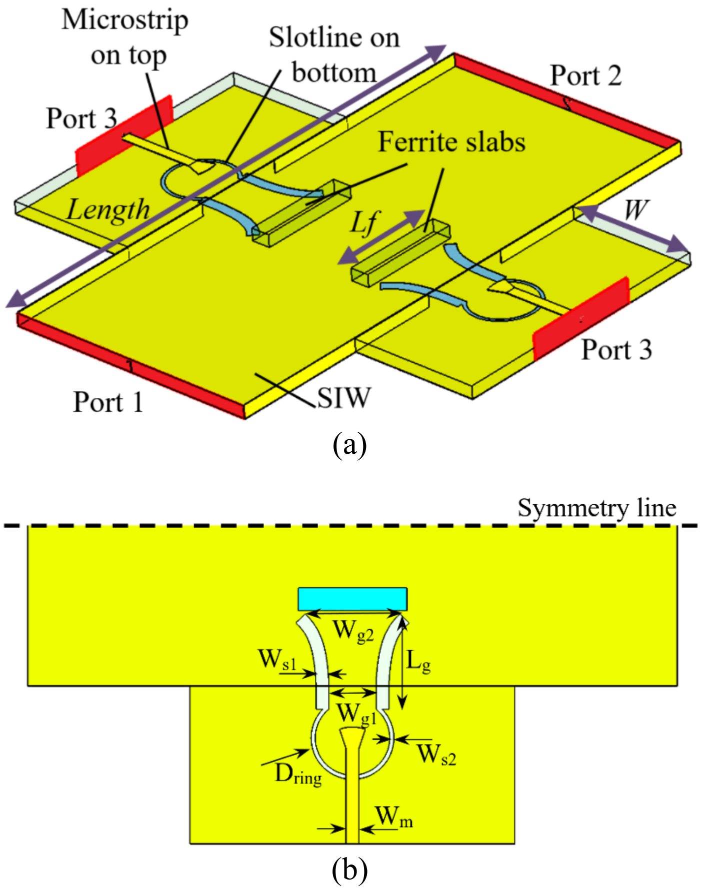

(a)

(b)

Figure 5.11 Schematic of proposed dual-mode circulator: (a) perspective view, and (b) top view

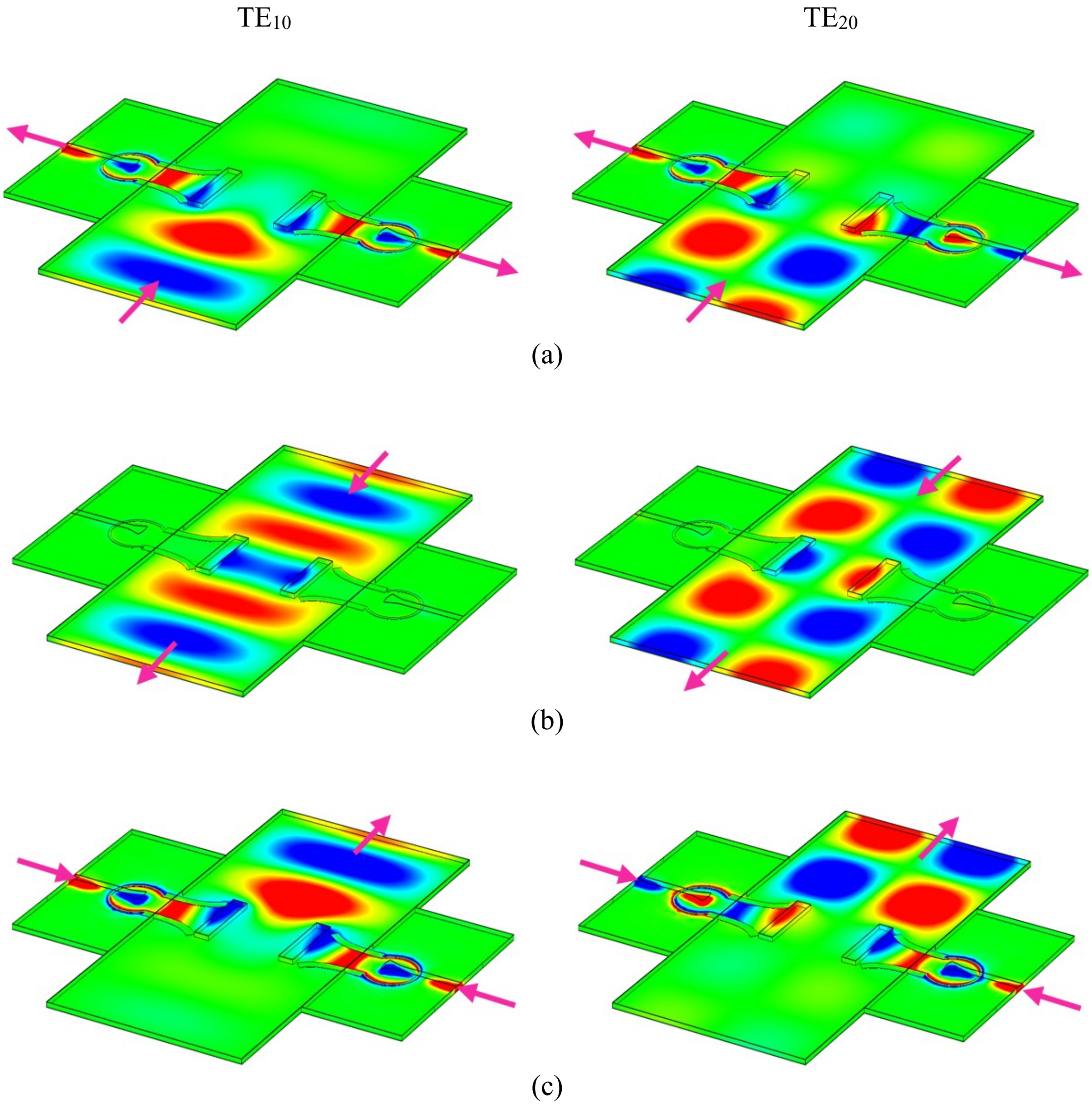

(a)

(b)

(c)

Figure 5.12 Simulation of E-field patterns and wave circulations in the proposed dual-mode circulator. Dual-mode excitation at (a) port 1, (b) port 2, (c) port3. Left and right pictures illustrate $TE_{10}$ and $TE_{20}$ mode of operation, respectively.

In this configuration, the side planar ports together create one dual-input and dual-mode port, where their in-phase and out-phase excitation excites the $TE_{10}$ and $TE_{20}$ modes within the SIW, respectively. Each side port involves a transition from the CPW-to-slotline-to-microstrip line. The

CPW section is a grounded CPW where gaps are etched at the bottom of the SIW. The CPW section is a nonreciprocal junction, which transfers the incoming and accumulated fields incident from the SIW toward the planar port or vice versa. The ungrounded slotline creates the loop resonance necessary for circulation by creating a ring between ports. Furthermore, the slot line consists of two sections of wide and narrow slots for impedance matching purposes. Finally, the microstrip port transfers the power into or out of the resonance junction. The length and impedance of each transition must be tuned to achieve good impedance matching and phase matching for the creation of the magnetic field null. In this design, we utilized CST Microwave Studio to optimize the design. The optimized dimensions are given in Figure 5.11(b). It should be noted that other topologies and configurations could also be explored to create the resonance junction, and it is not limited to this showcase study.

The simulated electric field is shown in Figure 5.12, where the wave propagation is depicted for each port excitation and for both $TE_{10}$ and $TE_{20}$ modes. These figures demonstrate the successful operation of the proposed concurrent dual-mode circulator.

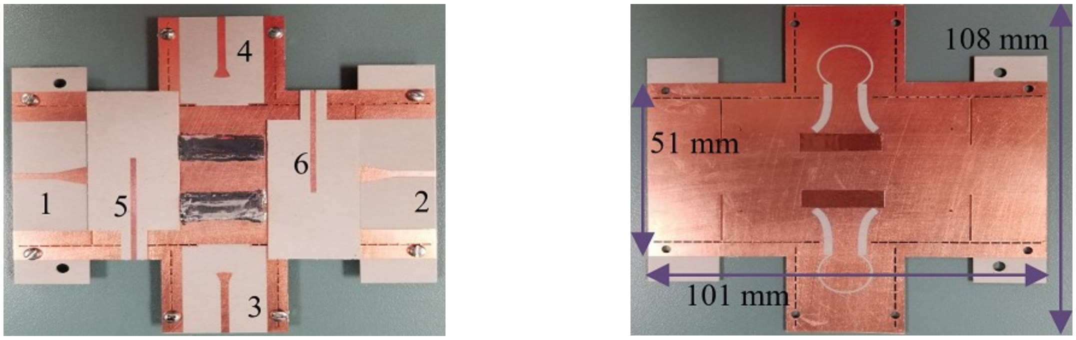

(a) (b)

Figure 5.13 Fabricated prototype of the proposed dual-mode circulator with 6 ports (each mode of operation 3 ports), (a) top view and (b) bottom view

### 5.6.2 Measurement and Fabrication Results

For the fabrication of the proposed dual-mode circulator, a Rogers 6002 substrate was used. Ferrite pieces were purchased from TCI Ceramics with a dielectric constant of ($\mathcal{E}_f$) 13.9, saturation magnetization ($M_s$) of 800 G, and linewidth ($\Delta H$) of 30 Oe. For the concurrent and dual-mode excitation of the SIW ports, the proposed configuration in [117] was the inspiration, where a two-layer configuration is deployed to minimize the cross-coupling between the modes. The picture of the fabricated prototype is provided in Figure 5.13. The soldered areas are ferrite pieces embedded within the SIW and covered with a copper taper before soldering. Additional layers at the two sides for the excitation of the $TE_{20}$ mode were glued to the first substrate using epoxy at high temperatures and pressure. The magnetic bias field was provided with an electromagnet tuned for the circuit's best possible performance. In this picture, ports 3 and 4 together form dual-input port 3 in Figure 5.11. The *S*-parameters were measured using a Keysight vector network analyzer (VNA), plotted in Figure 5.14. Displaying the *S*-parameters for all six ports would be long and

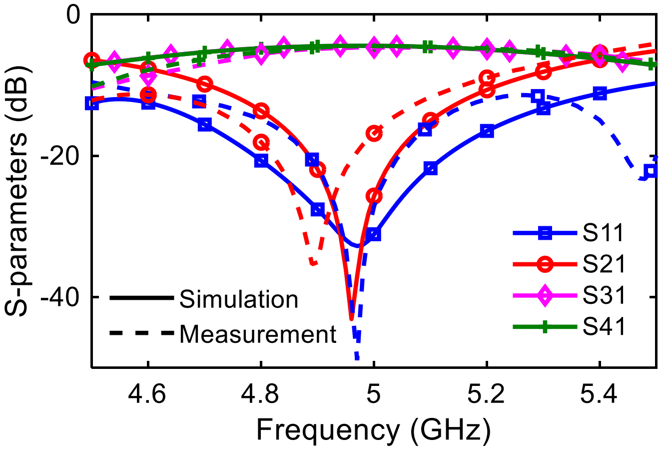

(a)

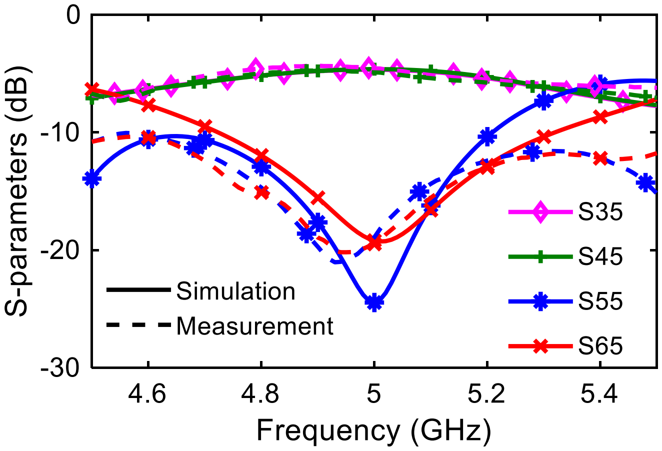

(b)

Figure 5.14 Measurement and simulation results for port 1 excitation at (a) 1st and (b) 2nd mode unnecessary; therefore, for easier illustration, the measurement results of only two orthogonal ports are shown and compared to simulation results obtained by CST.

The proposed device has a bandwidth of 400 MHz. The insertion loss is better than 1.5 and 1.6 dB for $TE_{10}$ and $TE_{20}$ modes, respectively, including the transitions and connector loss. Since ports 3 and 4 are considered together as a single dual-input port, it should be noted that the insertion loss of these curves must be added together to yield the actual insertion loss. Furthermore, the port isolation is better than 25 and 19 dB for $TE_{10}$ and $TE_{20}$ modes, respectively. In general, measurements are in excellent agreement with simulations, demonstrating the proposed concurrent dual-mode circulator and the developed principal theory of multimode ferrite devices.

## 5.7 Concurrent Triple Mode Nonreciprocal 180o Phase Shifter/Gyrator

This section will exploit the discussed triple-mode ferrite-loaded SIW of Section IV to devise a concurrent triple-mode gyrator. A triple-mode gyrator can exhibit a nonreciprocal 180-degree phase shift concurrently for the first three dominant modes within a SIW. This is the first time that a multimode gyrator is introduced and demonstrated. A multimode gyrator can find applications in a radar array antenna, or it can be utilized as three separate gyrators in a compact and economic package.

### 5.7.1 Gyrator Design

The initial design procedure benefits from the proposed triple-mode ferrite-loaded SIW. As previously mentioned, the *S*-parameter response for a triple ferrite-loaded SIW with ferrites biased in the same direction is reciprocal. However, since the gyrator is nonreciprocal, the nonreciprocal field inclination in the structure is exploited to achieve the nonreciprocal response. Hence, we introduce longitudinal slots on the top and bottom of the SIW at proper distances from the ferrites to separate each ferrite slab's forward and reverse propagation channels. Then, using the conductor swapping technique [120], the upper and lower conductors of the SIW are swapped only for the forward channels. This methodology offers a wideband solution, although the device's bandwidth is limited due to ferrite performances. The proposed gyrator's schematic is depicted in Figure 5.15. Due to ferrite's presence, this structure is not symmetrical, and therefore mode conversion may occur. In the proposed gyrator, the mode conversion effect may become pronounced. In turn, to counter-react to this undesired effect, ferrite slabs' position and the width of channels are slightly tuned asymmetrically and optimized in CST simulation software. The structure's exact dimensions are provided in Figure 5.15(b), where design parameters are: Lvia=11.8, Wvia=20.25, a=63.37, Lf =23.55, Lswap=5, Wslot=0.4, C1=14.3, C2=11.9, C3=16.2, W1=W2=W3=4.8, W4=5.4, W5=W6=W7=W9=W10=W11= 2.3 and W8=10. It is noted that all dimensions are in mm. Furthermore, two via holes are implemented to match the gyrator to the unloaded SIW sections.

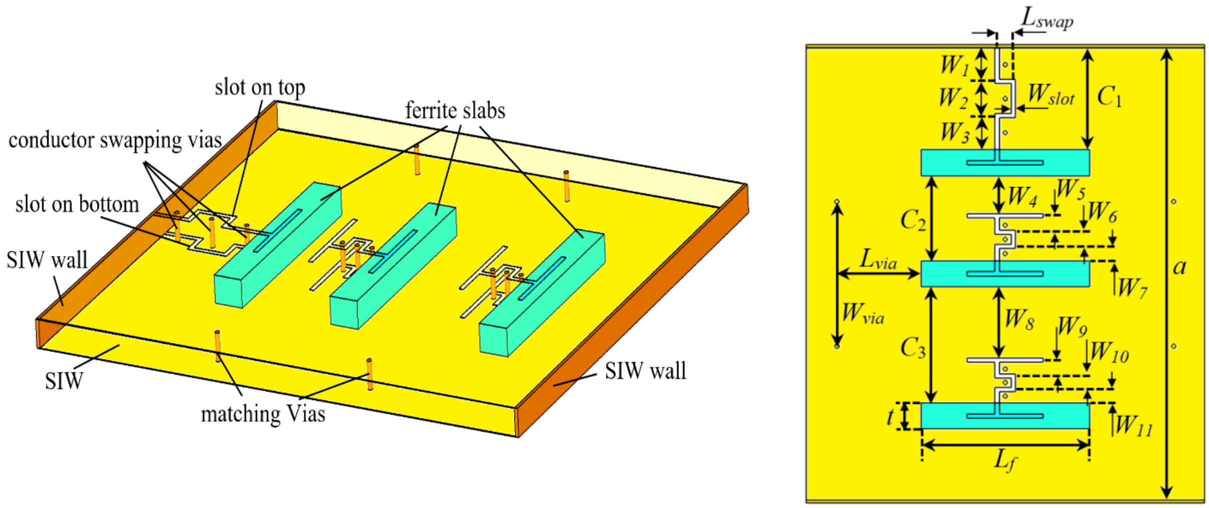

(a) (b)

Figure 5.15 Schematic of the proposed triple-mode gyrator: (a) perspective view with exaggerated substrate thickness, (b) top view

The field illustration of the triple-mode gyrator is described in Figure 5.16, thereby revealing the device's operation mechanism. This figure indicates that separate and distinct channels are devised within the structure, where the wave passes from the channels at each ferrite's left interface in the forward direction, while in the reverse direction, the wave passes through channels at each ferrite's right interface. The conductor swapping technique reverses the wave's polarization in the forward direction, resulting in a 180° phase shift. In Figure 5.16, the nonreciprocal 180° phase shift is distinguishable by comparing the phase of entering and exiting waves between the forward and reverse propagations for all three modes.

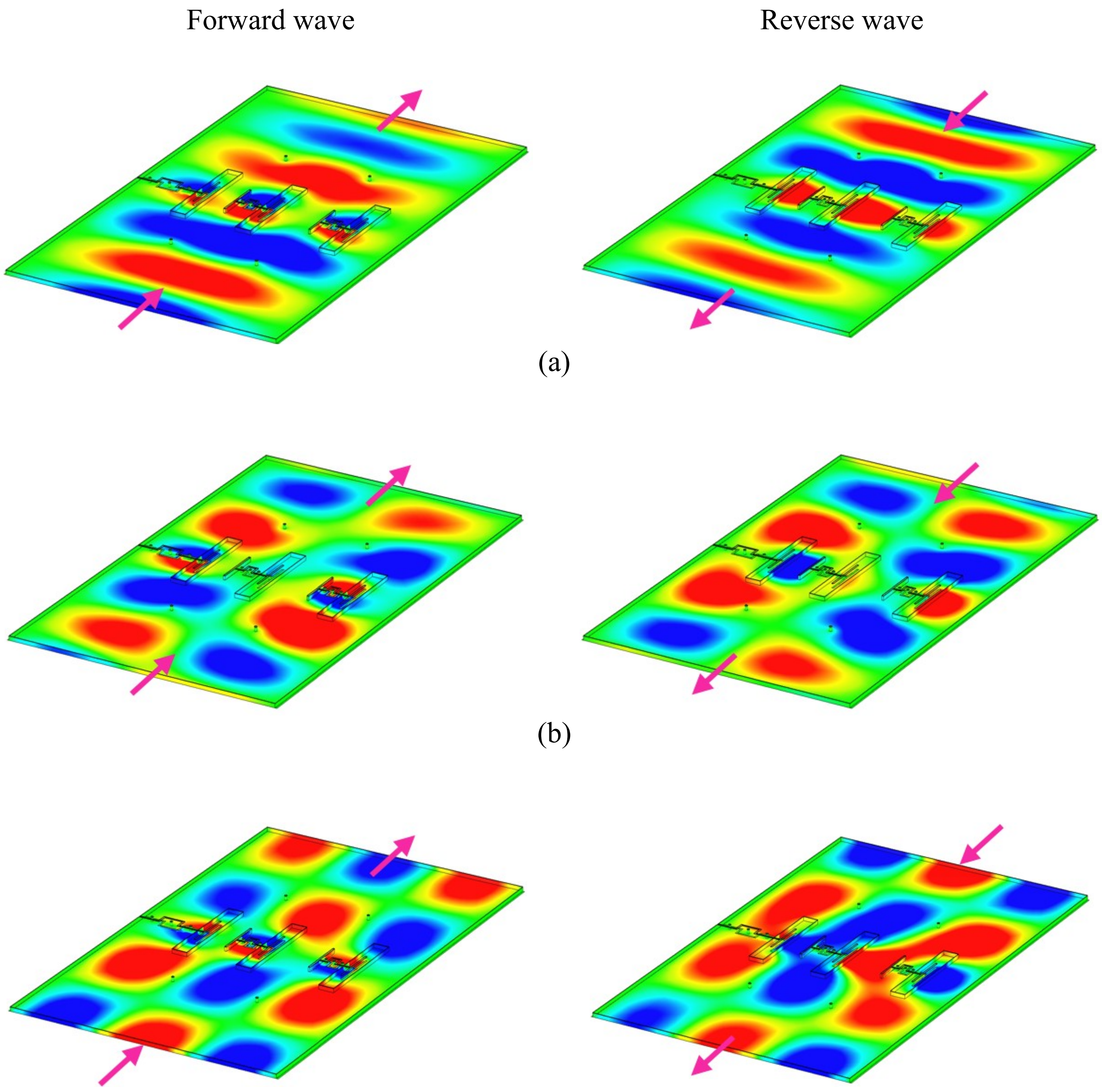

(a)

(b)

(c)

Figure 5.16 Simulation of E-field patterns in the proposed triple-mode gyrator: (a) $TE_{10}$, (b) $TE_{20}$, and (c) $TE_{30}$ modes

### 5.7.2 Fabrication and Measurement Results

A Rogers 6002 substrate and the same ferrite for the fabrication of the circulator in the previous section are adopted in this fabrication process. The fabrication challenge lies in embedding ferrite pieces within the SIW while slots must be etched on ferrites' top and bottom. We had to use extra layers on the top and bottom of the main SIW substrate to accomplish this. Therefore, the top and bottom coppers layouts were masked on separate substrates and glued to the top and bottom of the main SIW substrate after first embedding the ferrite slabs. Finally, via holes were laser cut through three layers, followed by the metallization process. The extra top and bottom substrates only provide the conductors; their dielectric does not contribute to the gyrator's performance. Therefore, those substrates were chosen to be as thin as possible for better metallization and to avoid the need for a larger external magnetic bias in return for any extra thickness. The photo of the fabricated device is shown in Figure 5.17.

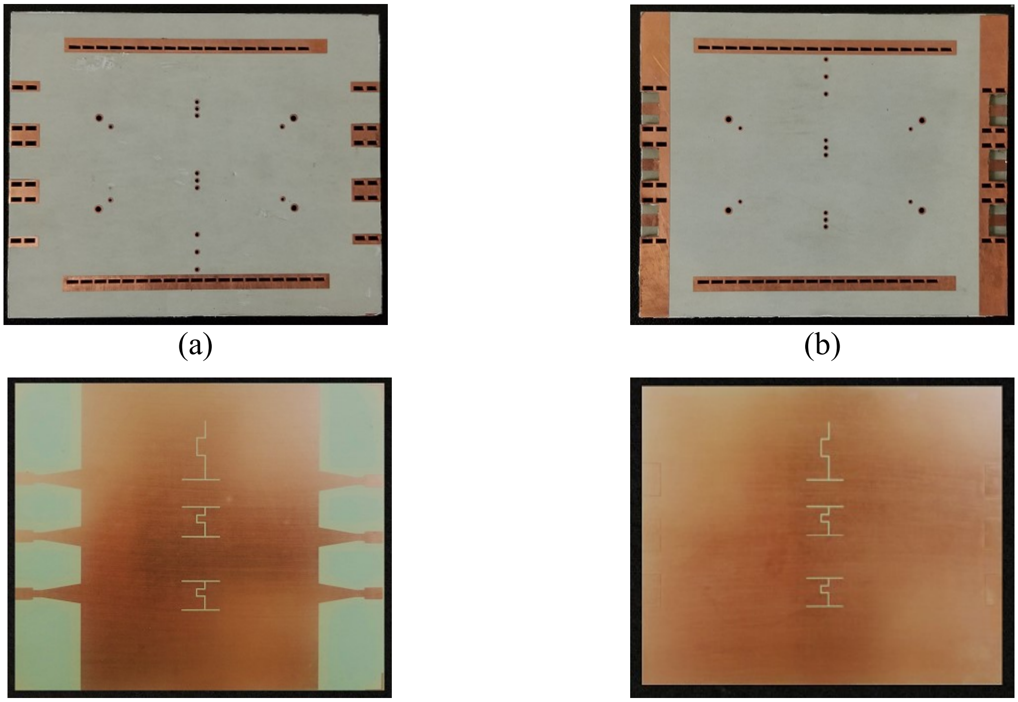
(a) (b)
(c) (d)

Figure 5.17 Fabricated prototype of the proposed triple-mode gyrator with 6 single-end ports: (a) bottom, (b) top view of gyrator, (c) bottom view of top layer, and (d) top view of bottom layer

For measurement purposes, concurrent triple-mode SIW-to-microstrip transitions must be implemented. However, designing and implementing such a transition is novel work requiring extensive discussions, which are avoided here to focus on nonreciprocal devices. Instead, three

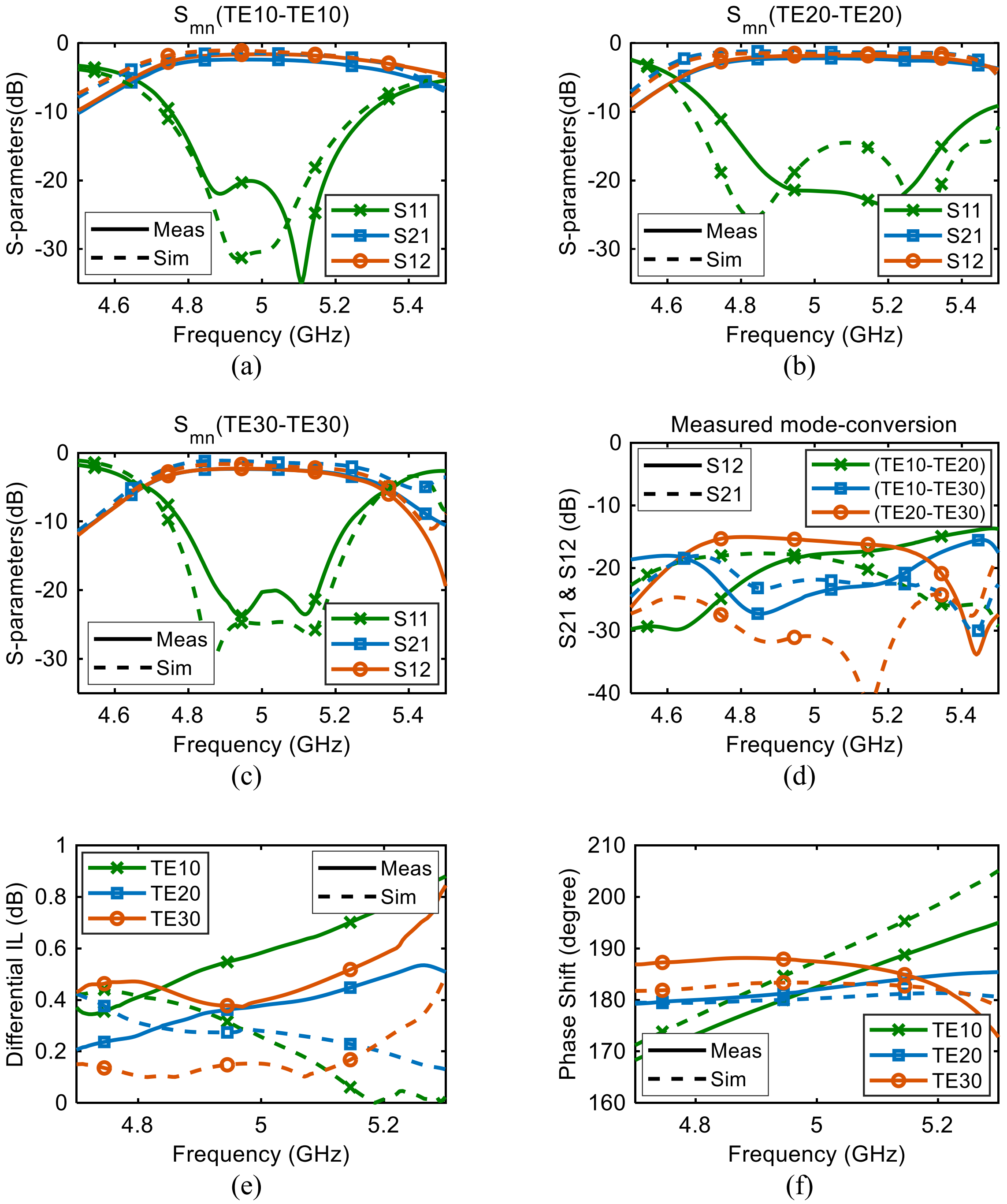

(a) (b) (c) (d) (e) (f)

Figure 5.18 Measured and simulated results of the triple-mode Gyrator with microstrip transitions: (a) TE10 mode, (b) TE20 mode, (c) TE30 mode. (d) measured S-parameter results for mode conversion in both forward and reverse propagation, measured versus simulation results for (e) differential insertion loss and (f) phase shift of forward and reverse directed waves for each mode excitation parallel microstrip-to-SIW transitions are implemented at each port of the SIW. These transitions provide ways to excite all three modes separately based on the theory of Section II, yielding an easy method to measure the performance of the SIW-gyrator itself.

The gyrator is biased using an electromagnet. The 6-port S-parameter measurement of the device was carried out by a Keysight M9019A PXIe Chassis incorporating seven Keysight M9375A two-port Network Analyzer modules providing a total of 14 ports for the simultaneous measurement of the S-parameters. Measurement results are reported in Figure 5.18 and compared to the simulation results from CST. The 6-port single-end S-parameter measurement results contain reflection and transmission information for all the modes, including inter-mode (input and output waveguide modes are the same) and mode-conversion (input and output waveguide modes are different) results. The single-end S-parameter results are transformed into waveguide TEn0 excitation modes using Table. I to portray a better picture of the device's performance. Inter-mode S-parameter results are displayed in Figure 5.18(a)-(c) for the $TE_{10}$, $TE_{20}$, and $TE_{30}$ mode excitations, respectively. These figures indicate that the device has a bandwidth better than 460 MHz, from 4.78 GHz to 5.24 GHz, for all three modes, where the return loss is better than -10 dB. Besides, the measured insertion loss is semi-flat, with a loss better than -2.1 dB for all three modes (considering transitions and connector loss), thus indicating a successful triple-mode implementation. Figure 18(d) plots only the mode conversion measurement results. Simulation results follow the measurement results closely; however, to avoid a messy figure simulation, results were excluded from this plot. It is discerned that the mode conversion in the worst case ($TE_{20}$ to $TE_{30}$) is better than -15 dB for the whole bandwidth, which is sufficient for most applications. The differential inter-mode insertion loss of the forward and reverse directed waves for each mode excitation is depicted in Figure 5.18(e). It shows that the insertion loss in both directions for all modes in the gyrator differs by less than 0.8 dB, which is within the typical range for commercial single-mode phase shifters. Finally, Figure 5.18(f) displays the differential phase shift for each mode of the triple-gyrator. It is observed that the concurrent triple-mode 180° phase shift (gyrator) at the center frequency is realized for the device. In addition, the device has a semi-flat differential phase response suitable for a broad bandwidth operation, thanks to the conductor-swapping technique exploited in this structure. As a final note, it should be mentioned that the simulation and measurement results are in excellent agreement. Some minor discrepancies are caused by fabrication tolerances, connector effects, and magnetic bias differences used in simulation and practice.

## 5.8 Conclusion

In this paper, we have proposed and established a comprehensive approach to investigating and demonstrating multimode reciprocal and/or nonreciprocal ferrite-loaded SIW components for emerging and future microwave systems. A theoretical investigation was first carried out and revealed that the modification of $N$ discrete points is sufficient to manipulate all $N$ propagating modes within a SIW. In relation to the previous theory, an NRUC that could localize power within the ferrite slab interface and nonreciprocally displace the field toward only one interface was proposed. Next, these two properties were exploited to propose a methodology for developing a multimode kernel topology by arranging several NRUCs next to each other within the SIW. Since the incoming wave is broken down into several segments within the kernel topology, where each segment propagates along a different NRUC, the kernel structure can provide a basis for the multimode manipulation of signals. To further explore this discussion, three separate kernels (including dual-mode reciprocal, dual-mode nonreciprocal, and triple-mode reciprocal kernels) were developed, simulated, and assessed in detail to support the corresponding theory and set the groundwork to demonstrate two novel components as application examples. Finally, a dual-mode circulator and a triple-mode gyrator were successfully experimentally demonstrated for the first time.

It must be pointed out that the presented theory is not limited to the two demonstrated application examples of circulator and gyrator components. Multimode isolators or nonreciprocal/reciprocal phase shifter are other applications of the proposed theory, as arbitrary phase and amplitude manipulation is always applicable using various perturbations within each separate channel in the kernel structure. Moreover, multi-purpose ferrite devices can be integrated into the same package as a compact solution. For example, within a dual-mode kernel topology, one mode may be used to design a phase shifter, and the other mode may be exploited to design an isolator, both existing within one single SIW channel. In addition, the proposed multimode kernel topology can find applications in developing multimode nonreciprocal antennas, where transmitting and receiving patterns are different, and each mode contributes to a different pattern. Finally, a nonreciprocal

$TE_{10}$ and $TE_{20}$ SIW mode converter was introduced in our earlier work in [117], which can be categorized as another application of the multimode multi-ferrite loaded SIW devices.

## 5.9 Acknowledgment

The authors would like to thank T. Antonescu, S. Dubé and J. Gauthier of Poly-Grames Research Center, École Polytechnique de Montréal, Montréal, QC, Canada, for their support in the realization of the prototypes.

# CHAPTER 6 ARTICLE 4: DUAL-POLARIZED PATCH ANTENNA EXCITED CONCURRENTLY BY A DUAL-MODE SIW

Amir Afshani, Graduate Student Member, IEEE, and Ke Wu, Fellow, IEEE

This article follows our third our third objective which is realizing a dual-polarized monostatic antenna with dual-mode SIW excitation. This article is submitted to IEEE Transactions on Antennas and Propagation as a Communication paper (March 2021).

## 6.1 Abstract

In this work, we propose and demonstrate an integrated dual linearly polarized cavity-backed patch antenna, which is excited by a concurrent dual-mode substrate integrated waveguide (SIW) structure. For the first time, we have exploited the $TE_{10}$ and $TE_{20}$ modes of a traveling wave in a dual-mode SIW configuration to excite the horizontal and vertical polarizations of the patch antenna. The proposed methodology yields a low-profile structure with a high inter-port isolation thanks to the inherent symmetry of the structure. Measurement results indicate an isolation performing better than 42 dB over a 600-MHz impedance bandwidth of the antenna. Moreover, a methodology is developed to implement transitions from the dual-mode SIW to the two different TEM transmission lines for separate but concurrent excitations of the device. A detailed field and impedance analyses are presented to explain the operation principle of the proposed antenna, which are supported by an excellent agreement between the obtained measurement and simulation results.

*Index Terms*—dual-polarized antenna, full duplex, high isolation, patch antenna, substrate integrated waveguide (SIW), SIW cavity-backed patch antenna, $TE_{10}$ mode, $TE_{20}$ mode.

## 6.2 Introduction

Dual-polarized (DP) antennas are becoming a popular and widespread choice explored in various applications, including radar, MIMO antenna systems and full-duplex transceivers. Among many antenna specifications like impedance bandwidth, efficiency, gain, pattern, etc., the high inter-port isolation in DP antennas has become a critical property, and a challenging task to accomplish. For example, the state-of-the-art weather-measurement radar systems are inclined to deploy a dual-polarized antenna that significantly enhances related polarimetric measurements of interest.

However, high-isolation and low-cross polarization are essential assets that such antennas must possess [121]. On the other hand, the promising potential of yielding a high inter-port isolation in dual-polarized antennas has already inspired many research teams to adopt this technique to enable the development of full-duplex transceivers [26]. Thus, numerous methods have been explored in the literature for realizing a high-isolation dual-polarized antenna; however, only few methodologies seem to be capable of meeting the required specifications in emerging wireless systems, particularly for realizing an integrated antenna of high isolation and relatively large bandwidth.

The substrate integrated waveguide (SIW)-fed dual-polarized antenna is a promising candidate to meet the demanding specifications thanks to its many crucial properties. SIWs are closed and shielded structures that can significantly lower leakage, through-the-air couplings between the ports, and the interference with other parasitic elements which may contribute to the inter-port leakage. Moreover, SIW structures offer a robust, low-loss and simple solution for unfolding a single-antenna unit to an antenna array system, which is a ubiquitous trend in future wireless systems. Finally, SIW techniques feature low-cost, high power, integrability, low profile and simple fabrication properties, which are all attractive and crucial for the next generation of wireless systems [122-124]. Therefore, in this work, we will explore and investigate an SIW-fed dual linearly polarized cavity-backed patch antenna.

The SIW feeding of a singly-polarized patch antenna is well-known for both transversely and longitudinally oriented apertures atop the SIW [125], and other variations of the SIW like ridge gap waveguide (RGW) [126]. For dual-polarized excitation of a single patch antenna, this methodology is simply expanded by using two single-mode SIWs positioned perpendicularly relative to each other, which derive a cross-shaped slot under the patch. The perpendicular SIWs are employed either in a single-layer [127, 128] or two-layer configurations [122-124]. Although the single-layer configurations lead to a simple fabrication, they suffer from low isolation due to a direct coupling between the input ports. On the other hand, the two-layer structure offers a more promising isolation, even though it must be fabricated in a dual-layer configuration, at the very least, or in a multi-layer configuration for improved isolation.

In Section II, for the first time, we propose and investigate a single dual-mode SIW—which carries both $TE_{10}$ and $TE_{20}$ modes simultaneously—to excite a dual-polarized patch antenna. Since the

$TE_{10}$ and $TE_{20}$ modes within the same SIW are orthogonal, the resulted methodology offers a wideband high isolation solution within a compact structure that uses less layers than traditional methods for feeding the patch. Furthermore, since the structure is completely symmetrical, the isolation is theoretically lower than the traditional dual-polarized SIW-fed methods. This structure can be employed effectively in the development of a large array antenna systems for an easier and symmetrical structure. Although in this paper we have focused on the demonstration of a single element antenna, the extension of this topology into the scenario of an antenna array can be exploited straightforwardly. Section III discusses the operation principle of the antenna in detail through both field and impedance analyses. In Section IV, a concurrent transition from dual-mode SIW to TEM ports with a high inter-port isolation is presented. Finally, measurement results are presented and discussed in Section V and are compared to other similar works in the literature.

## 6.3 Proposed Antenna Topology

The schematic of the proposed dual-polarized cavity backed monostatic patch antenna excited by a concurrent dual-mode SIW is shown in Figure 6.1, and its related dimensions are listed in Table I. The antenna consists of two layers constituting the SIW and patch antenna. Although the two orthogonal polarizations radiate at the same frequency, the width and length of the patch are chosen to be slightly different (non-square patch) to account for different excitation modes ($TE_{10}$ and $TE_{20}$ modes) and, consequently, different impedances. The starting point for determining the patch length/width was about half of the patch's effective wavelength ($\lambda_p/2$) minus the edge extension length due to the fringing fields, i.e. about 17.3 mm, to create a resonance in the patch. However, after optimizing the initial design in CST Microwave Studio and implementing a non-square patch for a better dual-mode impedance matching, the final values in Table I were opted. The patch is etched on a relatively thick substrate of 200 mils and has a low dielectric constant of 2.0 to achieve a relatively wide bandwidth. In addition, a cavity is implemented to suppress the surface wave propagation, which contributes to a lower cross-polarization and an increased gain. The size of the cavity can also affect the impedance bandwidth, though in our simulations we observed a trade-off, relative to the cavity size, between the antenna gain, cross-polarization and bandwidth. Therefore, we chose a cavity size resulting in a larger gain and lower cross-polarization. In this work, the SIW and cavity sidewalls are implemented using rectangular slot vias with 10-mils spacing rather than traditional circular vias, which would lower the leakage due to the minimizing gaps.

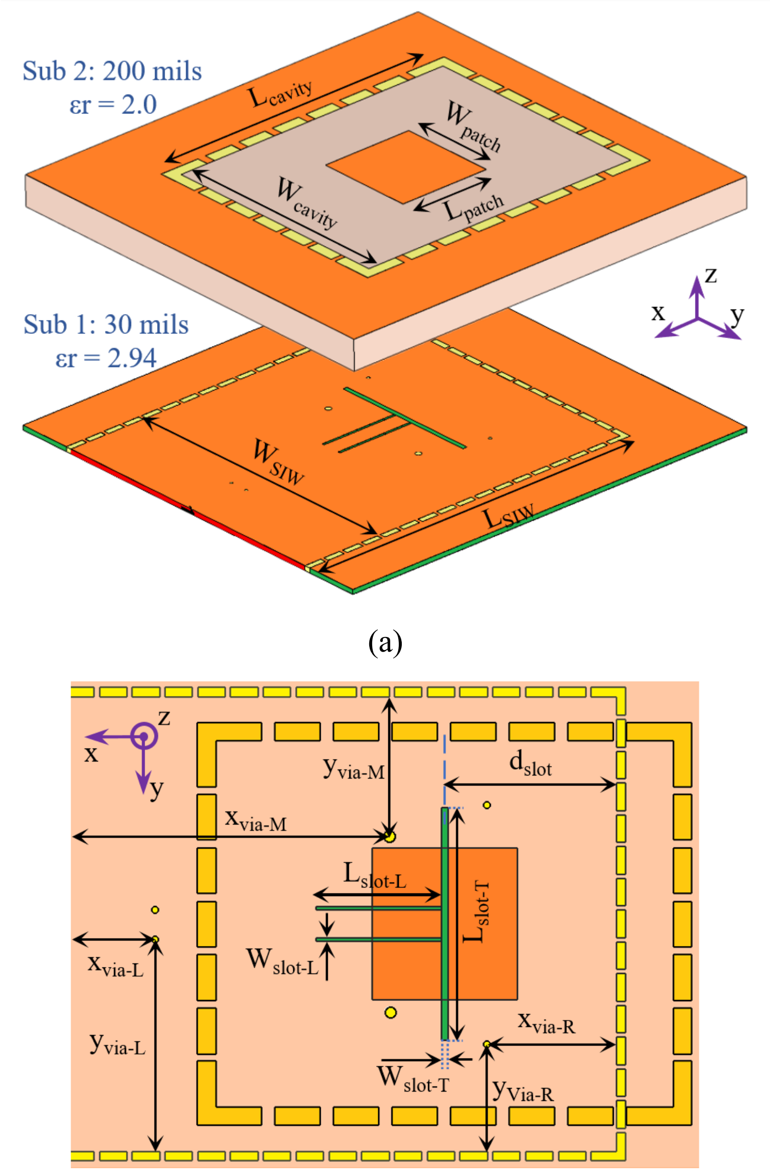

(a)

(b)

Figure 6.1 Schematic of the proposed dual-polarized cavity-backed patch antenna, excited by a concurrent dual-mode SIW: (a) Perspective and (b) top view

The SIW substrate has a dielectric constant of 2.94 and supports both $TE_{10}$ and $TE_{20}$ modes. To couple waves between the SIW and cavity-backed patch antenna, a modified T-shaped slot is etched on the top wall of the SIW. The length of each arm of the T-shaped slot is about a quarter of the slotline wavelength to create a resonance close to the resonance of the patch. The transverse slot is excited with the $TE_{10}$ mode resulting in a horizontally polarized radiation. Whereas, the longitudinal slots are excited by the $TE_{20}$ mode leading to a vertically polarized radiation from the patch antenna. Here, instead of one single longitudinal slot, two slightly off-centered parallel slots have been adopted, granting an extra degree of freedom for a fine impedance tuning of the $TE_{20}$ mode [129]. Finally, three pairs of vias are implemented within the SIW for impedance matching and field manipulation, which will be explained in the next section.

Table 6.1 Design parameters of the proposed antenna in Figure 6.1

| Parameter | Value (mm) | Parameter | Value (mm) | Parameter | Value (mm) |
|---|---|---|---|---|---|
| $W_{cavity}$ | 40 | $D_{slot}$ | 18.71 | $y_{via-L}$ | 23.26 |
| $L_{cavity}$ | 50 | $W_{slot-H}$ | 0.4 | $x_{via-M}$ | 27.27 |
| $W_{patch}$ | 16.54 | $W_{slot-T}$ | 0.765 | $y_{via-M}$ | 15.26 |
| $L_{patch}$ | 15.93 | $L_{slot-H}$ | 25.47 | $x_{via-R}$ | 14.1 |
| $W_{SIW}$ | 49.66 | $L_{slot-T}$ | 13.67 | $y_{via-R}$ | 11.9 |
| $L_{SIW}$ | 60 | $x_{via-L}$ | 7.67 | | |

## 6.4 Principle of Operation

An SIW structure is capable of carrying orthogonal modes simultaneously. In this work, the first two dominant modes of the SIW are of interest for the orthogonal excitation of the patch antenna. To exploit this feature, the width of the SIW must be chosen so that the $TE_{20}$ mode can propagate within the SIW in addition to the $TE_{10}$ mode. Therefore, the waveguide width is determined using [82]:

$$W_{SIW} = \frac{3c}{2f_e\sqrt{\varepsilon_r}} \qquad (7.1)$$

where $c$ is the speed of light in the vacuum; $\varepsilon_r$ is the dielectric constant of the SIW; and $f_e$ is the maximum edge frequency of the band. This equation fixes the maximum frequency to the onset of the $TE_{30}$ mode. Thus, the maximum concurrent available bandwidth is the frequency range between the cut-off frequencies of the second and third modes.

The main design challenge in the proposed antenna is having the field manipulation and impedance matching realized for $TE_{10}$ and $TE_{20}$ modes simultaneously. In other words, we should be extremely careful as any perturbation or change in fixing one mode may violate the performance of the other mode. Moreover, since high isolation between the two inputs ports are desired, it is of crucial importance that the structure be designed symmetrically about the middle plane of the SIW to avoid any mode-conversion between the $TE_{10}$ and $TE_{20}$ modes.

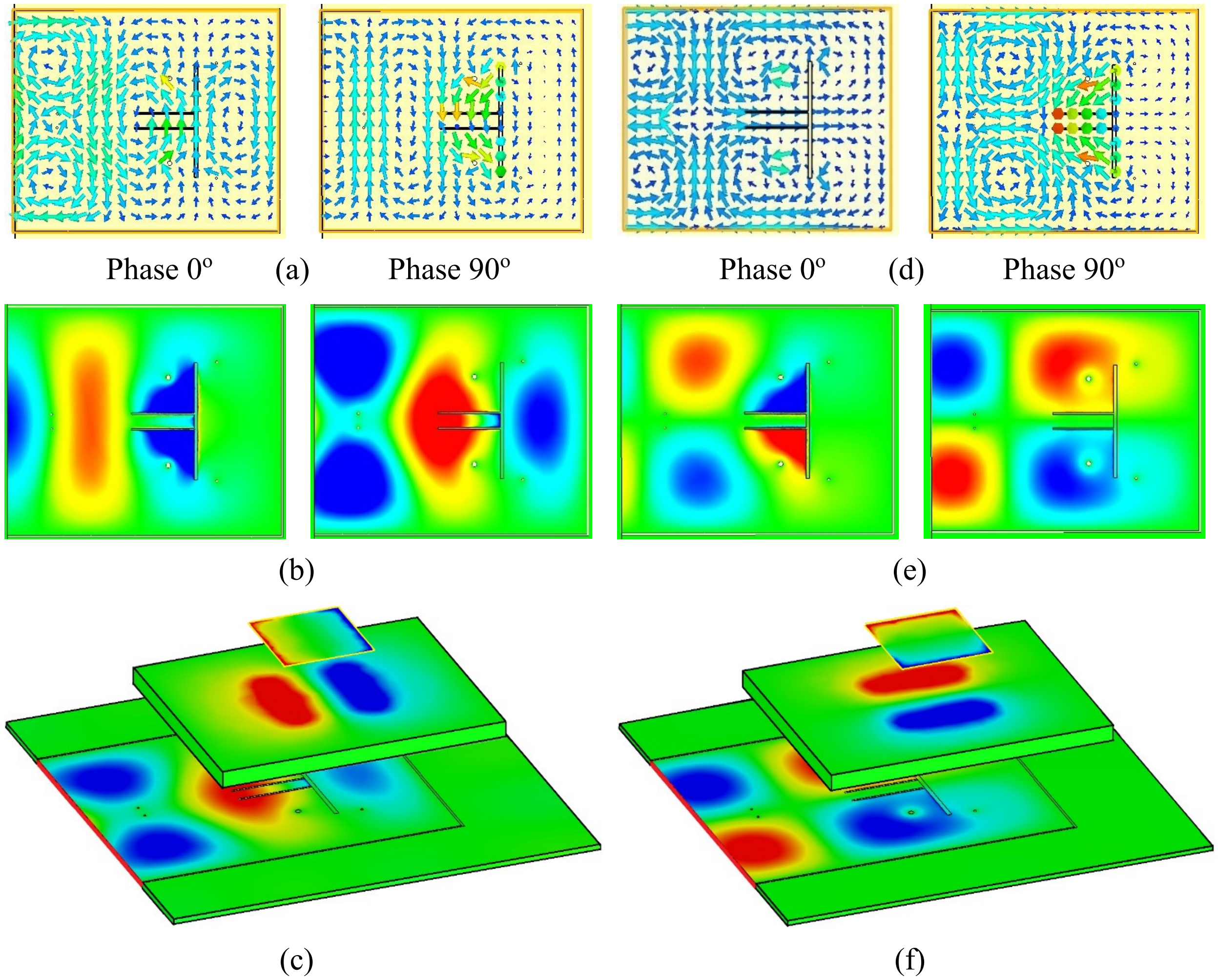

Figure 6.2 Field pattern within the proposed antenna showing the principle of operation: TE10 excitation: (a) magnetic and (b) electric field pattern at two different time instants within the feeding SIW, (c) electric field pattern within the whole structure; TE20 excitation: (d) magnetic and (e) electric field pattern at two different time instants within the feeding SIW, (f) electric field pattern within the whole structure

To mitigate this issue, we exploit a symmetrical via-loading technique within the SIW at critical positions where the electric field is strongest for one of the modes, so as to minimize the effect on the other mode. In this section, we will first give a general picture of the mechanism of operation for the whole structure, and then we will focus on the role of via-loading for field manipulation and impedance matching of the device.

Electric and magnetic field patterns for both modes at the center frequency are illustrated in Figure 6.2, which shows a comprehensive and self-explanatory view of the principle of operation for the proposed antenna. From Figure 6.2(a) and (d), it is discerned that, for both modes, the magnetic coupling is the dominant mechanism in excitation of the cavity through slots. In this case, the transverse and longitudinal components of the magnetic fields produce radiation for the $TE_{10}$ and $TE_{20}$ modes, respectively. It is further observed that in one half of the period, waves from either mode couple from the SIW with the cavity, while in the other half of the period the waves are stored and resonate. Figure 6.2(c) and (f) illustrate the electric field pattern within the whole structure for both modes. As illustrated, the $TE_{10}$ mode excites the $TM_{210}$ mode within the semi-square cavity, while the $TE_{20}$ mode excites the $TM_{120}$ mode. Furthermore, these two orthogonal modes of the cavity drive the patch for dual-polarized radiation.

Now, turning our focus to the three pairs of vias inside the SIW, their roles will be first assessed from a field point of view, then from a matching point of view. In a shorted SIW without any vias, for the $TE_{10}$ radiation, the transverse slot should be positioned a half wavelength ($\lambda_{TE10}/2$) away from the short-circuit wall of the SIW where the $TE_{10}$ transverse magnetic fields are at their maximum due to the resonance. On the other hand, the same reasoning goes for the $TE_{20}$ mode; the center of the longitudinal slot should be positioned a quarter wavelength ($\lambda_{TE20}/4$) away from the short-circuit wall. Since the propagation constants of the $TE_{10}$ and $TE_{20}$ modes are different, the corresponding magnetic fields resonate at distant positions from each other, which generally demand the use of separate patches and slots for each mode. In this work, we have manipulated the field pattern for the $TE_{20}$ mode so that the corresponding magnetic fields for the first and second mode resonate exactly underneath the patch and the slots, as shown in Figure 6.2. Hence, it yields the potential to exploit a T-shaped coupling slot which grants a compact configuration.

To bring together the resonance of the two modes beneath the patch, a pair of vias (Via-R) are introduced immediately at the right side of the slots. These vias are positioned symmetrically about the symmetry plane of the SIW. Also, each via is a quarter width of the SIW ($W_{SIW}/4$) away from the center of the SIW, corresponding to the maxima of electric field in the second mode. Therefore, these vias effectively block the $TE_{20}$ mode and create a virtual short wall for the second mode, fixing the maximum of the longitudinal component of the second mode a quarter wavelength away from the transverse slot as desired. The field patterns of Figure 6.2(d-e) confirm our claim as a negligible portion of the power in the second mode reaches beyond the blocking vias (Via-R). On the other hand, Figure 6.2(a-b) indicates that these vias have little effect on the first mode ($TE_{10}$) as a strong resonance is witnessed between the SIW short-circuit wall and the via-R pairs. The middle pair of vias (Via-M) has a major positive effect on both modes. However, it is mainly intended for focusing/pushing the $TE_{20}$ mode toward the center and longitudinal slots, thus resulting in stronger magnetic coupling, which is evident in Figure 6.2(d-e).

By assessing the field analysis within the structure using a Smith chart analysis, we now look into impedance matching. Despite the pair of Via-R vias, which merely has a virtual short-circuit wall role for the $TE_{20}$ mode, the other two pairs of vias have an inductive effect on the input impedance seen from the SIW ports. The Vias-M pair alters the input impedance for both modes. The position of these vias at the two sides of the longitudinal slots is tuned to achieve a proper impedance matching for the $TE_{20}$ mode. Contrarily, the pair of Via-L vias acts on the impedance matching of the first mode only. Because they are placed about the center of the SIW, the electric field is at its maximum and at zero for the first and second modes, respectively. It must be noted that since the SIW is oversized to support the $TE_{20}$ mode, the center vias split the signal rather than totally reflecting the incident wave.

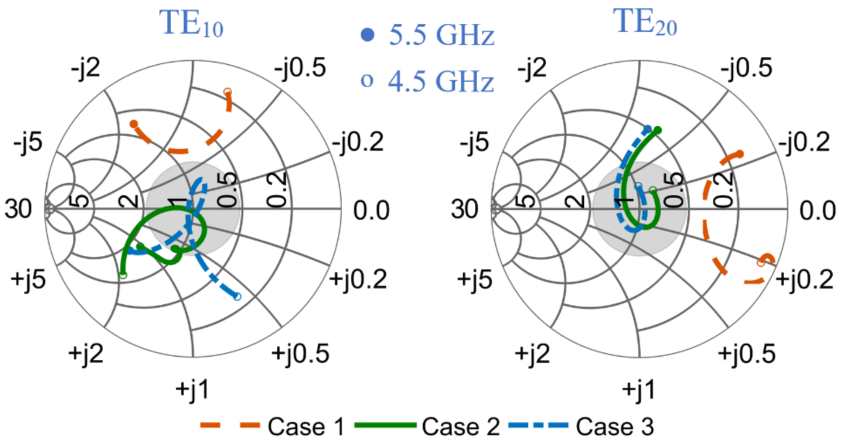

Figure 6.3 Impedance matching for (a) $TE_{10}$ and (b) $TE_{20}$ mode excitations

To visualize the role of these two pairs of vias, the input impedances for both modes are plotted in the Smith charts for three different cases, as described in Figure 6.3. Case 1 corresponds to the scenario where only the Via-R pair is implemented within the SIW. In case 2, the Via-M vias are also added to the SIW. And finally, in case 3, all three pairs of vias exist in the structure. For both modes in case 1, the two loops away from the center, as seen in the Smith chart of Figure 6.3, indicate that the device is not matched without the middle and left pairs of vias. First, the position of the middle vias were adjusted to match the $TE_{20}$ mode. As discerned in Figure 6.3, the middle vias have contributed to an impedance matching by moving the root locus toward the center and around it (case 2). The middle vias have also improved the $TE_{10}$ impedance matching since more electromagnetic waves are conducted toward the center of waveguide and the transverse slot. However, for an accurate matching of the first mode, another via is needed without disturbing the $TE_{20}$ matching. Therefore, the left pair of vias are added about the center of the SIW and, by adjusting the longitudinal position of these vias, the $TE_{10}$ is matched. As observed in Figure 6.3, these vias move the root locus of the $TE_{10}$ mode toward the center with negligible effect on the $TE_{20}$ mode (case 3). The loop around the center of the Smith chart indicates double resonance in both modes and, hence, improves the overall bandwidth [130]. However, it is noted that the presence of a loop in the Smith chart, even without matching vias, indicates that the double resonance is intrinsic to the antenna structure and caused by the resonances of the patch and slots.

## 6.5 Transition Design

The proposed dual-polarized antenna can be employed in the development of dual-polarized antenna array systems by using SIW feeding techniques for a compact and single-layered feeding network. However, to characterize and measure the proposed single element antenna, a concurrent SIW to planar TEM transmission line transitions must be designed for each mode. Although various techniques may be used to realize such concurrent excitation schemes, a novel technique is used in this work. To avoid any leakage contribution from the TL ports, the concurrent transitions must be effectively decoupled from each other. Furthermore, the feeding technique for both modes must be symmetrical about the feeding SIW; otherwise, the mode conversion will lead to a lower isolation.

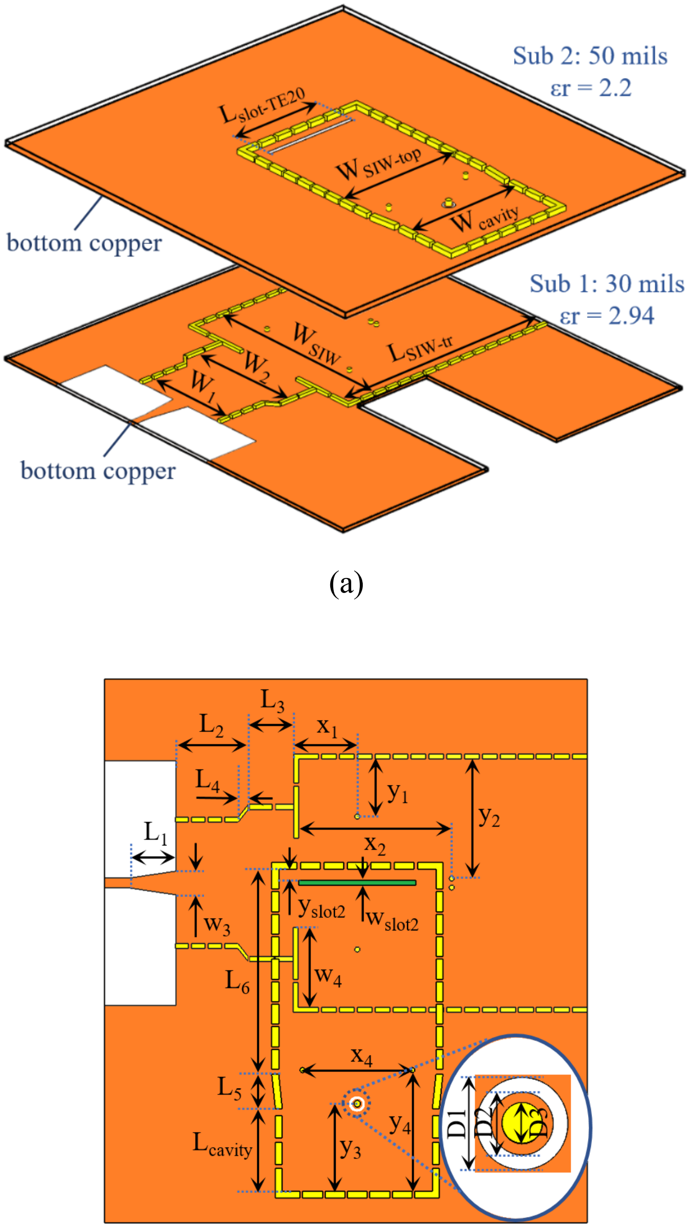

(a)

(b)

Figure 6.4 Schematic of the proposed transitions from SIW to TEM lines for concurrent excitation of the dual-mode SIW: (a) perspective and (b) top view

The schematic of the proposed concurrent transitions to the input of the feeding SIW is illustrated in Figure 6.4, and its dimensions are listed in Table II. The proposed concurrent transition is similar to the transition in [117] but with a better isolation. The $TE_{10}$ mode of the SIW is matched to a microstrip through a typical taper transition from the bottom copper of the SIW. However, between the main SIW and the microstrip line, two sections of the narrower single-mode SIWs are used to increase the isolation between the two inputs for two reasons. First, the narrow SIWs suppress any likely $TE_{20}$ or higher-order modes of the excited SIW because of discontinuity in the taper transition. Second, they increase the physical distance between the microstrip line and the second input. The presence of partial short-circuit walls at either side is necessary to create a resonance for the $TE_{20}$ mode, while also creating a large inductive impedance for the incident $TE_{10}$ mode. Therefore, it creates a seesaw effect on $TE_{10}$ and $TE_{20}$ matching, which must be compromised. Furthermore, to improve the isolation and lower the coupling between the patch and the microstrip feeding line, the microstrip feeding line is implemented over the bottom of the first layer.

To excite the $TE_{20}$ mode within the antenna, a longitudinal slot is etched atop the SIW, which couples the waves from the top SIW to the main SIW. Similar to the antenna matching, a pair of vias are positioned at the two sides of the slot to concentrate the $TE_{20}$ wave toward the slot for a stronger coupling. Also, an additional pair of vias are added about the center of the waveguide to match the $TE_{10}$ mode; the matching procedure is similar to the antenna matching. The top SIW supports only the $TE_{10}$ mode and is matched to a pin that is excited by a shielded coaxial connector. An additional pair of vias are used in the top SIW to improve the impedance matching. In practice, the probe is excited by a coaxial connector that is attached to the bottom copper of the second layer to minimize any undesired coupling between the two input ports through the air. The simulation results are given in the next section along with measurement results for comparison.

Table 6.2 Design parameters of the proposed transitions in Figure 6.4

| Parameter | Value (mm) | Parameter | Value (mm) | Parameter | Value (mm) |
|---|---|---|---|---|---|
| $W_1$ | 24.23 | $L_1$ | 9.38 | $y_1$ | 11.74 |
| $W_2$ | 29.4 | $L_2$ | 14.53 | $y_2$ | 23.93 |
| $W_3$ | 4.72 | $L_3$ | 10.36 | $y_3$ | 17.46 |
| $W_4$ | 15.47 | $L_4$ | 2.06 | $y_4$ | 24.13 |
| $W_{\text{SIW-top}}$ | 31.58 | $L_5$ | 6.95 | $W_{\text{slot2}}$ | 0.4 |
| $W_{\text{cavity-top}}$ | 30.11 | $L_6$ | 40.1 | $y_{\text{slot2}}$ | 2.45 |
| $L_{\text{cavity-top}}$ | 16.37 | $x_1$ | 10.55 | $D_1$ | 2.95 |
| $L_{\text{slot-TE20}}$ | 23.63 | $x_2$ | 29.32 | $D_2$ | 2 |
| $L_{\text{SIW-tr}}$ | 46.3 | $x_4$ | 22.02 | $D_3$ | 1.3 |

## 6.6 Measurement Results

The proposed dual-polarized antenna with the proposed SIW to TL transitions were fabricated in our Poly-Grames Research Center. For fabrication, Rogers 6002 substrates with a dielectric constant of 2.94 and loss tangent of 0.0012 was utilized as the bottom substrates with a 30 mils thickness to implement the main SIW, modified T-shaped slots, narrower SIWs and tapered transition for port 1. The antenna substrate, which was 200 mils, was too thick to be laser cut in our lab, so instead we used four similar 50-mils thick Rogers 5880LZ substrates with a dielectric constant of 2.0 and loss tangent of 0.0021. The first layer of the Rogers 5880Lz was also used to implement the top SIW to match to the coaxial input of port 2. After printing and metalizing each layer, all layers were glued to each other with epoxy and pressed under high pressure for a homogenous connection between the layers. To lower the coupling from the antenna to the microstrip port, a metallic base was fabricated and attached underneath and partially above the substrate. The picture of the fabricated circuit and the metallic base are shown in Figure 6.5.

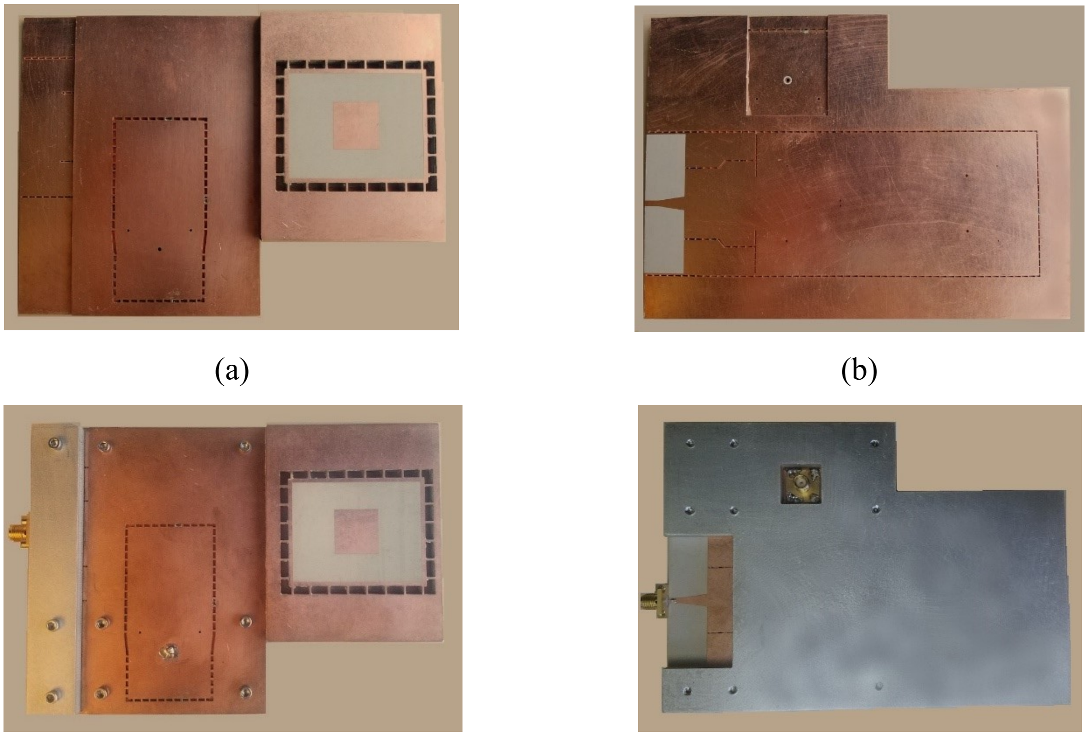
(a) (b)

(c) (d)

Figure 6.5 Fabricated prototype of the proposed dual-polarized patch antenna: (a) top, (b) bottom view without connectors, (c) top and (d) bottom view with connectors and the base

The S-parameters of the proposed antenna were measured with a Keysight two-port vector network analyzer (VNA), which are plotted in Figure 6.6 and are compared with the simulation results using CST Microwave Studio. It is discerned that the measurement and simulation results are in excellent agreement for the reflection parameters and acceptable for the isolation parameter. The -10-dB impedance bandwidth of the device is 610 MHz, ranging from 4.69 GHz to 5.3 GHz. The simulations display an isolation better than 50 dB between the input ports; however, the measurements indicate an isolation level better than 42 dB within the impedance bandwidth. The discrepancy between measurement and simulation results is probably caused by fabrication tolerances and infinitesimal misalignments in the measurement setup.

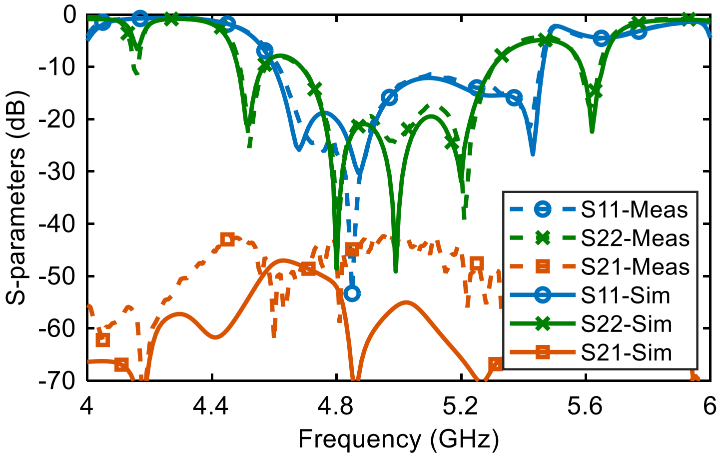

Figure 6.6 Measured and simulated S-parameters of the proposed dual-polarized antenna with concurrent transitions

The normalized antenna radiation patterns are plotted in Figure 6.7 and are compared with the simulation results from CST Microwave Studio, showing an excellent agreement. The antenna has a gain of 8.57 and 8.2 dBi at the center frequency for the $TE_{10}$ and $TE_{20}$ modes, respectively. From Figure 6.7, it is observed that for the port 1 excitation the measured front-to-back ratio (FBR), maximum cross polarization level (X -pol), and half power beam width (HPBW) are 22.3, -26 dB and 54°, respectively, in the XOZ plane; whereas, they are 22 dB, -27 dB and 64° in the YOZ plane. Similarly, for the port 2 excitation, these specifications are 25 dB, -27 dB and 73°, respectively, in the XOZ plane and are 25 dB, -21.6 dB and 74°, respectively, in the YOZ plane. Furthermore, it should be mentioned that in the broad side where the co-polarized radiation is maximum, the cross-polarization levels are better than -33 and -35 dB for ports 1 and 2, respectively and in both planes. Such low levels of cross-polarization are related to a low inter-port isolation over a wide bandwidth.

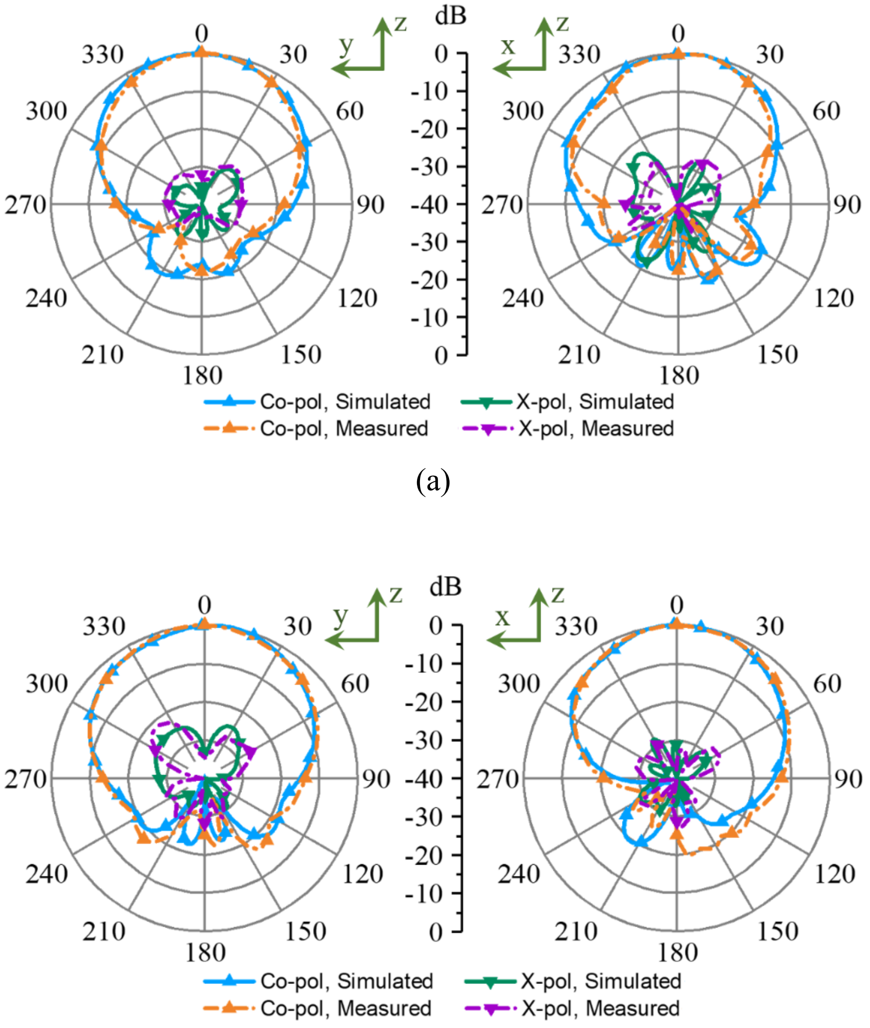

(a)

(b)

Figure 6.7 Measured and simulated normalized radiation patterns for (a) $TE_{10}$ and (b) $TE_{20}$ mode excitations of the proposed antenna for yoz (left pictures) and xoz (right pictures) planes

In Table III, we have compared our proposed DP patch antenna to similar works in the literature that have reported high port-to-port isolation. In this table, only the sub-6 GHz monostatic single element antennas with at least 10% impedance bandwidth are considered for comparison. Comparing our work with the state-of-art results reveals that our proposed DP antenna excels and outperforms other works as a whole. In Table III, only [34] has a better isolation than our proposed antenna, though its profile is relatively 3 times larger and it is not integrated. Our proposed high isolation DP antenna is fabricated using simple integrated PCB technology, which is comparable to many complex and non-integrated structures in Table III and in the literature. Furthermore, [30], [32], [35, 36] in Table III use differential feeding to achieve their lower isolations; however, the differential feeding network is not implemented, and differential responses are theoretically calculated. Considering that unbalanced differential inputs degrade the performance of the system, it is expected that these works would have a lower isolation in practice.

Table 6.3 Comparison of the proposed and reference DP Antennas

| Ref. | Frequency (GHz) | Isolation (dB) | Technology/ Topology | Profile $\lambda_0$ | Integrability |
|---|---|---|---|---|---|
| [30] | 3.10 - 3.85 | >43* | Slot Antenna with Microstrip | 0.13 | no |
| [31] | 2.25 - 2.99 | >39 | (APS) / Magnetically Coupled Patch | 0.146 | no |
| [32] | 3.28 - 3.72<br>4.80 - 5.18 | >37*<br>>38* | Patch with Slots | 0.13 | no |
| [33] | 4.33 - 5.81 | >35 | Laminated Resonator Antenna | 0.115 | yes |
| [34] | 5.10 - 5.80 | >45.2 | Magnetic Dipole | 0.32 | no |
| [35] | 3.30 - 3.70<br>4.75 - 5.0 | >40* | Stacked Patch Antenna | 0.085 | yes |
| [36] | 2.31 - 2.81 | >35* | Stacked Patch Antenna | 0.08 | yes |
| [37] | 1.7 - 2.81 | >39* | Patch Antenna with Printed Open Slots and Stair-Shaped Strips | 0.25 | no |
| Pro. | 4.69 - 5.30 | >42 | SIW Cavity Backed Patch; Excited by a Dual-Mode SIW. | 0.097 | yes |

* Differential feeding is not implemented, so isolation in the practice might be lower than this.

## 6.7 Conclusion

In this work, we proposed and presented for the first time a unique methodology to implement an integrated dual-polarized cavity-backed patch antenna, which is excited by a concurrent dual-mode travelling-wave SIW structure. Also, we presented and discussed a scheme to implement the concurrent transitions for the dual-mode SIW to TEM lines. The measured S-parameters of the proposed DP antenna show a high isolation that is better than 42 dB over the impedance bandwidth of 610 MHz. Moreover, the simulated and measured antenna radiation patterns were presented with excellent agreement.

# CHAPTER 7 A FULL-DUPLEX SYSTEM DEMONSTRATION BASED ON INTEGRATED DUAL-MODE CIRCULATOR AND DUAL-POLARIZED ANTENNA WITH 70 DB ISOLATION

This chapter exploits the nonreciprocal mode conversion theory and dual-mode circulator presented in previous chapters (Figure 5.11) to enable the development of a full-duplex transceiver. Therefore, in this chapter, we propose developing an integrated dual-mode (DM) dual-polarized (DP) antenna with very high isolation suitable for full-duplex transceivers. The DP antenna generally has the same configuration proposed in chapter 5; nevertheless, the antenna's dual-mode SIW port is directly connected to the dual-mode circulator's waveguide port without any SIW-to-transmission line transitions. The integration, co-design, and co-simulation of the antenna and the circulator result in several improvements, including a robust and monolithic design and avoiding losses due to transitions. However, the most critical benefit is that intermediate transitions are eliminated, which could cause inter-port mode-conversion and mode coupling; hence, isolation in the integrated module is enhanced.

In this chapter, we will first present the proposed integrated circulator antenna structure with ultra-high isolation, followed by simulation and measurement results. Later we will present a system demonstration of a full-duplex transceiver and relative measurements.

## 7.1 The proposed integrated DM circulator and DP Antenna

### 7.1.1 Component configuration

The schematic of the proposed integrated DM circulator and DP antenna is illustrated in Figure 7.1, and the dimensions are provided in Table 7.1. The structure consists of six layers. The DM circulator is implemented in the first layer with a dielectric of 2.94 and a thickness of 30 mils. The T-shaped slots at the end of the SIW are etched on top of the first layer. These slots excite the dual-polarized patch through the cavity that is formed within the other five layers. The second and third layers are used to implement strip lines for Port 2 (Rx Port) and Port 3 (Tx Port), where each layer has a dielectric constant of 2.0 and a thickness of 20 mils. The strips are etched on top of layer 2, while the bottom of layer 2 and top of layer 3 serve as the ground plane for the strip lines. Via holes cutting through the second and third layers are implemented to avoid higher-order modes' excitation and shield two ports from each other. The cavity thickness is overall 190 mils for the

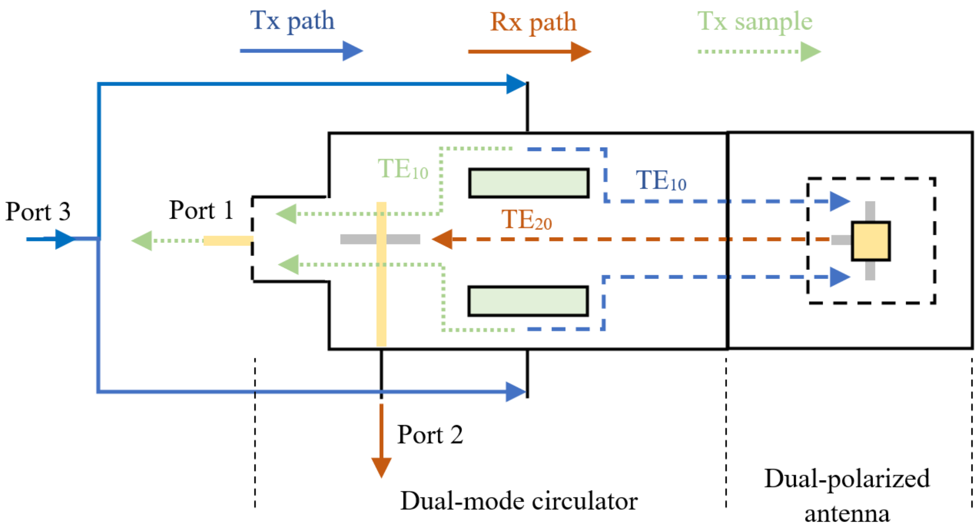
Tx path
Rx path
Tx sample
Port 3
Port 1
$TE_{10}$
$TE_{10}$
$TE_{20}$
Port 2
Dual-mode circulator
Dual-polarized antenna

(a)

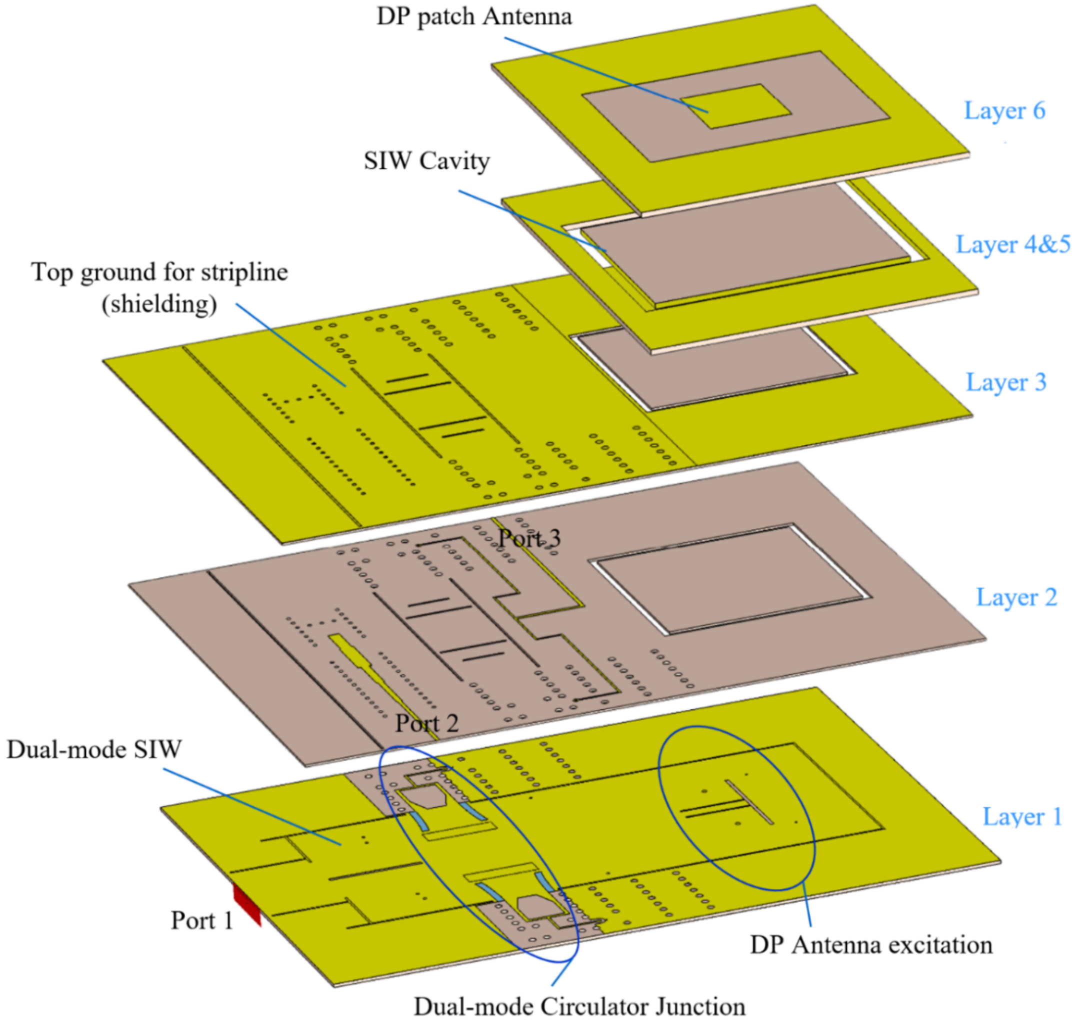
DP patch Antenna
Layer 6
SIW Cavity
Layer 4&5
Top ground for stripline (shielding)
Layer 3
Port 3
Layer 2
Port 2
Dual-mode SIW
Layer 1
Port 1
DP Antenna excitation
Dual-mode Circulator Junction

(b)

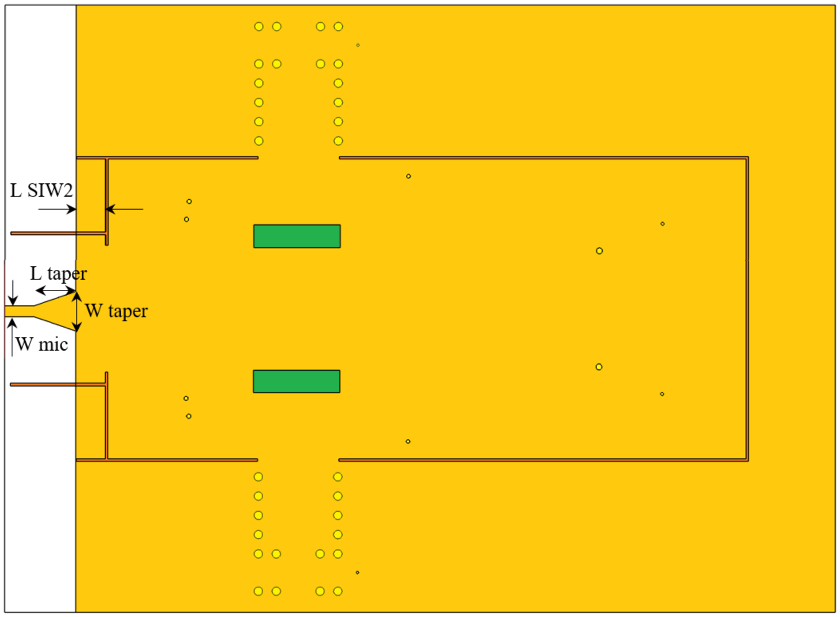
L SIW2
L taper
W taper
W mic

(c)

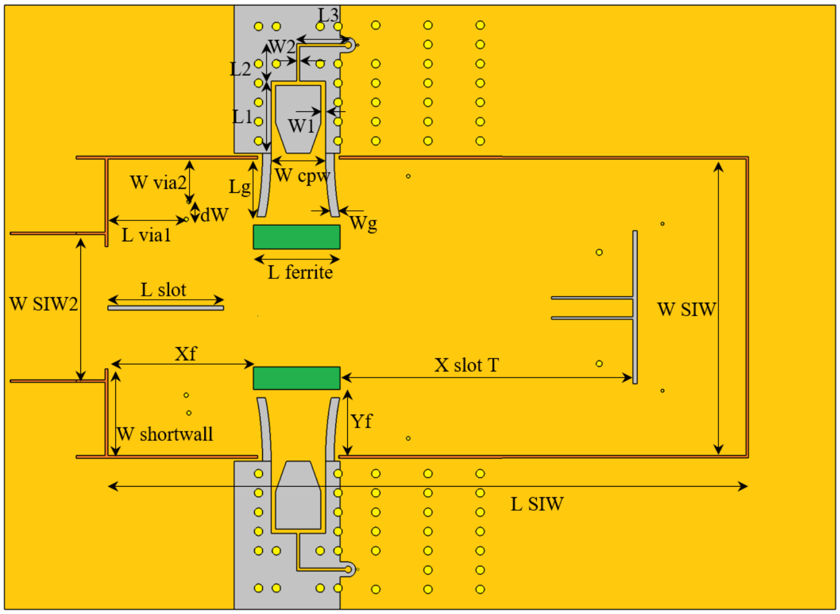
L3
W2
L2
L1
W1
W cpw
W via2
Lg
dW
Wg
L via1
L ferrite
L slot
W SIW2
W SIW
Xf
X slot T
Yf
W shortwall
L SIW

(d)

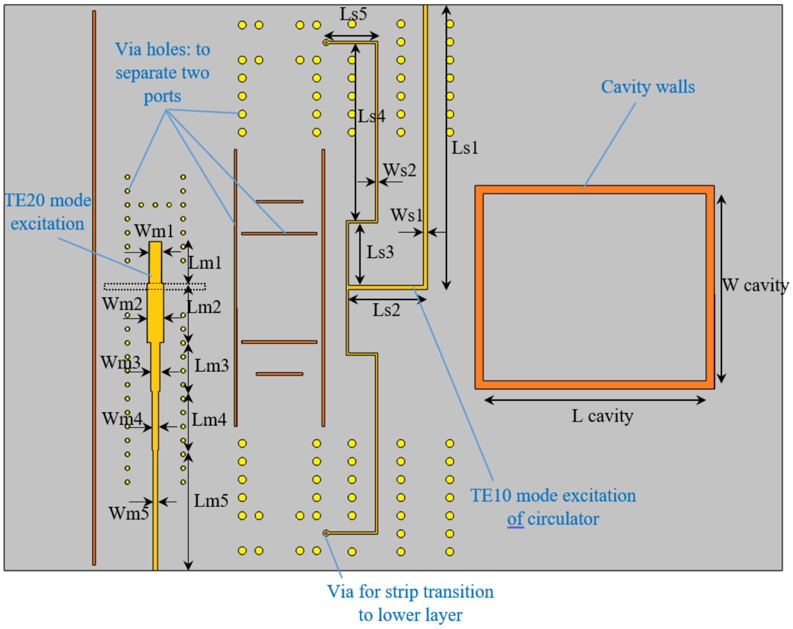

(e)

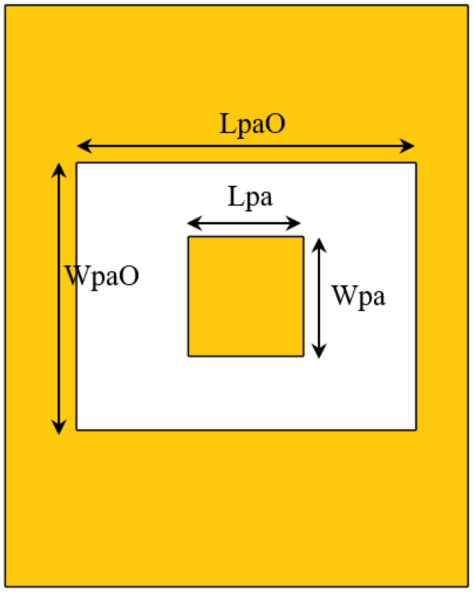

(f)

Figure 7.1 Schematic of the proposed integrated DM circulator and DP antenna: (a) block diagram of integrated dual-mode circulator and dual-polarized antenna and corresponding field excitations, (b) exploded view, (c) bottom and (d) top view of layer 1, (e) top view of layer 2, and (f) top view of layer 5

Table 7.1 Dimensions of the proposed DM circulator and DP antenna in Figure 7.1

| Parameter | Value (mm) | Parameter | Value (mm) | Parameter | Value (mm) | Parameter | Value (mm) |
|---|---|---|---|---|---|---|---|
| Lpa | 15.92 | L slot | 19.46 | L2 | 6.55 | Lm3 | 8.8 |
| Wpa | 16.53 | L via1 | 13.16 | L3 | 9.17 | Lm4 | 10.6 |
| LpaO | 42 | W via2 | 7.5 | L taper | 8.05 | Lm5 | 21.63 |
| WpaO | 37 | dW | 3 | W taper | 6.68 | Ws1 | 0.79 |
| W SIW | 49.66 | L ferrite | 14.52 | W mic | 1.85 | Ws2 | 0.415 |
| L SIW | 107.34 | t ferrite | 3.83 | Wm1 | 2.35 | Ls1 | 50.75 |
| W SIW2 | 24.2 | Wg | 1.44 | Wm2 | 2.9 | Ls2 | 14.18 |
| L SIW2 | 5 | Lg | 10.65 | Wm3 | 1.65 | Ls3 | 11.6 |
| W shortwall | 14.54 | Wcpw | 9.16 | Wm4 | 1.15 | Ls4 | 32.2 |
| Xf | 24.48 | W1 | 0.79 | Wm5 | 0.79 | Ls5 | 15.7 |
| Yf | 11.1 | W2 | 0.49 | Lm1 | 7.418 | W cavity | 40 |
| X slot T | 49.2 | L1 | 11.4 | Lm2 | 10.5 | L cavity | 45 |

realization of a relatively wide bandwidth antenna. Cavity consists of the top five layers with a dielectric of 2.0, where the top three layers each have a thickness of 50 mils.

The structure consists of three ports. Port 2 and 3 excite $TE_{20}$ and $TE_{10}$ modes within the SIW, respectively. Since these two modes are orthogonal, inherently, the isolation between these two ports is considerable. Furthermore, additional isolation between these two ports is imposed due to the circulator's nonreciprocity. Hence, port 2 and 3 are reserved for Rx and Tx ports, respectively. Port 1 is extra and connected to a 50-ohm load if unused. Port 1 and 3 excite the same mode in SIW; however, due to the circulator's nonreciprocity, port 1 is isolated from port 3. Therefore, port 1 samples the Tx signal with a factor of circulator isolation, which is predicted for RF active cancelation if needed in some applications. In other words, this port eliminates the need for a coupler in conventional active RF SI cancelation techniques to sample the Tx signal.

### 7.1.2 Module design and simulation results

The proposed module in Figure 7.1 is complex and massive, so the design and simulation of the whole circuit at once would be significantly time-consuming and inefficient. To tackle this problem and also to create an efficient simulation, we have exploited the System Assembly and Modeling feature of CST Microwave Studio to break the whole structure into three sub-circuits and optimize each circuit separately. Thus, the proposed structure was divided into three sub-components: antenna, circulator, and input transitions. The DP antenna has the same configuration as the DP antenna proposed in chapter 6. The circulator is essentially like the dual-mode circulator proposed in chapter 5. The main difference is that instead of the slotline resonance junction, a stripline resonance junction is implemented to avoid radiation and port coupling as well as to lower the transition loss associated with slotline.

Furthermore, a common-mode excitation scheme is devised to excite only $TE_{10}$ mode within the SIW circulator from external side ports. The common-mode or $TE_{10}$ excitation is accomplished through a stripline at the second and third layers, as displayed in Figure 7.1(e). The common-mode excitation line is implemented in two layers. The line's endpoints are connected to the circulator's junction at the second layer's bottom side. A via transition in the second layer transfers the line from the bottom to the top. The bisected section of this line's total length is about (2n-1)λs/4, where n is an integer number, and λs is the stripline's wavelength. Because at the bisection of this line, there is a virtual ground for $TE_{20}$ mode excited in the circulator, input impedance at the junction of the circulator seen from $TE_{20}$ mode would be an open circuit at this length.

Since the antenna is integrated with the circulator, the antenna's loading effect changes the input impedance seen from the circulator's ports comparing with the previous design in chapter 5, in which ports terminated in 50-ohm impedances. Therefore, the dimensions of the junction of the circulator are redesigned and optimized in the CST Microwave Studio. $TE_{20}$ mode within the SIW is excited through a separate stripline at layers 2 and 3, as shown in Figure 7.1(e). This stripline is electromagnetically shielded from other ports through a plethora of circular and rectangular via loadings. Magnetic fields are coupled from the open quarter-wavelength resonator of the stripline to the aperture beneath it and the SIW. A three-section transformer is implemented to match the stripline resonator to a 50-ohm line, where each section's length is about a quarter-wavelength of the stripline.

After optimizing the proposed components separately in CST to maximize the operation bandwidth, the monolithic structure is simulated with increased accuracy, and further a fine optimization is applied. The CST simulation results are plotted in Figures 7.2(a) and 7.2(b), demonstrating a successful structure design. The simulated device's S-parameters concerning return loss are exhibited in Figure 7.1(a), indicating a device bandwidth of 700 MHz for a criterion of -10 dB return loss. The 700 MHz bandwidth is relatively broad enough for many communication applications in 5G and future wireless systems. Figure 7.2(b) shows the inter-port S-parameters. Two of the transmission coefficients have lower values than other coefficients, which are expected since they are related to transmission coefficients between port 1 and port 3, which are not orthogonal (both excite the $TE_{10}$ mode in the SIW). The insertion loss from port 1 to port 3 is less than 1dB indicating a low loss component. The S13 indicates a better than 15 dB isolation from port 3 to port 1, suitable for any likely Tx sampling if other SIC methods would be incorporated in the architecture. Other transmission coefficients indicate the inter-mode isolation between different ports is better than 50 dB in simulation.

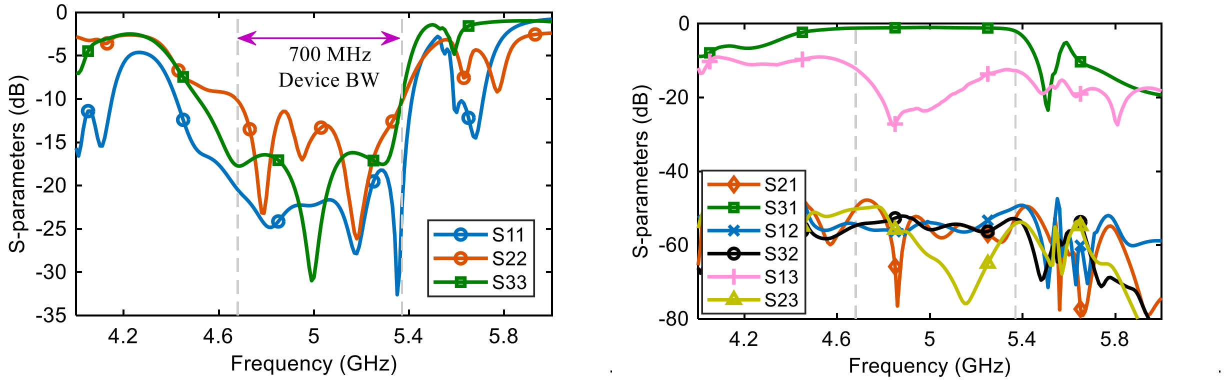

Figure 7.2 Simulation results of the proposed module: (a) Return losses indicating 700 MHz operating bandwidth, (b) insertion loss, and inter-port isolations

## 7.2 Fabrication and measurement results

### 7.2.1 Fabrication process

The proposed integrated dual-mode circulator and dual-polarized antenna have been fabricated. The first layer is a Rogers 6002 substrate with a dielectric constant of 2.94 and a loss tangent of 0.0012, which encompasses the main SIW and the ferrites. The second and third layers are Rogers 5880 substrates with a dielectric constant of 2.2 and a loss tangent of 0.0009. The other three remaining layers are Rogers 5880LZ substrates with a dielectric constant of 2.0 and a loss tangent of 0.0021. After each layer's preparation, layers two and three have been glued together with epoxy and under high pressure. Then vias between these two layers have been implemented and metalized. Next, these two layers are glued to layer one and three-layer via holes are cut through and metalized. Finally, the other three layers are glued to the first three layers to complete the PCB fabrication process. After PCB preparation, ferrite pieces were embedded within layer one and are covered by copper tape. For continuity of the bottom conductor, the copper tapes were soldered to the circuit. The ferrite material is purchased from TCI Ceramics with a saturation magnetization (Ms) of 800 G, linewidth (ΔH) of 30 Oe, and a dielectric constant of (Ɛf) 13.9.

A metallic base was fabricated for the bottom and partially the top of the component for enhanced electromagnetic shielding of ports from each other and protecting the component from any damage. Two rectangular slots in the bottom base have been cut to accommodate the magnets. Pictures of the fabricated prototype are shown in Figures 7.3 (a) and 7.3(b).

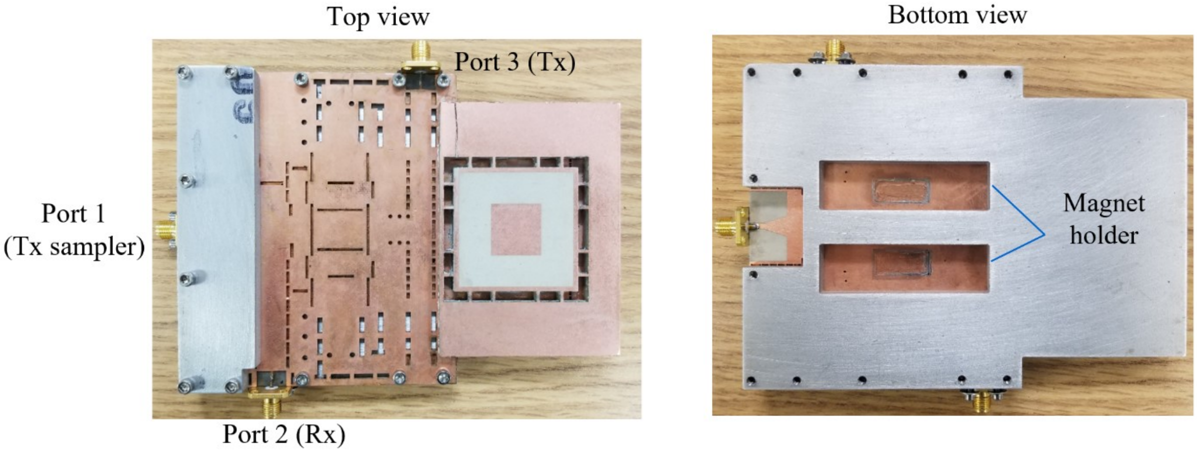

(a)

(b)

Figure 7.3 pictures of the fabricated prototype: (a) top and (b) bottom views

## 7.2.2 Measurement results

The S-parameters were measured using a Keysight vector network analyzer (VNA), and results are plotted and compared to simulation results for each port excitation separately in Figure 7.4(a)-(c). Measurement results are in excellent agreement with simulation results, with slight and acceptable discrepancies. Discrepancies such as higher insertion loss in S31 are due to the connector loss, which was not considered in simulations. On the other hand, some other discrepancies are due to non-homogenous ferrite biasing, which deviates the device's performance from simulation results.

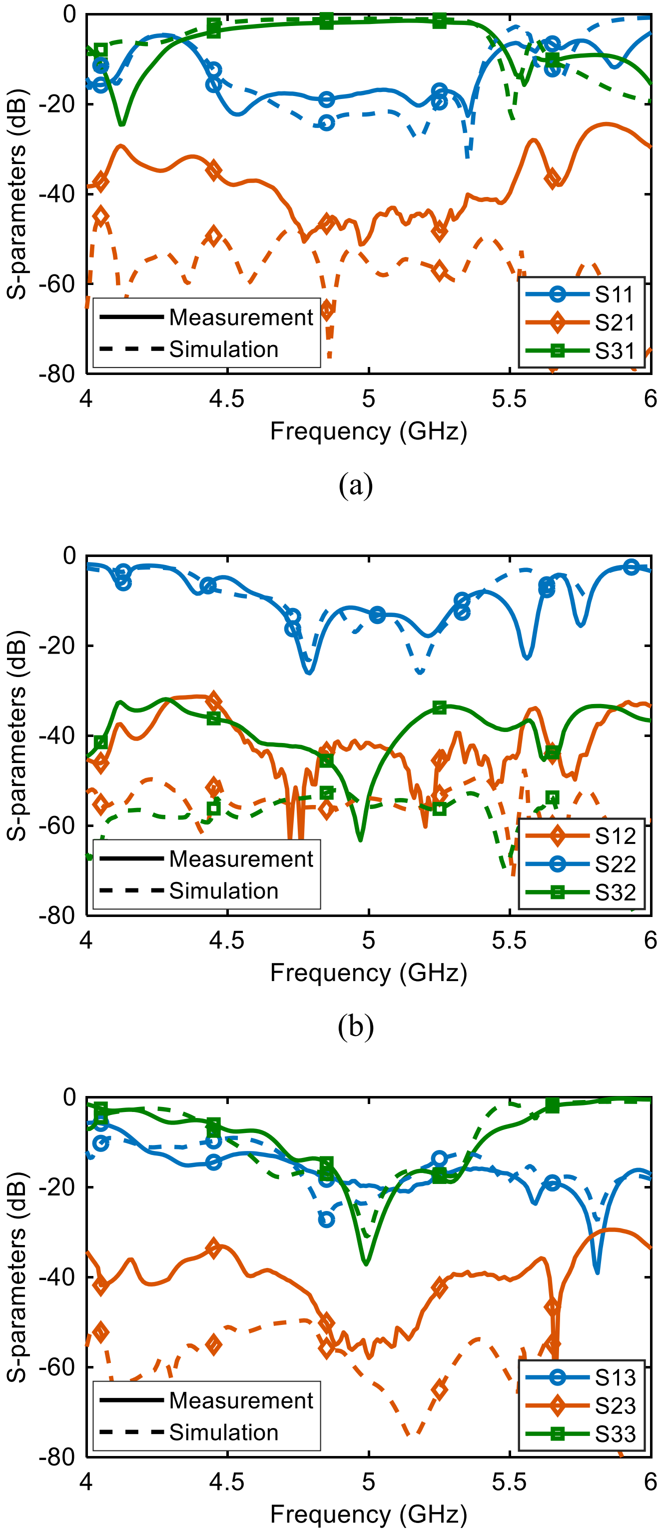

(a)

(b)

(c)

Figure 7.4 Measured results compared to simulation results for port excitation of (a) 1, (b) 2 and (c) 3

Finally, fabrication tolerance affects discrepancies between simulation and measurement results for very small transmission coefficients. Measurements indicate at least 700 MHz impedance bandwidth in all three ports, from 4.65 GHz to 5.35 GHz, for a -10 dB return loss. It is noted that these results have been achieved under symmetrical magnetic biasing.

The S23 in Figure 7.4(c) is the subject of our interest since it manifests the isolation between Tx and Rx ports. The figure indicates that isolation better than 50 dB over 340 MHz bandwidth in the center of the operating region is realized in measurements. These results were measured while the magnetic biasing setup was symmetrical, applying the same magnetic field magnitude to each ferrite.

However, the isolation can be bolstered by applying a slightly asymmetrical and non-homogeneous magnetic bias. From chapters 3 and 4, we have learned that twin-ferrite loaded SIW can convert the mode if asymmetries are imposed on the SIW. Thus, an asymmetrical magnetic bias can result in mode conversion within the SIW. This mode conversion can be exploited to generate an adjustable $TE_{20}$ signal feeding into the receiver port to cancel the residual leakage. In other words, the twin-ferrite loaded SIW structure consists of an inherent passive SIC scheme that can enhance the isolation. Compared to a single tap active SIC approach that consists of a variable attenuator and phase shifter to tune the cancelation signal, the converted signal's amplitude and phase can be adjusted similarly. The amplitude of the converted signal can be intensified or weakened by increasing or decreasing the degree of asymmetrical biasing. On the other hand, the phase can be tuned by applying a non-homogeneous magnetic bias over a ferrite's length because the phase constant of the wave in the ferrite-loaded SIW depends on the magnetic bias. Due to the high primary isolation of about -50 dB, the leakage signal is feeble. Therefore, the mode-converted signal should be tiny, requiring very minute asymmetrical magnetic biasing that can be simply fulfilled in practice, as shown soon.

Figure 7.5 shows one set of results that yield isolations better than 50 dB in different center frequencies and over relatively broad bandwidths using the asymmetrical magnetic bias tuning. Similarly, Figure 7.6 shows another set of results where isolations better than 70 dB over at least 90 MHz bandwidth and at different center frequencies were achieved. The achieved isolations are impressively high and satisfy the required isolation in the analog domain to enable a full-duplex transceiver for even high-power applications. Further, the achieved bandwidth is sufficient for advanced 5G applications in the sub-6 GHz region. Finally, the simple, though efficient, tunability mechanism of the isolation's depth and the center frequency is a significant advantage of the proposed structure. Moreover, with the ultra-fine tuning of the magnetic bias, it is possible to get even higher isolation but within smaller bandwidth. In this regard, Figure 7.7 reports a measurement with isolation better than 80 dB over a 36MHz bandwidth.

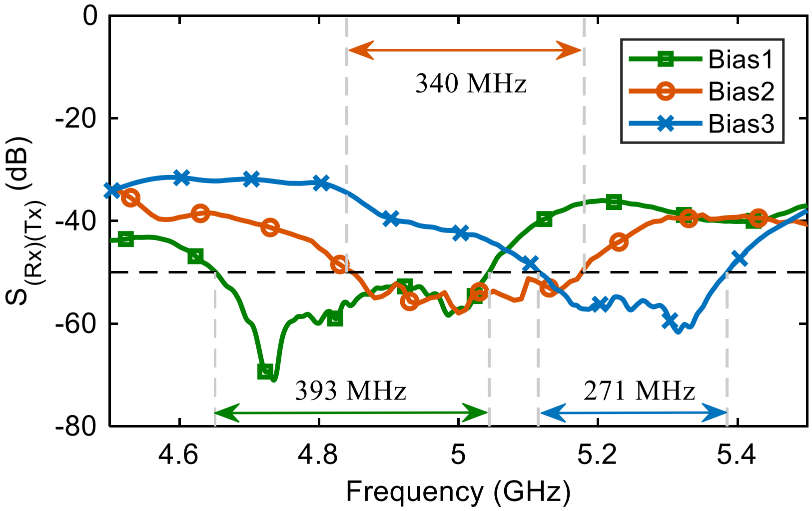

Figure 7.5 Measured isolations better than 50 dB at different center frequencies tuned with magnetic bias

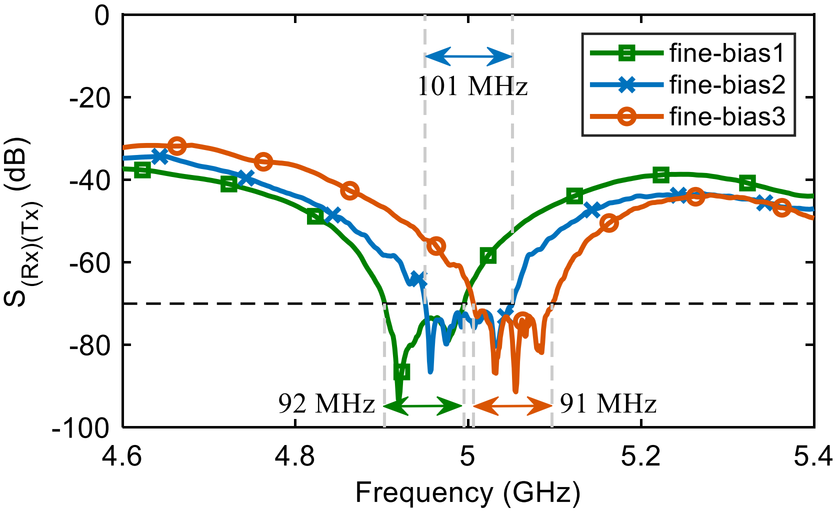

Figure 7.6 Measured isolations better than 70 dB at different center frequencies tuned with magnetic bias over 90 MHz bandwidth

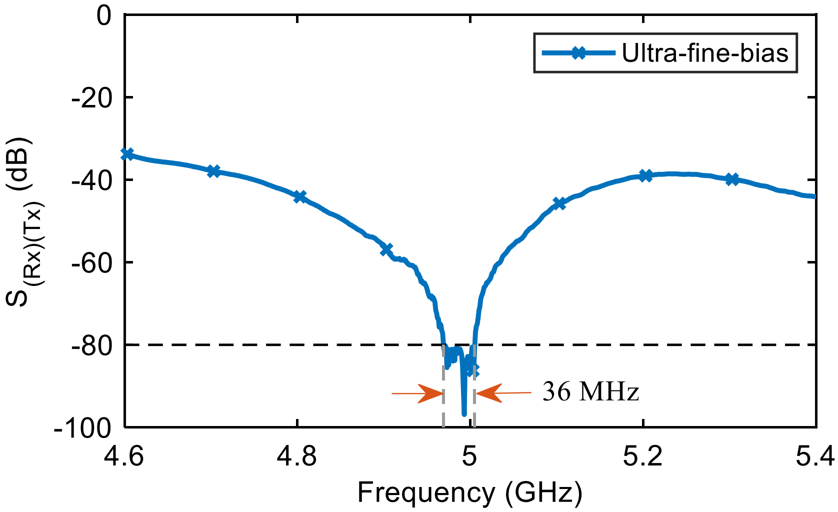

Figure 7.7 Measured isolations better than 80 dB at center frequencies tuned with magnetic bias at 36 MHz bandwidth

As shown in Figure 7.3, essential magnetic biasing is provided by two identical magnet pieces on the bottom of the device. Iron sheets are attached to the device's bottom and top to enclose the magnetic flux. To provide tiny asymmetrical biasing, we used some iron and ferrite RF sheets that are typically used for electromagnetic shielding. These sheets contain iron or ferroelectric materials that conduct magnetic flux. Therefore, by placing them on top of the device, magnetic flux can be slightly tuned. In conventional magnetic devices, these sheets' magnetic contributions would be negligible; however, they are perfect for adjusting the mode-converted signal in our application. The DUT picture with these sheets for some tuning cases is shown in Figure 7.8 for illustration purposes. More layers were added to increase the magnetic bias, and to apply asymmetrical or non-homogeneous biasing, some sheets were moved off-center.

This section provided S-parameter measurement results demonstrating high isolation between Tx and Rx ports of the proposed component, enabling full-duplex communication. In the next section, a full-duplex system will be demonstrated using the proposed module.

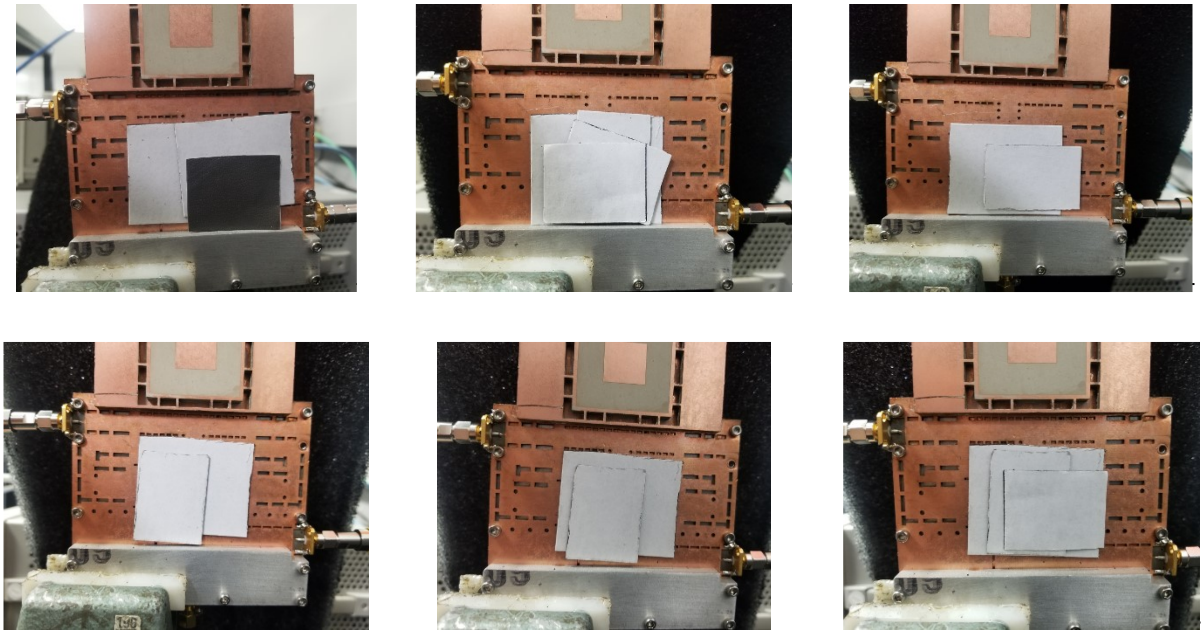

Figure 7.8 Magnetic fine and ultra-fine tuning using iron or ferrite RF sheets at various positions and configurations

### 7.2.3 System-level measurements

Two sets of measurements are carried out to evaluate the proposed front-end module's performance in a full-duplex system. In the first measurement, the proposed module's isolation is investigated while a pulse-shaped modulated signal is applied to its Tx port. On the other hand, in the second measurement, a communication link is established between the proposed module and another transmitting antenna. Then, while the other transmitting antenna's power is varied, the distortion in the Rx node's demodulated signal is investigated to assess the error vector magnitude (EVM) of the proposed component.

Moreover, to compare the proposed module's performance with state-of-art approaches, a single tap RF SI canceler is designed and fabricated, presented in the next section.

#### 7.2.3.1 RF Signal Interference (SI) Canceler

RF SI canceler has become a widespread technique in canceling the leakage signal from Tx to Rx port and realizing higher isolation. A single tap RF SI canceler is a series of RF variable-voltage attenuator and a phase shifter that can be tuned to manipulate a Tx signal sample and add it destructively with the leakage signal at the center frequency. The Tx signal sample is typically provided using a 20 dB coupler using a tap at power amplifier output and before the antenna. On the other hand, the manipulated Tx sample signal is added to the Rx channel using a 10 to 20 dB coupler to avoid noise figure degradation on the desired Rx signal at the Rx side.

This section presents the fabrication of a single-tap analog RF SI canceler. The fabricated RF SI canceler circuit consists of an analog voltage variable attenuator and a digital step phase shifter for signal manipulation. A 10 dB coupler at the output adds Rx and RF SI canceler signals with a ratio of 10 dB. It is assumed that a Tx sample signal is provided at the input of the RF canceler.

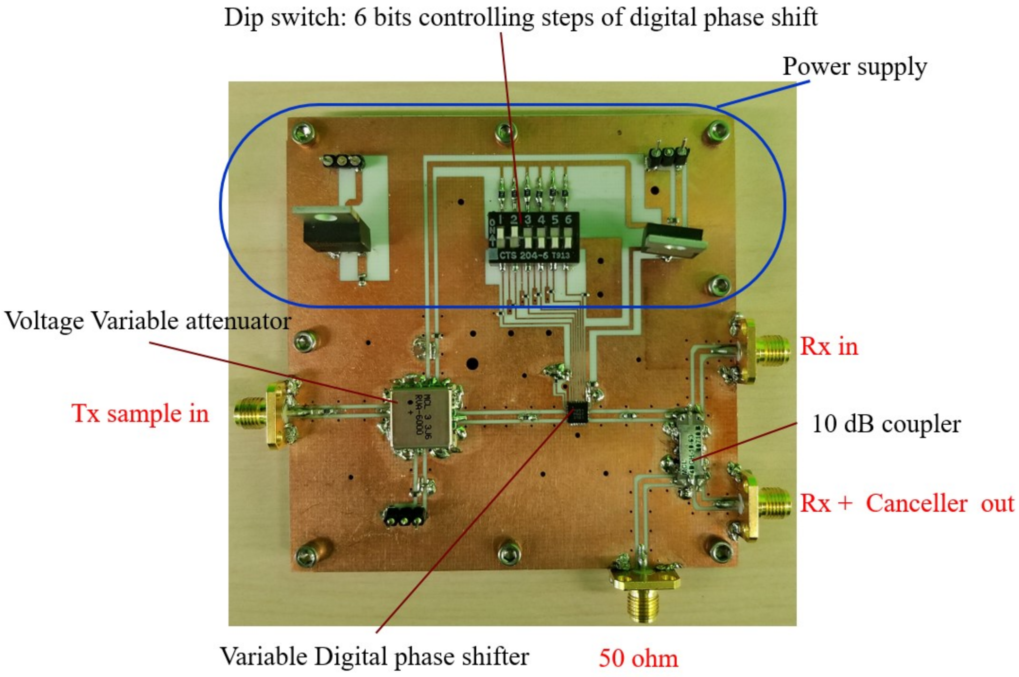

Figure 7.9 Fabricated single tap RF active canceler

The picture of the fabricated circuit is shown in Figure 7.9. Different parts of the circuit are explained in the picture. The top part of the circuit provides regulated +5 and -5 V voltages for both ICs, using commercial LM7805CT and LM7905CT IC linear regulators. The sampled Tx signal is input at the left side of the circuit as indicated and through 50-ohm transmission lines feeding the voltage variable attenuator. The variable attenuator is provided from Mini-Circuits with the model number of 'RVA-6000+' with a tuning range of 32.7 dB over the 2.0-6.0 GHz frequency range. The variable attenuator is controlled using 0-13V bias from an external power supply, with input pins provided below the IC in Figure 7.9. The digital step-phase shifter is a 6-BIT phase shifter in the frequency range of 3.5-6.0 GHz and from Macom Company with the model number MAPS-010165. The digital step-phase shifter has six parallel pins for including/excluding any of the internal six different fixed phase shifts, giving complete 360o phase-shifting coverage in steps of 5.625o. Phase-controlling pins are connected to a pulled-up SPST Dip Switch for simple manipulation of the phase. The digital phase shifter's output is connected to a commercial 10 dB Bi-directional coupler from Mini-circuits with the model number BDCH-10-63. The coupler's through-port output is accessible through a connector for testing purposes, though in actual measurement, it can be terminated to a 50-ohm load. The isolated port should be connected to the antenna's input Rx signal. The coupler's coupling port delivers the supposedly cleaned Rx signal from SI. In other words, this port provides a summation of the Rx signal and manipulated RF signal from the RF SI canceler.

The attenuator and the phase shifter have roughly a minimum insertion loss of 4 and 5 dB, respectively. Excluding a minimum of 10 dB coupling loss, the RF attenuator can cancel a leakage signal in the range of -19 dB to -51.7 dB below the input power. If we assume that a 20 dB coupler is used for Tx sampling, then the mentioned range shifts 20 dB lower. Therefore, if the leakage signal falls within this range, the RF SI canceler circuit can successfully cancel it. If not, a fixed attenuator should be used to push the leakage signal into this range.

In the next section, the RF SI canceler will be used together with the DP Antenna from chapter 6 for performance comparison with the proposed integrated DM circulator and DP antenna.

#### 7.2.3.2 Isolation evaluation in a demo Full-duplex system measurement

A transceiver setup at the analog front-end has been established to assess the proposed integrated DM circulator and DP antenna's isolation within an implemented Full-duplex system. The picture of the setup for this measurement is shown in Figure 7.10. In this setup, a PNA with a spectrum analyzer capability is used as the receiver, and the Rx signal is connected to it. Nevertheless, the Tx setup is a little more complex since we aim to transmit various modulated high-power signals that need to be upconverted from the baseband into the RF domain.

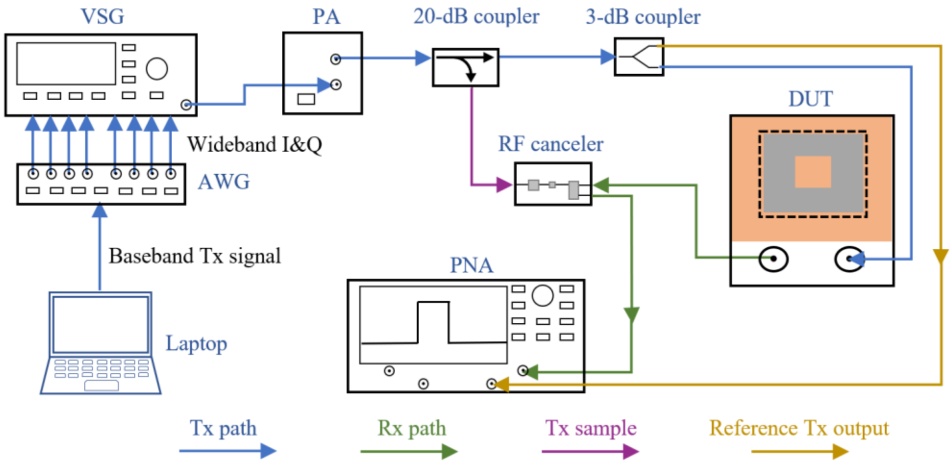

(a)

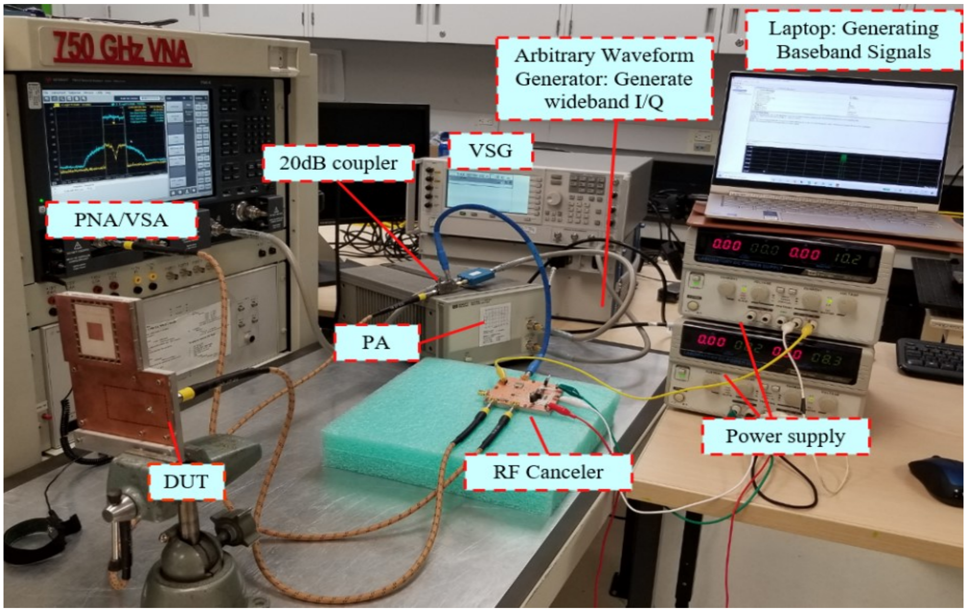

(b)

Figure 7.10 Full-duplex system demonstration of the proposed module and measurement of the isolation within a transceiver setup: (a) Schematic and (b) photo of the measurement setup

First, a Keysight Arbitrary Waveform Generator (AWG) 8190A is used to generate wideband I/Q RF signals. The AWG is connected to a Laptop through a LAN connection. The licensed 'Signal Studio Pro for Custom Modulation' software from Keysight controls the AWG and generates advanced 5G signals at desired bandwidth and modulation. The AWG provides wideband RF I/Q channels at its outputs fed into the Vector Signal Generator (VSG) E8267D from Keysight. The mentioned VSG has a built-in digital modulation system; however, it has a maximum symbol rate of 50 Mbps. Therefore, to generate RF signals with a higher symbol rate, AWG is used to feed the E8762D VSG. Although the VSG can connect directly to the DUT, we have used a commercial power amplifier (PA) following the VSG. The commercial power amplifier is an HP 8348A PA with a 30 dB gain at the operating frequency range, and it produces slightly cleaner signals at high powers relative to the E8267D in the desired frequency range. The output signal of the PA is fed into a power splitter. One output of the power splitter is connected to PNA/VSA to copy the transmitted Tx signal. The other output is connected to the input of the DUT. For measurements concerning RF SI canceler, a 20 dB coupler is added before the DUT to provide a Tx signal sample to the RF SI canceler.

Figure 7.11 exhibits the measurement results for two DUTs. A 64 QAM signal with a bandwidth of 90 MHz and band power of 10 dBm is transmitted from the Tx chain in these measurements. Figure 7.11(a) displays measurement concerning the DP antenna from chapter 6 in conjunction with the presented active RF SI canceler circuit. This measurement confirms that the DP antenna itself can provide up to 42 dB SI cancelation. By tuning the RF SI canceler, a SI cancelation up to 70 dB has been realized; however, over a significantly narrow bandwidth. The Rx signal's V-shaped response acknowledges the RF SI canceler's narrowband nature, failing to fulfill the high isolation requirement for full-duplex transceivers over wideband signals needed in 5G systems.

On the other hand, Figure 7.11(b) concerns measuring the proposed integrated DM circulator and DP antenna without the RF SI canceler. This figure reveals that the proposed module is solely capable of canceling SI signals up to 70 dB over an extensive bandwidth of 90 MHz, which is suitable for 5G full-duplex transceivers. The addition of the RF SI canceler to the proposed module resulted in small and narrowband enhancement, proving that our proposed device outperforms the active RF SI canceler methodology.

The significant difference between the two results and the proposed all-passive module’s excellent performance promises an efficient enabling solution for full-duplex systems.

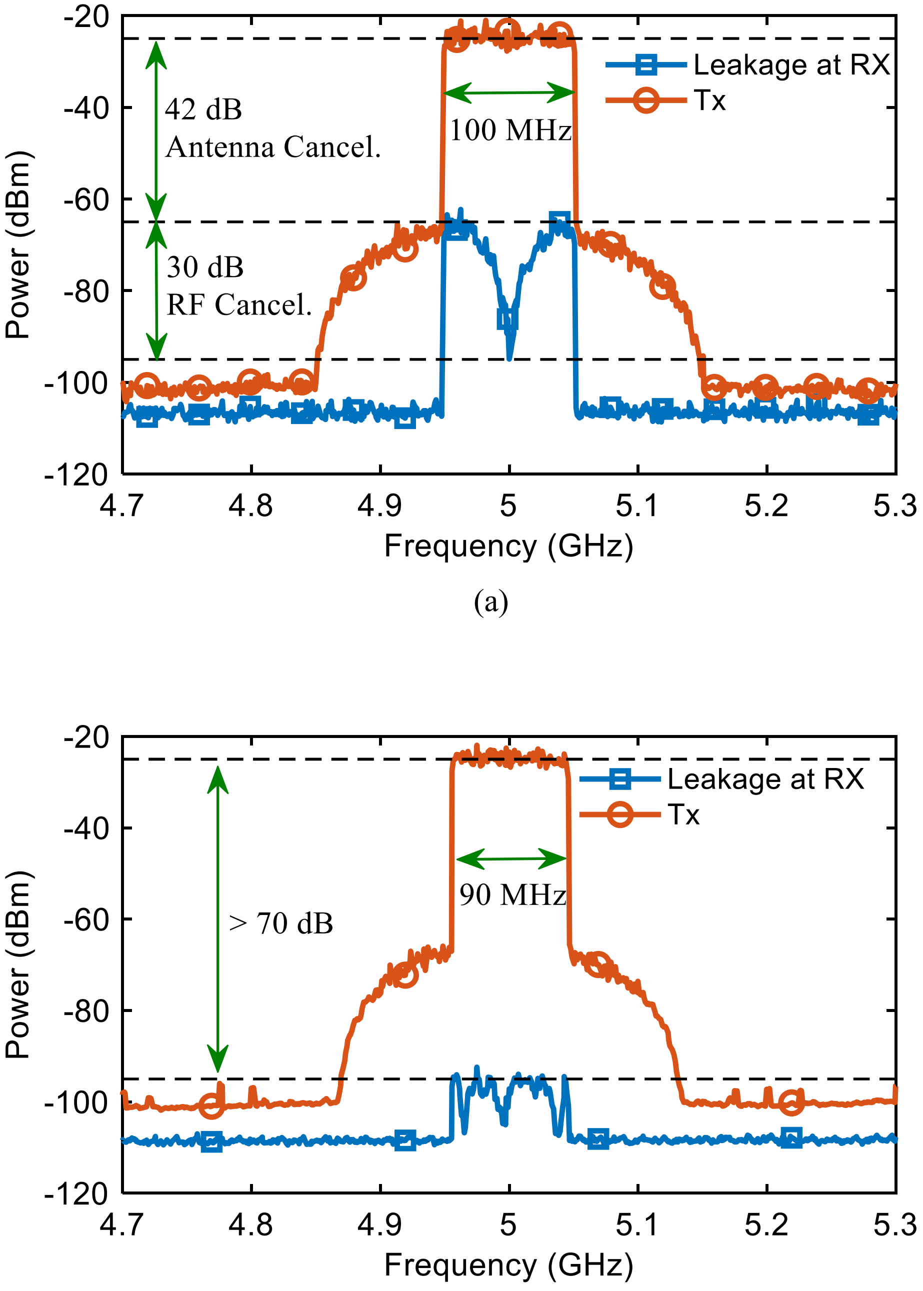

(a)

(b)

Figure 7.11 Measured Tx/Rx isolation in a Full-duplex front-end system for two components: (a) DP antenna with the active single tap RF canceler, demonstrating 70 dB isolation over a very narrow band frequency range, (b) Proposed DM circulator and DP antenna without the RF canceler, demonstrating 70 dB isolation over 90 MHz bandwidth

#### 7.2.3.3 Full-Duplex communication-link measurement

In the second system measurement, we focused on the module's communication performance, where the effect of the interference signal (which can be considered noise) on the desired Rx signals is investigated. Several communication metrics are available for measuring the effect of noise on the desired signal, including SNR, EVM, and BER that all are related directly or indirectly to each other. Here in this work, we consider EVM measurement to give us a clear picture and information on digital modulation distortions.

Figure 7.12 illustrates the measurement setup for the communication link measurement, which is like the previous setup. Here, two VSGs are utilized for transmitting high-power modulated RF signals at two nodes. The first node or full-duplex (FD) node denotes the proposed integrated DM circulator and DP antenna component, where port 3 (exciting $TE_{10}$ waveguide mode and vertical polarization in the antenna) and port 2 (exciting $TE_{20}$ waveguide mode and horizontal polarization in the antenna) are dedicated for Tx and Rx signals, respectively. A transmitting antenna is placed at the second node to transmit the desired signal to the FD node. For this measurement, we used the DP antenna from chapter 6 as the transmitting antenna, where a Tx signal from the second VGA was connected to antenna's port 2 (exciting $TE_{20}$ waveguide mode and horizontal polarization in the antenna), and port 1 was left unused and matched to a 50-ohm load. Another difference is that an N9030A PXA Signal Analyzer from Keysight is substituted with the PNA at the receiver side. The advantage is that the PXA also measures the signal's phase information and can demodulate and analyze the complex received signal. The PXA is connected to a Laptop for demodulation, where a licensed software '89601 VSA' from Keysight is used. The software can perform advanced digital demodulation and various digital analysis on the measured Rx signal.

Two nodes are placed about 60 cm apart. This distance is far enough that the antenna at node two does not interfere with the antenna's radiation at node 1. The RF path loss for this distance is about 42 dB. Considering an average antenna gain of 8 dBi for each antenna and an aggregated RF loss of about 3 dB accounted for long cables, connectors, and the antennas' insertion losses, the resulted power loss from node two to node one is about 29 dB. In this measurement, VSG 1 is connected to the Tx port of node one and transmits an 80 MHz 256 QAM signal at 10 dBm power. The VSG 2 is connected to the Tx port of node two and transmits an 80 MHz signal at various QAM modulations and various output powers. This measurement aims to assess the effect of noise (leakage from VSG 1 to Rx channel on node one) on the input received signal for various modulation schemes and variations of input powers. Therefore, VSG 2 output power varies from +10 to -30 dBm, which translates to a received power of -19 to -54 dBm at the receiver of node one. Moreover, it should be mentioned that RF absorbers are placed around two antennas to minimize environmental reflections.

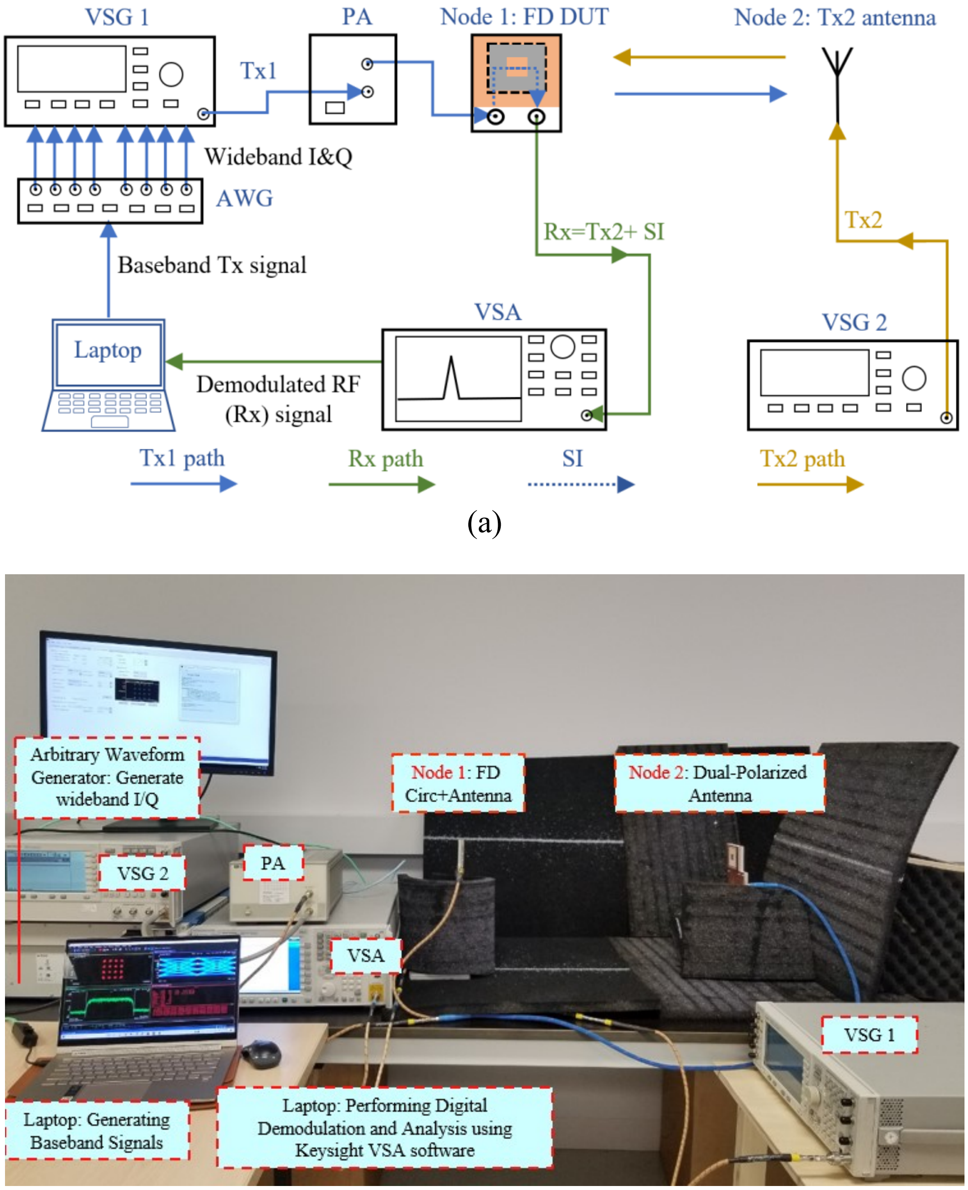

(a)

(b)

Figure 7.12 Full-duplex communication link demonstration of the proposed module and measurement of the demodulated received data signal in the presence of SI: (a) Schematic and (b) photo of the measurement setup

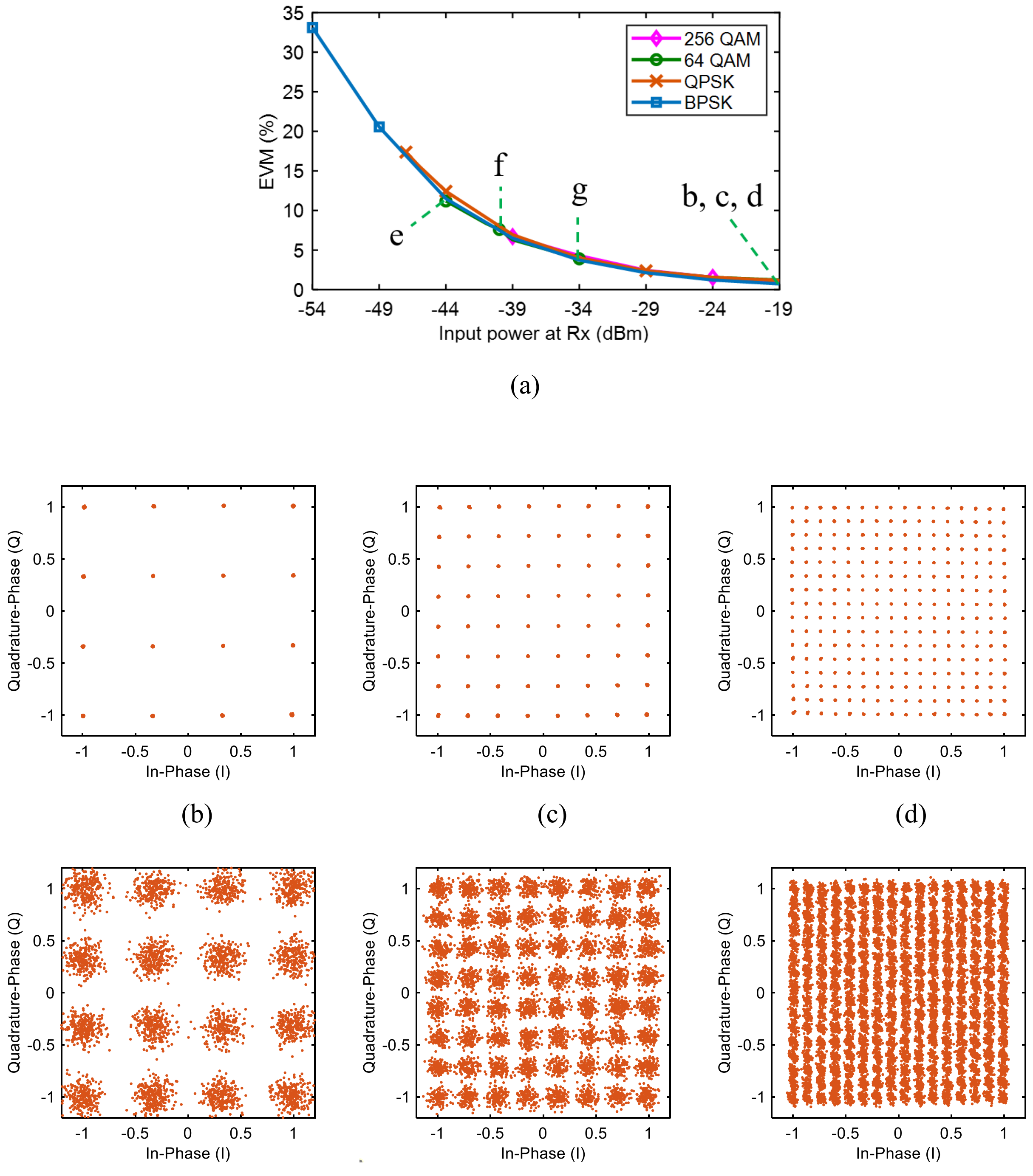

(a)

(b) (c) (d)

(e) (f) (g)

Figure 7.13 EVM measurement versus input power of the received signal: (b-d) 16, 64, and 256 QAM constellations at maximum power, (e-d) same constellations at their maximum acceptable limit corresponding to -44, -40, -34 dBm RX input power

Figure 7.13(a) displays measured EVM for different modulation schemes while received power of the desired signal was swept as explained above. It is discerned that as the input power decreases, the EVM increases since the Signal to Noise Ratio (SNR) decreases. In addition, since EVM is independent of the modulation scheme, the EVM measurements for all modulations yield similar results. Figure 7.13(b)-(d) illustrates the QAM constellation of the received signal at -19dBm input power and for 16, 64, and 256 QAM modulations. EVM requirement for different 5G QAM modulation schemes specifies that maximum EVM for QPSK, 16 QAM, 64 QAM and 256 QAM signals are 17.5, 12.5, 8 and 3.5 %, respectively [131]. Hence, the required input power for a proper 5G communication link increases as the order of modulation increases. Figure 7.13(e)-(g) exhibits the constellations for 16, 64, and 256 QAM schemes near their maximum acceptable value, which correspond to -34, -40, and -44 dBm input powers, respectively.

The last two measurements demonstrate that the proposed integrated DM circulator and DP antenna front-end component can effectively enable FD systems in the sub-6GHz frequency range according to 5G and future wireless systems' requirements.

### 7.2.4 Design consideration that has enabled a breakthrough in realizing ultra-high isolation in a passive structure

As mentioned in the last section of chapter 2, four critical constraints set the benchmark in realizing high isolation in passive structures. To accomplish the reported high isolation, we considered all the mentioned constraints and devised a solution for each of them. To minimize the effect of higher-order modes and undesired inter-port coupling, we employed SIW and stripline structures that provide high electromagnetic shielding and restrains inter-port couplings. Further, via loadings around the stripline provided sufficient shielding to avoid inter-substrate couplings. Second, the dual-polarized antenna was employed that eliminates the inherent input reflection problem associated with single-polarized antenna configurations. Third, the antenna was designed to have low cross-polarization, resulting in high-inter-port isolation at the antenna interface itself. Forth, we employed an integrated DM circulator and DP antenna, which enhanced primary isolation for two main reasons. First, the structure provided two leakage cancelation stages thanks to both the DP antenna and the DM circulator's inherent isolations that were harvested in connection with each other. Second, the integrated solution eliminated the intermediate transitions between the antenna and the circulator, a significant source of mode conversion and inter-port couplings due to the introduction of numerous asymmetrical discontinuities.

Despite all these attempts still, fabrication tolerance and cross-coupling at antenna interface limit the isolation critically. As we mentioned in chapter 2, to battle against these two restrictions, the only option is to generate a replica signal and subtract it from the leakage signal. In active SIC methods this procedure is done using a complex RF active solution. However, we demonstrated that our proposed solution contains a self-consistent passive SIC scheme by exploiting the ferrite's tunability in controlling the mode conversion within a dual-mode SIW.

Therefore, thanks to all these contributions, realizing ultra-high isolation in a passive structure became a reality.

# CHAPTER 8 GENERAL DISCUSSIONS

In this thesis, we proposed a novel and fundamental solution to enable a full-duplex transceiver by achieving ultra-high isolation in the analog domain at the front end. Theoretically, our approach was based on employing an integrated dual-polarized antenna and dual-mode circulator instead of the using separately conventional single polarize antenna and single-mode circulator.

Our main aim was to present a solution that can be deployed in future wireless systems as a ubiquitous solution. To achieve this goal, the proposed solution must have certain features which are mostly absent in the proposed solutions in the literature. For example, such a system should be low-cost and easy to fabricate for mass productions. In this regard, we aimed to implement our circuit as an integrated PCB solution, which is the most popular and low-cost technique currently. In addition, the proposed solution must be efficient, highly linear, low noise, consume low power and have the capability to be extended into other techniques such as MIMO. While a majority of these features are not satisfied with current state-of-art solutions introduced in the literature, our solution meets them since it is an all-passive structure.

From a technical point of view, employing a dual-polarized antenna had already been studied and investigated by other authors as covered in the literature review section as an effective way to achieve better than 40 dB isolation. However, yielding isolations over this value has been a significant obstacle that has pushed the researchers to resort to other techniques. The main and most common approach to realize ultra-high isolations (over 60 dB) currently is limited to RF active SIC techniques, which use active circuits to create a replica of the transmitted signal and then subtract it from the receiver chain. This method which was thoroughly covered in the literature review has some major drawbacks such as having a complex RF structure, large power consumption, low bandwidth, low-linearity, and high input noise. However, our proposed solution solves the problem from a fundamental point of view. In the proposed solution, orthogonality of the transmitter and receiver signals have been maintained through the entire front-end channel using a dual-mode circulator and antenna.

Further, fabrication and measurement results are in excellent agreement with theoretical foundations and simulations, validating the proposed theory. Therefore, we claim that we have been able to propose, develop and demonstrate a full-duplex system that excels current existing solutions as covered in the literature.

Finally, it should be mentioned that in this thesis electromagnetic simulations were performed using CST Microwave Studio, numerical coding was scripted in MATLAB software and PCB drawings were done in ADS software. All fabrication and measurements were done and carried out at the fully equipped labs of the Poly-Grames.

# CHAPTER 9 CONCLUSION AND RECOMMENDATIONS

## 9.1 Conclusion

This thesis aims to propose a novel methodology to demonstrate a passive front-end module to enable the development of truly full-duplex transceivers to be employed in 5G and future wireless systems. To accomplish this task, we developed a fundamental and mathematical model and theory to attain novel nonreciprocal components based on ferrite materials. Based on the proposed theories, we proposed unprecedented and fresh insights revealing new and far more efficient methodologies to deal with self-interference (SI) problems associated with Full-duplex transceivers. We envision that this new methodology would light the path for future research to expand this solution and employ full-duplex transceivers as a prevalent and best-performing architecture according to new radio 5G and future wireless systems.

In this Ph.D. thesis, we have accomplished four objectives that were defined at the beginning of our research journey. We developed a novel passive SIC method, like active SIC methods, to boost the isolation by exploiting a nonreciprocal mode conversion mechanism in chapters 3 and 4. Second, in chapter 5, not only we developed a DM circulator that significantly enhances the isolation benchmark of the typical circulators, but also we presented a generalized theory that presents a comprehensive procedure for the design of nonreciprocal components into a multi-mode configuration. Besides the DM circulator, a triple-mode gyrator was demonstrated for the first time, showing the applicability of the developed theory. Third, in chapter 6, we developed and demonstrated a novel DP antenna based on the dual-mode SIW. This special antenna was designed according to the structure of the DM circulator to operate concurrently with two dominant modes of the waveguide. Finally, in chapter 7, we integrated the DM circulator and DP antenna into a monolithic design to enhance isolation with significant suppression of higher modes and electromagnetic shielding to avoid cross-coupling. The fabricated prototype was successfully tested and demonstrated in a Full-duplex system fulfilling the primary goal of this thesis.

In particular, in this work, we developed and prototyped six novel components, including a nonreciprocal mode-converter waveguide for ferrite materials with high saturation magnetization, a nonreciprocal mode-converter waveguide for ferrite materials with low saturation magnetization, a dual-mode circulator, a triple-mode gyrator, a dual-polarized antenna and an integrated dual-mode circulator and dual-polarized antenna with ultra-high isolation for full-duplex transceivers.

These components were supported with extensive and fundamental theories that all resulted in the introduction of novel concepts and components for the first time.

## 9.2 Constraints

It should be mentioned that the presented methodology has its constraints. The main constraint is that ferrite materials require external magnetic biasing. Providing this external magnetic biasing might not be desired in some applications. Further, and in connection to magnetic biasing, the proposed theories and components are fundamentally scalable in frequency; however, as frequency increases, the required magnetic bias increase linearly with frequency. Therefore, in practice and due to magnetic biasing limitations, these techniques are not applicable in millimetre-wave and higher frequencies. Finally, the use of ferrites and waveguide components limits the use of this technique in radio-frequency integrated circuit (RFIC) technologies, which might hinder their applicability in some applications regarding hand-held communication devices.

## 9.3 Future works

This work can be continued or be expanded in several paths. The future works can be either in system-level or component level research, that here we mention some of our recommendations to interested researchers:

- The developed nonreciprocal mode-converter components can be exploited to design novel integrated components such as integrated isolator and balun, integrated isolator, and combiner.
- Regarding the limitations of this work mentioned earlier, self-biased ferrite materials can be explored in future research to investigate their potential in being employed within the proposed concepts and theories in millimetre-wave frequencies. Self-biased ferrites are another type of ferrite material that posses an internal strong anisotropy field that eliminates the need for an external biasing field and, for this reason, can be deployed in millimetre-wave frequencies.
- The high isolation achieved in this work is not critically dependent on antenna topology. As long as a dual-polarized antenna can achieve isolation better than 40 dB and a methodology to integrate it with the DM circulator is available, it can be substituted with

the present antenna. Therefore, novel and enhanced DP antenna configurations can be explored to improve or modify the antenna's radiation performance or bandwidth for future work.

- In connection to the previous suggestion, this work can be expanded into an array antenna to achieve a MIMO FD transceiver.
- Higher-order waveguide modes can be the subject of future works to realize multi-function components and systems. In particular, multi-mode nonreciprocal ferrite-loaded SIWs can be exploited for this purpose.
- Finally, and in the most appealing configuration, this work can be expanded to integrate an FD radio with a radar system to yield a joint FD radio and radar system. This integration is entirely within grasp since radar systems are based on full-duplex simultaneous transmission and reception too.

# REFERENCES

[1] Z. Zhang, X. Chai, K. Long, A. V. Vasilakos, and L. Hanzo, "Full duplex techniques for 5G networks: self-interference cancellation, protocol design, and relay selection," *IEEE Communications Magazine,* vol. 53, 5, pp. 128-137, 2015.

[2] F. Boccardi, R. W. Heath, A. Lozano, T. L. Marzetta, and P. Popovski, "Five disruptive technology directions for 5G," *IEEE Communications Magazine,* vol. 52, 3, pp. 74-80, 2014.

[3] C. Wang *et al.*, "Cellular architecture and key technologies for 5G wireless communication networks," *IEEE Communications Magazine,* vol. 52, 2, pp. 122-130, 2014.

[4] L. Zhang and N. Ansari, "A Framework for 5G Networks with In-Band Full-Duplex Enabled Drone-Mounted Base-Stations," *IEEE Wireless Communications,* vol. 26, no. 5, pp. 121-127, 2019, doi: 10.1109/mwc.2019.1800486.

[5] X. Xia, K. Xu, Y. Wang, and Y. Xu, "A 5G-Enabling Technology: Benefits, Feasibility, and Limitations of In-Band Full-Duplex mMIMO," *IEEE Vehicular Technology Magazine,* vol. 13, no. 3, pp. 81-90, 2018, doi: 10.1109/mvt.2018.2792198.

[6] Z. Xiao, P. Xia, and X.-G. Xia, "Full-Duplex Millimeter-Wave Communication," *IEEE Wireless Communications,* vol. 24, no. 6, pp. 136-143, 2017, doi: 10.1109/mwc.2017.1700058.

[7] R. Li, Y. Chen, G. Y. Li, and G. Liu, "Full-Duplex Cellular Networks," *IEEE Communications Magazine,* vol. 55, no. 4, pp. 184-191, 2017, doi: 10.1109/mcom.2017.1600361cm.

[8] K. E. Kolodziej, B. T. Perry, and J. S. Herd, "In-Band Full-Duplex Technology: Techniques and Systems Survey," *IEEE Transactions on Microwave Theory and Techniques,* vol. 67, no. 7, pp. 3025-3041, 2019, doi: 10.1109/tmtt.2019.2896561.

[9] M. S. Sim, M. Chung, D. Kim, J. Chung, D. K. Kim, and C.-B. Chae, "Nonlinear Self-Interference Cancellation for Full-Duplex Radios: From Link-Level and System-Level Performance Perspectives," *IEEE Communications Magazine,* vol. 55, no. 9, pp. 158-167, 2017, doi: 10.1109/mcom.2017.1600264.

[10] C. Sexton, N. J. Kaminski, J. M. Marquez-Barja, N. Marchetti, and L. A. DaSilva, "5G: Adaptable Networks Enabled by Versatile Radio Access Technologies," *IEEE Communications Surveys & Tutorials,* vol. 19, no. 2, pp. 688-720, 2017, doi: 10.1109/comst.2017.2652495.

[11] J. Zhou *et al.*, "Integrated full duplex radios," *IEEE Communications Magazine,* vol. 55, no. 4, pp. 142-151, 2017, doi: 10.1109/mcom.2017.1600583.

[12] L. Zhang, M. Xiao, G. Wu, M. Alam, Y.-C. Liang, and S. Li, "A Survey of Advanced Techniques for Spectrum Sharing in 5G Networks," *IEEE Wireless Communications,* vol. 24, no. 5, pp. 44-51, 2017, doi: 10.1109/mwc.2017.1700069.

[13] A. Goldsmith, *Wireless Communications*. Cambridge: Cambridge University Press, 2005.

[14] A. C. Cirik, M. C. Filippou, and T. Ratnarajah, "Transceiver Design in Full-Duplex MIMO Cognitive Radios Under Channel Uncertainties," *IEEE Transactions on Cognitive*

*Communications and Networking,* vol. 2, no. 1, pp. 1-14, 2016, doi: 10.1109/tccn.2016.2572691.

[15] M. Zhou, L. Song, Y. Li, and X. Li, "Simultaneous Bidirectional Link Selection in Full Duplex MIMO Systems," *IEEE Transactions on Wireless Communications,* vol. 14, no. 7, pp. 4052-4062, 2015, doi: 10.1109/twc.2015.2416187.

[16] Y. Hua, P. Liang, Y. Ma, A. C. Cirik, and Q. Gao, "A Method for Broadband Full-Duplex MIMO Radio," *IEEE Signal Processing Letters,* vol. 19, no. 12, pp. 793-796, 2012, doi: 10.1109/lsp.2012.2221710.

[17] D. Bharadia, E. McMilin, and S. Katti, "Full duplex radios," *SIGCOMM Comput. Commun. Rev.,* vol. 43, no. 4, pp. 375–386, 2013, doi: 10.1145/2534169.2486033.

[18] S. Hong *et al.*, "Applications of self-interference cancellation in 5G and beyond," *IEEE Communications Magazine,* vol. 52, 2, pp. 114-121, 2014.

[19] M. Katanbaf, K.-D. Chu, T. Zhang, C. Su, and J. C. Rudell, "Two-Way Traffic Ahead: RF\/Analog Self-Interference Cancellation Techniques and the Challenges for Future Integrated Full-Duplex Transceivers," *IEEE Microwave Magazine,* vol. 20, no. 2, pp. 22-35, 2019, doi: 10.1109/mmm.2018.2880489.

[20] W. Li, J. Lilleberg, and K. Rikkinen, "On Rate Region Analysis Of Half- and Full-Duplex OFDM Communication Links," *IEEE Journal on Selected Areas in Communications,* vol. 32, no. 9, pp. 1688-1698, 2014, doi: 10.1109/jsac.2014.2330131.

[21] A. Sahai, G. Patel, C. Dick, and A. Sabharwal, "On the Impact of Phase Noise on Active Cancelation in Wireless Full-Duplex," *IEEE Transactions on Vehicular Technology,* vol. 62, no. 9, pp. 4494-4510, 2013, doi: 10.1109/tvt.2013.2266359.

[22] J. I. Choi, M. Jain, K. Srinivasan, P. Levis, and S. Katti, "Achieving Single Channel, Full Duplex Wireless Communication," in *ACM MOBICOM*, Chicago, 2010.

[23] A. Masmoudi and T. Le-Ngoc, "Channel estimation and self-interference cancelation in full-duplex communication systems," *IEEE Transactions on Vehicular Technology,* vol. 66, no. 1, pp. 321-334, 2017, doi: 10.1109/tvt.2016.2540538.

[24] M. Bernhardt, F. Gregorio, J. Cousseau, and T. Riihonen, "Self-interference cancelation through advanced sampling," *IEEE Transactions on Signal Processing,* vol. 66, no. 7, pp. 1721-1733, 2018, doi: 10.1109/tsp.2018.2793864.

[25] Y. Liu, X. Zhu, E. G. Lim, Y. Jiang, and Y. Huang, "Fast Iterative Semi-Blind Receiver for URLLC in Short-Frame Full-Duplex Systems With CFO," *IEEE Journal on Selected Areas in Communications,* vol. 37, no. 4, pp. 839-853, 2019, doi: 10.1109/jsac.2019.2898746.

[26] B. Debaillie *et al.*, "Analog/RF Solutions Enabling Compact Full-Duplex Radios," *IEEE Journal on Selected Areas in Communications,* vol. 32, no. 9, pp. 1662-1673, 2014, doi: 10.1109/jsac.2014.2330171.

[27] L. Laughlin, M. A. Beach, K. A. Morris, and J. L. Haine, "Electrical balance duplexing for small form factor realization of in-band full duplex," *IEEE Communications Magazine,* vol. 53, no. 5, pp. 102-110, 2015, doi: 10.1109/MCOM.2015.7105648.

[28] Y. Jin and S. Hong, "28-GHz In-Band Full-Duplex Power Amplifier Integrated With an Impedance Matched Hybrid Transformer," *IEEE Microwave and Wireless Components Letters,* vol. 30, no. 4, pp. 410-413, 2020, doi: 10.1109/lmwc.2020.2968551.

[29] N. Van Thienen, Y. Zhang, and P. Reynaert, "Bidirectional Communication Circuits for a 120-GHz PMF Data Link in 40-nm CMOS," *IEEE Journal of Solid-State Circuits,* vol. 53, no. 7, pp. 2023-2031, 2018, doi: 10.1109/jssc.2018.2822714.

[30] Y. Liu, S. Wang, X. Wang, and Y. Jia, "A Differentially Fed Dual-Polarized Slot Antenna With High Isolation and Low Profile for Base Station Application," *IEEE Antennas and Wireless Propagation Letters,* vol. 18, no. 2, pp. 303-307, 2019, doi: 10.1109/lawp.2018.2889645.

[31] J. Li, S. Yang, Y. Gou, J. Hu, and Z. Nie, "Wideband Dual-Polarized Magnetically Coupled Patch Antenna Array With High Port Isolation," *IEEE Transactions on Antennas and Propagation,* vol. 64, no. 1, pp. 117-125, 2016, doi: 10.1109/tap.2015.2502264.

[32] Y. Li, Z. Zhao, Z. Tang, and Y. Yin, "Differentially Fed, Dual-Band Dual-Polarized Filtering Antenna With High Selectivity for 5G Sub-6 GHz Base Station Applications," *IEEE Transactions on Antennas and Propagation,* vol. 68, no. 4, pp. 3231-3236, 2020, doi: 10.1109/tap.2019.2957720.

[33] Y. Hou, Z. Shao, Y. Zhang, and J. Mao, "A Wideband Differentially-fed Dual-polarized Laminated Resonator Antenna," *IEEE Transactions on Antennas and Propagation,* pp. 1-1, 2021, doi: 10.1109/tap.2020.3048537.

[34] X. Ren, S. Liao, and Q. Xue, "A Differentially Fed Dual-Polarized Magnetic Dipole Antenna for Spaceborne Applications," *IEEE Transactions on Antennas and Propagation,* vol. 67, no. 2, pp. 861-871, 2019, doi: 10.1109/tap.2018.2883526.

[35] B. Feng, L. Li, J.-C. Cheng, and C.-Y.-D. Sim, "A Dual-Band Dual-Polarized Stacked Microstrip Antenna With High-Isolation and Band-Notch Characteristics for 5G Microcell Communications," *IEEE Transactions on Antennas and Propagation,* vol. 67, no. 7, pp. 4506-4516, 2019, doi: 10.1109/tap.2019.2911619.

[36] X. Yang, L. Ge, J. Wang, and C.-Y.-D. Sim, "A Differentially Driven Dual-Polarized High-Gain Stacked Patch Antenna," *IEEE Antennas and Wireless Propagation Letters,* vol. 17, no. 7, pp. 1181-1185, 2018, doi: 10.1109/lawp.2018.2837116.

[37] L.-H. Wen *et al.*, "A Wideband Differentially Fed Dual-Polarized Antenna With Wideband Harmonic Suppression," *IEEE Transactions on Antennas and Propagation,* vol. 67, no. 9, pp. 6176-6181, 2019, doi: 10.1109/tap.2019.2920230.

[38] J. Zhou, T.-H. Chuang, T. Dinc, and H. Krishnaswamy, "Integrated Wideband Self-Interference Cancellation in the RF Domain for FDD and Full-Duplex Wireless," *IEEE Journal of Solid-State Circuits,* vol. 50, no. 12, pp. 3015-3031, 2015, doi: 10.1109/jssc.2015.2477043.

[39] A. Nagulu, T. Chen, G. Zussman, and H. Krishnaswamy, "A Full-Duplex Radio Using a CMOS Non-Magnetic Circulator Achieving +95 dB Overall SIC," presented at the USNC-URSI Radio Science Meeting (Joint with AP-S Symposium), Atlanta, GA, USA, 2019.

[40] M. Jain *et al.*, "Practical, Real-time, Full Duplex Wireless," *MobiCom '11: Proceedings of the 17th annual international conference on Mobile computing and networking,* pp. 301–312, 2011.

[41] T. Dinc, A. Chakrabarti, and H. Krishnaswamy, "A 60 GHz CMOS Full-Duplex Transceiver and Link with Polarization-Based Antenna and RF Cancellation," *IEEE Journal of Solid-State Circuits,* vol. 51, no. 5, pp. 1125-1140, 2016, doi: 10.1109/jssc.2015.2507367.

[42] K. Park, J. Myeong, G. M. Rebeiz, and B.-W. Min, "A 28-GHz Full-Duplex Phased Array Front-End Using Two Cross-Polarized Arrays and a Canceller," *IEEE Transactions on Microwave Theory and Techniques,* vol. 69, no. 1, pp. 1127-1135, 2021, doi: 10.1109/tmtt.2020.3039782.

[43] T. Chi, J. S. Park, S. Li, and H. Wang, "A Millimeter-Wave Polarization-Division-Duplex Transceiver Front-End With an On-Chip Multifeed Self-Interference-Canceling Antenna and an All-Passive Reconfigurable Canceller," *IEEE Journal of Solid-State Circuits,* vol. 53, no. 12, pp. 3628-3639, 2018, doi: 10.1109/jssc.2018.2878823.

[44] S. Maddio, A. Cidronali, and G. Manes, "Real-Time Adaptive Transmitter Leakage Cancelling in 5.8-GHz Full-Duplex Transceivers," *IEEE Transactions on Microwave Theory and Techniques,* vol. 63, no. 2, pp. 509-519, 2015, doi: 10.1109/tmtt.2014.2387841.

[45] K. E. Kolodziej, J. G. McMichael, and B. T. Perry, "Multitap RF Canceller for In-Band Full-Duplex Wireless Communications," *IEEE Transactions on Wireless Communications,* vol. 15, no. 6, pp. 4321-4334, 2016, doi: 10.1109/twc.2016.2539169.

[46] L. Zhang, M. Ma, and B. Jiao, "Design and Implementation of Adaptive Multi-Tap Analog Interference Canceller," *IEEE Transactions on Wireless Communications,* vol. 18, no. 3, pp. 1698-1706, 2019, doi: 10.1109/twc.2019.2895635.

[47] T. Zhang, C. Su, A. Najafi, and J. C. Rudell, "Wideband Dual-Injection Path Self-Interference Cancellation Architecture for Full-Duplex Transceivers," *IEEE Journal of Solid-State Circuits,* vol. 53, no. 6, pp. 1563-1576, 2018, doi: 10.1109/jssc.2018.2805874.

[48] M. Baraani Dastjerdi, S. Jain, N. Reiskarimian, A. Natarajan, and H. Krishnaswamy, "Analysis and Design of a Full-Duplex Two-Element MIMO Circulator-Receiver With High TX Power Handling Exploiting MIMO RF and Shared-Delay Baseband Self-Interference Cancellation," *IEEE Journal of Solid-State Circuits,* vol. 54, no. 12, pp. 3525-3540, 2019, doi: 10.1109/jssc.2019.2945303.

[49] A. Mirzaei, H. Darabi, A. Yazdi, Z. Zhou, E. Chang, and P. Suri, "A 65 nm CMOS Quad-Band SAW-Less Receiver SoC for GSM/GPRS/EDGE," *IEEE Journal of Solid-State Circuits,* vol. 46, no. 4, pp. 950-964, 2011, doi: 10.1109/jssc.2011.2109570.

[50] A. Ghaffari, E. A. M. Klumperink, M. C. M. Soer, and B. Nauta, "Tunable High-Q N-Path Band-Pass Filters: Modeling and Verification," *IEEE Journal of Solid-State Circuits,* vol. 46, no. 5, pp. 998-1010, 2011, doi: 10.1109/jssc.2011.2117010.

[51] Y. Cao and J. Zhou, "Integrated Self-Adaptive and Power-Scalable Wideband Interference Cancellation for Full-Duplex MIMO Wireless," *IEEE Journal of Solid-State Circuits,* vol. 55, no. 11, pp. 2984-2996, 2020, doi: 10.1109/jssc.2020.3005755.

[52] Y. Liu, P. Roblin, X. Quan, W. Pan, S. Shao, and Y. Tang, "A Full-Duplex Transceiver With Two-Stage Analog Cancellations for Multipath Self-Interference," *IEEE Transactions on Microwave Theory and Techniques,* vol. 65, no. 12, pp. 5263-5273, 2017, doi: 10.1109/tmtt.2017.2752167.

[53] B. King, J. Xia, and S. Boumaiza, "Digitally Assisted RF-Analog Self Interference Cancellation for Wideband Full-Duplex Radios," *IEEE Transactions on Circuits and Systems II: Express Briefs,* vol. 65, no. 3, pp. 336-340, 2018, doi: 10.1109/tcsii.2017.2736252.

[54] A. Kiayani *et al.*, "Adaptive Nonlinear RF Cancellation for Improved Isolation in Simultaneous Transmit–Receive Systems," *IEEE Transactions on Microwave Theory and Techniques,* vol. 66, no. 5, pp. 2299-2312, 2018, doi: 10.1109/tmtt.2017.2786729.

[55] W. J. Ince and E. Stern, "Nonreciprocal Remanence Phase Shifters in Rectangular Waveguide," IEEE Trans. Microw. Theory Techn., vol. 15, no. 2, pp. 87-95, February 1967.

[56] Cham Kiong Queck and L. E. Davis, "Microstrip and stripline ferrite-coupled-line (FCL) circulator's," IEEE Trans. Microw. Theory Techn., vol. 50, no. 12, pp. 2910-2917, Dec 2002.

[57] J. Yamauchi, T. Ueda, Y. Kubo and T. Itoh, "Enhancement of Phase-Shifting Nonreciprocity in Microstrip-Line-Based Metamaterials by Using a Combination of Their Curvatures and Asymmetrical Insertion of Stubs," IEEE Trans. Microw. Theory Techn., vol. 65, no. 12, pp. 5123-5132, Dec. 2017.

[58] S. Adhikari, S. Hemour, A. Ghiotto and K. Wu, "Magnetically Tunable Ferrite-Loaded Half-Mode Substrate Integrated Waveguide," IEEE Microw. Wireless Compon. Lett., vol. 25, no. 3, pp. 172-174, March 2015.

[59] S. Adhikari, A. Ghiott o and K. Wu, "Simultaneous Electric and Magnetic Two-Dimensionally Tuned Parameter-Agile SIW Devices," IEEsE Trans. Microw. Theory Techn., vol. 61, no. 1, pp. 423-435, Jan. 2013.

[60] S. Hemour, S. Adhikari, A. Ghiotto, and K. Wu, “Low magnetic biased SIW-based isolator: Effect of the rising temperature on the performance of the isolator,” Proc. IEEE Wireless Microw. Technol. Conf., Jun. 2014, pp. 1–3.

[61] L. Tan, R. Wu, C. Wang and Y. Poo, "Ferrite-Loaded SIW Bowtie Slot Antenna with Broadband Frequency Tunability," IEEE Antennas and Wireless Propag. Lett., vol. 13, pp. 325-328, 2014.

[62] A. Nafe, F. A. Ghaffar, M. F. Farooqui and A. Shamim, "A Ferrite LTCC-Based Monolithic SIW Phased Antenna Array," IEEE Trans. Antennas Propag., vol. 65, no. 1, pp. 196-205, Jan. 2017.

[63] Y. J. Cheng, Q. D. Huang, Y. R. Wang and J. L. Li, "Narrowband Substrate Integrated Waveguide Isolators," IEEE Microw. Wireless Compon. Lett., vol. 24, no. 10, pp. 698-700, Oct. 2014.

[64] L. Tan, R. Wu and Y. Poo, "Magnetically Reconfigurable SIW Antenna with Tunable Frequencies and Polarizations," IEEE Trans. Antennas Propag., vol. 63, no. 6, pp. 2772-2776, June 2015.

[65] C. E. Fay and R. L. Comstock, "Operation of the Ferrite Junction Circulator," IEEE Trans. Microw. Theory Techn., vol. 13, no. 1, pp. 15-27, January 1965.

[66] H. Bosma, “On the principle of stripline circulation,” Proc. Inst. Elect. Eng., vol. 109B, pp. 137–146, Jan. 1962.

[67] W. D'Orazio and K. Wu, "Substrate-Integrated-Waveguide Circulators Suitable for Millimeter-Wave Integration," IEEE Trans. Microw. Theory Techn., vol. 54, no. 10, pp. 3675-3680, Oct. 2006.

[68] A. Nafe and A. Shamim, "An Integrable SIW Phase Shifter in a Partially Magnetized Ferrite LTCC Package," IEEE Trans. Microw. Theory Techn., vol. 63, no. 7, pp. 2264-2274, July 2015.

[69] J. R. Bray and L. Roy, "Development of a millimeter-wave ferrite-filled antisymmetrically biased rectangular waveguide phase shifter embedded in low-temperature cofired ceramic," IEEE Trans. Microw. Theory Techn., vol. 52, no. 7, pp. 1732-1739, July 2004.

[70] E. Schlomann, "Theoretical Analysis of Twin-Slab Phase Shifters in Rectangular Waveguide," IEEE Trans. Microw. Theory Techn., vol. 14, no. 1, pp. 15-23, January 1966.

[71] F. Fesharaki, C. Akyel and K. Wu, "Broadband substrate integrated waveguide edge-guided mode isolator," Electron. Lett., vol. 49, no. 4, pp. 269-271, Feb. 14 2013.

[72] C. K. Seewald and J. R. Bray, "Ferrite-Filled Antisymmetrically Biased Rectangular Waveguide Isolator Using Magnetostatic Surface Wave Modes," IEEE Trans. Microw. Theory Techn., vol. 58, no. 6, pp. 1493-1501, June 2010.

[73] R. W. Damon and J. R. Eshbach, “Magnetostatic modes of a ferromagnetic slab,” J. Phys. Chem. Solids, vol. 19, pp. 308–320, 1961.

[74] N. C. Srivastava, “Surface wave propagation through a small gap between oppositely magnetized ferrite substrates,” IEEE Trans. Microw. Theory Techn., vol. MTT-26, no. 3, pp. 213–215, Mar. 1978.

[75] N. Apaydin, K. Sertel and J. L. Volakis, "Nonreciprocal and Magnetically Scanned Leaky-Wave Antenna Using Coupled CRLH Lines," IEEE Trans. Antennas Propag., vol. 62, no. 6, pp. 2954-2961, June 2014.

[76] Ren-Pei Jiang and Ke-Zhu Wei, "A nonreciprocal birefringence effect in microwave ferrite and its applications," IEEE Trans. Magn., vol. 16, no. 5, pp. 1171-1173, September 1980.

[77] A. G. Fox, S. E. Miller and M. T. Weiss, "Behavior and applications of ferrites in the microwave region," Bell Labs Tech. J, vol. 34, no. 1, pp. 5-103, Jan. 1955.

[78] A. Afshani and K. Wu, "Nonreciprocal mode-converting substrate integrated waveguide," in Proc. 47th Eur. Microw. Conf. (EuMC), Nuremberg, Germany, Oct. 2017, pp. 532-535.

[79] Q. Zhang, C. W. Yuan and L. Liu, "Theoretical Design and Analysis for TE20 - TE10 Rectangular Waveguide Mode Converters," IEEE Trans. Microw. Theory Techn., vol. 60, no. 4, pp. 1018-1026, April 2012.

[80] K. Button and B. Lax, "Theory of ferrites in rectangular waveguides," IRE Trans. Antennas Propag., vol. 4, no. 3, pp. 531-537, July 1956.

[81] D. M. Pozar, “Theory and Design of Ferrimagnetic Components,” in Microwave Engineering, 4th ed., John Wiley & Sons, 2005, ch. 9, pp. 451-515.

[82] Y. Cassivi, L. Perregrini, P. Arcioni, M. Bressan, K. Wu, and G. Conciauro, “Dispersion characteristics of substrate integrated rectangular waveguide,” IEEE Microw. Wireless Compon. Lett., vol. 12, no. 9, pp. 333–335, Sep. 2002.

[83] L. Zeng, C. E. Tong, R. Blundell, P. K. Grimes and S. N. Paine, "A Low-Loss Edge-Mode Isolator With Improved Bandwidth for Cryogenic Operation," IEEE Trans. Microw. Theory Techn., vol. 66, no. 5, pp. 2154-2160, May 2018.

[84] C. K. Seewald and J. R. Bray, "Ferrite-Filled Antisymmetrically Biased Rectangular Waveguide Isolator Using Magnetostatic Surface Wave Modes," IEEE Trans. Microw. Theory Techn., vol. 58, no. 6, pp. 1493-1501, June 2010.

[85] Meng Cao and R. Pietig, "Ferrite coupled-line circulator with reduced length," IEEE Trans. Microw. Theory Techn., vol. 53, no. 8, pp. 2572-2579, Aug. 2005.

[86] H. How and C. Vittoria, "Microwave phase shifter utilizing nonreciprocal wave propagation," IEEE Trans. Microw. Theory Techn., vol. 52, no. 8, pp. 1813-1819, Aug. 2004.

[87] J. Chang, J. Kao, Y. Lin and H. Wang, "Design and Analysis of 24-GHz Active Isolator and Quasi-Circulator," IEEE Trans. Microw. Theory Techn., vol. 63, no. 8, pp. 2638-2649, Aug. 2015.

[88] S. A. Ayati, D. Mandal, B. Bakkaloglu and S. Kiaei, "Integrated Quasi-Circulator With RF Leakage Cancellation for Full-Duplex Wireless Transceivers," IEEE Trans. Microw. Theory Techn., vol. 66, no. 3, pp. 1421-1430, March 2018.

[89] S. K. Cheung, T. P. Halloran, W. H. Weedon and C. P. Caldwell, "MMIC-Based Quadrature Hybrid Quasi-Circulators for Simultaneous Transmit and Receive," IEEE Trans. Microw. Theory Techn., vol. 58, no. 3, pp. 489-497, March 2010.

[90] S. Qin, Q. Xu and Y. E. Wang, "Nonreciprocal Components With Distributedly Modulated Capacitors," IEEE Trans. Microw. Theory Techn., vol. 62, no. 10, pp. 2260-2272, Oct. 2014.

[91] Y. S. Li, X. P. Yu and Z. H. Lu, "Nonreciprocal Time-Varying Transmission Line with Carrier Boosting Technique for Low-Noise RF Front Ends," IEEE Microw. Wireless Compon. Lett., vol. 28, no. 11, pp. 1011-1013, Nov. 2018.

[92] Y. E. Wang, "Time-varying transmission lines (TVTL) - A new pathway to nonreciprocal and intelligent RF front-ends," IEEE Radio and Wireless Symp. (RWS), Newport Beach, CA, 2014, pp. 148-150.

[93] N. A. Estep, D. L. Sounas, and A. Alù, “Magnetless microwave circulators based on spatiotemporally modulated rings of coupled resonators,” IEEE Trans. Microw. Theory Techn., vol. 64, no. 2, pp. 502–518, Feb. 2016.

[94] N. Reiskarimian and H. Krishnaswamy, “Magnetic-free non-reciprocity based on staggered commutation,” Nature Commun., vol. 7, Apr. 2016, Art. no. 11217.

[95] M. M. Biedka, R. Zhu, Q. M. Xu, and Y. E. Wang, “Ultra-wide band nonreciprocity through sequentially-switched delay lines,” Sci. Rep., vol. 7, Jan. 2017, Art. no. 40014.

[96] W. D'Orazio, K. Wu and J. Helszajn, "A substrate integrated waveguide degree-2 circulator," IEEE Microw. Wireless Compon. Lett., vol. 14, no. 5, pp. 207-209, May 2004.

[97] A. V. Sadovnikov et al., "Magnon Straintronics: Reconfigurable Spin-Wave Routing in Strain-Controlled Bilateral Magnetic Stripes," Phys. Rev. Lett., vol. 120, pp. 257203, June 2018.

[98] A. V. Sadovnikov et al., "Route toward semiconductor magnonics: Light-induced spin-wave nonreciprocity in a YIG/GaAs structure," Phys. Rev. B, vol. 99, pp. 054424, February 2019.

[99] R. F. Soohoo, "Theory of Dielectric-Loaded and Tapered-Field Ferrite Devices," in IRE Trans. Microw. Theory Techn., vol. 9, no. 3, pp. 220-224, May 1961

[100] G. N. Tsandoulas, D. H. Temme and F. G. Willwerth, "Longitudinal Section Mode Analysis of Dielectrically Loaded Rectangular Waveguides with Application to Phase Shifter Design," IEEE Trans. Microw. Theory Techn., vol. 18, no. 2, pp. 88-95, February 1970.

[101] J. Uher, F. Arndt and J. Bornemann, "Field Theory Design of Ferrite-Loaded Waveguide Nonreciprocal Phase Shifters with Multisection Ferrite Or Dielectric Slab Impedance Transformers," IEEE Trans. Microw. Theory Techn., vol. 35, no. 6, pp. 552-560, June 1987.

[102] B. Lax, K. J. Button, and L. M. Roth, “Ferrite phase shifters in rectangular waveguide,” J. Appl. Phys. 25(6), 1413–1421 (1954).

[103] M. E. Hines, "Reciprocal and Nonreciprocal Modes of Propagation in Ferrite Stripline and Microstrip Devices," IEEE Trans. Microw. Theory Techn., vol. 19, no. 5, pp. 442-451, May 1971.

[104] J. D. Adam, L. E. Davis, G. F. Dionne, E. F. Schloemann and S. N. Stitzer, "Ferrite devices and materials," IEEE Trans. Microw. Theory Techn., vol. 50, no. 3, pp. 721-737, March 2002.

[105] A. Afshani and K. Wu, "Nonreciprocal Mode Converting Waveguide and Circulator," IEEE Trans. Microw. Theory Techn., vol. 67, no. 8, pp. 3350-3360, Aug. 2019.

[106] A. Afshani and K. Wu, “Nonreciprocal Mode Converting Substrate Integrated Waveguide with Unsymmetrical Perturbation,” in IEEE MTT-S Int. Microw. Symp. Dig., Boston, MA, USA, June 2019.

[107] F. Taringou, D. Dousset, J. Bornemann, and K. Wu, “Substrate-integrated waveguide transitions to planar transmission-line technologies,” in IEEE MTT-S Int. Microw. Symp. Dig., Montreal, QC, Canada, Jun. 2012, pp. 1–3.

[108] Z. Kordiboroujeni and J. Bornemann, “New wideband transition from microstrip line to substrate integrated waveguide” IEEE Trans. Microw. Theory Techn., vol. 62, no. 12, pp. 2983–2989, Dec. 2014.

[109] Y. Ding and K. Wu, "Substrate Integrated Waveguide-to-Microstrip Transition in Multilayer Substrate," IEEE Trans. Microw. Theory Techn. vol. 55, no. 12, pp. 2839-2844, Dec. 2007.

[110] P. Wu, J. Liu and Q. Xue, "Wideband Excitation Technology of TE20 Mode Substrate Integrated Waveguide (SIW) and Its Applications," IEEE Trans. Microw. Theory Techn, vol. 63, no. 6, pp. 1863-1874, June 2015.

[111] H. Chou, C. Chang and Y. Chen, "Ferrite Circulator Integrated Phased-Array Antenna Module for Dual-Link Beamforming at Millimeter Frequencies," in IEEE Transactions on Antennas and Propagation, vol. 66, no. 11, pp. 5934-5942, Nov. 2018, doi: 10.1109/TAP.2018.2862343.

[112] H. Turki, L. Huitema, T. Monediere, B. Lenoir and C. Breuil, "New Concept Validation of Low-Loss Dual-Band Stripline Circulator," in IEEE Transactions on Microwave Theory and Techniques, vol. 67, no. 3, pp. 845-850, March 2019, doi: 10.1109/TMTT.2018.2890632.

[113] V. Olivier et al., "Dual-Band Ferrite Circulators Operating on Weak Field Conditions: Design Methodology and Bandwidths' Improvement," in IEEE Transactions on Microwave Theory and Techniques, vol. 68, no. 7, pp. 2521-2530, July 2020, doi: 10.1109/TMTT.2020.2988003.

[114] C. R. Boyd, "A Dual-Mode Latching Reciprocal Ferrite Phase Shifter," in IEEE Transactions on Microwave Theory and Techniques, vol. 18, no. 12, pp. 1119-1124, December 1970, doi: 10.1109/TMTT.1970.1127421.

[115] W. E. Hord, C. R. Boyd and D. Diaz, "A New Type of Fast-Switching Dual-Mode Ferrite Phase Shifter," in IEEE Transactions on Microwave Theory and Techniques, vol. 35, no. 12, pp. 1219-1225, Dec 1987, doi: 10.1109/TMTT.1987.1133840.

[116] A. Afshani and K. Wu, "Concurrent Dual-Mode Circulator," 2019 49th European Microwave Conference (EuMC), Paris, France, 2019, pp. 284-287, doi: 10.23919/EuMC.2019.8910904.

[117] A. Afshani and K. Wu, "Modal Nonreciprocity and Circulator Based on Nonreciprocal Mode Conversion," in IEEE Transactions on Microwave Theory and Techniques, vol. 67, no. 12, pp. 4922-4934, Dec. 2019, doi: 10.1109/TMTT.2019.2951566.

[118] Nai-Shuo Cheng, A. Alexanian, M. G. Case, D. B. Rensch and R. A. York, "40-W CW broad-band spatial power combiner using dense finline arrays," in IEEE Transactions on Microwave Theory and Techniques, vol. 47, no. 7, pp. 1070-1076, July 1999, doi: 10.1109/22.775438.

[119] M. Belaid, R. Martinez and Ke Wu, "A mode transformer using fin-line array for spatial power-combiner applications," in IEEE Transactions on Microwave Theory and Techniques, vol. 52, no. 4, pp. 1191-1198, April 2004, doi: 10.1109/TMTT.2004.825707.

[120] X. Zou, F. Geng, Y. Li and Y. Leng, "Phase Inverters Based on Substrate Integrated Waveguide," in IEEE Microwave and Wireless Components Letters, vol. 27, no. 3, pp. 227-229, March 2017, doi: 10.1109/LMWC.2017.2663106.

[121] J. D. Díaz et al., "A Cross-Stacked Radiating Antenna With Enhanced Scanning Performance for Digital Beamforming Multifunction Phased-Array Radars,"

in IEEE Transactions on Antennas and Propagation, vol. 66, no. 10, pp. 5258-5267, Oct. 2018.

[122] Y. Li and K. Luk, "60-GHz Dual-Polarized Two-Dimensional Switch-Beam Wideband Antenna Array of Aperture-Coupled Magneto-Electric Dipoles," in IEEE Transactions on Antennas and Propagation, vol. 64, no. 2, pp. 554-563, Feb. 2016.

[123] Z. Chen, H. Liu, J. Yu and X. Chen, "High Gain, Broadband and Dual-Polarized Substrate Integrated Waveguide Cavity-Backed Slot Antenna Array for 60 GHz Band," in IEEE Access, vol. 6, pp. 31012-31022, 2018.

[124] B. Feng, Y. Tu, J. Chen, S. Yin and K. L. Chung, "Dual Linearly-Polarized Antenna Array With High Gain and High Isolation for 5G Millimeter-Wave Applications," in IEEE Access, vol. 8, pp. 82471-82480, 2020.

[125] W. M. Abdel-Wahab and S. Safavi-Naeini, "Wide-Bandwidth 60-GHz Aperture-Coupled Microstrip Patch Antennas (MPAs) Fed by Substrate Integrated Waveguide (SIW)," in IEEE Antennas and Wireless Propagation Letters, vol. 10, pp. 1003-1005, 2011.

[126] A. Beltayib, I. Afifi and A. Sebak, "4 × 4-Element Cavity Slot Antenna Differentially-Fed by Odd Mode Ridge Gap Waveguide," in IEEE Access, vol. 7, pp. 48185-48195, 2019.

[127] Zhao and K. Luk, "Dual Circular-Polarized SIW-Fed High-Gain Scalable Antenna Array for 60 GHz Applications," in IEEE Transactions on Antennas and Propagation, vol. 66, no. 3, pp. 1288-1298, March 2018.

[128] T. Yang, Z. Zhao, D. Yang, X. Liu and Q. Liu, "A Single-Layer SIW Slots Array Monopulse Antenna Excited by a Dual-Mode Resonator," in IEEE Access, vol. 7, pp. 131282-131288, 2019.

[129] H. Jin, W. Che, K. Chin, W. Yang and Q. Xue, "Millimeter-Wave TE20-Mode SIW Dual-Slot-Fed Patch Antenna Array With a Compact Differential Feeding Network," in IEEE Transactions on Antennas and Propagation, vol. 66, no. 1, pp. 456-461, Jan. 2018.

[130] S. D. Targonski, R. B. Waterhouse and D. M. Pozar, "Design of wide-band aperture-stacked patch microstrip antennas," in IEEE Transactions on Antennas and Propagation, vol. 46, no. 9, pp. 1245-1251, Sept. 1998.

[131] 3GPP TS 38.104, "5G; NR; Base Station (BS) radio transmission and reception",v.15.2.0, (2018).

# APPENDIX A LIST OF PUBLICATIONS

## Patent

- **Afshani**, Amir, & Wu, Ke. (2017). “NONRECIPROCAL MODE CONVERTING SUBSTRATE INTEGRATED WAVEGUIDE.” U.S. Patent No. 15/612,450, filed June 02, 2017.

## Peer reviewed Journal Papers

- **A. Afshani** and K. Wu, "Modal Nonreciprocity and Circulator Based on Nonreciprocal Mode Conversion," in *IEEE Transactions on Microwave Theory and Techniques*, vol. 67, no. 12, pp. 4922-4934, Dec. 2019, doi: 10.1109/TMTT.2019.2951566.
- **A. Afshani** and K. Wu, "Nonreciprocal Mode Converting Waveguide and Circulator," in *IEEE Transactions on Microwave Theory and Techniques*, vol. 67, no. 8, pp. 3350-3360, Aug. 2019, doi: 10.1109/TMTT.2019.2919591.
- **A. Afshani** and K. Wu, "Generalized Theory of Concurrent Multi-Mode Reciprocal and/or Nonreciprocal SIW Ferrite Devices," IEEE Transactions on Microwave Theory and Techniques, (submitted April 2021).
- **A. Afshani** and K. Wu, "Dual-Polarized Patch Antenna Excited Concurrently by a Dual-Mode SIW," IEEE Transactions on Antennas and Propagation, (submitted March 2021).

## Conference Papers

- **A. Afshani** and K. Wu, "Concurrent Dual-Mode Circulator," 2019 49th European Microwave Conference (EuMC), Paris, France, 2019, pp. 284-287, doi: 10.23919/EuMC.2019.8910904.
- **A. Afshani** and K. Wu, "Nonreciprocal Mode Converting Substrate Integrated Waveguide with Unsymmetrical Perturbation," 2019 IEEE MTT-S International Microwave Symposium (IMS), Boston, MA, USA, 2019, pp. 861-864, doi: 10.1109/MWSYM.2019.8701053.

- **A. Afshani** and K. Wu, "Nonreciprocal mode-converting substrate integrated waveguide," 2017 47th European Microwave Conference (EuMC), Nuremberg, 2017, pp. 532-535, doi: 10.23919/EuMC.2017.8230907.